
Transport processes and instabilities induced by electric fields acting on fluidic interfaces

Durch elektrische Felder an fluiden Grenzflächen hervorgerufene Transportprozesse und Instabilitäten

Zur Erlangung des akademischen Grades Doktor-Ingenieur (Dr.-Ing.)

Genehmigte Dissertation von Sebastian Dehe aus Wiesbaden

Tag der Einreichung: 16.08.2021, Tag der Prüfung: 19.10.2021

1. Gutachten: Prof. Dr. rer. nat. Steffen Hardt

2. Gutachten: Prof. Moran Bercovici, Ph.D.

Darmstadt – D 17



TECHNISCHE
UNIVERSITÄT
DARMSTADT

Mechanical Engineering
Department
Nano- and Microfluidics

Transport processes and instabilities induced by electric fields acting on fluidic interfaces
Durch elektrische Felder an fluiden Grenzflächen hervorgerufene Transportprozesse und Instabilitäten

Accepted doctoral thesis by Sebastian Dehe

1. Review: Prof. Dr. rer. nat. Steffen Hardt
2. Review: Prof. Moran Bercovici, Ph.D.

Date of submission: 16.08.2021

Date of thesis defense: 19.10.2021

Darmstadt – D 17

Bitte zitieren Sie dieses Dokument als:

URN: urn:nbn:de:tuda-tuprints-198128

URL: <http://tuprints.ulb.tu-darmstadt.de/19812>

Dieses Dokument wird bereitgestellt von tuprints,

E-Publishing-Service der TU Darmstadt

<http://tuprints.ulb.tu-darmstadt.de>

tuprints@ulb.tu-darmstadt.de

Darmstadt, Technische Universität Darmstadt,

Jahr der Veröffentlichung der Dissertation auf TUprints: 2022

Die Veröffentlichung steht unter folgender Creative Commons Lizenz:

Namensnennung - Nicht kommerziell - Keine Bearbeitungen 4.0 International (CC BY-NC-ND 4.0)

<https://creativecommons.org/licenses/by-nc-nd/4.0/deed.de>

Erklärungen laut Promotionsordnung

§8 Abs. 1 lit. c PromO

Ich versichere hiermit, dass die elektronische Version meiner Dissertation mit der schriftlichen Version übereinstimmt.

§8 Abs. 1 lit. d PromO

Ich versichere hiermit, dass zu einem vorherigen Zeitpunkt noch keine Promotion versucht wurde. In diesem Fall sind nähere Angaben über Zeitpunkt, Hochschule, Dissertationsthema und Ergebnis dieses Versuchs mitzuteilen.

§9 Abs. 1 PromO

Ich versichere hiermit, dass die vorliegende Dissertation selbstständig und nur unter Verwendung der angegebenen Quellen verfasst wurde.

§9 Abs. 2 PromO

Die Arbeit hat bisher noch nicht zu Prüfungszwecken gedient.

Darmstadt, 16.08.2021

Sebastian Dehe

Abstract

Electrohydrodynamics (EHD) describes the area of research, which studies the interactions of fluid motion and electric fields. In liquids with non-negligible conductivity, charged regions are confined to thin layers closest to boundaries, where EHD effects are most pronounced. In the present work, different phenomena that involve the actuation of fluidic interfaces by electric fields are studied.

Electro-osmosis describes the fluid flow due to electric fields acting on charged regions close to the interface of a fluidic domain. When a liquid is deposited above a microstructured superhydrophobic surface, additional charges can be brought to the enclosed gas-liquid interface by placing a gate electrode below the surface. In this work, the production of a superhydrophobic surface with both micro- and nano-scales is described. In addition to inducing charges, a gate electrode exerts a force on the gas-liquid interface, pulling it in between the structures. Experimentally, the wetting state stability is characterized using reflection microscopy, revealing a continuous range of wetting states at dual-scale surfaces.

By using non-constant electro-osmotic flow, complex height-averaged flow fields can be induced in a Hele-Shaw cell, which is characterized by a small distance between the parallel bounding walls compared to a characteristic lateral length scale. The governing equations for of the flow field are derived, accounting both for stationary and oscillatory electric fields. The electro-osmotic flow field is characterized above a single disc-shaped gate electrode in a microfluidic channel, using particle tracking velocimetry. In addition, using proof-of-principle experiments, the ability to create complex flow patterns is demonstrated.

In order to use flow shaping in biochemical applications, a height-averaged transport model for a passive species is derived using a perturbation method, accounting for advection, diffusion and sample dispersion. The effects of sample dispersion are represented by a non-isotropic dispersion tensor. The reduced-order model shows good agreement to three-dimensional simulations, and potential applications are discussed.

Electric fields lead to forces on fluidic interfaces, and in this work, two different EHD instabilities at an interface between a dielectric and a conducting liquid are investigated. Upon application of a spatially homogeneous, harmonically oscillating electric field, a resonant response of the interface can be observed above a critical amplitude. An experimental setup with a circular domain is used to observe the spatial structure of the instability, which is extracted from light-refraction at the liquid-liquid interface. The resulting dominant wavelengths and instability modes show good agreement to an analytical model. Furthermore, the role of the domain boundary is investigated.

Upon applying a spatially inhomogeneous, but time-constant electric field, the interface exhibits EHD tip streaming above a critical voltage, emitting droplets into the dielectric phase. The presence of conducting droplets alters the spatial structure from a Taylor cone located centric below the pin electrode to a surface depression, where the interface moves away from the electrode and cones emerge from the rim. By experimentally characterizing a submerged electrospray and using additional numerical modeling, it is shown that the droplets induce a flow in the dielectric liquid, which is responsible for the change of the spatial structure of the instability.

Kurzfassung

Die Elektrohydrodynamik (EHD) ist das Forschungsgebiet, das sich mit den Wechselwirkungen zwischen Strömungen und elektrischen Feldern befasst. In leitenden Flüssigkeiten sind Ladungen auf dünne Schichten in der Nähe von Grenzflächen mit stark ausgeprägten EHD-Effekten beschränkt. In der vorliegenden Arbeit werden verschiedene Phänomene untersucht, in denen fluide Grenzflächen durch elektrische Felder beeinflusst werden.

Elektroosmose beschreibt die Flüssigkeitsströmung aufgrund von elektrischen Feldern, die auf Ladungen in der Nähe einer Grenzfläche wirken. Wenn eine Flüssigkeit in Kontakt mit einer mikrostrukturierten, superhydrophoben Oberfläche ist, können zusätzliche Ladungen an der eingeschlossenen Gas-Flüssigkeits-Grenzfläche durch eine Gate-Elektrode unter der Oberfläche induziert werden. In dieser Arbeit wird die Herstellung einer superhydrophoben Oberfläche mit Mikro- und Nanostrukturen beschrieben. Neben der Induktion von Ladungen übt eine Gate-Elektrode eine Kraft auf die Grenzfläche aus, die den Benetzungszustand beeinflusst. Experimentell wird mittels Lichtmikroskopie die Stabilität der Benetzungszustände charakterisiert, welche an hierarchischen Oberflächen ein kontinuierliches Spektrum aufweisen.

Durch eine räumlich variierende elektroosmotische Strömung können komplexe höhengemittelte Strömungsfelder in einer Hele-Shaw Zelle induziert werden, die durch einen geringen Wandabstand im Vergleich zu einer typischen lateralen Längenskala gekennzeichnet ist. Die Bestimmungsgleichungen für das Strömungsfeld werden abgeleitet, welche sowohl stationäre als auch oszillierende elektrische Felder berücksichtigen. Das Geschwindigkeitsfeld wird experimentell über einer kreisförmigen Gate-Elektrode in einem mikrofluidischen Kanal mit Hilfe partikelgestützter Geschwindigkeitsmessungen charakterisiert. Außerdem wird die Fähigkeit zur Erzeugung komplexer Strömungsfelder experimentell demonstriert.

Um die Strömungen in Hele-Shaw-Zellen für biochemische Anwendungen nutzen zu können, wird ein höhengemitteltes Transportmodell für eine passive chemische Spezies mit Hilfe einer Störungsrechnung abgeleitet, welches Advektion, Diffusion und Dispersion berücksichtigt. Die Dispersion wird durch einen nicht-isotropen Dispersionstensor abgebildet. Das höhengemittelte Modell zeigt eine gute Übereinstimmung mit 3D-Simulationen, und abschließend werden mögliche Anwendungen diskutiert.

Elektrische Felder üben Kräfte auf fluide Grenzflächen aus, und in dieser Arbeit werden zwei EHD-Instabilitäten an der Grenzfläche zwischen einer dielektrischen und einer leitenden Flüssigkeit untersucht. Beim Anlegen eines räumlich homogenen, harmonisch oszillierenden elektrischen Feldes tritt oberhalb einer kritischen Amplitude eine resonante Antwort der Grenzfläche auf. In einem Versuchsaufbau mit einer kreisförmigen Berandung wird die räumliche Struktur der Instabilität untersucht, welche mit Hilfe der Lichtbrechung an der Grenzfläche extrahiert wird. Die resultierenden Wellenlängen und Instabilitätsmoden zeigen eine gute Übereinstimmung mit einem analytischen Modell. Außerdem wird der Einfluss der Berandung untersucht.

Beim Anlegen eines räumlich inhomogenen, aber zeitlich konstanten elektrischen Feldes wird die Grenzfläche oberhalb einer kritischen Spannung instabil und emittiert Tropfen in die dielektrische Phase. Die geladenen Tropfen ändern die räumliche Struktur der Instabilität von einem Taylor-Konus, welcher sich mittig unter der Stiftelektrode befindet, zu einer Senke, in welcher sich die Grenzfläche von der Elektrode wegbewegt und zusätzliche Instabilitäten am Rand hervortreten. Experimente mit einem eingetauchten Elektrospray sowie zusätzliche numerische Modellbildung zeigen, dass die Tropfen eine Strömung in der dielektrischen Phase hervorrufen, welche für die Änderung der räumlichen Struktur der Instabilität verantwortlich ist.

Preface and acknowledgments

This thesis is a result of my time as a PhD student at the Institute for Nano- and Microfluidics at the Department of Mechanical Engineering at Technische Universität Darmstadt. It would have been impossible to write without the extensive support I received throughout the projects.

First of all, I would like to express my gratitude to my advisor, Prof. Dr. rer. nat. Steffen Hardt, for providing me with the opportunity to conduct my doctoral studies under his guidance. His insight and mentoring were invaluable for navigating the deep waters of both the underlying physics and academia, while simultaneously giving me the chance to bring in own ideas. Furthermore, I would like to thank Prof. Moran Bercovici for his guidance and support during our cooperation, and especially for hosting me at his lab and the experiences during this stay. In addition, I am grateful to him for agreeing to act as referee for this thesis.

Next, I would like to thank all my present and past colleagues for the great working environment. Special thanks are due to Tobias Baier, Johannes Hartmann, Maximilian Hartmann, Maximilian Schür, Michael Eigenbrod and Henning Bonart for unique insights, both work-related and beyond, and their endurance when I showed up once again in their office. The technical aspects of this work would not have been possible without the support of Klaus-Dieter Voss, Jörg Bültemann and Frank Plückebaum, as well as the IT support by Lidia Querling and the rest of the IT-Team. In addition, the administrative support of Corinna Neumann is highly appreciated.

The work presented in this thesis would not have been possible without the interesting and versatile collaborations over the past 4 years. I thank Baruch Rofman, Khaled Ghommed and Valeri Frumkin for the joint work in the framework of the GIF-project, and the rest of the microfluidic technologies laboratory at Technion for welcoming me during my stay in Haifa. Furthermore, the collaborations with Maximilian Hartmann, Shijie Zhu and Aditya Bandopadhyay in the framework of the DFG-funding are highly appreciated. Also, the support of both the Target Laboratory at the IKP and the Institute of Microwave Engineering and Photonics is highly valued, who provided their facilities and know-how without expecting compensation. Furthermore, I thank both Imke Rehm and Julian Keller for their work as "my" students during their final thesis.

Aside the acknowledgments to specific persons, the generous financial support of both the *German-Israeli Foundation for Scientific Research and Development* (Grant No. I-1346-401.10/2016) and the *Deutsche Forschungsgemeinschaft* (DFG, Grant No. HA 2696/45-1) is kindly acknowledged. Also, I would like to thank TU Darmstadt and its subsidiary institutions in general, and the SFB 1194 in particular for creating and maintaining an inspiring environment and providing various opportunities for stimulating input.

I am no wordsmith, so the following lines can only roughly sketch out my gratitude. I would like to thank my family and friends for their support and understanding throughout the years. Your thoughts and perspective have helped me through the rougher patches, and your presence made the lighter ones even more enjoyable. Last but not least, I would like to thank Tina for being a part of my life. Your patience, encouragement and support have had a big part in this thesis seeing the light of day, and your occasional nudge motivated me to see the same without an intermittent window.

Contents

1	Introduction	1
2	Fundamentals	5
2.1	General assumptions	5
2.2	Electrostatics	6
2.2.1	Electrostatic jump conditions at material interfaces	7
2.3	Hydrodynamics	8
2.3.1	Conservation of mass: Continuity equation	8
2.3.2	Conservation of momentum: Navier-Stokes equations	9
2.3.3	Hydrodynamic boundary conditions at a free interface	13
2.3.4	Hydrodynamic boundary conditions at solid interfaces	16
2.4	Conservation of chemical species	17
2.5	Electric double layer	20
2.6	Cross-references	21
3	The gas-liquid interface at a superhydrophobic surface under normal electric fields	23
3.1	Introduction	23
3.2	Wetting states on microstructured surfaces	25
3.2.1	Contact angles on flat and structured surfaces	25
3.2.2	Wetting state transitions	28
3.2.3	Strategies to prevent wetting state transition	30
3.3	Production of superhydrophobic surfaces	32
3.3.1	Single-scale microstructures: PDMS micropillars	33
3.3.2	Dual-scale microstructures: Application of a secondary nanostructure	34
3.4	Characterization of wetting states: Light reflection microscopy	35
3.5	Discussion	41
3.5.1	Wetting state reversibility	41
3.5.2	Contact angle hysteresis in the nano Cassie-Baxter state: Contact angle measurement	43
3.6	Summary and Outlook	46
4	Electro-osmotic flow at a gas-liquid interface over a superhydrophobic surface	49
4.1	Introduction	49
4.2	Electro-osmotic flow	51
4.2.1	Electro-osmotic flow over flat surfaces	51
4.2.2	Electro-osmotic flow over heterogeneous surfaces	53
4.3	Flow in Hele-Shaw cells: Governing equations	57
4.3.1	Shallow flow regime	58
4.3.2	Governing equations for the flow	59
4.3.3	Flow field of a circular wall mobility	62
4.4	Characterization of electro-osmotic flow over superhydrophobic surfaces	63
4.4.1	Experimental setup	63



4.4.2	Flow velocity measurements	64
4.4.3	Rescaled flow velocity	66
4.4.4	Influence of the electrolyte	69
4.5	Discussion	70
4.5.1	Comparison to no-slip surfaces	70
4.5.2	Influence of surfactants	70
4.5.3	Demonstration of flow shaping by multiple electrodes	71
4.5.4	Relation to electrowetting stability	72
4.6	Summary and Outlook	74
5	Dispersion in electrokinetic Hele-Shaw flows	75
5.1	Introduction	75
5.2	Shear-induced sample dispersion	76
5.2.1	Dispersion in stationary pressure-driven flow through a capillary: Taylor-Aris dispersion	76
5.2.2	Dispersion in oscillatory flow fields	79
5.2.3	Dispersion in the context of microfluidics	80
5.3	Species transport in inhomogeneous Hele-Shaw flows	82
5.3.1	Introduction	82
5.3.2	Leading order perturbation: $O = (\epsilon^0)$	85
5.3.3	First-order perturbation: $O = (\epsilon^1)$	85
5.3.4	Second-order perturbation: $O = (\epsilon^2)$	87
5.3.5	Resulting macrotransport equation	88
5.3.6	Thermodynamic consistency of the dispersion tensor	89
5.3.7	Resulting dispersion tensor for a parametrized flow field	90
5.4	Comparison between 3D and 2D numerical computations	91
5.4.1	Numerical methods	91
5.4.2	Test case A: Dispersion in steady flow	95
5.4.3	Test case B: Dispersion in oscillatory flow	96
5.4.4	Test case C: Dispersion in circulatory flow field	98
5.5	Discussion	102
5.5.1	Experimental demonstration of the blinking vortex principle	102
5.5.2	The inverse problem: Dispersion shaping	104
5.6	Summary and conclusion	108
6	Instabilities at liquid-liquid interfaces under homogeneous AC fields	109
6.1	Introduction	109
6.2	Fundamentals	111
6.2.1	Faraday instability	111
6.2.2	Refraction	118
6.3	Methods	118
6.3.1	Experimental setup	118
6.3.2	Experimental procedure	120
6.3.3	Data evaluation algorithm	120
6.3.4	Fluid data	125
6.4	Results	126
6.4.1	Influence of the salt concentration	126
6.4.2	Influence of the dielectric's viscosity	128
6.4.3	Influence of the conducting liquid viscosity	129
6.4.4	Spatial structure of the instability pattern	129

6.5	Discussion	134
6.5.1	Comparison to observations of Ward et al.	134
6.5.2	Robustness analysis of wavelength determination algorithm versus measurement uncertainty	135
6.5.3	Potential influence of the discrete modes on the stability map	137
6.6	Summary and conclusion	138
7	Instabilities at liquid-liquid interfaces under inhomogeneous DC fields	139
7.1	Introduction	139
7.2	Fundamentals of electrohydrodynamic tip streaming	141
7.2.1	Steady cone-jet mode	142
7.2.2	Alternative operating modes of electrohydrodynamic tip streaming	143
7.2.3	Submerged electrosprays	144
7.2.4	Properties of the electrospray	145
7.3	Experimental methods	146
7.3.1	Experimental setup	146
7.3.2	Fluid data	148
7.4	EHD tip streaming induced by a pin electrode	149
7.5	Dimple formation by a submerged electrospray	152
7.5.1	Experimental results	154
7.6	Numerical modeling	159
7.7	Summary and conclusion	165
8	Concluding remarks	167
	Bibliography	169
	Symbols and Abbreviations	187
	List of Figures	197
	List of Tables	211

1 Introduction

The first experiments involving interactions of electric fields and fluid motion were performed by electrifying amber or glass, and bringing it in close proximity to a liquid surface. Among the first written reports, Gray (1731) reported the deformation of a liquid interface towards an electrified glass tube, and ultimately observed sparking and the transfer of droplets. These observations showed that electric fields can be used to manipulate liquids. When Volta (1800) invented the first electric battery, a continuous source of electric current became available to researchers, enabling new experimental designs. Reuss (1809) was among the first to utilize such a voltaic pile in an experiment (Biscombe, 2017): Two reservoirs were separated by a porous barrier made of quartz powder and were equally filled with water. When the reservoirs were connected to the battery, the water flowed from one reservoir to the other. Today, this effect is known as electro-osmosis, and it provides a mechanism to induce fluidic motion by applying electric fields. In the next 160 years, experiments and theoretical descriptions advanced rapidly in the area of EHD, with a wide range of aspects illuminated.

Electrohydrodynamics (EHD) describes the area of research which is concerned with the interaction of fluid motion and electric fields. In 1969, Melcher and Taylor provided a review of electrohydrodynamics in the context of ohmic fluids and dominant interfacial electrical shear stress, which up to today remains one of the hallmark papers of electrohydrodynamics. Its value lies in the unified description of perfectly insulating and perfectly conducting liquids as limiting cases of the more general *leaky dielectric* with finite conductivity. In their introduction, the authors raise a series of important aspects of EHD, which are worthwhile to discuss:

”The word ”electrohydrodynamics” is relatively new; the area it represents is not. The related literature is as venerable as that for the subject of electricity itself. Even more, to generate an engineering interest there is no need to emphasize the great technological promise of the area, since applications already form the basis for major industries. But the center of attention in almost any discussion is the lack of reproducibility in experiments and the inadequacies of theoretical models. Electrostatic effects in fluids are known for their vagaries; often they are extremely dependent on electrical conduction that investigators are discouraged from carefully relating analytical models and simple experiments. Yet the foundations of fluid mechanics are formed from work that relates carefully designed experiments to analytical models [...]”
(Melcher and Taylor, 1969)

First, let us address the *”great technological promise”* of EHD: Melcher and Taylor published their review roughly 50 years ago. Today, EHD phenomena have found entrance into a wide range of technological applications important for our every-day life, and in the following, three different utilizations are discussed to highlight the continuing relevance of this field. The first example is capillary electrophoresis (CE), which is one of the standard techniques to separate chemical analytes according to their ionic mobility. It allows the detection and quantification of specific species within a sample (Jorgenson and DeArman Lukacs, 1981). Possibly among the widest-known, yet least-recognized applications for CE is human identity testing (Butler, 2007). DNA profiling utilizes the fact that specific regions of the DNA show repeating patterns, with the number of repeats varying between individuals. Using CE, the

number of repeats is determined for a standardized set of patterns, which allows a statistically significant discrimination of DNA samples from different individuals. Here, an EHD phenomenon enabled the development of a standardized process, which has revolutionized forensic analysis.

Another widely established technology based on EHD effects is electrospray ionization (ESI). Here, a liquid with dissolved molecules is dispersed into a fine aerosol using electric fields, with the same physical mechanism that was described by Gray (1731) nearly 300 years ago. As the spray undergoes subsequent evaporation and secondary breakup, macromolecules leave the droplets and are present as ions (Fenn et al., 1989). Consequently, ESI enables ionization of macromolecules without fragmentation of the analytes, overcoming a critical limitation of alternative ionization techniques (Banerjee and Mazumdar, 2012). Subsequently, these ions can be analyzed using mass spectrometry, yielding information about the charge-to-mass ratio of the molecules as well as structural information. Since electrospray ionization enabled the characterization of large biomolecules, John Fenn was jointly awarded the Nobel Prize in Chemistry in 2002.

A third field of application for EHD phenomena is the miniaturization of biochemical processes, often associated with the idea to provide the functionality of a macroscopic laboratory on one integrated, much smaller platform ("Lab-on-a-Chip"). EHD effects are often most pronounced close to boundaries, thus becoming more important in systems with increasing surface-to-volume ratios. On small scales, EHD effects are therefore at the basis of fluidic pumping, particle manipulation and sample concentration on small scales, and thus provide a comprehensive toolkit for miniaturized systems. For example, it has been shown that the detection of SARS-CoV-2 in human specimen can be performed using a microfluidic chip based on EHD effects (Ramachandran et al., 2020). However, this example also highlights one of the challenges of process miniaturization. In principle, every step of the SARS-CoV-2 was performed using a microfluidic environment and EHD phenomena, nevertheless, it required human interaction between each processing step such as sample loading. The full integration of the detection procedure from start to finish on one platform remains challenging, but also shows further promise.

These three examples of techniques exemplify the range of state-of-the-art applications, for which electrohydrodynamic effects have been successfully employed since the work of Melcher and Taylor. Both in standardized processes as well as in research applications, electric field driven effects have supplied a range of potent tools, which can be used in the realms of physics, chemistry, and biology. So far, it has kept up with its "*great technological promise*". With emerging technologies such as gene editing and DNA sequencing, new fields of applications arise, which benefit from the already developed toolkit and require the development of new applications.

The second point addressed by Melcher and Taylor regards the "*lack of reproducibility in experiments and the inadequacies of theoretical models*". Often enough, researchers are confronted with unexpected experimental observations. The discrepancy between prediction and outcome can be attributed to at least two reasons: First, controlling all experimental parameters can be challenging, since EHD phenomena are based on an intricate interplay between electric effects, fluid flow, species transport, energy transport and chemical reactions. Apart from the strong dependence on conductivity mentioned by Melcher and Taylor, other properties of the liquids, e.g., buffer strength and pH value of electrolytes, ion mobilities, and impurities, can significantly change the outcome of the experiments. In addition, not only the fluids themselves, but also their interactions with solid interfaces can strongly alter the observed phenomena. Among others, the surface material composition, the wall chemistry, and the exact form of the charged layer next to the wall are of importance. Furthermore, effects related to fluid-fluid interfaces can become important, e.g., due to the existence of surface active substances, miscibility effects of liquids, or dissolution of gas. In principle, descriptions of the impact of the aforementioned effects exist, but due to the sheer amount of mechanisms, it is not realistic to account for all parameters in every experiment. Therefore, it is important to identify the relevant effects, and in turn, determine

the negligible parameters. Sometimes, effects thought to be irrelevant couple in surprising ways, leading to unexpected results, and if the experimental parameters are not well controlled, to seemingly lacking reproducibility.

A second reason for discrepancies between prediction and outcome is the lack of comprehensive theoretical descriptions. Not least through the efforts of Melcher and Taylor, the agreement of theoretical models and experimental observations has increased over time (Saville, 1997). Also, with the rise of microfluidics and the use of electric field effects therein, theoretical descriptions of experimental observations have been employed successfully alongside numerous times. However, conditions can occur, for which the underlying descriptions of EHD flow phenomena have to be revisited. One prominent example is the effect of liquid slip at a solid-liquid interface. In classical textbooks (see e.g. Batchelor (2000)), it is widely accepted that fluids obey a no-slip condition at a solid-liquid interface, with the liquid volume closest to the wall being immobile. This boundary condition is based on empirical observation rather than a first-order principle, but seems to yield realistic results in many applications of classical fluid dynamics. However, over the past 20 years, evidence has accumulated that at hydrophobic surfaces the fluid volumes closest to the wall are in fact able to slip along the boundary. In a classical, macroscopic pipe-flow, this effect is too small to cause results differing from the results obtained using a classical no-slip condition. However, this phenomenon has a profound influence on the flow field nearby the wall, which is the region where EHD effects manifest the strongest. Thus, through the coupling of flow and electric field effects, considerable changes of macroscopic EHD parameters can be measured, such as the ζ potential of surfaces. This example elucidates very well how a lacking theoretical description can lead to deviations between expectation and observation and necessitates reevaluating the underlying assumptions of established models.

The third aspect of the statement by Melcher and Taylor addresses the knowledge creation: Only "*work that relates carefully designed experiments to analytical models*" provides a foundation for fluid mechanics. In the past 50 years, the duality of experiments and analytical models has been extended to a trifold by adding numerical methods. Nowadays, the wide-spread accessibility of numerical codes enables researchers to supplement or even replace experiments, especially in situations where specific properties need to be accessed that are not measurable otherwise. Also, numerical modeling allows to design and optimize processes, thereby reducing the need for extensive laboratory experiments. Even though numerical models can provide an additional verification tool for theory and experiments, they require sound underlying models to produce meaningful results. In turn, this requires experimental validation to at least some degree, emphasizing that the different approaches should be applied jointly to study new phenomena.

Overall, the three discussed aspects provide an excellent overview over the applications, challenges and relevance of the field of electrohydrodynamics. First, it provides a set of established tools, which are already used intensively, and offers constant progress of technological advances. Second, EHD phenomena are based on an interplay of a large variety of mechanisms, which are highly coupled and require a sound understanding of the relevant parameter space and underlying theory. Third, advances can only be made if relations between different methods, namely analytical, experimental and numerical, are established. As the presented work addresses several topics from the field of EHD, the above-mentioned issues exist in various constellations throughout the following chapters. They all have in common that fluidic interfaces and electric fields effect are present. While the cross-thematic fundamentals are summarized in chapter 2, each chapter is designed such that it is self-contained, and can be understood without extensive cross-references. At the beginning of each chapter, a short summary is given, jointly with the respective acknowledgments of cooperation partners and funding agencies. Due to the diversity of the investigated phenomena and the utilized methods, each chapter contains a separate introduction into the topic with a corresponding overview over the relevant literature.

In the first half of this thesis (chapters 3 to 5), the concept of creating a reprogrammable microfluidic platform based on electro-osmosis over superhydrophobic surfaces is explored. In classical microfluidic applications, the process parameters and the wall design are strongly coupled, and a change of the process often requires redesigning the boundary configurations. The overall idea is to decouple the wall-configurations from the flow field using electro-osmotic flow, such that the flow can be changed in situ. Such a microfluidic platform would allow the reconfiguration of the flow field on demand, and thus addresses one of the current limitations of microfluidics using electric field effects.

In chapter 3, the wetting states at microstructured superhydrophobic surfaces are studied, with a focus on the stability and longevity of the gas-liquid interface. The production of superhydrophobic surfaces is described, where a single-scale, soft-lithography microstructure is modified by adding a secondary nanostructure. Using light-reflection microscopy, the stability versus applied electric fields perpendicular to the interface is characterized experimentally.

In chapter 4, the electro-osmotic flow over superhydrophobic surfaces is experimentally characterized, with a gate electrode introducing additional charges to the gas-liquid interface. As a prototypic experimental configuration, the flow field above a single circular electrode is studied. Here, a height-averaged analytical model based on Hele-Shaw flows is compared to height-averaged velocity measurements. Subsequently, the ability to induce complex flow fields based on multiple gate electrodes is demonstrated, and potential reasons for discrepancies between theory and observations are identified.

In chapter 5, a height-averaged transport model of a passive species in a Hele-Shaw flow is derived using an analytic perturbation method. While hydrodynamic dispersion is well-studied in the context of CE with one main flow direction, its description is here extended to the height-averaged, 2D flow fields of the previous chapter. Subsequently, this reduced-order model is compared to three-dimensional Lagrangian particle simulations for defined test cases, allowing an assessment of the model performance. Furthermore, the ability to perform micromixing based on flow-shaping is demonstrated experimentally. To summarize, the first part (chapters 3 to 5) provides the necessary tools to make Hele-Shaw flows based on electro-osmosis over superhydrophobic surfaces accessible for biological and chemical processes, accounting for the flow fields and species transport. Overall, the required governing equations are defined, the experimental performance of electro-osmosis over superhydrophobic surfaces is assessed, and the ability to perform complex flow shaping and species transport is demonstrated.

In the second half of this thesis (chapters 6 and 7), instabilities at liquid-liquid interfaces are studied, which are induced by means of electric fields. In both chapters, the research was triggered by surprising observations made in similar systems, which are attempted to be reproduced and explained here.

In chapter 6, the instability of an interface between a dielectric and a conducting liquid actuated by a spatially homogeneous, but periodically oscillating electric field is studied. This configuration poses an equivalent to the mechanically induced Faraday instability. Especially the wavelength and the discrete modes of the interface instability are under investigation. A combination of high-speed imaging and an algorithm evaluating light refraction at the interface is used to extract the spatial structure of the instability. The experimental results are related to analytic predictions and other experimental results from literature.

In chapter 7, the instability of an interface between a dielectric and a conducting liquid induced by a time-constant, but spatially inhomogeneous electric field is analyzed. One peculiar observation is studied in more detail, where under similar external conditions either a Taylor-cone or a surface depression is formed. The governing mechanism is investigated using a combination of experiments with a submerged electrospray and additional numerical modeling.

To summarize, chapters 6 and 7 address instabilities at liquid-liquid interfaces and their spatial structure. Overall, they provide clarifications for apparent discrepancies between observations and expectations, and explain the overall system behavior.

2 Fundamentals

In this chapter, the theoretical background and the governing equations relevant for this work are introduced. While the mathematical derivation can be found in classical textbooks, it is summarized here both for completeness, as well as to provide the common nomenclature. This chapter focuses on the fundamental conservation laws repeatedly used over the course of this work. Due to the diverse nature of topics presented in this thesis, each chapter contains an additional introductory section incorporating the respective fundamentals. As this work focuses on electrohydrodynamic effects, first the governing equations of electrostatics and their corresponding jump conditions at an interface are presented (section 2.2). In section 2.3, the hydrodynamic conservation equations of mass and momentum are presented. Also, the boundary conditions at solid and free interfaces are introduced, including the coupling mechanism to electrostatics. In section 2.4, the conservation of chemical species is summarized, followed by a short introduction to electric double layers in section 2.5. Finally, in section 2.6, an overview over the fundamentals of other chapters with the respective references is summarized.

2.1 General assumptions

The governing equations of electrostatics and hydrodynamics are described using continuum theory. In principle, fluids are composed of single molecules with typical intermolecular distances on the order of 0.3 nm for liquids and 3 nm for gases (Bruus, 2008, p. 5). Also, electric charges occur only in integer multiples of the elementary charge e . Thus, physical quantities such as mass, momentum and charge density can vary due to the discrete nature of mass and charge on length scales of a few molecules. However, by averaging over a fluid volume containing a sufficient number of molecules or charges, measured quantities can be taken as the average over all molecules. On a macroscopic scale, the fluid volume behaves as if it was continuous in structure. The size of a volume element has to be sufficiently large to minimize statistical fluctuations during averaging over the contained molecules, while simultaneously being sufficiently small compared to the typical length scale of the macroscopical problem. Then, the physical quantities become independent of the fluid volume (Bruus, 2008, p. 5). As for many microfluidic applications, the flow phenomena studied in this work occur over length scales of several μm to several mm, fulfilling this condition.

The relevant governing equations for fluid flow concern conservation of mass, momentum, and energy. While the conservation of mass and momentum will be covered extensively, the conservation of energy will be simplified by assuming isothermal conditions within the system. In order to fulfill this condition, the flow velocity has to be sufficiently slow, such that viscous dissipation is negligible (Koo and Kleinstreuer, 2003). Also, other heating mechanisms such as Joule heating and radiation due to illumination have to be sufficiently small. It is important to keep in mind that the fluidic parameters such as density and viscosity depend strongly on the temperature. Even at isothermal conditions, the environmental temperature at which experiments were conducted, can influence the results by changing fluid properties. Unless otherwise noted, experiments reported in this work were performed at a laboratory temperature of $T = 20^\circ\text{C}$.

In the following, the interaction of electrostatic effects and fluid flow phenomena, coupled at fluidic interfaces are of high interest. The fluids considered are assumed to be immiscible in nature, with sharp jumps of properties over fluidic interfaces. In conjunction with the governing equations, the jump conditions ensuring the conservation of charge and momentum over sharp interfaces will be presented.

2.2 Electrostatics

The governing equations for electrodynamics are Maxwell's equations and can be found in textbooks (e.g., Melcher (1981)). They describe the interactions between electric fields, magnetic fields, and free charges. During the course of this work, the quasi-static approximation of Maxwell's equations is utilized, as other dynamic processes occur on much longer time scales (Melcher, 1981, p. 2.2 ff.). If over the course of this work the term electrostatics is used, it refers to this quasi-static approximation, which still allows temporal changes of the electric fields. In addition, magnetic field effects are neglected. In the following, the differential form of the governing equations will be summarized.

The relation between the electric field \mathbf{E} and the free charge density ρ_{el} is described by *Gauss' law* as

$$\epsilon_0 \nabla \cdot \mathbf{E} + \nabla \cdot \mathbf{P} = \nabla \cdot (\epsilon_0 \epsilon_{\text{rel}} \mathbf{E}) = \rho_{\text{el}}, \quad (2.1)$$

where \mathbf{P} denotes the polarization field, $\nabla = (\partial/\partial x_1, \dots, \partial/\partial x_n)$ the nabla operator, ϵ_0 the vacuum permittivity and ϵ_{rel} the relative permittivity. Here, it is assumed that the medium is linearly polarizable, making it proportional to the electric field as $\mathbf{P} = \epsilon_0 \chi \mathbf{E}$, where χ denotes the susceptibility. This assumption holds for liquids and for isotropic solids (Bruus, 2008, p. 143).

Secondly, in the absence of magnetic effects, *Faraday's law* shows that the electric field is irrotational, as

$$\nabla \times \mathbf{E} = 0. \quad (2.2)$$

Therefore, the electric field can be represented as the gradient of an electric potential ϕ as $\mathbf{E} = -\nabla\phi$. By inserting the electric potential into eq. 2.1, *Poisson's equation* is obtained as

$$\nabla^2 \phi = -\frac{\rho_{\text{el}}}{\epsilon_0 \epsilon_{\text{rel}}}, \quad (2.3)$$

which relates the electric potential to the free charge density ρ_{el} .

The conservation of the free charge density inside a fluid volume can be described by

$$\frac{\partial \rho_{\text{el}}}{\partial t} + \nabla \cdot \mathbf{J}_{\text{el}} = 0, \quad (2.4)$$

where \mathbf{J}_{el} denotes the free current density. It has to be modeled appropriately, dependent on relevant transport mechanisms. For example, if ohmic conduction and convective transport with a background velocity \mathbf{u} are present, the free current density can be expressed as

$$\mathbf{J}_{\text{el}} = K(\mathbf{x}, t) \mathbf{E} + \mathbf{J}_{\text{u}}(\mathbf{u}, \rho_{\text{el}}) = K(\mathbf{x}, t) \mathbf{E} + \rho_{\text{el}} \mathbf{u}, \quad (2.5)$$

where K denotes the electric conductivity and $\mathbf{J}_{\text{u}} = \rho_{\text{el}} \mathbf{u}$ the convective flux. Here, the electric conductivity is denoted by K contrary to the common nomenclature σ to avoid confusion with the stress tensor $\boldsymbol{\sigma}$.

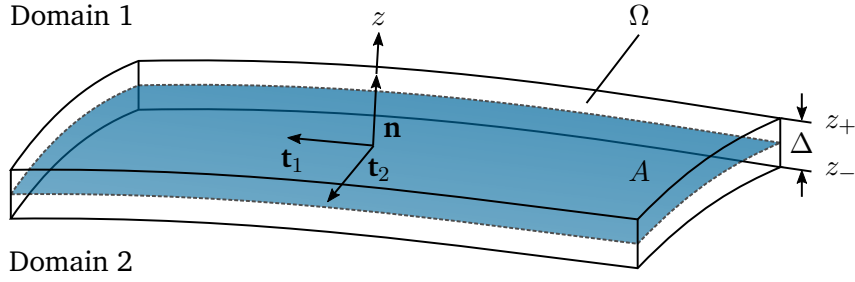


Figure 2.1: Shell balance used to derive the jump conditions at a sharp interface (blue). The interface normal \mathbf{n} is directed into domain 1. The interface of area A is enclosed by an volume element Ω of thickness Δ .

2.2.1 Electrostatic jump conditions at material interfaces

Equations 2.1-2.5 describe the electrostatic problem within a bulk. At boundaries between subsystems, the system properties can change discontinuously. The jump conditions derived from the integral formulation ensure that the governing equations are satisfied over these discontinuities. A detailed derivation of the jump conditions can be found in Melcher (1981), section 2.10. In the following, only the results and their phenomenological interpretation will be discussed.

The jump conditions can be derived by considering a volume element Ω with fixed boundaries $\partial\Omega$ enclosing a portion of an interface, as illustrated in Fig. 2.1. The interface has an area of A and the volume element has a thickness Δ . The interface normal \mathbf{n} is directed into domain 1 at the interface, and the interface-normal coordinate is denoted by z . Considering Gauss' law (eq. 2.1) inside region Ω , transforming it to a boundary integral on $\partial\Omega$, leads to the jump condition of the interface normal electric field component as

$$\mathbf{n} \cdot \llbracket \epsilon_0 \epsilon_{\text{rel}} \mathbf{E} \rrbracket = \sigma_{\text{el}}, \quad (2.6)$$

where $\llbracket A \rrbracket = A_1 - A_2$ denotes the jump of the quantity A over the interface with the interface normal directed into domain 1, and σ_{el} represents the free surface charge defined as

$$\sigma_{\text{el}} = \lim_{A, \Delta \rightarrow 0} \frac{1}{A} \int_{\Omega} \rho_{\text{el}} dV. \quad (2.7)$$

At an interface without surface charge, the normal component of the electric displacement field $\mathbf{D} = \epsilon_0 \epsilon_{\text{el}} \mathbf{E}$ is continuous. On the other hand, if a surface exhibits a free surface charge, the displacement field exhibits a discontinuity. A special case of the discontinuity concerns the case of a vanishing electric field in domain 2. Physically, this situation can occur when the electric conductivity in domain 2 is large, corresponding to a perfect conductor. Then, the free surface charge results in $\sigma_{\text{el}} = \mathbf{n} \cdot \mathbf{D}_1$, completely shielding the displacement field from domain 1.

A second jump condition for the tangential electric field components $\mathbf{E}_t = (\mathbf{E} \cdot \mathbf{t}_i) \mathbf{t}_i$, using Einstein summation convention, can be derived by considering Gauss' law multiplied by the interface normal coordinate z . It results in

$$(\epsilon_0 \mathbf{t}_i \cdot \llbracket \mathbf{E}_t \rrbracket) t_i = \nabla_S \sigma_{\text{DL}}, \quad (2.8)$$

where \mathbf{t}_i with $i = 1, 2$ denotes the tangential vectors to the interface, $\nabla_S = \nabla - \mathbf{n}(\mathbf{n} \cdot \nabla)$ the surface gradient, and σ_{DL} the *surface double layer density*. It is present when the interface has a charge density of varying magnitude on each side of the interface. It is defined as

$$\sigma_{\text{DL}} = \lim_{A \rightarrow 0} \frac{1}{A} \int_{\Omega} z (\rho_{\text{el}} + \rho_{\text{pol}}) dV = \int_{z_-}^{z_+} z (\rho_{\text{el}} + \rho_{\text{pol}}) dz, \quad (2.9)$$

where ρ_{pol} denotes the polarization density $\rho_{\text{pol}} = -\nabla \cdot \mathbf{P}$, and z the coordinate perpendicular to the interface. The coordinate origin is placed in such a way, that the additional condition $(z_+ \mathbf{E}_1 - z_- \mathbf{E}_2) \cdot \mathbf{n} = 0$ is satisfied. Condition 2.9 states that in the absence of a surface double layer density, the tangential field component is continuous at the interface. Alternatively, the jump condition 2.8 can be expressed using the electrostatic potential as

$$\epsilon_0 \llbracket \phi \rrbracket = \sigma_{\text{DL}}. \quad (2.10)$$

A third jump condition at the interface describes the conservation of the free surface charge σ_{el} . It can be derived by using the free current conservation 2.4 in region Ω , expressing it as a surface integral on $\partial\Omega$, ultimately leading to

$$\frac{\partial \sigma_{\text{el}}}{\partial t} + \nabla_S \cdot \mathbf{J}_S - \sigma_{\text{el}} \mathbf{n} \cdot (\mathbf{n} \cdot \nabla) \mathbf{u} = - \llbracket K \mathbf{E} \rrbracket \cdot \mathbf{n} \quad (2.11)$$

where \mathbf{J}_S denotes the free surface current density transported along the interface, and \mathbf{u} a background fluid velocity convectively transporting the charge density ρ_{el} . The second term on the left-hand side denotes in-plane current transport, for example by interface convection. The third term on the left-hand side denotes a source term accounting for changes of the surface charge due to changes of the interface area. The term on the right-hand side captures the transport of charge normal to the interface by conduction. The notation of eq. 2.11 differs from Melcher (1981), explicitly accounting for the change surface area (see Saville (1997)).

The jump conditions 2.6, 2.8 and 2.11 enable the coupling of electrostatic effects over sharp interfaces and fulfill the integral governing equations. Moreover, they allow to attribute a surface charge to the interface, which from a macroscopical point of view is made up of volumetric charges confined to a close region around the boundary. The physical reasoning will be discussed in section 2.5. The effects occurring within this small layer are captured on a macroscopic scale without resolving it. However, accurately capturing the charge transport along the interface might require additional models accounting for effects within this layer.

2.3 Hydrodynamics

In this section, the governing equations of the fluid flow are summarized. In each section, the rate of change of a conserved quantity (mass, momentum) due to different transport mechanisms will be discussed.

2.3.1 Conservation of mass: Continuity equation

In order to derive the governing equation for the mass conservation, a spatially fixed region Ω of arbitrary shape within the fluidic domain is considered, as depicted in Fig. 2.2. The total mass M contained in this region can be obtained by integrating over the mass density ρ as

$$M(\Omega, t) = \int_{\Omega} \rho(\mathbf{x}, t) \, d\mathbf{x}, \quad (2.12)$$

where \mathbf{x} denotes the position vector and t the time. In the absence of sources or sinks within the volume element, the only contribution to the change of mass stems from the mass current density \mathbf{J} , which describes the mass transport in a background flow field \mathbf{u} as

$$\mathbf{J}(\mathbf{x}, t) = \rho(\mathbf{x}, t) \mathbf{u}(\mathbf{x}, t). \quad (2.13)$$

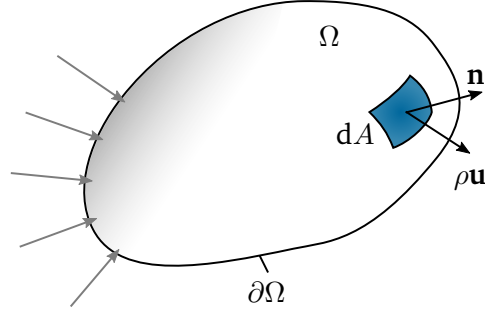


Figure 2.2: Depiction of the region Ω with corresponding mass flux density and area dA .

The change of mass within the fluid volume Ω can be obtained by differentiation of eq. 2.12, and since the volume is fixed in space, the time-derivative can be placed inside the integral as

$$\frac{\partial}{\partial t} M(\Omega, t) = \frac{\partial}{\partial t} \int_{\Omega} \rho(\mathbf{x}, t) d\mathbf{x} = \int_{\Omega} \frac{\partial}{\partial t} \rho(\mathbf{x}, t) d\mathbf{x}. \quad (2.14)$$

Alternatively, the change of mass within the volume can be described by computing the surface integral of the mass current density over $\partial\Omega$ as

$$\frac{\partial}{\partial t} M(\Omega, t) = - \int_{\partial\Omega} \mathbf{n} \cdot (\rho(\mathbf{x}, t) \mathbf{u}(\mathbf{x}, t)) dA = - \int_{\Omega} \nabla \cdot (\rho(\mathbf{x}, t) \mathbf{u}(\mathbf{x}, t)) d\mathbf{x}, \quad (2.15)$$

where \mathbf{n} is the surface normal vector in the outward direction. Then, the surface integral is transformed by use of Gauss' theorem into a volume integral. Equating both expressions 2.14 and 2.15 leads to the conservation law of mass. Since Ω can be any arbitrary, fixed region, the integral can be dropped and the *continuity equation* in differential form follows as

$$\frac{\partial \rho}{\partial t} = -\nabla \cdot (\rho \mathbf{u}). \quad (2.16)$$

It is important to note that the density $\rho(\mathbf{x}, t)$ can vary over time and space.

A classical assumption in microfluidics is the incompressibility of the fluids concerned. The sound velocity c characterizes the velocity of pressure waves that lead to density fluctuations propagating through the fluid ($c \approx 1480 \text{ m s}^{-1}$ for water at 20°C (Smith and Lawson, 1954), $c \approx 331 \text{ m s}^{-1}$ for air at 20°C (Hardy et al., 1942)). With characteristic flow velocities comparatively small, a fluid volume can be assumed to exhibit a negligible material derivative of the mass density ρ (Bruus, 2008, p. 20), and the continuity equation simplifies to

$$\nabla \cdot \mathbf{u} = 0. \quad (2.17)$$

2.3.2 Conservation of momentum: Navier-Stokes equations

Analogous to the conservation of the mass density, a conservation law for the momentum density $\rho\mathbf{u}$ can be formulated. The rate change of the total momentum \mathbf{P} of the fluid inside an arbitrarily shaped region Ω fixed in space can be expressed as

$$\frac{\partial}{\partial t} \mathbf{P}(\Omega, t) = \int_{\Omega} \frac{\partial}{\partial t} (\rho(\mathbf{x}, t) \mathbf{u}(\mathbf{x}, t)) d\mathbf{x}. \quad (2.18)$$

The momentum inside the region Ω can change due to convective transport over the interface $\partial\Omega$ and by forces acting on the fluid. The forces can act either on the boundary $\partial\Omega$ or on the fluid inside the

region Ω . The former class include viscous forces (index visc) and pressure forces (index p), and the later include body forces such as gravitation (index body) and electrical forces (index el). To summarize, the rate of momentum change can be expressed as the sum over the respective transport mechanisms as (see e.g., Bird et al. (2007, p. 40 ff.), Bruus (2008, p. 21 ff.))

$$\frac{\partial}{\partial t} \mathbf{P}(\Omega, t) = \frac{\partial}{\partial t} \mathbf{P}^{\text{conv}}(\Omega, t) + \frac{\partial}{\partial t} \mathbf{P}^{\text{p}}(\Omega, t) + \frac{\partial}{\partial t} \mathbf{P}^{\text{visc}}(\Omega, t) + \frac{\partial}{\partial t} \mathbf{P}^{\text{el}}(\Omega, t) + \frac{\partial}{\partial t} \mathbf{P}^{\text{body}}(\Omega, t). \quad (2.19)$$

Momentum change due to convection

The transport of the momentum density $\rho \mathbf{u}$ in the velocity field \mathbf{u} is described by a momentum flux density tensor

$$\mathbf{\Pi}' = \rho \mathbf{u} \otimes \mathbf{u}, \quad (2.20)$$

where \otimes denotes the dyadic product ($u_i u_j$ in index notation). Locally, the momentum density transported over the boundary $\partial\Omega$ can be expressed as $(\rho \mathbf{u}) \mathbf{u} \cdot \mathbf{n} dA$. Thus, the total rate of change due to convective transport can be calculated as

$$\frac{\partial}{\partial t} \mathbf{P}^{\text{conv}}(\Omega, t) = - \int_{\partial\Omega} \mathbf{n} \cdot (\rho \mathbf{u} \otimes \mathbf{u}) dA. \quad (2.21)$$

In order to express the surface integral as a volume integral, it can be transformed by Gauss' law, resulting in

$$\frac{\partial}{\partial t} \mathbf{P}^{\text{conv}}(\Omega, t) = - \int_{\Omega} \nabla \cdot (\rho \mathbf{u} \otimes \mathbf{u}) d\mathbf{x}. \quad (2.22)$$

Momentum change due to pressure force

Pressure forces of the surrounding fluid act on the boundary $\partial\Omega$. At the infinitesimal area dA , the force $-p \mathbf{n} dA$ acts on the fluid, leading to the momentum change $(-p \mathbf{n} dA) \cdot \mathbf{I}$, with the identity matrix $\mathbf{I} = \mathbf{e}_i \otimes \mathbf{e}_i$ consisting of the product of unit vectors, denoted by \mathbf{e}_i . Then, the rate of change of momentum due to the pressure force on the interface is denoted by

$$\frac{\partial}{\partial t} \mathbf{P}^{\text{p}}(\Omega, t) = - \int_{\partial\Omega} \mathbf{n} \cdot (p \mathbf{I}) dA. \quad (2.23)$$

In analogy to the momentum change due to convection, the surface integral is transformed using Gauss' law, resulting in

$$\frac{\partial}{\partial t} \mathbf{P}^{\text{p}}(\Omega, t) = - \int_{\Omega} \nabla p d\mathbf{x}. \quad (2.24)$$

Momentum change due to viscous forces

The surrounding liquid exerts a friction force on the surface $\partial\Omega$. The friction force $d\mathbf{F}$ on the surface dA can be defined by a viscous stress tensor $\boldsymbol{\sigma}^{\text{visc}}$ as

$$d\mathbf{F} = \boldsymbol{\sigma}^{\text{visc}} \cdot \mathbf{n} dA. \quad (2.25)$$

The rate of change of momentum density readily follows as

$$\frac{\partial}{\partial t} \mathbf{P}^{\text{visc}}(\Omega, t) = \int_{\partial\Omega} \boldsymbol{\sigma}^{\text{visc}} \cdot \mathbf{n} dA. \quad (2.26)$$

Without imposing a specific form of the viscous stress tensor, eq. 2.25 can be transformed into a volume integral leading to

$$\frac{\partial}{\partial t} \mathbf{P}^{\text{visc}}(\Omega, t) = \int_{\Omega} \nabla \cdot \boldsymbol{\sigma}^{\text{visc}} \mathbf{d}\mathbf{x}. \quad (2.27)$$

Here, only incompressible Newtonian fluids with constant viscosity coefficients will be considered. The corresponding stress tensor has the form (Bruus, 2008, p. 22)

$$\boldsymbol{\sigma}^{\text{visc}} = \mu (\nabla \otimes \mathbf{u} + (\nabla \otimes \mathbf{u})^{\top}), \quad (2.28)$$

where μ denotes the dynamic viscosity constant, $\nabla \otimes \mathbf{u}$ represents the velocity gradient tensor ($\partial u_i / \partial x_j$ in index notation), and $(\nabla \otimes \mathbf{u})^{\top}$ its transpose ($\partial u_j / \partial x_i$ in index notation). Then, eq. 2.26 simplifies to

$$\frac{\partial}{\partial t} \mathbf{P}^{\text{visc}}(\Omega, t) = \int_{\Omega} \nabla \cdot \boldsymbol{\sigma}^{\text{visc}} \mathbf{d}\mathbf{x} = \int_{\Omega} \mu \nabla^2 \mathbf{u} \mathbf{d}\mathbf{x}. \quad (2.29)$$

Momentum change due to electrostatic force

Electrostatic forces act on the fluid inside the region Ω in form of a force density. As outlined in section 2.2, the fluid exhibits an electrically linear behavior ($\mathbf{P} = \epsilon_0 \chi \mathbf{E}$). Phenomenologically, a dielectric force acts on the induced dipoles within the liquid, and additionally, the Coulomb force acts on the free charge density. The resulting electric volume force density on the liquid can be written as (Melcher, 1981, p. 3.18)

$$\mathbf{f}_{\text{el}} = \rho_{\text{el}} \mathbf{E} - \frac{1}{2} (\mathbf{E} \cdot \mathbf{E}) \nabla \epsilon + \frac{1}{2} \nabla \left(\rho \frac{\partial \epsilon}{\partial \rho} (\mathbf{E} \cdot \mathbf{E}) \right). \quad (2.30)$$

The first contribution denotes the Coulomb force, the second term the dielectric force, and the last term the electrostriction force density. As before, the force density can be interpreted as the divergence of a tensor, the so-called *Maxwell stress tensor* $\boldsymbol{\sigma}^{\text{el}}$. It reads

$$\boldsymbol{\sigma}^{\text{el}} = \epsilon_0 \epsilon_{\text{rel}} \mathbf{E} \otimes \mathbf{E} - \frac{1}{2} \epsilon_0 \epsilon_{\text{rel}} (\mathbf{E} \cdot \mathbf{E}) \left(1 - \frac{\rho}{\epsilon} \frac{\partial \epsilon}{\partial \rho} \right) \mathbf{I}, \quad (2.31)$$

where \mathbf{I} denotes the identity tensor. This tensor formulation will become useful during the derivation of the boundary condition at interfaces in section 2.3.3. Following the arguments presented by Gabay et al. (2021), the contribution of the electrostriction force is assumed to vanish for the remainder of this work.

The rate of change of momentum due to the electrostatic forces leads to

$$\frac{\partial}{\partial t} \mathbf{P}^{\text{el}}(\Omega, t) = \int_{\Omega} \nabla \cdot \boldsymbol{\sigma}^{\text{el}} \mathbf{d}\mathbf{x} = \int_{\Omega} \left(\rho_{\text{el}} \mathbf{E} - \frac{1}{2} \epsilon_0 (\mathbf{E} \cdot \mathbf{E}) \nabla \epsilon \right) \mathbf{d}\mathbf{x}. \quad (2.32)$$

Momentum change due to body forces

Additional body forces enter the momentum conservation equation in a similar manner as the electrostatic body force. Over the course of this work, the only other body force considered is gravity, which exerts a force density on the fluid inside the region Ω as $\mathbf{f}_{\text{g}} = \rho \mathbf{g}$, where \mathbf{g} represents the gravitational acceleration. The resulting rate of change of momentum can be computed as

$$\frac{\partial}{\partial t} \mathbf{P}^{\text{body}}(\Omega, t) = \int_{\Omega} \rho \mathbf{g} \mathbf{d}\mathbf{x}. \quad (2.33)$$

Navier-Stokes equation

The final conservation equation for momentum can now be assembled by collecting the terms of eq. 2.19. Since the region Ω represents an arbitrary, fixed region, the integrand must vanish, leading to the Navier-Stokes equation for incompressible fluids (using eq. 2.16)

$$\rho \frac{\partial \mathbf{u}}{\partial t} + \rho (\mathbf{u} \cdot \nabla) \mathbf{u} = \nabla \cdot \left(-p \mathbf{I} + \boldsymbol{\sigma}^{\text{visc}} + \boldsymbol{\sigma}^{\text{el}} \right) + \rho \mathbf{g}, \quad (2.34)$$

or alternatively using the expressions for the viscous and electric stress tensors to

$$\rho \frac{\partial \mathbf{u}}{\partial t} + \rho (\mathbf{u} \cdot \nabla) \mathbf{u} = -\nabla p + \mu \nabla^2 \mathbf{u} + \rho_{\text{el}} \mathbf{E} - \frac{1}{2} (\mathbf{E} \cdot \mathbf{E}) \nabla \epsilon + \rho \mathbf{g}. \quad (2.35)$$

It is a non-linear partial differential equation, that combined with the continuity equation 2.17, provides the constitutional equations for the fluid flow. The appropriate boundary conditions at interfaces will be discussed in sections 2.3.3 and 2.3.4.

Stokes flow

The Navier-Stokes equation can be expressed in dimensionless form by introducing typical scales of the variables. Taking equation 2.35 without the body forces, and introducing the typical length scale L_0 and the velocity scale U_0 , the position and velocity can be expressed as $\mathbf{x} = L_0 \hat{\mathbf{x}}$, $\mathbf{u} = U_0 \hat{\mathbf{u}}$ and $t = L_0/U_0 \hat{t}$. Here, the symbol $(\hat{\cdot})$ denotes the corresponding non-dimensional variables and operators. Upon inserting into equation 2.35, the Navier-Stokes equation can be expressed as

$$\rho \frac{U_0}{T_0} \frac{\partial \hat{\mathbf{u}}}{\partial \hat{t}} + \rho \frac{U_0^2}{L_0} \left(\hat{\mathbf{u}} \cdot \hat{\nabla} \right) \hat{\mathbf{u}} = -\frac{P_0}{L_0} \hat{\nabla} \hat{p} + \frac{\mu U_0}{L_0^2} \hat{\nabla}^2 \hat{\mathbf{u}}. \quad (2.36)$$

While the choice of the pressure is not unique, the pressure scale P_0 can then be introduced using the viscosity scale $P_0 = \frac{\mu U_0}{L_0}$, leading to

$$Re \left(\frac{\partial}{\partial \hat{t}} \hat{\mathbf{u}} + \left(\hat{\mathbf{u}} \cdot \hat{\nabla} \right) \hat{\mathbf{u}} \right) = -\hat{\nabla} \hat{p} + \hat{\nabla}^2 \hat{\mathbf{u}}, \quad (2.37)$$

where $Re = \frac{\rho U_0 L_0}{\mu}$ is the Reynolds number. The Reynolds number denotes the relative importance of inertial forces compared to viscous forces. In microfluidic applications, the viscous effects usually dominate over inertial effects ($Re \ll 1$). Then, the Navier-Stokes equation reduces to the linear *Stokes equation* in dimensional form as

$$0 = -\nabla p + \mu \nabla^2 \mathbf{u}. \quad (2.38)$$

It is important to keep in mind that the time scale T_0 of the problem was defined by the intrinsic length and velocity scale as $T_0 = L_0/U_0$. However, in case that the characteristic time scale is determined by an external forcing, for example an oscillatory time scale of a moving wall, the first term in eq. 2.35 does not necessarily vanish, and the time-dependent Stokes equation reads as

$$\rho \frac{\partial \mathbf{u}}{\partial t} = -\nabla p + \mu \nabla^2 \mathbf{u}. \quad (2.39)$$

On a second note, the length and velocity scales of the problem were assumed to be uniform in all directions. In chapter 4, this principle is adapted to incorporate varying length scales in shallow channels, where the crosschannel length scale is much smaller than than the planar length scales.

2.3.3 Hydrodynamic boundary conditions at a free interface

Gibbs free energy

For obtaining the boundary conditions at a curved interface, it is instructive to introduce the Gibbs free energy G , which represents the energy of a system with controlled temperature T , pressure p and number of molecules N (Bruus, 2008, p. 213). The total Gibbs free energy of a system can be computed by considering the different contributions, namely the energetic contributions of the different subsystems, and the energy of the dividing interfaces in between. At equilibrium or quasi-equilibrium, a global or local minimum in the Gibbs free energy is obtained, respectively. At (quasi-)equilibrium, the condition

$$\partial G / \partial \xi = 0 \quad (2.40)$$

has to be fulfilled, where ξ denotes a generalized coordinate in the parameter space, introducing a variation from equilibrium.

The contribution of the surface to the Gibbs free energy can be characterized by the interfacial tension γ between two adjacent phases. It is defined as the Gibbs free energy per area for fixed pressure, temperature and molecule number N as (Butt et al., 2003, p. 32)

$$\gamma = \left(\frac{\partial G}{\partial A} \right)_{p,T,N}. \quad (2.41)$$

Molecules at an interface have fewer interaction partners than the molecules in the bulk phase. Therefore, less binding energy is obtained, and the molecules remain in a higher energy state. Thus, the formation of an interface requires energy. Aside the thermodynamic parameters, the interfacial tension depends on the specific nature of the adjacent phases, and different fluid pairs exhibit different interfacial tensions.

Young-Laplace surface force density

Now, a clean interface is considered, where the effect of an incremental energy input δE by some external forcing is analyzed. Considering solely the stored energy of the interface δG_s or the work δG_f on the external adjacent phase by displacing the interface area A by an amount of $\delta \xi$ with a force density of magnitude $\| \mathbf{f}_s \|$, leads to the energy conservation (Bruus, 2008, p. 125)

$$\delta G = \delta G_s + \delta G_f = \gamma \delta A + \| \mathbf{f}_s \| A \delta \xi = 0. \quad (2.42)$$

As depicted in Fig. 2.3, the surface force density \mathbf{f}_s is directed normal to the interface.

Following, the change of area δA can be related to the displacement $\delta \xi$ by geometrical considerations. A curved interface with the two principal radii of curvature is depicted in Fig. 2.3. The displacement leads to a change of the radii to $R_1 (1 + \delta \xi / R_1)$ and $R_2 (1 + \delta \xi / R_2)$. The side lengths change accordingly, and the displaced interface has an area of $(1 + \delta \xi / R_1) (1 + \delta \xi / R_2) A$. By only keeping the first order terms, the change in area can be expressed as

$$\delta A \approx \left(\frac{1}{R_1} + \frac{1}{R_2} \right) A \delta \xi. \quad (2.43)$$

Inserting this result into eq. 2.42 leads to

$$\left(\| \mathbf{f}_s \| + \gamma \left(\frac{1}{R_1} + \frac{1}{R_2} \right) \right) \delta \xi = 0. \quad (2.44)$$

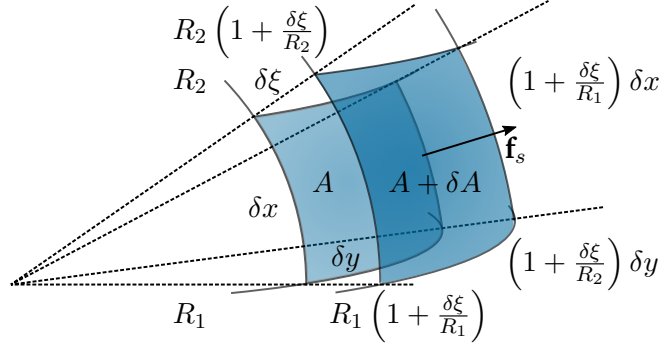


Figure 2.3: Geometric relations of a curved interface with the two principle radii R_1, R_2 displaced by $\delta\xi$. Based on Bruus (2008, p. 125).

The surface force density \mathbf{f}_s is named after *Young* and *Laplace* and can be written as

$$\mathbf{f}_s = -\gamma \left(\frac{1}{R_1} + \frac{1}{R_2} \right) \mathbf{n}, \quad (2.45)$$

where \mathbf{n} denotes the outwards pointing normal vector on the interface. It is important to stress the underlying condition of a clean interface. In case of spatially varying surface tension, additional terms have to be considered, e.g., due to surfactants inducing surface tension gradients.

Mass conservation at a free massless interface

In order to conserve mass at a free interface, the continuity equation can be written in a control volume Ω enclosing the interface A , moving with the interface, as depicted in Fig. 2.4. Here, it is assumed that the interface itself is massless. Then, the contributions to the mass conservation stem from the regions enclosed above and below the interface. Here, the surface normal vector n points upwards into domain 1, and the surface normals on the volume Ω are denoted by \mathbf{n}_i . Considering continuity equation 2.17 inside Ω leads to

$$\int_{\Omega} \nabla \cdot \mathbf{u} \, d\mathbf{x} = 0. \quad (2.46)$$

Then, by using Gauss' theorem on the remaining term, the volume integral is transferred into a surface integrals, leading to

$$\int_{\partial\Omega} \mathbf{u} \cdot \mathbf{n}_i \, dA = 0. \quad (2.47)$$

In the limit $\Delta \rightarrow 0$, the contributions of the sides of the pillbox with \mathbf{n}_i parallel to the interface vanish, and only the contributions normal to the interface remain. Overall, the mass continuity results in

$$(\mathbf{u}_1 - \mathbf{u}_2) \cdot \mathbf{n} = \llbracket \mathbf{u} \rrbracket \cdot \mathbf{n} = 0, \quad (2.48)$$

where the subscripts denote the respective domain. The same condition can be obtained from purely kinematic considerations of an interface. An interface can be described by a function $F(x, y, z, t) = 0$ in an Eulerian framework. Since the interface is made up of particles that stay at the interface, the material derivative of a particle at the interface results in

$$\frac{\partial F}{\partial t} + \mathbf{u} \cdot \nabla F = 0. \quad (2.49)$$

The normal on the interface can be expressed as $\mathbf{n} = \nabla F / |\nabla F|$. Since the condition 2.49 must hold, independent on which side the velocity is evaluated at, condition 2.48 follows equivalently.

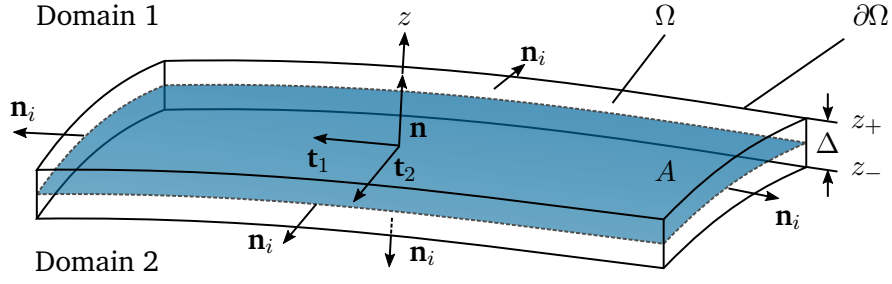


Figure 2.4: Shell balance used to derive the jump conditions at a free interface (blue). The interface normal \mathbf{n} is directed into domain 1. The interface of area dA is enclosed by an volume element dV of thickness Δ . The outward normal on the pillbox is denoted by \mathbf{n}_i .

Equation 2.48 invokes continuity of the normal velocity component at an interface. For the tangential component of the velocity, a similar condition can be imposed from experience, assuming $[[\mathbf{u}]] \cdot \mathbf{t}_i = 0$ for the tangential directions $i = 1, 2$. The reasoning is at least two-fold: First, from observations with flat, moving walls, it is often observed that the fluid at the wall coincides with the velocity at the wall. While this boundary condition is under question at the nanoscale, which will be discussed in chapter 4, it holds well in most circumstances. Second, momentum diffusion over the interface by the molecules of the adjacent bulk phases acts to counter any jump in velocity (Batchelor, 2000, p. 30). As the mean free path of molecules is small, a jump in velocities is balanced over similarly short length scales. Therefore, unless otherwise noted, the velocity over a material interface will be assumed to be continuous, as expressed by

$$[[\mathbf{u}]] = 0. \quad (2.50)$$

Momentum conservation at a free massless interface

In order to satisfy momentum conservation at a free interface, the Gaussian pillbox depicted in Fig. 2.4 is utilized, and the Navier-Stokes equation (eq. 2.34) is integrated over the volume Ω . An additional surface force term follows from the interface deformation (eq. 2.45). Then, the integral formulation of the momentum conservation reads

$$\int_{\Omega} \left(\rho \frac{\partial}{\partial t} \mathbf{u} + \rho (\mathbf{u} \cdot \nabla) \mathbf{u} \right) d\mathbf{x} = \int_{\Omega} \left(\nabla \cdot \left(-p\mathbf{I} + \boldsymbol{\sigma}^{\text{visc}} + \boldsymbol{\sigma}^{\text{el}} \right) + \rho \mathbf{g} \right) d\mathbf{x} + \int_A \mathbf{f}_s dA. \quad (2.51)$$

As discussed before, the volume integral on the right-hand side can be transformed into a surface integral by use of Gauss' theorem. Then, the integral changes to

$$\int_{\Omega} \left(\rho \frac{\partial}{\partial t} \mathbf{u} + \rho (\mathbf{u} \cdot \nabla) \mathbf{u} \right) d\mathbf{x} = \int_{\partial\Omega} \left(-p\mathbf{I} + \boldsymbol{\sigma}^{\text{visc}} + \boldsymbol{\sigma}^{\text{el}} + \phi_g \mathbf{I} \right) \cdot \mathbf{n}_i dA + \int_A \mathbf{f}_s dA. \quad (2.52)$$

Here, the gravitational force was expressed as the divergence of a gravitational potential $\rho \mathbf{g} = -\nabla \phi_g$. It is important to note that the first integral on the right-hand side is integrated over the pillbox surface $\partial\Omega$ with the corresponding outward pointing normals \mathbf{n}_i , and that the second term is integrated over the enclosed surface A .

Next, in the limit of vanishing thickness $\Delta \rightarrow 0$, the contributions of the volume integral of the inertia-terms on the left-hand side vanish. Also, the contribution of the surface integrals over the side wall of

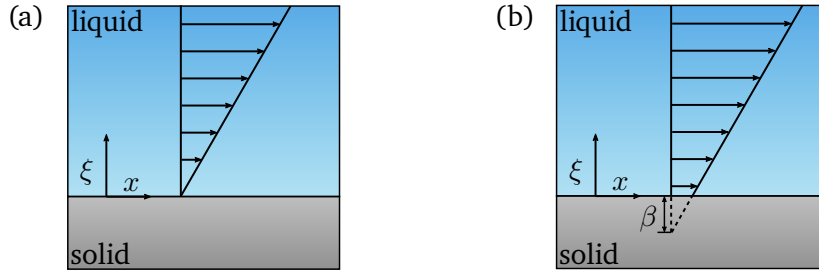


Figure 2.5: Wall boundary conditions at a solid wall for a velocity driven by a shear force far away from the interface. (a) No-slip boundary condition. (b) Navier-slip boundary condition with slip length β .

the pillbox with \mathbf{n}_i parallel to the interface become negligible. Additionally utilizing that the region of the integral was chosen to be arbitrary, the jump condition for the stress at the interface is obtained as

$$0 = \llbracket -p\mathbf{I} + \boldsymbol{\sigma}' + \boldsymbol{\sigma}^{\text{el}} + \phi_g\mathbf{I} \rrbracket \cdot \mathbf{n} - \gamma \left(\frac{1}{R_1} + \frac{1}{R_2} \right) \mathbf{n}. \quad (2.53)$$

This resulting stress condition is a vector condition, composed of three components.

A particularly common case of the stress condition 2.53 is the so-called *Young-Laplace equation*. In the limit of a fluid at rest, and in the absence of Maxwell stress, the normal component of condition 2.53 can be expressed as

$$\gamma \left(\frac{1}{R_1} + \frac{1}{R_2} \right) = \llbracket -p + \phi_g \rrbracket. \quad (2.54)$$

Phenomenologically, it shows that a pressure difference over an interface is balanced by an interface curvature. Increasing curvatures (smaller principle radii) lead to larger pressure differences. This normal stress balance leads to interesting effects such as capillary filling. Here, the wetting properties of a hydrophilic capillary induce a curved interface, which in turn leads to a pressure difference over the fluid interface and a resulting filling of the capillary. This simple system is one example how on the microscale, surface effects can dominate the bulk flow of a system.

2.3.4 Hydrodynamic boundary conditions at solid interfaces

Similarly to a free interface, at a stationary solid-liquid interface the continuity of the wall-normal velocity is required, leading to

$$\mathbf{u}(\xi = 0, t) \cdot \mathbf{n} = \mathbf{u}_w \cdot \mathbf{n}, \quad (2.55)$$

where ξ denotes a coordinate normal to the wall directed into the fluid, \mathbf{n} the local wall normal vector, and \mathbf{u}_w the wall velocity.

The tangential velocity at the wall exhibits a similar continuity over the interface. From observation, it is known that at an interface the tangential velocity conforms to the wall velocity u_w in many situations (Batchelor, 2000, p. 149). This *no-slip* boundary condition can be expressed as

$$(\mathbf{u}(\xi = 0, t_i) \cdot \mathbf{t}_i) \mathbf{t}_i = (\mathbf{u}_w \cdot \mathbf{t}_i) \mathbf{t}_i, \quad (2.56)$$

where \mathbf{t}_i denotes the tangential vectors on the interface. It is depicted in Fig. 2.5(a) for a fixed interface. This no-slip boundary condition is valid when the mean free path of a molecule is much smaller than the relevant length scale of the macroscopic problem (Bruus, 2008, p. 37).

For gaseous flows in nanochannels, the free mean path length of the molecules can be of the order of the channel size, which macroscopically appears like a slipping of the main phase flow over the surface. The corresponding boundary condition is the *Navier-slip* boundary condition, which reads

$$(\mathbf{u}(\xi = 0) \cdot \mathbf{t}_i) \mathbf{t}_i = \beta \frac{\partial(\mathbf{u} \cdot \mathbf{t}_i)}{\partial \xi} \Big|_{\xi=0} \mathbf{t}_i, \quad (2.57)$$

where ξ denotes the wall-normal coordinate, \mathbf{t}_i the tangential vectors parallel to the surface, and β the slip length (Rothstein, 2010). A depiction of the slip boundary condition is given in Fig. 2.5(b). Here, the wall velocity is proportional to the shear rate. While this boundary condition is motivated by gas flows, similar slipping effects for liquids flowing over hydrophobic materials have been discussed both using numerical simulations (Barrat and Bocquet, 1999), and verified experimentally (Bouzigues et al., 2008). The observed slip lengths reached several tens of nanometers. Especially for the interpretation of electrokinetic experiments, these slip lengths are of importance, which will be discussed in chapter 4 in detail. Also, for composite surfaces of gas-liquid and solid-liquid patches, the introduction of an effective boundary condition with an effective slip length β_{eff} can be useful. Here, slip-lengths can reach the micrometer scale (Rothstein, 2010), which will be discussed in chapter 4 as well.

2.4 Conservation of chemical species

In section 2.3.1, the conservation of the overall mass was considered. Similar arguments can be made for heterogeneous fluids consisting of $i = 1, \dots, N$ species. The mass density of each component has to be conserved. Nevertheless, the arguments presented for the total mass density persist. It can be expressed as the sum of the mass density ρ_i of the species i , leading to

$$\rho(\mathbf{x}, t) = \sum_i \rho_i(\mathbf{x}, t). \quad (2.58)$$

It is common to express the species conservation in terms of the fraction of the species i inside a fluid volume (Bruus, 2008, p. 94). For example, the mass fraction C_i denotes the mass of fraction i in a unit volume over the total mass inside a unit volume, reading

$$C_i(\mathbf{x}, t) = \frac{\rho_i(\mathbf{x}, t)}{\rho(\mathbf{x}, t)}. \quad (2.59)$$

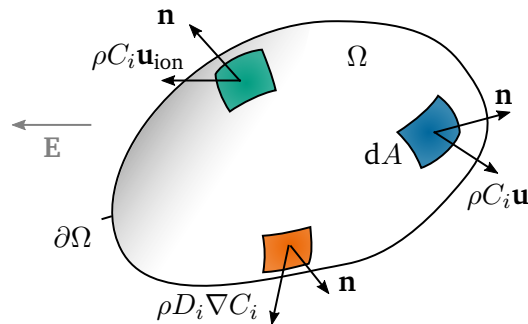


Figure 2.6: Depiction of the region Ω with corresponding species flux density and area dA . For better visibility, the contributions due to convection (blue), diffusion (orange) and electrophoresis (green) are shown in separate surface sections dA .

In analogy to the conservation of the overall mass M inside an arbitrarily shaped, fixed fluidic region Ω , the change of mass M_i of species i in region Ω can be described as

$$\frac{\partial}{\partial t} M_i(\Omega, t) = \int_{\Omega} \frac{\partial}{\partial t} (\rho_i(\mathbf{x}, t)) \, d\mathbf{x} = \int_{\Omega} \frac{\partial}{\partial t} (C_i(\mathbf{x}, t) \rho(\mathbf{x}, t)) \, d\mathbf{x}. \quad (2.60)$$

In the absence of source and sink terms, e.g., due to chemical reactions, the mass M_i can only change due to transport over the boundary $\partial\Omega$. Relevant transport mechanisms include convective transport in a background velocity field \mathbf{u} (index conv), diffusive transport due to molecular motion of the particles (index dif), and electrophoretic motion of charged species due to an external electric field \mathbf{E} (index el). In Fig. 2.6, the region Ω and the boundary fluxes are depicted. The conservation equation for species i then follows as

$$\frac{\partial}{\partial t} M_i(\Omega, t) = \frac{\partial}{\partial t} M_i^{\text{conv}}(\Omega, t) + \frac{\partial}{\partial t} M_i^{\text{dif}}(\Omega, t) + \frac{\partial}{\partial t} M_i^{\text{el}}(\Omega, t). \quad (2.61)$$

Mass change due to convection

The convective transport of species i with a background velocity field \mathbf{u} can be described as the total flux of the species mass density over the boundary $\partial\Omega$, which reads

$$\frac{\partial}{\partial t} M_i^{\text{conv}}(\Omega, t) = - \int_{\partial\Omega} \rho(\mathbf{x}, t) C_i(\mathbf{x}, t) \mathbf{u} \cdot \mathbf{n} dA = - \int_{\Omega} \nabla \cdot (\mathbf{u} \rho(\mathbf{x}, t) C_i(\mathbf{x}, t)) \, d\mathbf{x}. \quad (2.62)$$

Here, the surface integral was transformed into a volume integral using Gauss' theorem.

Mass change due to molecular diffusion

On a microscopic level, molecules exhibit a random motion, which is called *Brownian motion*. It leads to a spreading of initially confined molecules over time. For dilute solutions, the transport due to molecular diffusion is described by Fick's law (Bruus, 2008, p. 94), where the diffusive flux \mathbf{J}_{dif} is dominated by gradients of the concentration field as $\mathbf{J}_{\text{dif}} = -D_i \nabla C_i$, where the proportionality constant D_i is the diffusion coefficient. The rate of change due to diffusive transport then follows as

$$\frac{\partial}{\partial t} M_i^{\text{dif}}(\Omega, t) = - \int_{\partial\Omega} \rho(\mathbf{x}, t) D_i \nabla C_i(\mathbf{x}, t) \cdot \mathbf{n} dA = - \int_{\Omega} \nabla \cdot (\rho(\mathbf{x}, t) D_i \nabla C_i(\mathbf{x}, t)) \, d\mathbf{x}. \quad (2.63)$$

An approximation for the diffusion constant is the so-called *Einstein relation*. It models the molecules of species i as spherical molecules, where the resulting velocity is given as the balance of friction force acting on the molecule, and the diffusive force (Bruus, 2008, p. 117). The friction force can be obtained by assuming that the spherical molecules move in low Reynolds-number flow with their terminal velocity, using the Stokes-drag (Stokes, 1851). The diffusive force can be expressed as the gradient of a thermodynamic potential, ultimately leading to

$$D_i = \frac{k_B T}{6\pi\mu a_i}, \quad (2.64)$$

where k_B is the Boltzmann's constant, T the temperature, μ the background fluid's dynamic viscosity and a_i the molecule radius (Einstein, 1905; von Smoluchowski, 1906).

Mass change due to electrophoretic motion

If the species i exhibits a net charge, a flux forms in the presence of an electric field $\mathbf{E} = -\nabla\phi$. The resulting velocity is given as the balance of the friction force acting on the molecule, and the Coulomb force. In analogy to the derivation of Einstein's relation (eq. 2.64), the friction force can be obtained by assuming Stokes-drag (Stokes, 1851). The resulting terminal velocity can be expressed as

$$\mathbf{u}_{\text{ion}} = \frac{z_i e \nabla \phi}{6\pi\mu a_i} \quad (2.65)$$

where \mathbf{u}_{ion} represents the relative velocity of the species ions to the background fluid, z_i the charge number, e the elementary charge ($e = 1.60217 \times 10^{-19}$ C), and a_i the radius of a molecule of species i .

The overall rate of change of species i due to electrophoretic motion can be computed by inserting eq. 2.64 as

$$\frac{\partial}{\partial t} M_i^{\text{el}}(\Omega, t) = \int_{\partial\Omega} \rho(\mathbf{x}, t) C_i(\mathbf{x}, t) \frac{z_i e D_i}{k_B T} \nabla \phi \cdot \mathbf{n} dA = \int_{\Omega} \nabla \cdot \left(\rho(\mathbf{x}, t) C_i(\mathbf{x}, t) \frac{z_i e D_i}{k_B T} \nabla \phi \right) d\mathbf{x}. \quad (2.66)$$

Nernst-Planck equations

The conservation equation for the mass of species i in an incompressible fluid is obtained by inserting all contributions into eq. 2.61, and dropping the integral, since Ω can be chosen arbitrarily, as

$$\frac{\partial}{\partial t} C_i + \nabla \cdot (\mathbf{u} C_i) = \nabla \cdot (D_i \nabla C_i) + \nabla \cdot \left(C_i \frac{z_i e D_i}{k_B T} \nabla \phi \right). \quad (2.67)$$

It is important to keep in mind that the conservation is expressed in terms of the mass concentration. It is common, however, to express the conservation dependent on the molar concentration, which represents the number of molecules N_i of species i inside a unit volume V . For dilute solutions, the total mass density is approximately constant, and by using the definition of the mass concentration (eq. 2.59), the molar concentration c_i can be expressed as

$$c_i = \frac{N_i}{V} = \frac{\rho_{\text{sol}}}{m_i} \frac{N_i m_i}{\rho_{\text{sol}} V} = \frac{\rho_{\text{sol}}}{m_i} C_i, \quad (2.68)$$

where ρ_{sol} denotes the density of the solvent, m_i is the mass of a single molecule, and V the unit volume (Bruus, 2008, p. 94). The resulting conservation equation in terms of molar concentration is referred to as the *Nernst-Planck equation*

$$\frac{\partial}{\partial t} c_i + \mathbf{u} \cdot \nabla c_i = \nabla \cdot \left(D_i \nabla c_i + c_i \frac{z_i e D_i}{k_B T} \nabla \phi \right), \quad (2.69)$$

where the incompressibility of the fluid was used to change the convective term on the left-hand side. For a fluid containing $i = 1, \dots, N$ soluble species with a dilute concentration, a set of N equations is obtained.

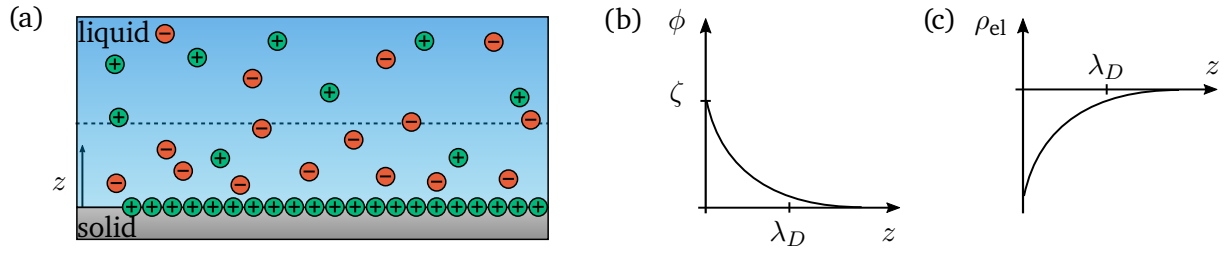


Figure 2.7: Schematic of a diffusive double layer forming due to a fixed charge at an solid-liquid interface, including a Schematic of the ion distribution (a), the Electric potential distribution (b) and the charge density distribution (c).

2.5 Electric double layer

Over the course of this work, electrostatic effects will often be contained within a small region close to the interface, with an extend much smaller compared to other length scales of the system. In this section, the mechanism behind the electric double layer (EDL) will be illuminated. To obtain physical insight into this problem, a dilute aqueous solution containing monovalent ions with a concentration $c_+ = c_- = c_0$ and charge numbers $z_+ = -z_- = 1$ next to a wall is considered. The wall interacts chemically with the solution, and obtains a positive surface charge. As a result, the surface charge attracts negatively charged ions and repels positive ions, forming a region next to the surface with a net charge, as depicted in Fig. 2.7. In the following, the distribution of ions inside the liquid is of interest.

In order to compute the ion distribution close to the surface, it is assumed that the fluid is stationary, and that the ion distribution has reached a steady state. Also, the wall extends infinitely into the wall-tangential directions, so that the problem can be treated to be one-dimensional. It is also impermeable to ions. Then, the Nernst-Planck equation (eq. 2.69) reads

$$0 = \frac{\partial}{\partial z} \left(D_i \frac{\partial}{\partial z} c_i + c_i \frac{z_i e D_i}{k_B T} \frac{\partial}{\partial z} \phi \right). \quad (2.70)$$

The electrophoretic motion of particles due to the surface charge is balanced by the molecular diffusion. The corresponding boundary conditions are

$$c_{\pm}(z \rightarrow \infty) = c_0, \quad \phi(z \rightarrow \infty) = 0, \quad \phi(z = 0) = \zeta. \quad (2.71)$$

Far away from the interface, the concentration reaches the bulk value, and the electric potential vanishes as well. The effect of the surface charge is modeled by replacing it by a surface potential ζ .

The solution of this problem is given by

$$c_{\pm} = c_0 \exp \left(\mp \frac{e}{k_B T} \phi(z) \right), \quad (2.72)$$

where the ionic concentrations c_+ , c_- depend exponentially on the electric potential ϕ (Bruus, 2008, p. 146). In order to solve for the potential distribution, the charge density can be expressed as

$$\rho_{el} = e(c_+ - c_-) = -ec_0 \left[-\exp \left(-\frac{e}{k_B T} \phi(z) \right) + \exp \left(+\frac{e}{k_B T} \phi(z) \right) \right] = 2ec_0 \sinh \left(-\frac{e}{k_B T} \phi(z) \right). \quad (2.73)$$

Inserting this equation into Poisson's equation (eq. 2.3), the *Poisson-Boltzmann* equation (Butt et al., 2003, p. 44) is obtained as

$$\frac{\partial^2}{\partial z^2} \phi = 2 \frac{ec_0}{\epsilon_0 \epsilon_{\text{rel}}} \sinh \left(-\frac{e}{k_B T} \phi(z) \right). \quad (2.74)$$

While equation 2.74 is solvable, in the following only the solution in the limit of small surface potentials ($e\zeta \ll k_B T$, *Debye-Hückel limit*, Butt et al. (2003, p. 44)) will be utilized. Then, the right hand side of eq. 2.74 can be approximated by a Taylor series expansion, resulting to the leading order in a second order ordinary differential equation of the form

$$\frac{d^2}{dz^2} \phi = \frac{1}{\lambda_D^2} \phi, \quad (2.75)$$

where λ_D is the Debye-length defined as

$$\lambda_D = \sqrt{\frac{\epsilon_0 \epsilon_{\text{rel}} k_B T}{2e^2 c_0}}. \quad (2.76)$$

The physical importance of this Debye length becomes apparent when writing out the solution as

$$\phi = -\zeta \exp \left(-\frac{z}{\lambda_D} \right). \quad (2.77)$$

The electric potential decays exponentially on a length scale λ_D . Similarly, the charge density (eq. 2.73) is restricted to a region of length scale λ_D adjacent to the interface as

$$\rho_{el} = \frac{\epsilon_0 \epsilon_{\text{rel}}}{\lambda_D^2} \zeta \exp \left(-\frac{z}{\lambda_D} \right). \quad (2.78)$$

For typical values of water ($\epsilon_{\text{rel}} \approx 78$) at $T = 20^\circ\text{C}$ and $c_0 = 1 \text{ mM}$, the resulting length scale equals $\lambda_D = 9.6 \text{ nm}$. With increasing ionic concentrations, the length scale decreases ($\lambda_D \propto \sqrt{1/c_0}$).

It is important to note that the surface potential ζ originated from surface chemistry. The result persists, however, in case of a gas-liquid interface with a perpendicular electric field to the interface, as used in chapter 3. At the interface, a charged region of thickness on the order of the Debye length is formed, which can be approximated as a surface charge.

On a second note, it is important to keep in mind that this simplified model of the electric double layer only takes the diffusive component into account. Additional effects can become important for higher ionic concentrations, such as ion adsorption to the interface. Then, a so-called *Stern-layer* forms, consisting of molecules fixed at the interface (Butt et al., 2003, p. 52 f.). However, here only weak solutions are considered, where the effects of the diffusive layer are dominant, and Stern-layer effects can be neglected.

2.6 Cross-references

This chapter is restricted to the underlying equations of electrohydrodynamics, forming the basis for the following chapters. Additional fundamental principles that are more relevant to specific chapters are introduced in the respective introductory sections, to provide the reader with self-contained chapters. In Table 2.1, these additional introductory sections are referenced for convenience.

Table 2.1: Overview over additional introductory sections with respective descriptions.

topic	description	section	page
Wetting states	Wetting states on flat and microstructured surfaces, including Young's equation, Cassie-Baxter equation and Wenzel's equation.	3.2	25 ff.
Electro-osmotic flow	Electro-osmotic flow over flat and heterogeneous surfaces, exhibiting no-slip and slip wall conditions, and ζ potential control using gate electrodes	4.2	51 ff.
Hydrodynamic dispersion	Dispersion in stationary pressure-driven flow, oscillatory flow, and in the context of microfluidics	5.2	76 ff.
Faraday instability	Analogies between different forcing types, Mathieu's equation, and surface harmonics	6.2.1	111 ff.
Refraction	Snell's law	6.2.2	118 f.
EHD tip streaming	Operating modes, scaling laws for steady cone-jets, submerged electrosprays, and Rayleigh limit	7.2	141 ff.

3 The gas-liquid interface at a superhydrophobic surface under normal electric fields

Superhydrophobicity describes the water-repelling property of a surface. Usually, this is achieved by microstructuring a surface, leading to enclosure of gas below a liquid, in between the microstructure. The existence and longevity of the gas-liquid interface is crucial to superhydrophobicity, and can be influenced by external forces. In this chapter, the influence of an electric field normal to the superhydrophobic surface is investigated, with focus on the influence of the microstructure on the stability of the gas-liquid interface.

The work presented in this chapter is a result of a collaboration with the group of Prof. Moran Bercovici at Technion, Haifa, in the framework of a fund by the *German-Israeli Foundation for Scientific Research and Development* (Grant No. I-1346-401.10/2016). The main body of the work was published in Rofman et al. (2020). The microfabrication of the soft-lithography master structures was performed by Dr. Khaled Gommed and Baruch Rofman at the cleanroom facilities of the Micro-Nano-Fabrication & Printing Unit at Technion, Haifa. The solvent-evaporation coating technique was refined during a research stay at the Lab of Moran Bercovici, by Valeri Frumkin, Baruch Rofman and the author of the present thesis. The soft-lithography, surface modification, experiments and data evaluation were performed by Baruch Rofman and the author of the present thesis at the Lab of NMF at TU Darmstadt. In their function as supervisors, Steffen Hardt and Moran Bercovici provided valuable input during the whole duration of this project. The SEM imaging of the microstructured PDMS surfaces without PVC was performed by Tina Ebert.

3.1 Introduction

The most famous example of a superhydrophobic surface is the Lotus leaf. Earliest mentions of the remarkable water-repellent properties can be found in the ancient scriptures of Bhagavad Gita, one of the main holy scriptures of Hinduism, commonly dated around 200 BC (von Brück, 1993, chapter 5). While the water-repellency of the Lotus was well-known for millennia, it took until 1997 to trace its origin to the dual-scale surface microstructures (Barthlott and Neinhuis, 1997). Since then, it has drawn the attention of many researchers, and inspired the field of bio-mimicking / bio-inspired superhydrophobic surfaces, where principles of special wettability of surfaces found in nature are adapted for artificially engineered surfaces (Liu and Jiang, 2012; Liu et al., 2010; Yan et al., 2011; Yao et al., 2011). Since the relative importance of these surface based wettability effects increases for flow phenomena with large surface-to-volume ratios, superhydrophobic surfaces are commonly investigated in the context of droplet-based phenomena, as well as microscale flows.

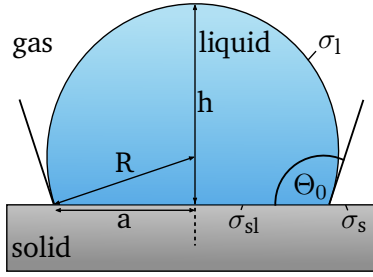
A surface is most commonly defined to be superhydrophobic when the macroscopic contact angle Θ on the surface exceeds 150° (Li et al., 2007). While this is a noteworthy property in itself, the interest towards superhydrophobic surfaces is usually driven by secondary properties that can accompany high contact angles. For example, droplets placed on superhydrophobic surfaces often exhibit a small contact

angle hysteresis, which leads to small roll-off angles and thus self-cleaning (Barthlott and Neinhuis, 1997; Wisdom et al., 2013), anti-icing (Lv et al., 2014a; Murphy et al., 2017) or anti-bacterial properties (Jokinen et al., 2018; Wu et al., 2016; Zhang et al., 2013). The source of the high contact angles can be traced to microstructures at the surface that enclose gas in between the structures (Bico et al., 1999; Lafuma and Quéré, 2003; Yoshimitsu et al., 2002). The droplet surface in contact with the superhydrophobic surface is then composed of gas-liquid and solid-liquid interfaces, changing the free surface energy compared to the case of a liquid perfectly conforming to the microstructure. In section 3.2.1, the Cassie-Baxter wetting state, where gas is entrapped below the liquid interface, and the Wenzel wetting state, where the liquid conforms to the solid surface completely, will be discussed in more detail. While the original interest in superhydrophobic surfaces was initiated by droplet based effects, the composition of solid-liquid and gas-liquid interfaces has other interesting properties that can be exploited for boundary dominated flows. A pressure-driven fluid flow over a composite surface of solid-liquid and gas-liquid interfaces exhibits less hydrodynamic drag (Choi and Kim, 2006; Lee and Kim, 2009; Rothstein, 2010; Shirtcliffe et al., 2009). This hydrodynamic drag reduction can be expressed as an effective slip length β_{eff} on the surface in a Navier's slip boundary condition (eq. 2.57), where the wall-normal gradient defines the wall-tangential velocity. In addition to hydrodynamic drag reduction, wall slip has been shown to be of particular interest to various boundary-driven effects, such as electrokinetic flows, diffusiophoretic flows as well as thermophoretic flows (see e.g., Ajdari et al. (2006); Huang et al. (2008); Squires (2008); Steffes et al. (2011)). Wall slip can lead to enhancement factors of several orders of magnitude over superhydrophobic surfaces. A more detailed overview over these effects and the enhancement mechanism, especially for electro-osmotic flow, will be given in chapter 4.

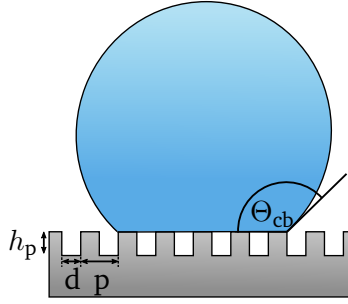
This chapter is motivated by the prospect of enhancing electro-osmotic flow over superhydrophobic surfaces (Bahga et al., 2010; Schönecker and Hardt, 2014; Squires, 2008; Steffes et al., 2011). Therefore, a thorough understanding of the wetting states and their interaction with electric fields is required. One of the key elements for enhancing electro-osmotic flows over superhydrophobic surfaces is to introduce additional charges onto the gas-liquid interface (Huang et al., 2008; Squires, 2008), which can be achieved by applying a perpendicular electric field to the gas-liquid interface (Schönecker and Hardt, 2014). However, as discussed in chapter 2, an electric field perpendicular to an interface leads to Maxwell stresses at the interface, effectively pulling the gas-liquid interface into the microstructure. Thus, the stability of the wetting state limits the ability to introduce charges at the gas-liquid interface. In this chapter, the following questions are addressed: How is the stability of a wetting state defined and how can it be assessed? How can we render the gas-liquid interface stable against perpendicular electric forces? What is the influence of the specific surface microstructure? And what is the maximum electric field the gas-liquid interface can withstand for a given microstructure?

The microstructure influences both the stability of the wetting state, as well as the resulting slip length. This results in a classical optimization problem, and requires evaluation of both aspects in parallel. While both aspects were evaluated simultaneously, this chapter solely focuses on the aspects of wetting state stability. The evaluation of the slip effects on electro-osmotic flows are discussed in the next chapter. This chapter is organized as follows: In section 3.2, the theoretical background and relevant literature related to wetting states and their transitions are presented. In section 3.3, the production of the superhydrophobic surfaces by soft lithography and the modification by secondary structures is discussed. In section 3.4, the response of the wetting states to electric fields is analyzed by light microscopy as well as contact angle measurements. The results are discussed in section 3.5 with focus on the reversibility of the wetting state transition and the contact angle hysteresis. A summary of the results is given in section 3.6.

(a) flat surface



(b) Cassie-Baxter state



(c) Wenzel state

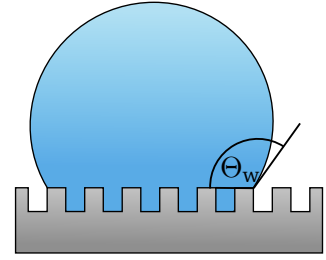


Figure 3.1: Macroscopic contact angles for different substrates and wetting states. (a) The contact angle on a flat surface is defined by Young's equation (eq. 3.10). (b) On a microstructured surface, a droplet in the Cassie-Baxter wetting state rests on a surface microstructure, with air entrapped under the droplet. The contact angle is defined by Cassie-Baxter equation (eq. 3.12). (c) A droplet in Wenzel state conforms to the surface microstructure, without air entrapment. The contact angle is governed by Wenzel's equation (eq. 3.18).

3.2 Wetting states on microstructured surfaces

3.2.1 Contact angles on flat and structured surfaces

Young's equation

Young's equation describes the relationship between the equilibrium contact angle Θ_0 on a flat surface and the solid-liquid surface tension σ_{sl} , the solid surface tension σ_s and the liquid-gas surface tension σ_1 , respectively. It can be derived by consideration of the change of Gibbs free energy G during an infinitesimal spreading of a droplet sitting on a surface, and the subsequent derivation follows closely the derivation outlined by Butt et al. (2003, p. 118 ff.). In order to obtain the equilibrium contact angle, G has to be minimized. The shape of a sessile droplet on a surface takes the form of a spherical cap, as long as gravitational forces are negligible. Then, the area of the spherical cap can be computed as

$$A_{\text{cap}} = \pi (a^2 + h^2), \quad (3.1)$$

where a denotes the radius of the contact line and h denotes the height of the spherical cap, as denoted in Fig. 3.1. The infinitesimal surface change can be expressed as

$$dA_{\text{cap}} = 2\pi a da + 2\pi h dh. \quad (3.2)$$

In eq. 3.2, the surface change depends both on the contact line radius a and the height h of the spherical cap. In order to denote the height change dh as a function of the contact line infinitesimal da , conservation of the drop volume provides the required interdependency. The volume of the drop can be expressed as

$$V = \frac{\pi}{6} (3a^2 h + h^3), \quad (3.3)$$

and the volume change follows as

$$dV = \pi a h da + \frac{\pi}{2} (a^2 + h^2) dh, \quad (3.4)$$

and requiring $dV = 0$ leads to

$$\frac{dh}{da} = -\frac{2ah}{a^2 + h^2}. \quad (3.5)$$

This equation can be further simplified by utilizing the geometrical dependence between the contact line radius a , the droplet height h and the spherical cap radius R , which reads as

$$R^2 = a^2 + (R - h)^2. \quad (3.6)$$

The relation between the change in height and contact line radius readily follows as

$$\frac{dh}{da} = -\frac{2ah}{2Rh - h^2 + h^2} = -\frac{a}{R}. \quad (3.7)$$

The change in spherical cap surface area is computed by inserting eq. 3.7 in eq. 3.2, resulting in

$$dA_{\text{cap}} = 2\pi a \frac{R - h}{R} da = 2\pi a \cos \Theta_0 da. \quad (3.8)$$

The expression for the change in surface area depends on the infinitesimal contact radius change da and the equilibrium contact angle Θ_0 .

In order to obtain the equilibrium contact angle, the change in Gibbs free energy has to be obtained, which depends on the different contributions of the solid-liquid, solid-gas and the gas-liquid interfaces. If the droplet changes its contact line radius, the contact region below the droplet increases by $dA_{\text{sl}} = 2\pi da$. Then, the change in Gibbs free energy results in

$$dG = (\sigma_{\text{sl}} - \sigma_{\text{s}}) dA_{\text{sl}} + \sigma_1 dA_{\text{cap}} = 2\pi a (\sigma_{\text{sl}} - \sigma_{\text{s}} + \cos \Theta_0 \sigma_1) da. \quad (3.9)$$

Invoking the equilibrium condition $dG/da = 0$ leads to *Young's equation* as

$$\sigma_1 \cos \Theta_0 = \sigma_{\text{s}} - \sigma_{\text{sl}}, \quad (3.10)$$

where Θ_0 denotes the equilibrium contact angle on the surface, σ_{s} the solid-gas surface tension, σ_1 the liquid-gas surface tension, and σ_{sl} the solid-liquid surface tension. Young's equation can also be interpreted as a force balance at the three-phase contact line. However, within the framework of Gibbs free energy minimization, the derivation can be modified to account for surface heterogeneities, as outlined below.

Before we continue with heterogeneous surfaces, it is important to keep in mind that the derivation of Young's equation is based on the assumption of a perfectly flat, homogeneous surface. Therefore, the Gibbs free energy exhibits only one global minimum, resulting in the equilibrium contact angle. Real surfaces, however, usually exhibit heterogeneities, both related to the surface chemistry as well as to the surface geometry (Li and Neumann, 1992). Therefore, the Gibbs free energy exhibits a range of local minima for varying contact angles, resulting in a *contact angle hysteresis* (see for comprehensive review e.g., de Gennes (1985) and Eral et al. (2013)). The range of contact angles Θ associated with the local minima in the energy landscape is bound by the advancing contact angle Θ_{adv} and the receding contact angle Θ_{rec} as $\Theta_{\text{rec}} \leq \Theta \leq \Theta_{\text{adv}}$, which are the contact angles observed in the limit of a slowly advancing and receding contact line. Also, the change of contact angles with increasing contact line velocity, the *dynamic contact angle*, is not captured within this framework.

Cassie-Baxter equation

Surface heterogeneities have an important influence on the observed contact angle. Superhydrophobicity, for example, is often achieved by geometrical structuring of a surface with features, such as micropillars. A liquid deposited on the surface can rest on the surface features, while air is enclosed below the liquid. Then, parts of the droplet surface contact the solid material, while others contact the gas below. The contact angle of a microstructured surface was first described by Cassie and Baxter (1944). The derivation applies to composite surfaces not only consisting of solid and gas, but also to surfaces composed of patches with varying surface chemistry, that exhibit different values of the surface tension. The contact angle on such a composite surface can be obtained similarly to the derivation of Young's equation. For the purpose of deriving the contact angle, a flat surface is assumed to consist of two materials with respective equilibrium contact angles Θ_1 and Θ_2 . The area fraction of each material is denoted as $f_1 = A_1/A_{sl}$ and $f_2 = A_2/A_{sl}$, where A_{sl} denotes the overall solid liquid interface, with $f_1 + f_2 = 1$.

Analogous to eq. 3.9, the change of the Gibbs free energy dG due to an infinitesimal contact line radius increase da can be computed as

$$\begin{aligned} dG &= (f_1\sigma_{sl,1} + f_2\sigma_{sl,2}) dA_{sl} - (f_1\sigma_{s1} + f_2\sigma_{s2}) dA_{sl} + \sigma_1 dA_{cap} \\ &= 2\pi a [(f_1\sigma_{sl,1} + f_2\sigma_{sl,2}) - (f_1\sigma_{s1} + f_2\sigma_{s2}) + \cos\Theta_{cb}\sigma_1] da, \end{aligned} \quad (3.11)$$

where Θ_{cb} indicates the macroscopically observed contact angle. As before, invoking the equilibrium condition as $dG/da = 0$, the equation can be rearranged as

$$\begin{aligned} \cos\Theta_{cb} &= -f_1 \frac{\sigma_{sl,1} - \sigma_{s,1}}{\sigma_1} - f_2 \frac{\sigma_{sl,2} - \sigma_{s,2}}{\sigma_1} \\ &= f_1 \cos\Theta_1 + f_2 \cos\Theta_2. \end{aligned} \quad (3.12)$$

Here, it becomes apparent that the cosine of the macroscopic contact angle Θ_{cb} results from an area-weighted average of the cosine of the equilibrium contact angles Θ_1, Θ_2 .

In Fig. 3.1(b), the special case of a microstructured surface is depicted, where the second material is a gas with a contact angle of $\Theta_2 = 180^\circ$. If the gas-liquid interface is assumed to be flat, the original *Cassie-Baxter equation* (Cassie and Baxter, 1944) is obtained as

$$\cos\Theta_{cb} = f_1 \cos\Theta_1 - f_2. \quad (3.13)$$

The Cassie-Baxter wetting state on superhydrophobic surfaces refers to the state where the liquid sits on top of the microstructures with an air layer in between the structures. Assuming that the surface consists of a square array of pillars with a pitch of p and a distance between the pillars of d , the area fractions can be computed as

$$f_1 = \frac{(p-d)^2}{p^2} \quad \text{and} \quad f_2 = \frac{p^2 - (p-d)^2}{p^2}. \quad (3.14)$$

Before we continue, it is important to reiterate the underlying assumptions of the derivation. It has been shown that the Cassie-Baxter equation is only applicable in the limit of large droplets compared to both the surface heterogeneity and wavelength of the change of heterogeneity. For example, Gao and McCarthy (2007) prepared surfaces with a circular structured region in the center. Then, a droplet was placed concentrically, and the contact angles were measured. When the contact line was outside the structured region, the contact angle was insensitive to the existence of the microstructure in the central region and took the value of the unstructured material. The Cassie-Baxter eq. 3.13 on the other hand predicts a change of contact angle. While the microstructure itself was much smaller than the droplet, the wavelength of the structure was not, as was pointed out in subsequent work (Marmur and Bittoun, 2009). Thus, the discrepancy between theory and experimental observations could be resolved, highlighting the range of validity of the Cassie-Baxter model-

Wenzel's equation

Instead of resting on top of the microstructure, the liquid can also penetrate into the crevices of the microstructure, replacing the gas in between. The theoretically expected contact angle of a liquid conforming perfectly to a rough surface was first discussed by Wenzel (1936). A schematic of the wetting state is shown in Fig. 3.1(c). Analogous to the preceding sections, the increase of Gibbs free energy can be formulated upon a infinitesimal change da . The change in liquid-solid contact area dA_{sl} follows as

$$dA_{sl} = 2\pi r a da, \quad (3.15)$$

where $r = A_{\text{real}}/A_{\text{proj}}$ denotes the ratio of the real surface in contact with the liquid to the projected surface under the liquid. In case of a square lattice of rectangular pillars of height h_p with sidewall length $(p - d)$ and pitch p between pillar centers, the ratio reads

$$r = \frac{p^2 + 4h(p - d)}{p^2} > 1. \quad (3.16)$$

Here, the first contribution stems from the surface area of the pillar tops and the base structure, and the second contribution from the area of the sidewalls of the pillars. The resulting Gibbs free energy infinitesimal dG then reads

$$\begin{aligned} dG &= (\sigma_{sl} - \sigma_s) dA_{sl} + \sigma_l dA_{\text{cap}} \\ &= 2\pi a [r (\sigma_{sl} - \sigma_s) + \cos \Theta_w \sigma_l] da. \end{aligned} \quad (3.17)$$

Invoking the equilibrium condition $dG/da = 0$ leads to *Wenzel's equation* as

$$\cos \Theta_w = r \frac{\sigma_s - \sigma_{sl}}{\sigma_l} = r \cos \Theta_0. \quad (3.18)$$

Interestingly, the resulting contact angle Θ_w can either be larger or smaller than the contact angle Θ_0 of the flat material. For hydrophobic base material ($\Theta_0 > 90^\circ$), the observed angle will be larger ($\Theta_w > \Theta_0$), for hydrophilic base material ($\Theta_0 < 90^\circ$), the observed angle will be smaller ($\Theta_w < \Theta_0$). Thus, the microstructure amplifies the hydrophilic or hydrophobic behavior of the surface. Also, the Wenzel model has similar underlying assumptions as the Cassie-Baxter equation, namely a large drop size compared to the surface structure and wavelength of the surface structure (Marmur and Bittoun, 2009).

3.2.2 Wetting state transitions

As discussed in the preceding section, structured surfaces can exhibit several wetting states that fulfill the energy minimization principle. Both the Cassie-Baxter as well as the Wenzel wetting state correspond to a local minimum in the Gibbs free energy, but only one of them corresponds to the global minimum, while the other one is metastable. Aside of the different contact angles, other properties of the surface are strongly affected by the wetting state. For example, the drag reduction on superhydrophobic interfaces depends strongly on the existence of gas-liquid interfaces (Rothstein, 2010). While a microstructured surface exhibits large drag reduction in Cassie-Baxter state, the drag reduction might not be significant in Wenzel state. This raises the questions which wetting state will be observed on a given surface, and how transitions between these states occur.

The calculation of the Gibbs free energy yields information about the absolute stability of a wetting state without information about the dynamics between states. Transitions between the states can only occur once the energy barriers between the wetting states is overcome, but without sufficient energy input, metastable states can exist for prolonged times. In the following, some of the transition

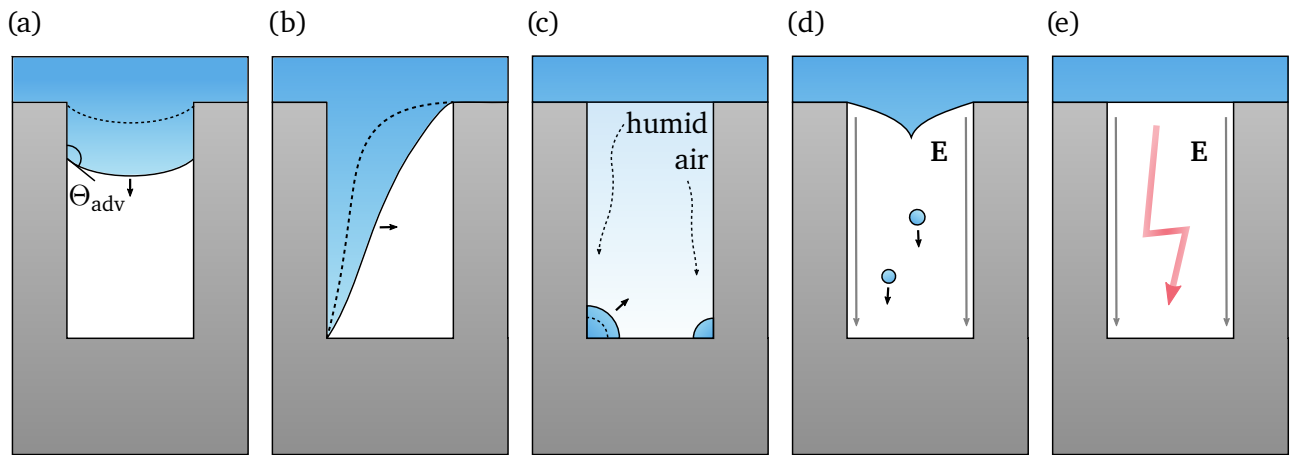


Figure 3.2: Possible collapse mechanisms on superhydrophobic surfaces with large aspect ratio structures. (a) Depinning instability. Once the advancing contact angle at the side-wall is reached, the contact line depins from the top of the microstructure, and starts moving downwards. (b) Advancing of a locally transitioned state from the side. If the surface collapsed locally, the Wenzel state can spread in between the microstructures. The condition for energetically favorable wetting front propagation is shown in eq. 3.19. (c) Condensation of microdroplets. Droplets can condensate from humid air into the microstructure, which ultimately fills up the whole gap. (d) Surface instability. Upon application of a sufficiently strong electric field, the Laplace-pressure at the interface cannot support the Maxwell stress anymore, and the interface breaks down in analogy to classical Taylor cones, leading to a local transition. (e) Electric breakdown of the gas. If the electric field strength in the air gap exceeds the breakdown strength, ionization of the gas and sparking between the liquid and a conducting bottom can occur.

mechanisms between wetting states relevant to this work are discussed. The situation considered is a liquid layer sitting on a pillar-like microstructure in a Cassie-Baxter state. In addition, it is assumed that the Cassie-Baxter state is metastable, and that the Wenzel state is the energetically favorable state.

In Figure 3.2(a), the *contact line depinning* mechanism is depicted. When an external force acts on the gas-liquid interface, the interface deforms, leading to a balance of the Laplace pressure and the external force. Initially, the three-phase contact line is pinned at the upper pillar edge. When the external force becomes sufficiently large, the local contact angle reaches the advancing contact angle of the pillar side-wall material, and starts sliding down the side-wall. Ultimately, the interface reaches the bottom plane, and the Wenzel wetting state can be formed, provided that the enclosed gas can escape the microstructure. The gas can either pass through the interconnected microstructure, due to a gas-permeability of the substrate, or by being compressed in the remaining region. The nature of the external forcing can vary. For example, the pressure of the upper liquid can increase, e.g., by external pumping (Forsberg et al., 2011), droplet evaporation (Papadopoulos et al., 2013) or by fluid flow (Verho et al., 2012). Also, the deformation can be induced by electrical forces, for example by a potential difference between the liquid and an electrode below the superhydrophobic surface (Berry et al., 2012; Chen et al., 2019; Herbertson et al., 2006; Manukyan et al., 2011). A third driving mechanism of a pressure difference between the gas phase and the liquid is the dissolution of the entrapped air into the liquid. Especially for enclosed pores or submerged superhydrophobic surfaces, this mechanism has shown to be of high relevance (Lv et al., 2014b; Poetes et al., 2010). However, between the mentioned collapse mechanisms, a distinct difference of time scales exists. For the first two driving forces, the onset of the contact line depinning and the touching of the meniscus occurs on the order of milliseconds (Sbragaglia et al., 2007), whereas the gas dissolution is limited by the diffusion, thus occurring on time

scales of minutes to hours (Lv et al., 2014a; Poetes et al., 2010). The depinning transition can only occur for sufficiently large pillar heights h_p . When the pillars are small compared to the interpillar distance, the deformed meniscus touches the lower surface before the contact line depins from the pillar top (*sagging mechanism*). Then, the Wenzel transition is induced by the spreading of the meniscus on the lower wall.

In real microstructured surfaces, not all points on the surface transition at once. Due to slight inhomogeneities, for example caused by the manufacturing process, some positions at the interface are more prone to transition than others. As soon as the first local transition on the surface occurs, the question arises whether the defect spreads to adjacent inter-pillar spacings, as illustrated in Fig. 3.2(b). Peters et al. (2009) showed that for a pillared surface, a critical gap size d_c between pillars exist, above which the *wetting front propagation* to adjacent interpillar spaces becomes energetically favorable. The critical gap size can be expressed as

$$d_c = 2h \left(\frac{1}{\cos \Theta_{adv} + 1} - 1 \right). \quad (3.19)$$

When the gap size between pillars is small ($d < d_c$), no spreading will occur, whereas for the case $d > d_c$, wetting is energetically favorable. However, in principle, this condition does not include a statement about a possible metastability or the transition dynamics. In the aforementioned work, the front propagation velocity showed a universal scaling with microstructure parameters and material properties.

A third collapse mechanism relevant to our work is the *condensation* of liquid from the gaseous phase in between the microstructures. When the air in between the microstructure becomes humid, droplets can condensate in between the microstructure, as depicted in Fig. 3.2(c) (Narhe and Beysens, 2004). Condensation is pronounced by temperature gradients between the gas and the solid substrate, as can be caused by joule heating in the liquid phase, or cooling of the superhydrophobic surface by the substrate holder. Initially, small microdroplets form in between the microstructure, which successively grow over time (Jung and Bhushan, 2008; Narhe and Beysens, 2004). Upon coalescence with the main liquid phase at the top, a local wetting state transition is formed. It is important to note that an energetically favorable Wenzel state was assumed. In case of a favorable Cassie-Baxter state, the situation differs: Boreyko and Chen (2009) observed that condensing microdroplets jumped off the surface upon coalescence.

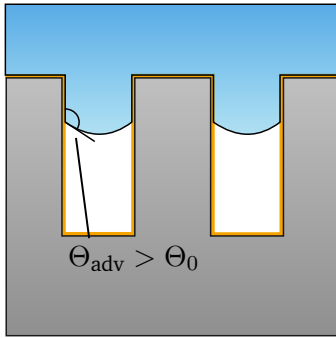
A fourth and fifth breakdown mechanism can occur when an electric field acts on the gas-liquid interface (Schönecker and Hardt, 2014), as depicted in Fig. 3.2(d-e). When the electric field strength becomes sufficiently high, the interface can become unstable, in analogy to electrospray from a needle tip. Then, small droplets are ejected from the interface into the gas phase, and are deposited on the surface. This process is denoted *electric interface instability*. Lastly, instead of an instability at the interface, an *electric breakdown* of the gaseous medium can occur when the breakdown field strength is exceeded, leading to sparking and plasma discharge from the interface.

3.2.3 Strategies to prevent wetting state transition

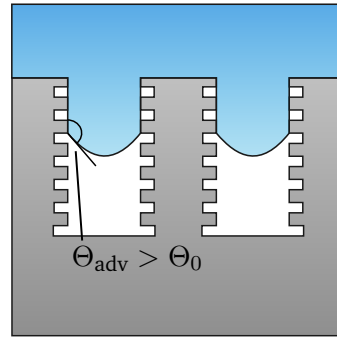
In order to utilize superhydrophobic surfaces to enhance electro-osmotic flow, the existence of a Cassie-Baxter wetting state is imperative. Therefore, a few common strategies to render the Cassie-Baxter wetting state more robust against wetting transitions to the Wenzel state are discussed. The main idea behind delaying wetting state transitions is increasing the energy barrier between the two wetting states, which an external forcing needs to overcome. In Fig. 3.3, some common countermeasures are depicted. In all cases, the solid-liquid contact area of an unperturbed interface is kept constant, so that other properties such as the slip length remain unaffected.

As the depinning of the contact line depends on the advancing contact angle on the side walls of the microstructured surface, a first common principle to delay wetting state transitions is the modification

(a) chemical modification



(b) secondary structures



(c) re-entrant structures

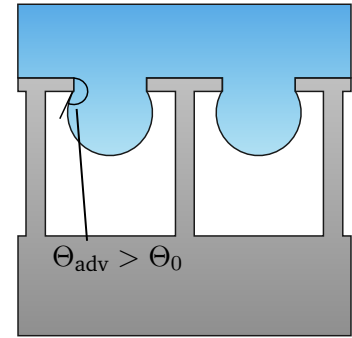


Figure 3.3: Strategies to delay wetting state transitions. (a) Chemical surface modification. By increasing the contact angle at the side-wall using chemical modification, the wetting state transition can be delayed. (b) Secondary structures increase the effective contact angle at the side-wall, delaying the wetting state transition. (c) Re-entrant structures. Instead of modifying the complete side-wall structure, only the top is modified, such that the effective contact angle increases.

of the surface chemistry. Microstructured surfaces can be produced by varying materials, where most commonly silicon, photoresists such as SU-8, and polymers such as Polydimethylsiloxane (PDMS) are used. Depending on the production mechanism, only a limited number of materials might be available, with fixed contact angles. For example, unmodified SU-8 has a water contact angle of $\Theta_0 \approx 95^\circ$ (Kim et al., 2016) and PDMS has a water contact angle of around $\Theta_0 = 108^\circ$ (measured by present author). However, by modification of the surface chemistry, higher contact angles are obtainable. For example, utilizing specific silanes (1H,1H,2H,2H-perfluorodecyl-trichlorosilane, PFDTs), results in an advancing contact angle of $\Theta_{adv} = 120^\circ$ (Hartmann and Hardt, 2019).

A second strategy to delay wetting transitions on microstructured surfaces involves the enhancement of the effective contact angle on the side wall by adding a secondary roughness. This technique was originally inspired by mimicking superhydrophobic surfaces occurring in nature, such as the Lotus-leaf, which consist of micro- and nanoscale structures, and has been investigated widely to enhance the surface stability (Guo and Liu, 2007; Koch et al., 2009; Nosonovsky and Bhushan, 2007; Verho et al., 2011, 2012). By applying a secondary structure that is superhydrophobic itself, effective contact angles on the side wall of higher than 150° can be achieved. A variety of strategies to produce these secondary structures has been employed, including anodization (Lee et al., 2007), laser etching (Yong et al., 2014) and microparticle deposition (Xue et al., 2014). As the existing literature is vast, the reader is referred to the dedicated reviews by Celia et al. (2013); Li et al. (2007) and the references therein. In addition to delaying transitions from the Cassie-Baxter to Wenzel state, nanostructures have also been shown to allow transitions from Wenzel state to Cassie-Baxter state, as long as the liquid did not penetrate in between the secondary structure (Verho et al., 2012).

A third strategy to enhance the stability of the Cassie-Baxter state relies on re-entrant structures, where slender columns are equipped with larger structures on the top. Due to the top-structure, even hydrophilic materials can exhibit superhydrophobic behavior. As shown in Fig. 3.3(c), effective contact angles exceeding 180° can be obtained. In experimental results by Liu and Kim (2014), double re-entrant structures showed superhydrophobic behavior even for completely wetting fluids. In their case, the production of re-entrant structures was achieved by a combination of isotropic and anisotropic etching.

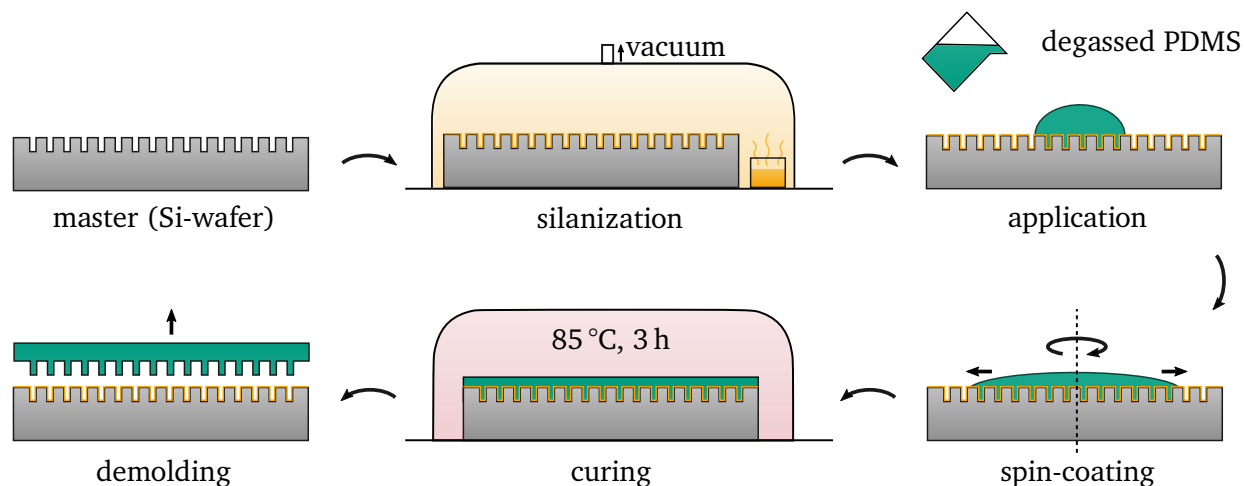


Figure 3.4: Schematic of the soft lithography process. A silicon wafer is used as the master structure, and an anti-sticking layer is applied by silanization in a vacuum chamber. Degassed PDMS is deposited on the wafer, and by spin-coating a structure of fixed thickness is created. Then, the PDMS is cured at 85 °C, and subsequently demolded.

3.3 Production of superhydrophobic surfaces

In this section, the choice of the superhydrophobic surfaces is motivated, and the production process is described. In order to be used in electro-osmotic experiments in the subsequent chapters, the superhydrophobic surfaces have to fulfill a range of requirements. First, the Cassie-Baxter wetting state has to be sufficiently stable to allow the filling of a microfluidic channel with one wall comprising of the superhydrophobic surface. Filling can be accompanied by a local pressure increase due to the dynamic fluidic pressure, and Laplace pressure when the liquid enters the channel, and both need to be supported by the microstructure without transitioning. Second, the Cassie-Baxter wetting state has to be sufficiently stable to support charge induction by electric fields normal to the gas-liquid interface. As discussed, the Maxwell stress at the interface can lead to wetting transitions. Third, the interface has to exhibit effective slip lengths sufficiently high so that electro-osmotic flow at the interface can be enhanced. Usually, this is achieved by interconnected gas-liquid interfaces with large area fractions. Fourth, the microstructure comprising the superhydrophobic surface has to be scalable to length scales of several mm utilizing the existing laboratory equipment. Lastly, the surfaces should be as generic as possible, allowing the utilization of existing theory of slip lengths for validating experimental observations.

Initially, iterative tests were performed on surfaces including electrospun microfibers produced in the laboratory of Prof. Zussman at Technion, Haifa, etched aluminium oxide surfaces (Song et al., 2012), SU-8 microstructures produced by photolithography, as well as pillared and grooved surfaces in PDMS made from soft-lithography. Ultimately, a combination of microstructured pillars made from PDMS and a secondary nanostructure produced from Polyvinylchloride (PVC) showed the best trade-off between the aforementioned requirements, in addition to reproducibility as well as the ability to evaluate the wetting states in-situ. In the following, the details of the production process of the surface will be provided.

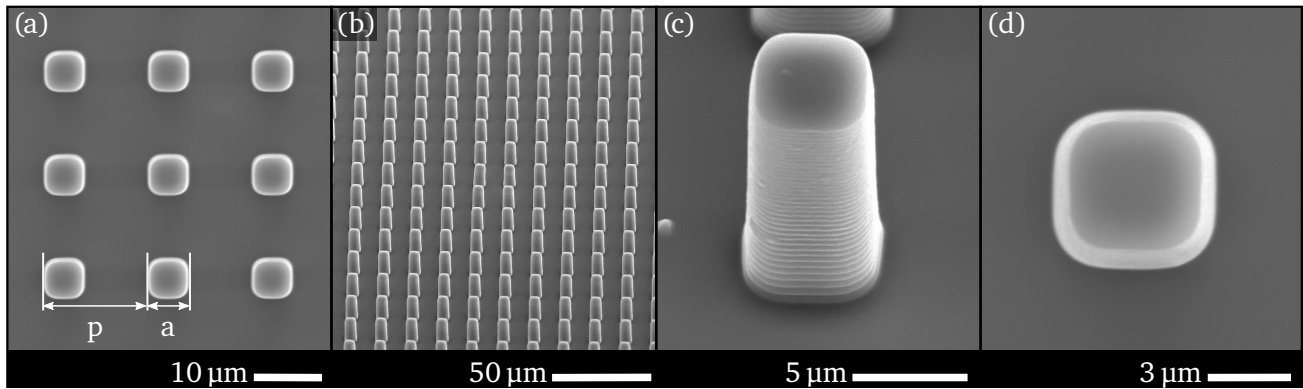


Figure 3.5: Scanning electron microscopy (SEM) images of the resulting PDMS microstructure. (a) Top-view of the rectangular grid with pillar pitch p and side-length a . (b) Side-view under 45° , illustrating the homogeneity of the microstructure. (c) Detailed pillar image under 45° with visible scalloped side-walls due to the homogeneous etching during the DRIE-process. Also, the pillar side-wall is slightly tilted inwards. (d) Detailed pillar top view with rounded off pillar edges.

3.3.1 Single-scale microstructures: PDMS micropillars

The micropillars were produced by soft-lithography from a casting mold from a silicon wafer. One master wafer contained several structured regions, with each microstructure patterning an area of $2\text{ cm} \times 1\text{ cm}$, surrounded by a sealing gasket of 5 mm width and a height of $100\text{ }\mu\text{m}$. The master mold was created using a two-step deep reactive ion etching (DRIE). First, the array of micro-cavities with square base was etched, serving as the cast for the micropillars. The pillars exhibited a varying pillar pitch of $p = 10, 15, 20, 25\text{ }\mu\text{m}$, and the height h_p of the pillars were etched to $h = 10\text{ }\mu\text{m}$ for the smallest pillar pitch ($p = 10\text{ }\mu\text{m}$), and $h = 15\text{ }\mu\text{m}$ in case of the other pillar pitches. In a second step, the surrounding trench was etched into the wafer with a depth of $100\text{ }\mu\text{m}$, producing the surrounding border upon casting. As a last step, the surface was coated with a monolayer of Polytetrafluoroethylene (PTFE) utilizing molecular vapor deposition (*MVD100E*, *applied microstructure ltd.*).

Next, the microstructured surfaces were created using soft-lithography. The process is depicted in Fig. 3.4. First, the silicon mold was rinsed with acetone (*Sigma-Aldrich*), ethanol absolute (*Sigma-Aldrich*) and DI-water (*Merck Millipore*). Then, an anti-sticking layer was applied by placing the mold inside a vacuum chamber for 30 min together with 0.2 ml of Chlorotrimethylsilane (*Sigma-Aldrich*). Concurrently, a mixture of Polydimethylsiloxane (PDMS, *Dowsil Sylgard™ 184*) using the ratio of 1:10 of crosslinker to monomer was mixed and degassed in a second vacuum bell. Then, the PDMS was applied onto the wafer, and spin-coated for 40 s at 200 rounds per minute (rpm) followed by 40 s at 600 rpm. The coated wafer was placed in an oven at 85°C . Finally, the PDMS was carefully removed from the mold and cut into the corresponding pieces.

Figure 3.5 shows scanning electron microscopy (SEM) images of the resulting microstructure made from PDMS. The pillars of rectangular nominal side length are arranged in a rectangular grid with a pillar pitch of p (Fig. 3.5(a)). The pillars are regularly spaced, as can be seen from Fig. 3.5(b) by observation under a 45° angle. However, due to the isotropic etching process during the creation of the master mold, the side of the pillars are not flat, but exhibit a scalloped structure, as seen in Fig. 3.5(c). Also, the side walls are not perfectly vertical with respect to the surface normal, but exhibit a slight angle. Also, the side wall edges are rounded off, leading to a rectangular top with rounded edges, as can be seen in Fig. 3.5(d).

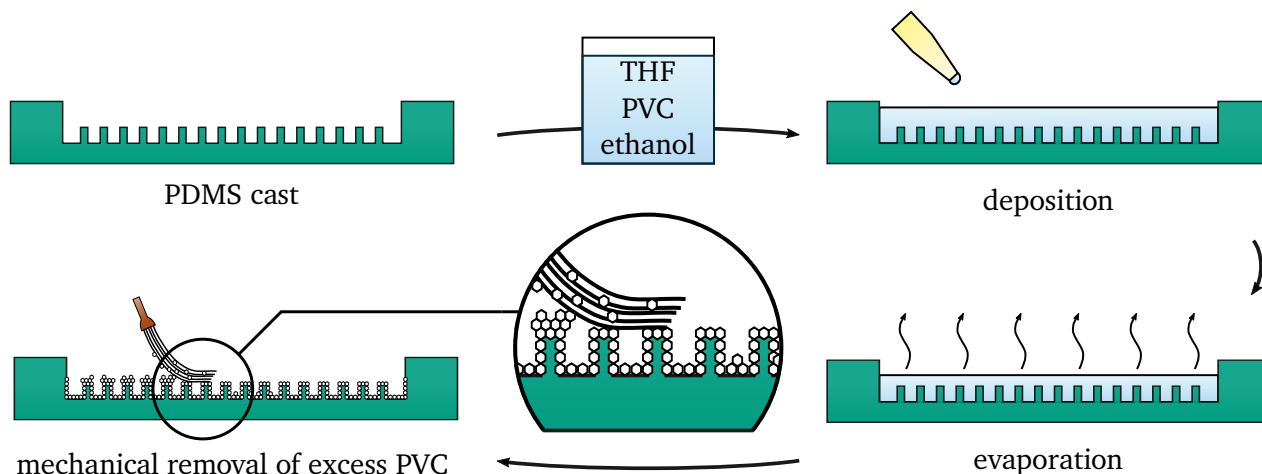


Figure 3.6: Schematic of the surface modification process. On a PDMS cast, a mixture of THF, PVC and ethanol is deposited. The solution is allowed to evaporate in a chemical fume hood, leading to the formation of a PVC nanostructure. Excess PVC is removed mechanically from the top of the pillars with a synthetic fiber brush.

3.3.2 Dual-scale microstructures: Application of a secondary nanostructure

In order to enhance the stability of the Cassie-Baxter wetting state, a hierarchical surface was created by adding a secondary nanostructure. The principle is based on a work by Chen *et al.* (2009), describing a solvent-nonsolvent coating method with polyvinyl chloride (PVC, *high molecular weight, product number 81387, Sigma-Aldrich*). First, the PVC is solved in tetrahydrofuran (THF, *Sigma-Aldrich*), and afterwards added to a nonsolvent (ethanol absolute, *Sigma-Aldrich*). Then, when the solution is deposited on a surface, it evaporates, and the PVC starts to precipitate out of the solution and forms nanocrystals. As Chen and co-workers showed, the ratio of the solvent to the non-solvent determines the nanostructure, with higher ethanol-ratios leading to smaller structures. As reported, the contact angle of water on a flat surface of PVC equals $\Theta \approx 97^\circ$. Increasing the ethanol-ratio up to 50 vol% leads to a superhydrophobic surface with a macroscopic contact angle of $\Theta = 154^\circ$.

The original protocol by Chen *et al.* for creating superhydrophobic films on flat surfaces was adapted to create superhydrophobic surfaces on microstructured surfaces, and is schematically shown in Fig. 3.6. First, the PDMS microstructure is prepared as discussed in the previous section. Then, a base solution was prepared using 50 mg PVC dissolved in 10 ml of THF. Since the original 1 : 1 volume ratio of solvent to nonsolvent resulted in the highest contact angle, 10 ml ethanol were added. Then, 60 μl of the base solution were added to the 2 cm \times 1 cm microstructured surface. The solution was allowed to evaporate at room temperature, resulting in a layer of nanostructured PVC covering the surface. The excess PVC at the pillar tops was removed mechanically by carefully brushing the surface with a synthetic fiber brush. Repeating this process twice resulted in a homogeneously distributed nanostructure.

Figure 3.7 shows the modified surface with the dual-scale microstructure. In Fig. 3.7(a), the surface was imaged under an angle of 53° . The PVC covers the bottom of the surface, as well as the pillars themselves. These images illustrate that the coating does not form a layer of homogeneous thickness, but interconnected nanostructures with thickness variations. Also, some PVC crystals form larger aggregates protruding away from the pillars, underlining the stochastic nature of the coating. In Fig. 3.7(b), a single pillar is shown in more detail, with the PVC attached to the side-walls clearly visible. The PVC provides the second scale roughness required for enhanced stability. In Fig. 3.7(c), the nanoscale

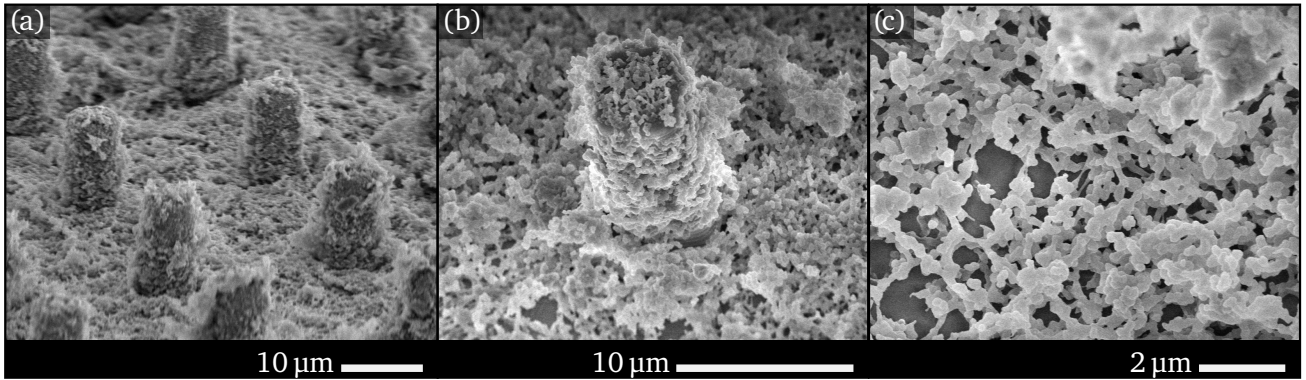


Figure 3.7: SEM images of the resulting dual-scale microstructure. (a) Modified microstructure, demonstrating the general distribution of the PVC. Both the surface bottom as well as the pillars are coated, with local variations in structure. (b) Detailed image of a single pillar. The scallops at the side-walls provide contact points of the PVC nanostructure. (c) Detailed image of the PVC nanostructure. Due to the solvent-nonsolvent process, submicron structures form. As is visible, they form interconnected agglomerates, leading to multiple length scales. Subfigure (c): Adapted with permission from Rofman et al. (2020). Copyright 2020 American Chemical Society.

roughness can be seen, imaged in a region between pillars. During the evaporation of the liquids, the PVC forms crystals, which are strongly interconnected. Also, some defects in the surface coating are visible, where the PDMS is visible as a darker layer from below. These defects provide pinning points for the gas-liquid interface. Overall, the modified surface exhibits varying length scales from the nanometer scale (crystals) to the micrometer scale (pillars), with local variations due to defects or agglomerates.

3.4 Characterization of wetting states: Light reflection microscopy

Interfaces reflect incoming light depending on the refractive indices of the adjacent media, according to Fresnel's equations (Sobral and Peña-Gomar, 2015). Light propagating normal to an interface from medium 1 with a refractive index n_1 into a second medium with a refractive index n_2 is partially reflected. The reflectance R_l , which is defined as the ratio of the power of the reflected light to the total power of the incident light, follows as

$$R_l = \left(\frac{n_2 - n_1}{n_2 + n_1} \right)^2. \quad (3.20)$$

This principle can be utilized to detect whether a surface is in a Cassie-Baxter state, where gas-liquid interfaces are present, or in a Wenzel state, where solely liquid-solid interfaces exist. PDMS exhibits a refractive index of $n_{\text{PDMS}} = 1.43$ (Raman et al., 2011), water $n_{\text{H}_2\text{O}} = 1.333$ (Sobral and Peña-Gomar, 2015) and air $n_{\text{air}} = 1$. At superhydrophobic surfaces in Cassie-Baxter state, light is reflected at the gas-liquid interface ($R_l = 0.02$), as well as the air-solid interface ($R_l = 0.031$), whereas in Wenzel state the reflection stems only from the PDMS-water interface ($R_l = 5 \times 10^{-4}$). In case of the Cassie-Baxter state with flat interfaces, around 5 % of the incoming light are reflected, whereas in Wenzel state only 0.05 % are reflected. This effect can be observed by bare eye in form of a silvery shine on submerged superhydrophobic surfaces (Poetes et al., 2010), but can also be used in microscopical imaging. For example, Manukyan et al. (2011) investigated the local wetting transitions on a superhydrophobic pillared array by using light-microscopy with illumination through the objective. The strong contrast in light reflection from the interface was used to identify transitions locally. Other detection methods reported in literature for gas-liquid interfaces include laser-scanning confocal microscopy (Papadopoulos

Table 3.1: Parameters of the PDMS microstructured surfaces. Also, the observed failure probability upon filling a gasket with a $2\text{ cm} \times 1\text{ cm}$ microstructured region at the bottom is shown, as described in the text.

pillar pitch p (μm)	pillar height h_p (μm)	sublayer height h_{sub} (μm)	failure probability during filling (%)
10	10	130	25
15	15	120	19
20	15	120	45
25	15	120	100

et al., 2013), reflection interference contrast microscopy (Moulinet and Bartolo, 2007) and diffraction pattern measurements (Lei et al., 2010). In the first two cases, the observation of a droplet was performed through the superhydrophobic surface, requiring partial transparency of the substrate. In case of the diffraction pattern measurement, the spatial resolution was limited, as a light beam was directed through a superhydrophobic surface and imaged on a screen, preventing detailed investigation of the interface position.

Figure 3.8(a) illustrates the experimental setup utilized to measure the critical electrowetting potential for non-hierarchical surfaces. The microstructured surface served as the bottom of a PDMS chamber with surrounding sidewalls of 2 mm height with a total volume of 400 μl . The microstructured surface was placed on top of a glass slide with an Indium tin oxide (ITO) coating serving as a conductive layer. The region was filled with DI-water using a syringe pump (*KD Scientific*) at a rate of 250 $\mu\text{l}/\text{min}$. By immersion of a metallic needle into the liquid layer, it was electrically contacted, and the ITO layer served as the ground electrode. The electric potential difference was increased linearly over time, using an electric power source (*LabSmith HVS448-6000D*), at a rate of 5 V/s up to 3000 V. As a result, the liquid-gas interface was pulled in between the microstructure. The transitions were imaged with reflected light microscopy and recorded at a rate of 1 frame per second (fps), using an inverted microscope (*Eclipse Ti, Nikon*) with a mercury light source (*C-HGFI INTENSILIGHT, Nikon*), a charge-coupled device (CCD) camera (*iXon+, Andor*) and a 4x objective (*S-FLUOR 0.2 NA, Nikon*).

The PVC nanostructure renders the surface opaque, thus an adapted experimental setup was used, as illustrated in Fig. 3.8(b). The chamber is closed off at the top by a glass slide, in order to prevent any aberrations due to curvature of the interface. An upright microscope (*Leitz Metallux 3*) with a Halogen light source and a complementary metal-oxide-semiconductor (CMOS) camera (*DS-Fi3, Nikon*) operated at 1 fps was used in combination with a 10x objective (*NPL Fluotar 10x/0.22 DF, Leitz*). For a pillar pitch of $p = 10\text{ }\mu\text{m}$, the magnification was insufficient, and a 20x objective (*NPL Fluotar 20x/0.45DF, Leitz*) was used instead. By measuring $p = 15\text{ }\mu\text{m}$ with both objectives, it was confirmed that the magnification power has no effect on the measured results.

Non-hierarchical surfaces can transition into Wenzel state spontaneously during the filling process without any additional external forcing. In principle, the surfaces can support a Cassie-Baxter wetting state, but singular defects can induce local transitions that propagate quickly over the whole surface. The probability of surface defects increases with the size of the microstructured area. For example, the microstructured surface with a pillar pitch of $p = 20\text{ }\mu\text{m}$ contains 500,000 pillars, where one tilted or deformed pillar suffices to induce a surface-wide wetting transition. In order to identify the Cassie-Baxter wetting transition on non-hierarchical surfaces, the number of pixels that decrease brightness significantly were counted. A surface is considered to be prone to a wetting transition when more than one percent

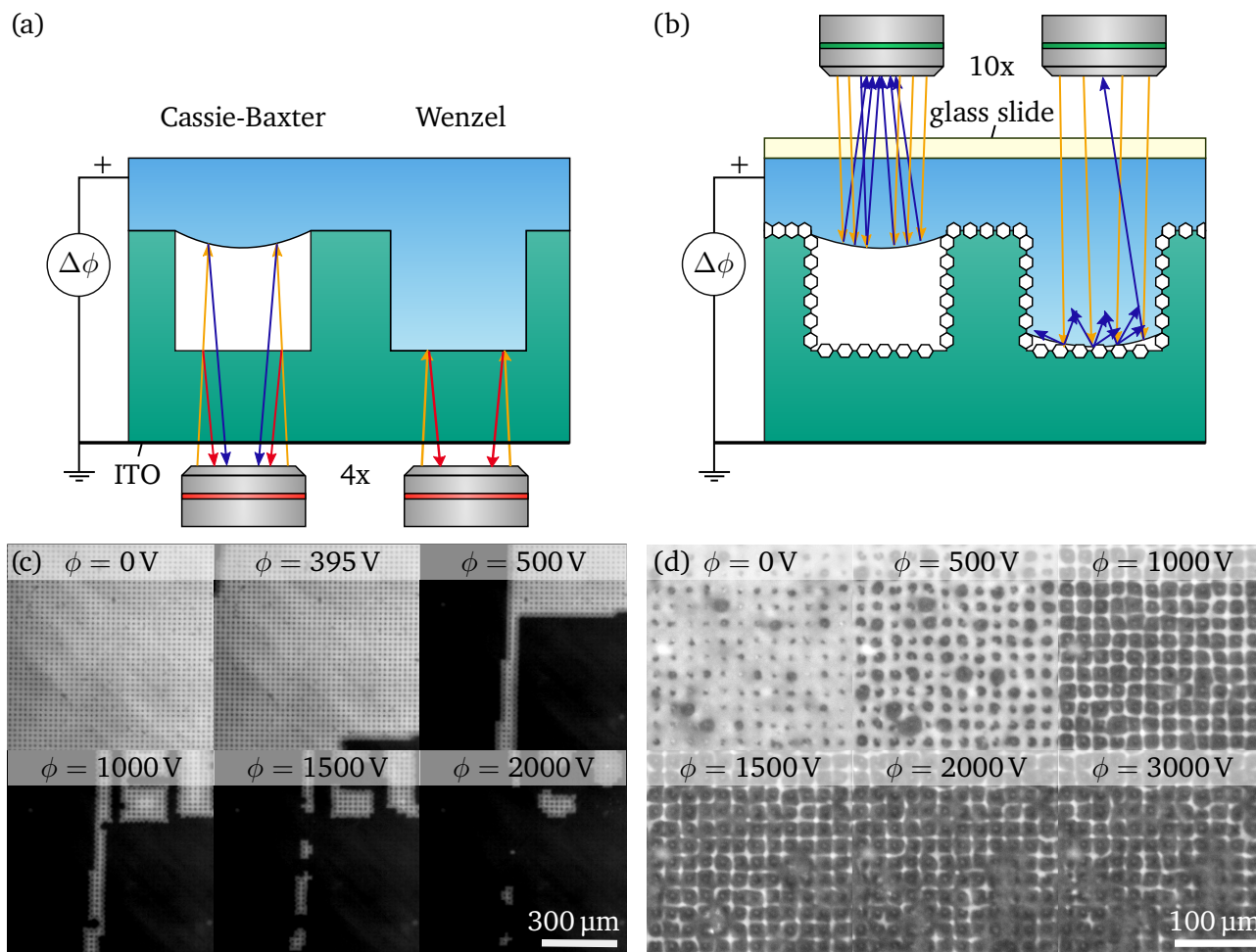


Figure 3.8: Schematic of the experimental setups used to characterize the wetting state stability (not drawn to scale). (a) Setup utilized for the single-scale microstructures. The interface is illuminated and observed from the bottom. Due to the change in reflectivity, the wetting states can be pictured directly. (b) Adapted setup utilized for the dual-scale microstructures. Due to the nano-structure, the surface is rendered opaque, requiring illumination and observation through the upper liquid phase. During the electrowetting, the interface changes the observed reflection pattern. (c) Exemplary dataset for the single-scale microstructure. Initially, only the pillar contact area appears as dark spots, whereas the rest of the surface appears as a bright region. Upon wetting state transition, a strong contrast is visible, with the dark regions corresponding to Wenzel state. (d) Exemplary dataset for the dual scale surface. Initially, the contact points of the pillar tops are visible. Due to PVC crystals at the top, the liquid meniscus is supported by regions of varying size. With increasing electric potential, the contact points at the pillars increase, and the distinct reflection pattern appears in form of a grid. With further increase of the electrowetting potential, the grid disappears locally. Additionally, local variations in the reflection intensity are observed in form of a blinking, most likely due to small shifts of the interface position. Adapted with permission from Rofman et al. (2020). Copyright 2020 American Chemical Society.

of the surface turned dark and transitioned to Wenzel state. In Table 3.1, the experimentally observed failure rate during the filling process is shown for the single-scale surfaces. For the largest pillar pitch, all surfaces transitioned into the Wenzel state upon filling. If a surface exhibited a Cassie-Baxter wetting state after filling, the stability versus electrowetting was measured by applying the linearly increasing

potential difference. In Fig. 3.8(c), an exemplary dataset is shown for a pillar pitch of $p = 20 \mu\text{m}$. Initially, only the solid-liquid contact areas on top of the pillars were dark. At an applied voltage difference of $\phi = 395 \text{ V}$, transitioned regions appeared. With increasing voltage difference, the Wenzel state propagated to adjacent inter-pillar spacings, until a large portion of the surface remained in Wenzel state.

Figure 3.8(d) shows an exemplary dataset for a hierarchical structure. Initially, the contact regions at the pillar tops were visible as dark spots with varying size, due to the stochastic coating of the surface. With increasing potential difference, the contact regions became larger, as the liquid conformed fully to the pillar tops, and a distinct grid appeared in between. This is a result of the curvature of the interface, focusing the reflected light into the microscope lens. With stronger electric fields pulling the interface in between the pillars, the grid became weaker. Locally, it vanished completely when the interface touched the PVC coating at the bottom surface, since the nanostructure diffuses the reflected light. For the highest electrowetting potentials, the interface conformed over large regions of the microstructure to the nanostructure at the base. At this stage, small intensity changes of the reflected light occurred over the surface, leading to a "blinking" of the surface. These random intensity changes can be explained by local movements of the trapped air in the nanostructure. Notably, the overall wetting state transition occurs more gradually compared to the abrupt change for the single-scale surfaces. Also, localized defects do not spread continuously to adjacent inter-pillar spaces, as was observed for the non-hierarchical surfaces.

In contrast to the distinct wetting transition on non-hierarchical surfaces, the characterization of the wetting states on the hierarchical surfaces requires a more detailed evaluation. As can be seen from the exemplary dataset in Fig. 3.8(d), the reflection pattern due to the interface curvature is a distinct feature of the wetting state transition. When the grid appears, the interface is fixed at the top of the pillars or starts to slide in between the pillars, but is not yet touching the nanostructure in between the pillars. Thus, the electrowetting potential associated with the existence of the grid can be used as a lower bound for the stability of the Cassie-Baxter wetting state. In order to detect the grid, the illumination intensity of the image is evaluated. In Fig. 3.9(a), the intensity integrated over the whole image is shown, which is defined as

$$I = \sum_{m=1}^M \sum_{n=1}^N H(m, n), \quad (3.21)$$

where the matrix H represents the greyscale values of the image of size $(M \times N)$. For better visibility, the intensity is normalized by the maximum value obtained. The intensity of the reflected light indicates that the gas-liquid area fraction is largest after filling. This result can be rationalized by the fact that the interface does not conform fully to the pillar tops immediately after filling, but is supported at single points by PVC crystal agglomerates. With increasing electrowetting potential, the interface conforms more closely to the interface, until the whole pillar top is wetted. This is also visible in the original images at time I.

In order to get information about the grid, a local background subtraction is used, where each pixel value is subtracted by the average intensity of a $100 \text{ px} \times 100 \text{ px}$ square region surrounding it. As a result, local gradients are emphasized. Uniform regions turn dark, whereas locally brighter regions than their surrounding, i.e., the grid, remain bright. The resulting images can be seen in Fig. 3.9(c). The grid intensity I_g , which is defined as the sum of the greyscale values in the modified images, shows a distinct peak at a certain electrowetting potential, which corresponds to the strongest reflection pattern. At this electrowetting potential, the interface is in a Cassie-Baxter state, and in the following this electrowetting potential is referred to as *reference state of transition* (RST, point II).

The RST can be used to quantify to which extend other wetting states differ from this classical Cassie-Baxter state. In order to quantify the similarity between images, the 2D cross-correlation between the

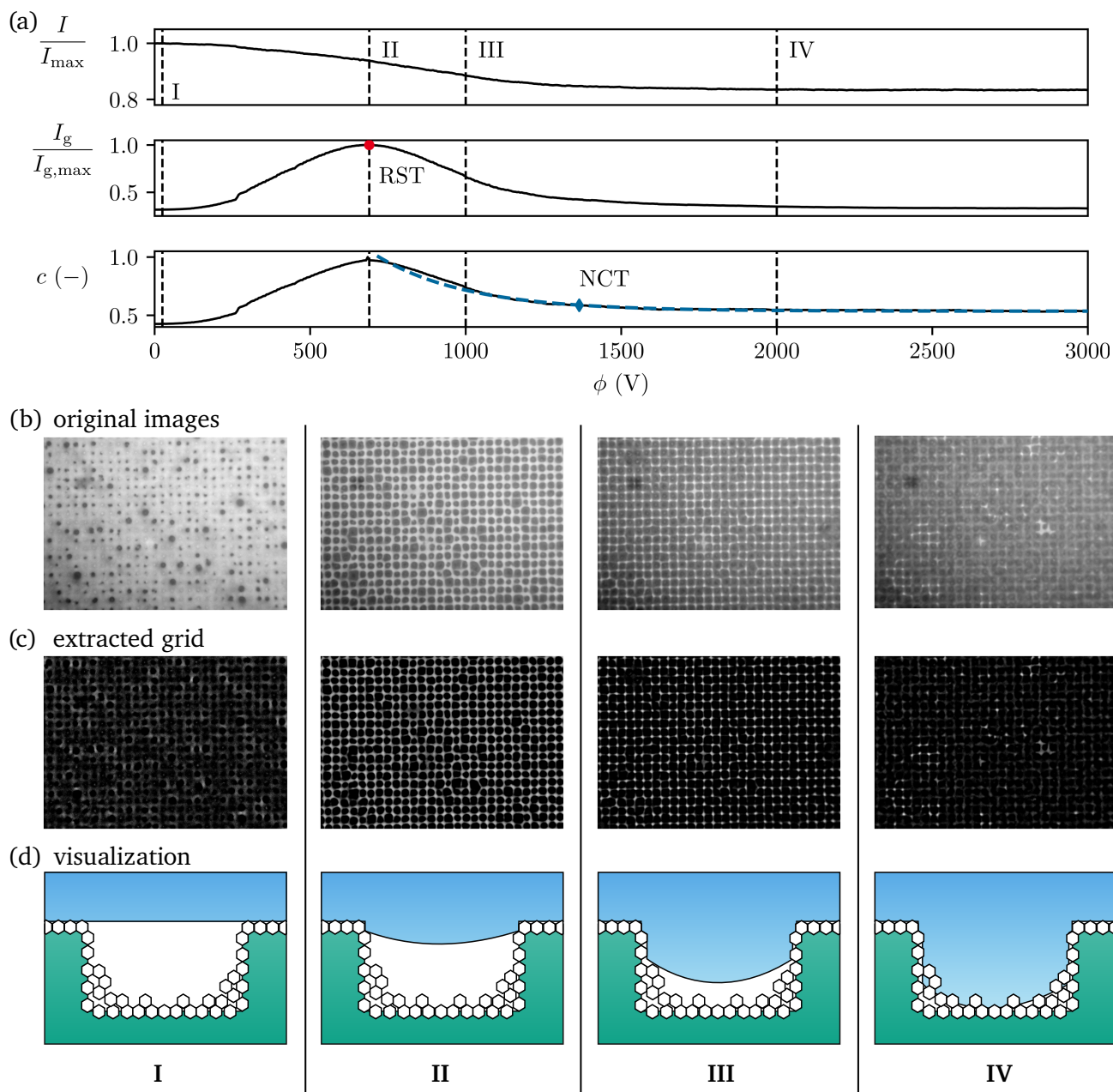


Figure 3.9: Electrowetting evaluation for the hierarchical surfaces. (a) The integrated intensity I shows a continuous decay over time. The grid intensity I_g shows a distinct maximum corresponding to the strongest reflection pattern, which is defined as the reference state of transition (RST, red circle). The cross-correlation c of the images with the image at the RST is used to extract the nano Cassie-Baxter transition point (NCT, blue diamond). The roman numerals indicate the electrowetting potentials corresponding to the images shown in (b-d). (b) Original images showing the decay in illumination. (c) Extracted grid reflection pattern obtained by subtracting the local background. (d) Illustration of the wetting states. Subfigure (d): Adapted with permission from Rofman et al. (2020). Copyright 2020 American Chemical Society.

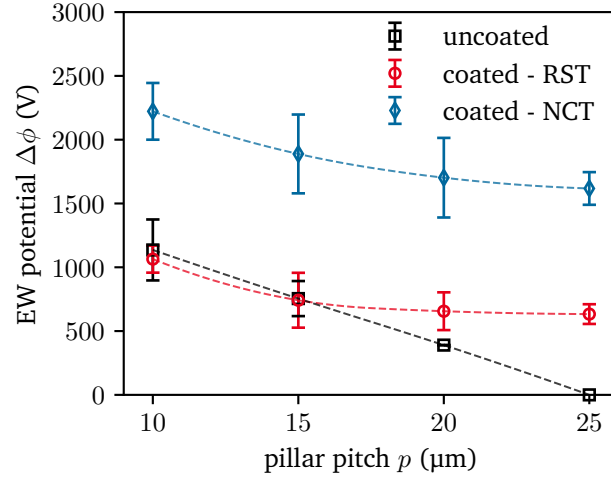


Figure 3.10: Resulting electrowetting transition points for varying pillar pitch. Only datapoints are shown where the filling of the basin was successful. For $p = 25 \mu\text{m}$, no single-scale surface could be filled without transition to Wenzel state. Therefore, 0 V is shown instead. The error bars represent the 95%-confidence interval based on at least 6 independent measurements. Datapoints are connected by quadratic interpolation to guide the eye. Adapted with permission from Rofman et al. (2020). Copyright 2020 American Chemical Society.

image at RST and all other images are computed. The normalized cross-correlation c is defined as

$$c(\phi) = \frac{\sum_{m=1}^M \sum_{n=1}^N H(m, n, \phi_{\text{RST}}) H(m, n, \phi)}{\sum_{m=1}^M \sum_{n=1}^N H(m, n, \phi_{\text{RST}}) H(m, n, \phi_{\text{RST}})}, \quad (3.22)$$

where $H(m, n, \phi_{\text{RST}})$ denotes the image matrix at the RST, and $H(m, n, \phi)$ the image matrix at an electrowetting potential ϕ . The cross-correlation curve can be divided into several distinct zones: Initially, the liquid is suspended on top of the pillars, without the grid emerging. Then, the grid starts to emerge, until the RST is reached. With increasing electrowetting potentials, the interface advances in between the pillars, until it reaches the bottom surface. For example, at point III, the grid is still mostly visible, with exceptions at some localized regions. This indicates that most of the interface has not yet reached the nanostructure at the bottom. Once the interface protruded to the bottom, further increase of the electrowetting potential does not significantly change the wetting state. The interface is supported by the nanostructure in between the pillars, without replacing the gas in between the nanostructure. In literature, this wetting state is often referred to as nano-Cassie state (Verho et al., 2012). Point IV is representative for this region. In order to identify a point at which the majority of the surface has reached this final state, an exponential function of the form $c_{\text{fit}} = A + B \exp(-\phi/\phi_0)$ is fitted to the cross-correlation after the RST. Here, A , B and ϕ_0 are fitting parameters. Then, the point at which the value $c_{\text{fit}} - A$ has decayed by a factor of $\exp(-2)$ is reached at $\phi_{\text{NCT}} = 2\phi_0$, which is termed *nano Cassie-Baxter transition point* (NCT). The NCT can be interpreted as an upper limit for the transition to the nano Cassie-Baxter wetting state, since the surface gradually transitions between the RST and the NCT.

After discussing the measurement methodology, the resulting electrowetting potentials are shown in Fig. 3.10. The Cassie-Baxter to Wenzel transition on the single-scale surfaces is depicted in red, and shows that the microstructures with the smallest pillar pitch transitions at 1135 V on average. It is important to keep in mind that only the fraction of surfaces that were stable after filling were used to determine the electrowetting potential. The stability limit decreases with pillar pitch, and since no microstructure

with a pillar pitch of $p = 25 \mu\text{m}$ exhibited a stable Cassie-Baxter wetting state after filling, a value of 0 V is indicated. The dual-scale surfaces exhibit two wetting limits. The RST corresponds to a situation where the interface conforms to the pillar tops, and is thus comparable to the wetting transition on the non-hierarchical surfaces. For the smaller pillar spacing, the wetting transitions between coated and uncoated surfaces show no significant change. However, for larger pillar spacings, the coated surfaces show a much higher stability versus electrowetting. This result can be attributed to two factors: First, the effective contact angle on the side walls increases with the nanostructure, thus making it more stable. Second, local defects do not spread on the hierarchical surfaces, whereas on the non-hierarchical surfaces a single defect can lead to a wetting state transition on a whole surface. Upon increasing the electric potential higher than the RST, local transitions to a nano Cassie-Baxter state occur, until the majority is transitioned at the NCT. Especially applications that are insensitive to local transitions to the nano Cassie-Baxter state could be operated successfully up to this limit. Applications that rely on the existence of a global Cassie-Baxter wetting state, however, such as electro-osmotic flow over superhydrophobic surfaces, are limited to voltages below the RST.

3.5 Discussion

Adding a secondary structure on a nanometric length scale to the microstructure increases the wetting state stability. An ideal secondary roughness would introduce a secondary length scale much smaller than the microscale. The coating deposited by the solvent-nonsolvent process, however, is not uniform over the whole surface, but varies locally. On the nanoscale, the size of the crystal structures change, as can be seen from Fig. 3.7(c). Also, some regions of the surface are not fully coated, forming pores of the size of several hundred nanometers. These defects can provide pinning points for the interface, potentially preventing a reversibility of the wetting state. Also, locally the crystals form agglomerates that influence the interpillar spacing on the micrometer scale. In addition, PVC accumulates at the pillar base. This results in a variation of the gap width, and an increasing Laplace pressure counteracting the advancing gas-liquid interface. The PVC-coated surface is therefore composed of structures spanning a wide range of length scales.

Single-scale pillared microstructures exhibit two clearly distinct wetting states, the Cassie-Baxter and the Wenzel wetting state. As this picture fails for dual-scale surfaces, additional wetting states were identified. For example, Verho et al. (2012) differentiated between the micro Cassie state, in which the interface was supported by the pillar tops, and the nano-Cassie state, where the liquid penetrated in between the pillars, but not in between the nanostructures. For the surfaces employed in this work, these states also only represent limiting wetting states. Due to the multiple length scales, the interface undergoes a wide range of intermediate wetting states in between both states. However, up to now it is not clear whether these intermediate states are metastable or unstable upon removal of the electrowetting potential. Also, the properties of the nano Cassie state (here denoted as nano Cassie-Baxter state for consistency) have to be investigated. On a single-scale surface, the Wenzel state results in a strong contact line pinning and thus a high contact angle hysteresis. As the nanostructure itself exhibits superhydrophobic properties, it is unclear how strong the resulting contact angle hysteresis will be for the prewetted case. Both questions will be discussed in this section.

3.5.1 Wetting state reversibility

As discussed, the dual-scale surfaces exhibit a continuum of intermediate states during electrowetting. However, it is not clear whether these states are fully reversible. In order to specifically probe the

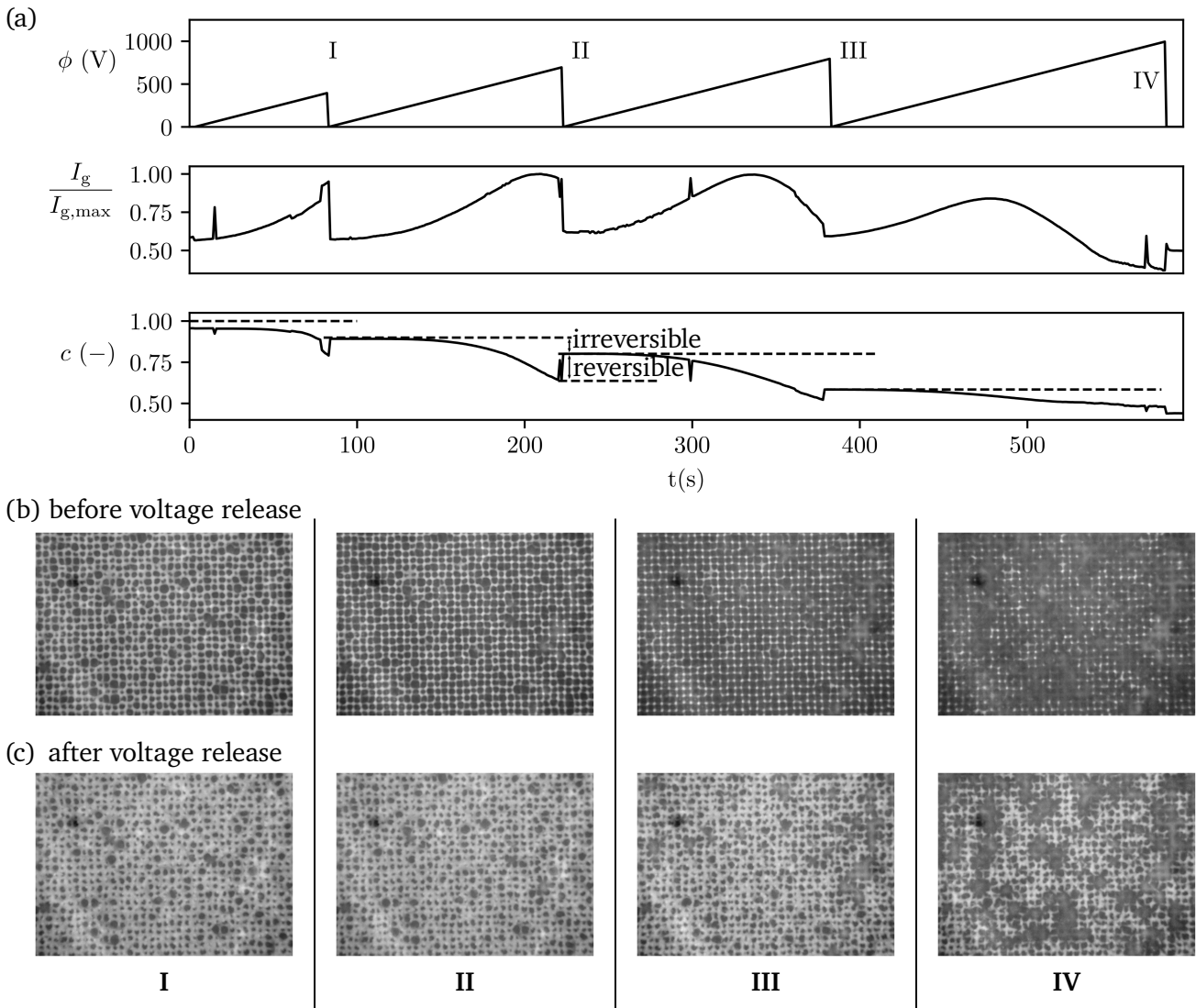


Figure 3.11: Evaluation of the reversibility of the wetting state transition. (a) The voltage difference is varied using a saw-tooth function with increasing maximum value. The grid intensity I_g follows the same initial increase, with the consecutive decrease once the RST is transitioned. The cross-correlation with the first image (note that this is different than for Fig. 3.9) shows a distinct decrease over time, which becomes stronger with emerging reflection grid. With each voltage release, the correlation increases, indicating that the wetting state returns closer to the initial state, but never fully recovers the plateau from the relaxation before. This indicates a partial reversible relaxation of the interface. (b,c) Images before and after the voltage is released at the denoted roman numerals. Note that the regions, in which the grid vanished, appear darker than their surrounding after releasing the voltage. Here, the interface still touches the PVC structure in between the pillars.

reversibility of the wetting state, the response of a microstructure with $p = 20 \mu\text{m}$ to a series of consecutive saw-tooth steps of increasing maximum voltage with constant slope is analyzed (see Fig. 3.11(a) for the voltage form). When an interface is actuated by an electric field, it deforms. When the voltage is released, the interface can either return to the initial position, or if the contact line moved during the actuation, remain at a different position. Therefore, the initial interface reflection before the first saw-tooth is utilized as the reference for the cross-correlation to the successive images. The 2D cross-correlation of all images with the initial image of the video is computed and shown in Fig. 3.11(a). It shows a distinct behavior for each voltage ramp: At low voltages, the interface did not change strongly, and the correlation remains nearly constant. Then, with a larger potential, a more pronounced reflection pattern emerged, as is visible from the grid intensity I_g . Also, the correlation decreases, which is due to the deformation of the interface. When the voltage reaches the maximum value, the cross-correlation exhibits a local minimum. The corresponding interface images are shown in Fig. 3.11(b). Next, when the voltage returned to $\phi = 0 \text{V}$, the interface relaxed, leading to an increasing correlation. However, the cross-correlation does not reach the value before the voltage ramp, indicating that the interface did not fully return to its initial position. The partial increase of the correlation function indicates a partial reversibility. With increasing voltage ramps, the irreversible deformation of the interface increased compared to the reversible transition. Once the maximum in the grid intensity (RST) is passed, the irreversibility becomes strongly visible. For example, the sawtooth between point II and III shows a clear peak in grid intensity, indicating that the RST is passed. The correlation function does only weakly increase at point III. This can be rationalized by remembering that the nanostructure exhibits specific localized defects that serve as pinning points for the interface. After the voltage is released (Fig. 3.11(c-III)), some darker regions were visible, where the interface was pinned at the bottom. This effect is even more pronounced in Fig. 3.11(c-IV). To summarize, up to the RST the wetting transitions are partially reversible. The decrease in cross-correlation is mainly due to the movement of the contact line at the pillars. After the RST is passed, the regions with irreversible wetting transitions, visible as darker regions, increases with applied voltage.

3.5.2 Contact angle hysteresis in the nano Cassie-Baxter state: Contact angle measurement

One common method to characterize superhydrophobic surfaces is to measure their respective advancing and receding contact angles, striving for larger contact angles and lower contact angle hysteresis. For applications that rely on fast droplet removal, this figure of merit poses a natural choice. Also, for single-scale roughness, the contact angle gives an indication of the wetting state on a superhydrophobic surface. As discussed in section 3.2, it is determined by the wetting state below a droplet, and in case of a known microstructure geometry, it can be compared to the theoretical Cassie-Baxter and Wenzel contact angles, Θ_{cb} and Θ_w , respectively. However, the contact angle poses only an integral figure of merit, without detailed information about localized wetting states. Also, in the context of wetting state stability, as is required for example for submerged superhydrophobic surfaces, or EHD applications, a high contact angle does not necessarily correspond to high stability of the wetting state, and can even be misleading. In this section, the contact angles are measured on both the single-scale and dual-scale structure. In Table 3.2, the parameter of the surfaces used are shown with the corresponding values of Θ_{cb} and Θ_w at the single scale surfaces. Note that the pillars are assumed to be perfectly vertical on the side walls, with sharp edges at the sides. While this is only an approximation of the true geometry, the contact angles match qualitatively. With increasing pillar pitch, the Cassie-Baxter contact angle increases, starting at $\Theta_{cb} = 145.8^\circ$, up to $\Theta_{cb} = 166.5^\circ$. The Wenzel contact angle decreases, on the other hand, from $\Theta_w = 157.9^\circ$ to $\Theta_w = 117.2^\circ$. For the highest pillar pitch, the Wenzel contact angle is close to the contact angle observed on a flat surface.

The contact angles were measured using the needle method with a *Kruess DSA-100*. As discussed in

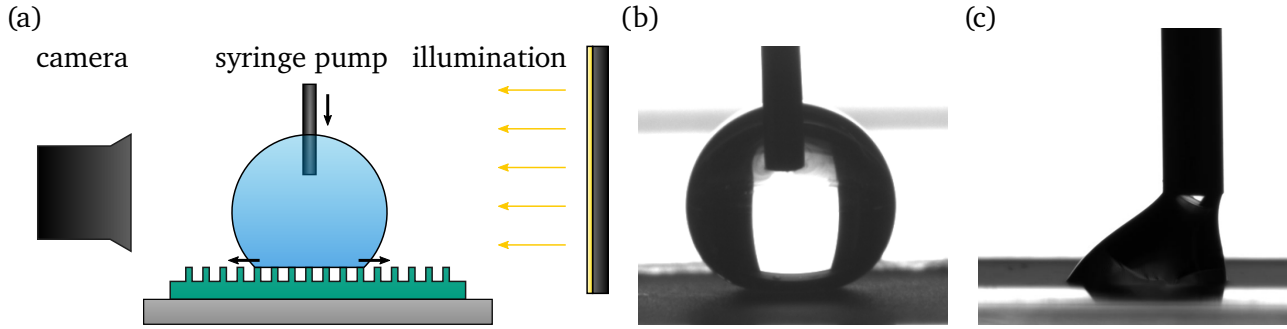


Figure 3.12: Setup utilized to measure the contact angle. (a) Kruess DSA-100 measurement setup. The sample is observed from the side using back-illumination, after a droplet is deposited on the surface, and its volume is increased. (b) Exemplary dataset of a dual-scale surface during the advancing contact angle measurement. (c) Exemplary dataset of a single-scale microstructure, with a local transition to Wenzel state providing a strong pinning of the contact line during the measurement of the receding contact angle.

section 3.2, real surfaces exhibit a range of contact angles due to local minima in the energy landscape. However, they are enclosed by the advancing and receding contact angle in the limit of a slowly moving contact line. As depicted in Fig. 3.12, a small droplet was deposited via an automated droplet dispenser needle on the surface. Then, the volume of the droplet was increased with a continuous volume flow rate of $0.25 \mu\text{l/s}$, and the contact angle drop shape was observed from the side. The droplet shape was evaluated every 10 s and the advancing contact angle Θ_{adv} was extracted by using the software *ImageJ* (Schneider et al., 2012) with the plugin *DropSnake* (Stalder et al., 2006). After the droplet reached a volume of $25 \mu\text{l}$, the droplet dispensation stopped and by drawing the droplet back into the needle, the receding contact angle Θ_{rec} was measured on the surface.

The resulting advancing and receding contact angles of the single-scale PDMS microstructure are depicted in Fig. 3.13(a). The measurements were repeated at three different positions of the interface, resulting in a minimum of 13 measured values per pillar pitch and condition (advancing or receding). The measured advancing angle Θ_{adv} increases slightly with pillar pitch, and is larger than the theoretical Cassie-Baxter angle Θ_{cb} . The microstructure remained in Cassie-Baxter wetting state, as confirmed by microscopic observation. The receding contact angle shows a stronger dependence on the pillar pitch and increases from 132° to 159° . These results show that the contact angle hysteresis can be significant, even with large contact angles. For the highest pillar pitch, it measures about 11° , with larger values for the smaller pillar pitches. These results can be explained by the higher density of pinning sites of the contact line at the pillar tops. Nevertheless, the observed contact angles are consistent with the theoretical Cassie-Baxter

Table 3.2: Theoretical contact angles predicted according to eq. 3.13 and eq. 3.18 for $\Theta_0 = 108^\circ$.

pillar pitch p (μm)	pillar height h_p (μm)	Cassie-Baxter CA Θ_{cb} ($^\circ$)	Wenzel CA Θ_w ($^\circ$)
10	10	145.8	157.9
15	15	157.4	136.1
20	15	163.1	122.7
25	15	166.5	117.2

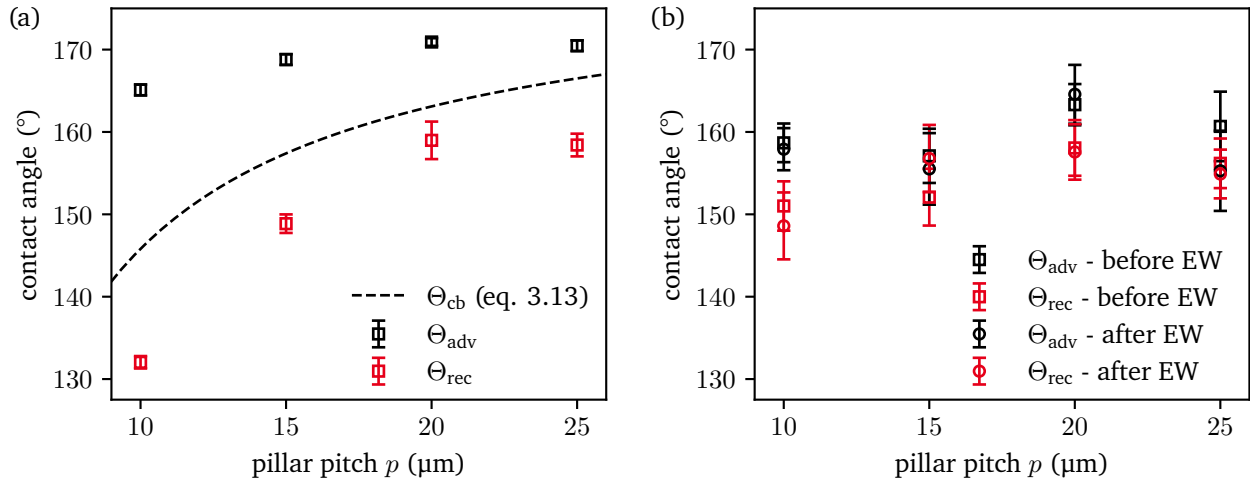


Figure 3.13: Experimentally obtained advancing and receding contact angles. (a) On single-scale microstructures, the measured advancing and receding angles enclose the theoretically predicted Cassie-Baxter contact angle. (b) The contact angles on a hierarchical microstructure show little change after prewetting the surface using electrowetting. The error bars represent the 95%-confidence interval on the mean. Subfigure (b): Adapted with permission from Rofman et al. (2020). Copyright 2020 American Chemical Society.

angle Θ_{cb} (eq. 3.13), which is enclosed by the experimental measurements.

Figure 3.13(b) depicts the resulting contact angles on the hierarchical microstructures. Here, it is visible that the advancing contact angle is nearly independent of the pillar pitch, and that the receding contact angle is closer to the advancing contact angle. This leads to a smaller contact angle hysteresis especially for smaller pillar pitches. As discussed in section 3.4, an unforced interface is supported by PVC crystals at the pillar tops, and not necessarily every pillar top is wetted. Thus, the small influence of the pillar pitch can be explained. Comparing the absolute values of the contact angles between the graphs shows that a smaller advancing contact angle is measured on the dual-scale structure. Two effects might play a role: First, pure PVC is less hydrophobic than PDMS with a contact angle of $\Theta_0 = 97^\circ$ (Chen et al., 2009). This can result in a smaller contact angle than a PDMS microstructure. Second, the dual scale surface exhibits a rough, diffuse texture, as can be seen in Fig. 3.12(b). Measuring large contact angles on diffuse surfaces leads to a poorly illuminated contact line region. As a result, the exact position might be obscured, thus systematically reducing the observed contact angle. Therefore, one should be cautious when comparing the absolute values of both subfigures.

As a next step, electrowetting is used to induce a wetting transition. The surface is placed within the electrowetting setup used in section 3.4, and an electric potential between the ITO surface and the liquid layer on top is applied, at a ramping speed of 5 V/s up to 3000 V. As discussed in section 3.4, this potential is sufficient to transition large portions of the surface to a Wenzel state for the PDMS microstructures or to a nano Cassie-Baxter state for the dual-scale surface. Afterwards, the basin with the outer layer is removed, and the contact angle measurement is repeated immediately. When the basin is removed, most of the water is removed from the surface as well, except for residue at some regions. For the non-hierarchical surfaces, the droplet is deposited either on a completely dry region, or on a region with water residue. The advancing contact angle is the same as before electrowetting (not shown), the receding contact angle however, shows a strong difference. When the droplet transitions locally into a Wenzel state, the contact line pins strongly upon receding. Figure 3.12(c) shows an exemplary

dataset for a pillar pitch $p = 25 \mu\text{m}$ with a receding contact line, where the meniscus pins strongly. A receding contact line further leads to a rupture of the droplet, where a portion stays at the transitioned defect. Therefore, the measurement of the receding contact angle was not systematically possible for the single-scale surfaces, and is thus not shown.

On hierarchical surfaces, the same procedure to induce a local wetting transition by electrowetting was repeated. At the applied potential differences of up to 3000 V, large portions of the interface reach the nanostructure in between the pillars, as discussed in section 3.4. When the basin was removed and the contact angles were measured, the resulting contact angles exhibited no significant difference, as shown in Fig. 3.13(b). In contrast to the uncoated surfaces, no pinning was observed on hierarchical surfaces, and they exhibit a small contact angle hysteresis even after reaching a nano Cassie-Baxter state. The small contact angle hysteresis indicates that the defects within the nanostructure, where the interface pins to the surface, are sparse enough to allow for swift removal of liquid in nano Cassie-Baxter state. Therefore, droplets roll off easily, thus allowing to operate potential applications with higher external forcing before the interface penetrates between the nano structure. In turn, this result also illustrates that the measurement of the contact angle gives little information about the wetting state. While both the Cassie-Baxter state and the nano Cassie-Baxter state have similar contact angles, the effective slip length decreases strongly in the latter state, significantly reducing the ability to induce electro-osmotic flow over superhydrophobic surfaces, as will be shown in chapter 4.

3.6 Summary and Outlook

In this chapter, we have studied the stability of the Cassie-Baxter state on microstructured surfaces against wetting transitions induced by electric fields normal to the interface. The microstructured surfaces were produced by soft lithography with PDMS as the base material with varying pillar pitch. In order to enhance the wetting state stability, a solvent-nonsolvent process was established to add a secondary nano-roughness made of PVC crystals. Evaluation of the coated surfaces by SEM confirmed the existence of a coating with multiple length scales.

In order to characterize the wetting states on the microstructured surfaces, the varying reflectivity of gas-liquid and solid-liquid interfaces was utilized via light microscopy. The surfaces were submerged in water, and an electric potential difference was applied between the water phase and an electrode below the surface, triggering wetting state transitions. For the single-scale surfaces comprising of PDMS pillars, the surfaces were imaged through the microstructures, following measurement principles reported in literature. Due to the diffuse nature of the PVC coating, the dual-scale surfaces were imaged from the top through the liquid phase. Since the difference in reflectivity was less pronounced, an alternative evaluation technique was utilized, based on cross-correlation of the reflection pattern at the interface. During electric forcing of the interface, a distinct reflection pattern appears due to the interface curvature, confirming the existence of a Cassie-Baxter wetting state. By cross-correlating subsequent images, a characteristic decay of the pattern is observed, which is used to characterize the nano Cassie-Baxter transition point.

The wetting state characterization shows that the dual-scale surfaces were at least as stable as the single-scale surfaces. Additionally, the surfaces with higher pillar pitch were less prone to transition during filling of the setup, enabling their use in electro-osmotic flow enhancement. Also, the partial reversibility of the surfaces was demonstrated by subsequent increase and relaxation of the electrowetting potential. The single-scale surfaces showed a duality of wetting states, being locally either in a Cassie-Baxter state or in a Wenzel state. In addition, the dual-scale microstructure showed a range of intermediate wetting states due to the stochastic nature of the surface coating. Finally, the advancing and receding contact

angles on the single-scale and dual scale surfaces were measured. Initially, all surfaces showed a small contact angle hysteresis, with the contact angle hysteresis on the dual-scale surfaces being smaller. When the single scale surfaces were pre-wetted by electrowetting, strong pinning of the contact line could be observed during the measurement of the receding contact angle. The dual-scale surfaces showed no contact line pinning, demonstrating a small contact angle hysteresis even after partial collapse to the nano Cassie-Baxter wetting state.

The understanding of the wetting states obtained in this chapter provides a solid basis for the evaluation of potential enhancement of electro-osmotic flow in the next chapter. By obtaining the stability limit on these surfaces, the maximum electric field normal to the interface is defined. However, further strides could be made for more stable surfaces. For example, the surface chemistry of the nanostructure PVC could additionally be modified, so that the contact angle on a flat surface would exceed the current angle of 97° . This can be achieved by silanization techniques, in analogy to the silanization of the silicon wafer. Also, by utilizing a different manufacturing process, re-entrant structures could be produced, without the need to introduce a secondary structure. This could significantly simplify the evaluation process, as the intermediate wetting states could be suppressed, and illumination through the bottom surface might be achievable. Also, even larger pillar spacings might be utilizable. Nevertheless, the obtained surfaces fulfill the defined requirements: The wetting state is stable during filling and electrowetting, with the gas-liquid interface being supported by the pillar tops. Also, a large fraction of an interconnected gas-liquid area is present. Furthermore, the production process is scalable to several square centimeters, with a generic, defined microstructure. Therefore, in the following of the present thesis, these surfaces are utilized for evaluating the enhancement of electro-osmotic flow over superhydrophobic surfaces.

4 Electro-osmotic flow at a gas-liquid interface over a superhydrophobic surface

In the previous chapter, the stability of the wetting state at a superhydrophobic surface under the influence of a normal electric field was discussed. In this chapter, the electro-osmotic flow over a superhydrophobic surface due to a surface-tangential field is investigated. A gate electrode is used to induce charge at the gas-liquid interface, leading to a variation of the resulting velocity. In this chapter, the flow velocity enhancement over superhydrophobic surfaces compared to flat surfaces is studied, as well as the ability to induce complex 2D-flow patterns in a Hele-Shaw geometry.

The work presented in this chapter is a result of a collaboration with the group of Prof. Moran Bercovici at Technion, Haifa, in the framework of a fund by the *German-Israeli Foundation for Scientific Research and Development* (Grant No. I-1346-401.10/2016). The microfabrication of the soft-lithography master structures was performed by Dr. Khaled Gommed and Baruch Rofman at the cleanroom facilities of the Micro-Nano-Fabrication & Printing Unit at Technion, Haifa. The gate electrodes were produced by Klaus-Dieter Voss at the clean-room facilities of the IMNS at TU Darmstadt and diced by Dr.-Ing. Holger Maune at IMP at TU Darmstadt. The work presented in this chapter was performed jointly with Baruch Rofman, including the production of the channels, and performing the experiments. Distinct contributions of the author include the introduction of the concept of AC-actuation, the derivation of the adapted governing equations, the development of the data processing, and the evaluation of the experimental data. In their function as supervisors, Steffen Hardt and Moran Bercovici provided valuable input during the whole process of this project. The experimental evaluation of the flow enhancement was published in Dehe et al. (2020), and the derivation of the governing equations is part of Dehe et al. (2021b).

4.1 Introduction

Electro-osmotic flow (EOF) describes the fluid motion due to the interaction of a wall-tangential electric field with the free charges inside the EDL. As discussed in section 2.5, the EDL can be created by different mechanisms, for example the wall chemistry interacting with the electrolyte, or an interface-normal electric field. It is a widely adopted driving mechanism in microfluidic applications, since its velocity gradients are confined to a small region close to the wall. It leads to a uniform velocity profile over the channel height, if the flow confinement has a much larger extend than the EDL and the EDL is uniform. Therefore, in the absence of pressure gradients, sample dispersion is reduced compared to pressure-driven flow, and the flow rate scales favorably in a capillary with decreasing channel size ($\propto R^2$ for EOF versus $\propto R^4$ for pressure-driven flow). Examples of applications using EOF include pumping (Laser and Santiago, 2004), chemical analysis using capillary electrophoresis (Monnig and Kennedy, 1994), mixing (Glasgow et al., 2004), and sample concentration (Bown and Meinhart, 2006).

A detailed introduction of the governing equations of EOF will be given in section 4.2, but in order to motivate the remainder of this chapter, it is helpful to discuss some of the key characteristics. One of the

main sources of the wall charge leading to an EDL is the surface chemistry. The chemical equilibrium depends strongly on the combination of the wall material and the electrolyte composition. First, the pH value of the electrolyte strongly influences the chemical equilibrium. For many wall materials utilized in microfluidics such as glass, the wall is charged positively at very low pH values, since the excess of H^+ ions leads to additional positive charges at the wall (Kirby and Hasselbrink, 2004a,b). With increasing pH value (decreasing concentration of H^+), the wall material becomes less positively charged, until the surface charge reverses its sign. In addition, higher ionic concentrations lead to pronounced ionic adsorption at the interface, screening of the wall charge, and reduction of the ζ potential (Falahati et al., 2014; Sze et al., 2003).

This short discussion outlines the most crucial drawback of EOF: The resulting flow velocity depends strongly on the electrolyte, with limited possibility to control the velocity resulting from a given solid-liquid pair. In principle, wall coatings and additives can be used to influence the wall mobility, but once the wall-electrolyte combination is fixed, the charge within the EDL is defined, leaving only the driving electric field to increase the velocity. However, the flow velocity cannot be increased indefinitely, since the Joule heating and electrochemical reactions introducing bubbles at the electrodes pose practical limits on the electric field. EOF over superhydrophobic surfaces offers an alternative mechanism to increase the flow velocity by utilizing the slip effects of the Cassie-Baxter wetting state to increase the resulting flow velocity.

In addition to flow enhancement, this chapter addresses the ability to create height-averaged flow fields in Hele-Shaw cells, where the fluidic domain is bounded by two parallel plates with a characteristic lateral length scale much larger than their intermittent gap. In classical microfluidic applications, the geometry of the fluidic domain, i.e. microchannels, is closely related to the specific process run within the domain. Usually, a process is designed a-priori, with an optimized parameter range in mind. Thereby, the geometry of the domain is adapted to the specific needs. Defining the wall geometry fixes and couples some process parameters, e.g., flow rate and velocity. Redesigning the process requires a redesign of the fluidic domain, with additional manufacturing involved. In a paper by Boyko et al. (2015), a potential method to remove this restriction was discussed theoretically. The authors showed that complex height-averaged flow fields can be created inside Hele-Shaw cells by driving electro-osmotic flow with varying electro-osmotic wall mobilities. Thereby, internal pressure gradients can be created, leading to superposed pressure-driven flow. In the aforementioned work, flow fields corresponding to flow guiding, splitting, mixing and merging were discussed, outlining the ability to run microfluidic applications in sequence on a wall-free microfluidic platform. Gate electrodes, which are embedded in the wall, can be used to change the surface mobilities capacitively. Thus, the wall mobilities can be controlled and a time-dependent change of the flow fields can be induced. In this chapter, the ability to leverage EOF over superhydrophobic surfaces is discussed, both theoretically and experimentally. In parallel to the research efforts outlined in this work, experimental validations of this principle were provided on flat surfaces, changing the wall mobility using surface chemistry (Paratore et al., 2019b) and gate electrodes (Paratore et al., 2019a). Also, in recent applications, this principle was utilized to sort particles by their respective diffusivity (Bacheva et al., 2020) and to cloak an obstacle inside a fluidic domain from a pressure-driven flow field (Boyko et al., 2021).

In the previous chapter, the stability of wetting states on superhydrophobic surfaces versus wall-normal electric fields was discussed. In this chapter, wall-tangential electric fields are leveraged to drive EOF over superhydrophobic surfaces. Specifically, the following questions are addressed: How strongly can the flow velocity be enhanced compared to flat surfaces? What are the limitations imposed by the electrolyte on the EOF? And finally, does EOF over superhydrophobic surfaces provide sufficient control to drive complex flow patterns for future applications? Therefore, the remainder of this chapter is organized as follows: In section 4.2, the theoretical background on electro-osmosis over flat and microstructured surfaces is presented. In section 4.3, the derivation of the governing equations of flow

shaping in Hele-Shaw geometries is adapted for wall boundary conditions incorporating slipping effects. In section 4.4, the EOF over a single gate electrode is characterized and the flow velocity is assessed for different experimental parameters. In section 4.5, different aspects of the results are discussed, specifically the flow enhancement compared to flat surfaces (section 4.5.1), the influence of surfactants on the resulting flow (section 4.5.2), the ability to create complex flow patterns (section 4.5.3) and the relation to the electrowetting stability (section 4.5.4). A summary of the results is given in section 4.6.

4.2 Electro-osmotic flow

The first description of electro-osmosis dates back to 1809, when F. F. Reuss published his observations that water flow could be induced through quartz powder by applying a potential difference between two reservoirs (Biscombe, 2017; Reuss, 1809). Later on, von Helmholtz and Smoluchowski provided the theoretical foundation for electro-osmotic flow (Helmholtz, 1879; von Smoluchowski, 1921). An historical overview over the early works in the field of electrokinetics is given by Lyklema (2003). In the following, the governing equations of electro-osmosis will be presented.

4.2.1 Electro-osmotic flow over flat surfaces

No-slip boundary condition

In order to derive the governing equations for electro-osmotic flow, a flat wall extending into x and y -direction is considered, with a small wall potential $\zeta \ll k_B T/e$. An electric field of magnitude E_0 is directed into the x - y -plane, as depicted in Fig. 4.1(a). Then, in the limit of small Reynolds-numbers Re , the hydrodynamic flow is governed by Stokes equation (eq. 2.38) with an additional electric body force $\mathbf{f}_{el} = \rho_{el}\mathbf{E}$, leading to

$$0 = -\nabla p + \mu \nabla^2 \mathbf{u} + \rho_{el} \mathbf{E}. \quad (4.1)$$

For small potentials, the charge density is governed by the linearized Poisson-Boltzmann equation (eq. 2.78) as

$$\rho_{el} = -\frac{\epsilon_0 \epsilon_{rel} \zeta(x, y)}{\lambda_D^2} \exp\left(-\frac{z}{\lambda_D}\right). \quad (4.2)$$

Here, it is assumed that $\zeta(x, y)$ changes on length scales much larger than λ_D . By integrating eq. 4.1 twice with respect to z , the solution of the flow field is obtained as

$$\mathbf{u}(x, y, z) = -\frac{\epsilon_0 \epsilon_{rel} \zeta(x, y) \mathbf{E}}{\mu} \left(1 - \exp\left(-\frac{z}{\lambda_D}\right)\right) + \frac{z}{\mu} \boldsymbol{\sigma}_z^{visc}(x, y) \cdot (\mathbf{e}_x, \mathbf{e}_y, 0)^T, \quad (4.3)$$

where the no-slip boundary condition at the wall is already utilized. The second term on the right-hand side denotes the external stress due to tangential shear rates of the large scale flow. Usually, the external stresses are negligible compared to the electroviscous stresses, thus the second term becomes negligible.

As is visible from eq. 4.3, the velocity gradients are confined to the EDL, representing a small region in the vicinity of the wall of length-scale λ_D . For fluidic domains of large extend compared to λ_D , a boundary condition in form of a slip velocity can be constructed for EOF. It is assumed that at a coordinate $z = d$, the electric driving term decayed to zero. The position d is denoted as the slip plane of the electro-osmotic flow, and is much smaller than the extend of the fluidic domain in z -direction. Then, the effects of electro-osmotic flow can be summarized in a wall slip velocity as

$$\mathbf{u}_{HS} = -\frac{\epsilon_0 \epsilon_{rel} \zeta \mathbf{E}}{\mu}. \quad (4.4)$$

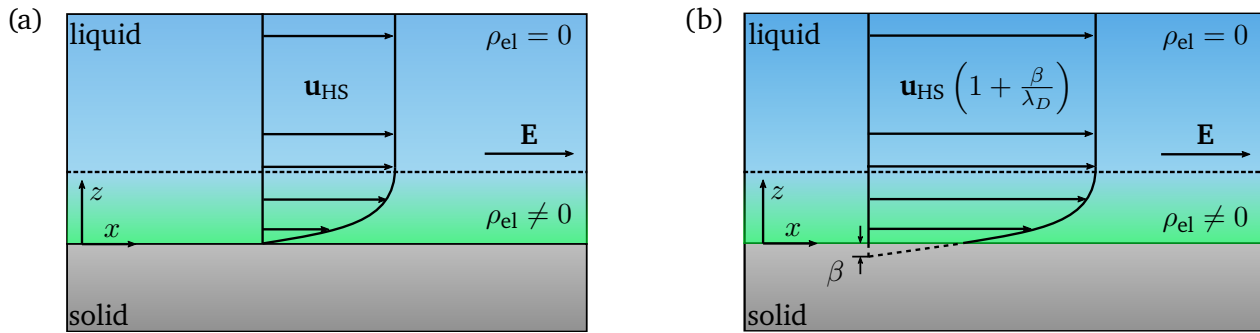


Figure 4.1: Schematic of electro-osmotic flow over a homogeneously charged surface, induced by an electric field directed in the $x - y$ -plane. Close to the wall, the EDL with a charge density ρ_{el} due to a surface potential ζ is present (depicted in green). Outside the EDL, the electrolyte is electroneutral. (a) In case of a no-slip boundary condition at the wall, the classical Helmholtz-Smoluchowski velocity u_{HS} (eq. 4.4) is obtained outside of the Debye-layer. (b) In case of a homogeneously charged surface with an isotropic slip length β , an equivalent to the Helmholtz-Smoluchowski equation is obtained, with an enhancement factor of β/λ_D compared to a no-slip surface of similar surface potential.

The fluid inside the bulk, on scales much larger than λ_D , experiences this electro-osmotic slip velocity, which is referred to as *Helmholtz-Smoluchowski velocity*. Using equation 4.4, the surface potential ζ can be characterized by measuring the fluid velocity due to a defined electric field. It has been used extensively and successfully to characterize different wall material - electrolyte combinations. For a review of materials used in the context of microfluidics, see Kirby and Hasselbrink (2004a,b).

Slip boundary condition

In the above derivation, the flow was assumed to obey a classical no-slip condition at the wall. However, it is important to keep in mind that the no-slip condition is based on observations rather than a first-principle derivation (Batchelor, 2000, p. 149). It is rationalized by the fact that any discontinuity of velocity leads to large stress at an interface, and thus a strong momentum transfer acting to reduce the discontinuity. While this picture seems to hold for clean liquid-liquid interfaces, the momentum transfer at solid-liquid interfaces exhibits some exceptions. Especially for hydrophobic wall materials, experimental observations suggest that a wall slip exists, obeying a Navier-slip boundary condition (eq. 2.57). Different potential sources of slip are identified in literature (see for example Vinogradova (1999)), including molecular slip, an underlying gas layer between liquid and solid, and a decreased viscosity of a wall boundary layer.

Following the renewed interest due to applications in microfluidics, a variety of experimental techniques was used to probe slip at solid-liquid interfaces. Pit et al. (1999) utilized a *total internal reflection fluorescence recovery after photobleaching* (TIR-FRAP) technique to probe the shear rate close to the wall, which showed evidence of slip. Choi et al. (2003) related the flow rate and pressure drop through hydrophilic and hydrophobic channels and observed negligible slip in the hydrophilic channel, and slip lengths on the order of tens of nanometer for hydrophobic channels. Jin et al. (2004) used *total internal reflection velocimetry* (TIRV) to resolve the velocities in the vicinity of the wall, but due to their measurement sensitivity, they concluded that the slip-length, if present, was below 10 nm. Joseph and Tabeling (2005) used *particle image velocimetry* (PIV) to observe slip lengths at the wall, and found that both for hydrophilic and hydrophobic channels, the slip length was below 100 nm. A review of measurements of slip lengths can be found in Lauga et al. (2007). The experimentally determined slip lengths for different wall materials vary over several orders of magnitude, up to hundreds of nanometers. In addition, molecular dynamics simulations support slip lengths of tens of nanometers on hydrophobic

materials (Lauga et al., 2007), thus further corroborating that slip lengths can be present on solid surfaces.

For electro-osmotic flow, slip lengths on the order of nanometer can have a significant impact. Repeating the derivation of the electro-osmotic wall velocity outlined above with a Navier-slip condition at the wall (eq. 2.57), the equivalent to the Helmholtz-Smoluchowski equation (eq. 4.4) follows as

$$\mathbf{u} = -\frac{\epsilon_0 \epsilon_{\text{rel}} \zeta \mathbf{E}}{\mu} \left(1 + \frac{\beta}{\lambda_D}\right) = \mathbf{u}_{\text{HS}} \left(1 + \frac{\beta}{\lambda_D}\right). \quad (4.5)$$

As is evident from eq. 4.5, the velocity is enhanced by a ratio of the slip length β to the Debye-length λ_D when compared to a non-slipping surface. Upon recalling typical length scales of the Debye-length of a few nm, enhancement of at least one order of magnitude is expected when the slip lengths reported in literature are utilized. A similar slip length correction was used to interpret ζ potential measurements in hydrophobic capillaries (Churaev et al., 2002). Similarly, the ability to enhance EOF was described by Stone et al. (2004), and molecular dynamics simulations corroborated these predictions (Joly et al., 2004). A generalization of the amplification of surface-driven transport mechanisms was provided by Ajdari et al. (2006), including diffusio-osmosis and thermo-osmosis. Experimentally, Bouzigues et al. (2008) observed a corresponding enhancement of EOF on the order of $(1 + \beta/\lambda_D) \approx 2$. An alternative experimental observation was provided by Audry et al. (2010), using atomic force microscopy. Thus, it is evident that wall slip can affect EOF over solid surfaces significantly.

4.2.2 Electro-osmotic flow over heterogeneous surfaces

The flow enhancement described in the previous section was derived for a surface exhibiting a uniform ζ potential as well as a uniform slip length. Superhydrophobic surfaces in a Cassie-Baxter wetting state, however, exhibit strong variations of both the local ζ potential as well as the local slip length. The ζ potential at the solid-liquid interfaces is determined by surface chemistry, and the local slip length will be similar to that of a flat surface of the same material. The gas-liquid interface, on the other hand, is often assumed to exhibit no net charge, and exhibits nearly no stress due to the small viscosity of the underlying gas layer.

For pressure-driven flow, these local variations can be averaged to yield an effective boundary condition similar to the Navier-slip condition, with an effective slip length β_{eff} that is assumed to be homogeneous over the surface. The effective wall slip describes the wall slip which the velocity field experiences on average sufficiently far away from the surface. Experimentally, this has been demonstrated by Ou et al. (2004), who measured effective slip lengths over micropillared surfaces in excess of 20 μm . Slip lengths on a similar order have been reported by Choi and Kim (2006), who analyzed the drag reduction of shear flow over a surface. Using a μPIV technique, Joseph et al. (2006) obtained much smaller effective slip lengths ($\beta < 1 \mu\text{m}$) over carbon nanotubes. Ybert et al. (2007) provided scaling laws for slip lengths over superhydrophobic surfaces, leading to achievable slip lengths up to 100 μm . Slip lengths larger than 100 μm have been reported by Lee et al. (2008), using flow over posts and grates in the same setup as Choi and Kim (2006). A review on slip length measurements over superhydrophobic surfaces is given by Rothstein (2010).

The large effective slip lengths of superhydrophobic surfaces suggest enhancement of EOF of several orders of magnitude compared to flat surfaces if naively inserted into eq. 4.5. However, due to the local heterogeneities of the ζ potential, the driving force of EOF is heterogeneously distributed. While the gas-liquid interfaces experience less resistance than the solid-liquid regions, they exhibit a different ζ potential as well (usually smaller). In the limiting case of uncharged gas-liquid interfaces, both the resistance as well as the driving force are smaller, thus raising the question of the resulting velocities.

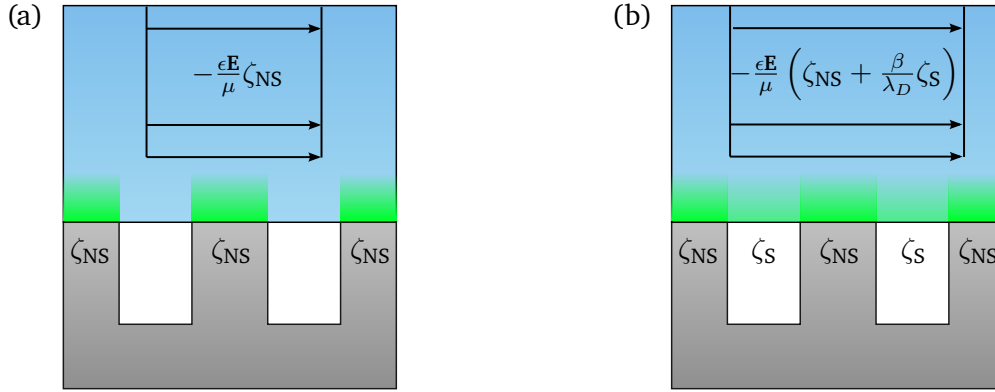


Figure 4.2: Schematic of the effective boundary condition for electro-osmotic flow over microstructured surfaces, exhibiting alternating no-slip patches and stress-free regions, following Squires (2008). The vertical dimension inside the liquid is not drawn to scale for better visibility. (a) In case of vanishing ζ_S potential at the gas-liquid interfaces, the only contribution to the flow stems from the no-slip regions exhibiting ζ_{NS} . The resulting velocity is equivalent to the Helmholtz-Smoluchowski velocity for a homogeneous no-slip surface without no-stress regions. (b) If the gas-liquid interface exhibits a surface potential ζ_S , the resulting velocity has an additional contribution due to the stress-free regions. Due to the ratio of the slip length compared to the Debye-length, already small potentials ζ_S suffice to dominate the resulting flow velocity for sufficiently large slip lengths.

Using the Lorentz reciprocal theorem, Squires (2008) derived the analogous wall slip velocities to the Helmholtz-Smoluchowski equation (eq. 4.4) over surfaces with varying local ζ potential and slip length distributions. In Fig. 4.2, the specific case of a surface exhibiting alternating slip patches and no-slip patches with different, but constant ζ potentials is depicted, for which the resulting velocity was reported as

$$\mathbf{u}_{\text{EOF}} = -\frac{\epsilon_0 \epsilon_{\text{rel}} \mathbf{E}}{\mu} \left(\mathbf{I} \zeta_{NS} + \frac{\beta}{\lambda_D} \zeta_S \right), \quad (4.6)$$

where ζ_{NS} and ζ_S denote the ζ potentials at the no-slip and slip surface, respectively, β denotes the effective slip tensor, and \mathbf{I} the identity tensor. While in principle the result accounts for tensorial slip lengths, only isotropic slip lengths will be discussed in the following. Equation 4.6 outlines some of the characteristics of EOF over superhydrophobic surfaces. First, the classical Helmholtz-Smoluchowski equation is recovered in case of vanishing slip lengths. Second, in case of vanishing ζ_S but with present effective slip length, the result reduces similarly to the electro-osmotic velocity obtained over flat non-slipping surfaces. While a perfectly slipping interface exhibits no drag acting on the liquid, it also does not provide additional forcing in the absence of ζ_S . And third, even small ζ_S potentials can lead to large flow enhancement, since the factor β/λ_D can be large. Along the same train of thought, Huang et al. (2008) concluded based on molecular dynamics simulations that no flow enhancement can be expected if the slipping surface does not exhibit a surface charge. This argument carried over to the review of Rothstein (2010), thus starting to form a narrative in literature that in real-world applications, no flow enhancement should be observed, due to the lack of net charge. Other work on EOF over slipping surfaces focused on the anisotropic response of electro-osmotic flow over slipping surfaces, leading to complex interactions of the slip and mobility tensors (Bahga et al., 2010; Belyaev and Vinogradova, 2011).

Effective slip over superhydrophobic surfaces

The resulting EOF velocity in eq. 4.6 can be enhanced by increasing the effective slip length β of the microstructured surface. Ybert et al. (2007) developed scaling laws for the effective slip length over microstructured geometries. Unsurprisingly, a larger ratio ϕ_S of the gas-liquid area compared to the total area leads to higher effective slip lengths. For a 2D pattern of rectangular posts, in the limit of high ϕ_S , the effective slip length scales as $\beta \propto L/\sqrt{1-\phi_S}$, where L is the length-scale of the periodicity (pillar pitch). A similar scaling of circular posts was calculated by Davis and Lauga (2010). Under the assumption that the gas-liquid interface experiences no shear stress, the resulting slip length of a square pattern of circular posts with small surface fraction results in

$$\frac{\beta}{L} \approx \frac{3}{16} \sqrt{\frac{\pi}{1-\phi_S}} - \frac{3}{2\pi} \ln(1+\sqrt{2}). \quad (4.7)$$

It is important to note that in the present work, the subscript S denotes the *slip* region, following the notation by Squires (2008), whereas in the original work the subscript denotes *solid*. In order to maximize the flow enhancement over superhydrophobic surfaces, the surface fraction ϕ_S has to be maximized.

Controlling the ζ potential by gate electrodes

A second way of enhancing the resulting flow velocity is to increase the ζ_S potential of the gas-liquid interface. In 1969, Melcher and Taylor demonstrated that EOF can be driven at a free interface, if both a surface charge as well as a tangential electric driving field are present (Melcher and Taylor, 1969). By placing a tilted electrode above the free interface, and applying a potential difference between the liquid and the electrode, they induced a surface charge on the interface. The attraction of the surface charge to the gas-liquid interface leads to EOF over an initially uncharged interface. Similarly, EOF over solid surfaces can be influenced by gate electrodes that are embedded below the substrate, without direct contact to the liquid. By applying a voltage difference between gate electrode and electrolyte, the naturally occurring surface charge at the wall can be changed capacitively. For example, Lee et al. (1990) controlled the ζ potential in capillary zone electrophoresis by applying an external, wall-normal field. Similarly, Schasfoort et al. (1999) used gate electrodes to control EOF in a channel, and demonstrated the ability to reverse the direction of the flow by changing the sign of the gate voltage. They also showed that the ability to control the flow is the strongest close to a pH value where the surface is naturally uncharged. Mutlu et al. (2004) extended the principle by using both a direct current (DC) driving signal, as well as an alternating current (AC) driving signal. For the AC driving with a frequency of 1 kHz, they alternated both the driving field direction, as well as the gate electrode direction, leading to a net flow in one direction. A synchronized AC driving signal was used by van der Wouden et al. (2006) for both the driving field and the gate electrodes and they identified the surface chemistry as one of the main limits of flow control. Also, Horiuchi and Dutta (2006) utilized an alternative approach of liquid electrodes instead of metal gate electrodes, separated from the main channel by a dielectric.

To avoid confusion, it is important to keep in mind that the driving based on AC fields as reported by van der Wouden et al. (2006) relies on the existence of a double layer that is fully developed (in quasi-equilibrium). Thus, a maximum frequency defined by electrical relaxation times of the EDL and the channel exists, above which the double layer is not fully developed, and thus the resulting flow is diminished. Other driving mechanisms based on AC electric fields exist, such as reported by González et al. (2000); Green et al. (2000) and Green et al. (2002), where the electric field acts on the non-equilibrated double layer, leading to a maximum flow at frequencies close to the inverted time scale of charge relaxation. The effects utilized in the remainder of this work are based on AC fields interacting

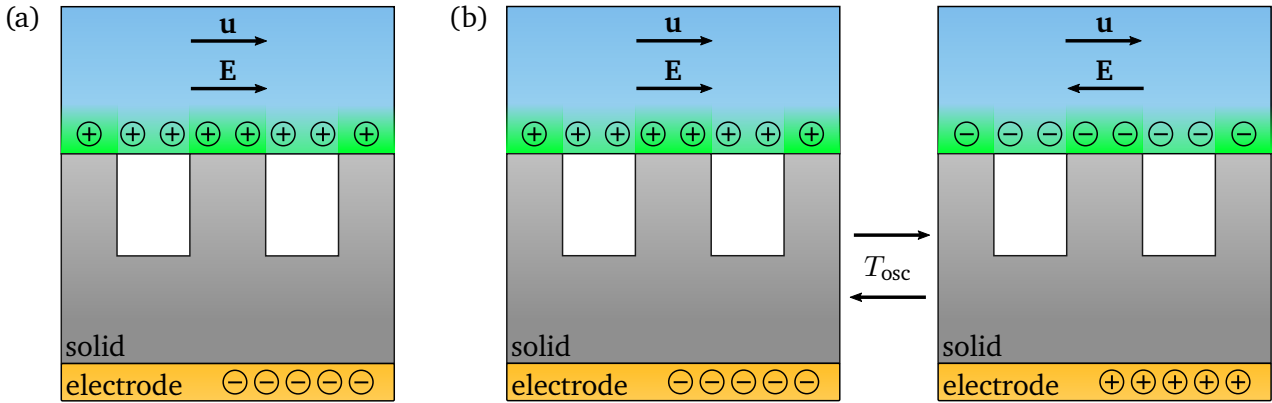


Figure 4.3: Principle of electro-osmotic flow induced by gate electrodes. By applying a potential difference between a gate electrode below the microstructured surface and the electrolyte, additional charges are brought into the proximity of the gas-liquid and the solid-liquid interface. For simplicity, only the induced charges are shown in this schematic, as if the interface was initially uncharged. The gas-liquid and the solid-liquid interface exhibit different ζ potentials due to the different permittivities of the gas and the solid. The EOF can be induced either by using a constant driving field (DC mode, subfigure (a)) or by using a synchronized, time-variant signal for both the driving field and gate potential, where T_{osc} denotes the period (AC mode, subfigure (b)). If a time-variant signal is used, the induced EOF is solely due to the induced potential, as the velocity contribution due to the native ζ potential averages to zero.

with equilibrated double layers, where the symmetry breaking required to induce net flow is due to synchronized gate voltage rather than non-equilibrated double layers.

Following the reasoning outlined above, Schönecker and coworkers suggested the use of gate electrodes below the gas-liquid interface in order to enhance EOF over superhydrophobic surfaces (Schönecker and Hardt, 2014; Steffes et al., 2011). Instead of increasing the effective slip length, the surface potential ζ_s in equation 4.6 is increased. By means of numerical computations and analytical considerations, it was shown that for realistic parameters, flow enhancement of at least two orders of magnitude can be expected. The work presented in this chapter implements this principle to influence EOF over superhydrophobic surfaces. Notably, the experimental implementation differs slightly compared to the aforementioned publications. Instead of providing electrodes solely below the gas-liquid interface, the electrodes are embedded below the superhydrophobic surfaces, due to manufacturing considerations. In Fig. 4.3(a), the driving mechanism using a DC driving field is depicted, where a gate electrode induces additional charges into the EDL, both above the gas-liquid as well as the solid-liquid interface.

Experimentally, it is beneficial to drive the flow over superhydrophobic surfaces using time-variant, synchronized driving and gate fields, in analogy to the work by van der Wouden et al. (2006). First, it allows to identify the flow due to the induced gate potential. EOF due to native ζ potential at the wall averages out over one period of oscillation of the driving field. Only contributions due to induced gate-potential lead to a net-flow. Second, any electrophoretic motion of tracer particles will average out over one period of oscillation as well. And third, it allows for a higher degree of control of the resulting flow field. In order to reverse the flow with a constant driving field above a solid wall, it is necessary to overcome the local native ζ potential. For AC fields, it is sufficient to be able to induce a change of ζ potential, which can be smaller than the native ζ potential. For a rectangular driving signal with amplitude E_0 and without a DC component, the resulting velocity will be of order $\epsilon \Delta \zeta E_0 / \mu$. Therefore, the experiments performed in this section are conducted using synchronized driving fields as well as

gate potentials to drive a net flow. Similar driving schemes have been implemented to induce flow over solid surfaces (Bacheva et al., 2020; Boyko et al., 2021; Paratore et al., 2019a).

4.3 Flow in Hele-Shaw cells: Governing equations

After discussing the fundamental principles of EOF over superhydrophobic surfaces, the governing equations of electro-osmotic flow in Hele-Shaw cells will be presented in this section. As discussed in the introductory section of this chapter, Boyko et al. (2015) derived the relevant governing equations for electro-osmotic flow in Hele-Shaw cells, showing that height-averaged flow fields can be created by variation of the wall mobility. Parallel to the research effort presented in this chapter, the modification of wall mobilities either by surface chemistry (Paratore et al., 2019b) or gate electrodes below a flat surface (Paratore et al., 2019a) was reported in Hele-Shaw flows. In order to derive the governing equations of EOF in Hele-Shaw cells accounting for EOF over superhydrophobic surfaces, the approach of Boyko et al. (2015) and Rubin et al. (2017) is modified to describe stationary and oscillatory flow with varying electro-osmotic mobilities and slip lengths at the walls. A Hele-Shaw cell is characterized by a fluidic domain exhibiting a small distance between the bounding plates. Therefore, it is commonly practiced to derive height-averaged equations, as will be done in the following. A schematic of the system under consideration is given in Fig. 4.4, consisting of a flow cell with constant distance h between the bounding plates, which is small compared to the length scale of change of the boundary conditions. In the following, it is assumed that the distance h is much larger than the Debye-length λ_D , such that the effect of the EOF can be incorporated into a wall boundary condition of the form of eq. 4.6. The bounding plates are assumed to have electro-osmotic mobilities leading to a slip-velocity at the boundaries of the form $\mathbf{u}_{\text{slip}} = \mu(x, y, t)\mathbf{E}(t)$. The mobilities can vary both in space and in time. In addition to the electro-osmotic mobility, the surfaces exhibit some (effective) slip length β . Thereby, the flow over superhydrophobic surfaces can be described and the influence of varying wall boundary conditions on fluid flow can be captured. In analogy to the mobility, the slip length on both surfaces can exhibit a spatial dependence, while there is usually no time dependence.

The governing equations of the fluid flow are the continuity equation (eq. 2.17) as well as the Navier-Stokes equation (eq. 2.35). As the effects of electro-osmosis are included into the wall conditions and the bulk liquid is assumed to be electro-neutral, the body force terms in eq. 2.35 vanish. In order to incorporate EOF as well as slipping effects into the wall boundary conditions, the boundary condition at the lower wall takes the form

$$\mathbf{u}_{\parallel}^L = \mu^L(x, y, t)\mathbf{E}_{\parallel} + \beta^L(x, y)\frac{\partial \mathbf{u}_{\parallel}}{\partial z}\Big|_{z=0}, \quad \mathbf{u}_{\perp}^L = 0, \quad (4.8)$$

where the notation of Boyko et al. (2015) is adapted, where vector-components parallel to the bounding walls are indicated by \parallel and perpendicular components by \perp , and \mathbf{E} denotes the driving electric field. In analogy, the upper wall boundary condition reads

$$\mathbf{u}_{\parallel}^U = \mu^U(x, y, t)\mathbf{E}_{\parallel} - \beta^U(x, y)\frac{\partial \mathbf{u}_{\parallel}}{\partial z}\Big|_{z=h}, \quad \mathbf{u}_{\perp}^U = 0, \quad (4.9)$$

where the changed sign in front of the gradient term is due to the coordinate direction. Before continuing, some characteristics of the boundary conditions need to be elaborated. From eq. 4.6 it follows that the mobility fields μ^L, μ^U depend on the slip length. Where applicable, this dependency needs to be incorporated into the EOF mobility. A second condition of the wall boundary condition is that the walls are considered to either exhibit an EOF velocity or a Navier-slip velocity, but not both at the same time. However, it is convenient to keep both contributions and require $\mu^U\beta^U = 0$ and $\mu^L\beta^L = 0$, at the upper and lower wall, respectively.

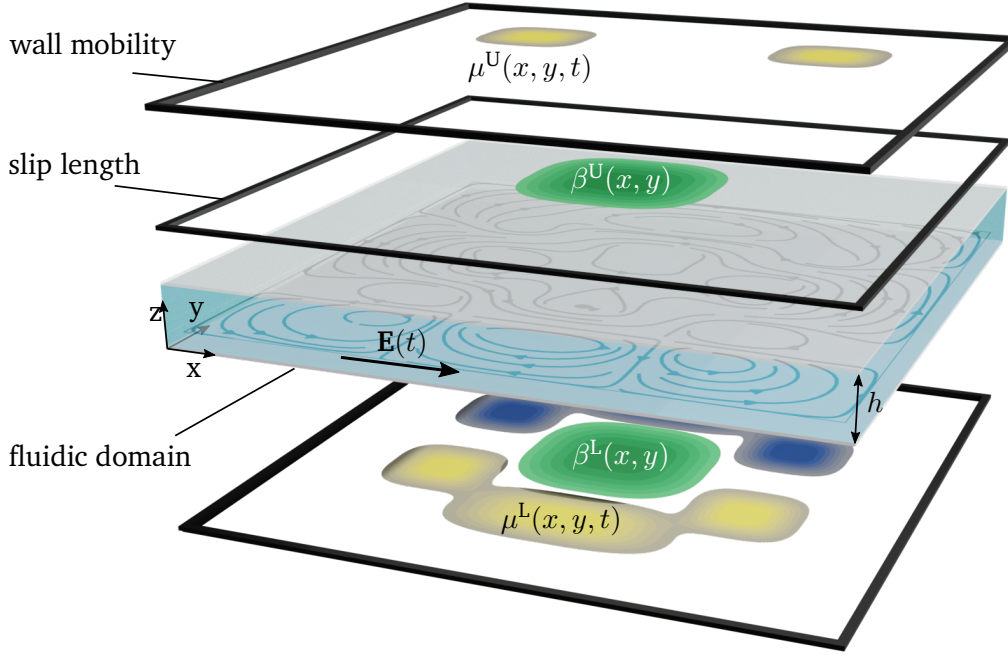


Figure 4.4: Illustration of a Hele-Shaw cell under electric field actuation. The fluidic domain of constant thickness h is bound by two plates with varying electro-osmotic wall mobilities μ^U, μ^L that can exhibit a spatial and temporal variation, and slip length distributions β^U, β^L that exhibit a spatial variation. The characteristic length scale L_0 of the variation of the wall mobilities is assumed to be much larger than the gap thickness ($h \ll L_0$). The variations of the wall mobilities can lead to internal pressure gradients, which in turn induce a height-averaged flow field.

4.3.1 Shallow flow regime

Now, the governing equations (eq. 2.17 and eq. 2.35) are non-dimensionalized. The principle procedure follows closely the work by Boyko et al. (2015), with additionally separating the resulting governing equations into a stationary and oscillatory component. The characteristic length scale in the plane-parallel directions is denoted as L_0 and as h in the z -direction. L_0 represents a scale of change of the wall boundary conditions, not the side-length of the domain. The velocities are scaled by U_0 and W_0 , respectively. The characteristic velocity U_0 follows from the specific problem investigated. For EOF, this velocity follows as the product of the electro-osmotic mobility scale $\mu_{\text{EOF},0}$ and the electric field scale E_0 . The characteristic velocity in wall-normal direction W_0 , the pressure scale P_0 , as well as the time scale T_0 remain to be specified following from order-of-magnitude arguments. The slip lengths β^U and β^L are non-dimensionalized using h .

From the non-dimensionalization, the small parameter

$$\epsilon = \frac{h}{L_0} \ll 1, \quad (4.10)$$

emerges, allowing the determination of the missing characteristic scales. From an order-of-magnitude analysis of the continuity equation 2.17, the z -velocity scale follows as $W_0 = \epsilon U_0$. From the in-plane components of the Navier-Stokes equation, the pressure scale results in $P_0 = \mu U_0 / L_0 \epsilon^2$. Inserting the

scales into the governing equations leads to

$$0 = \frac{\partial \hat{u}}{\partial \hat{x}} + \frac{\partial \hat{v}}{\partial \hat{y}} + \frac{\partial \hat{w}}{\partial \hat{z}}, \quad (4.11a)$$

$$\epsilon Re St \frac{\partial \hat{\mathbf{u}}_{\parallel}}{\partial \hat{t}} + Re \epsilon \left(\hat{u} \frac{\partial}{\partial \hat{x}} + \hat{v} \frac{\partial}{\partial \hat{y}} + \hat{w} \frac{\partial}{\partial \hat{z}} \right) \hat{\mathbf{u}}_{\parallel} = -\nabla_{\parallel} \hat{p} + \left(\epsilon^2 \left(\frac{\partial^2}{\partial \hat{x}^2} + \frac{\partial^2}{\partial \hat{y}^2} \right) + \frac{\partial^2}{\partial \hat{z}^2} \right) \hat{\mathbf{u}}_{\parallel}, \quad (4.11b)$$

$$\epsilon^3 Re St \frac{\partial \hat{w}}{\partial \hat{t}} + \epsilon^3 Re \left(\hat{u} \frac{\partial}{\partial \hat{x}} + \hat{v} \frac{\partial}{\partial \hat{y}} + \hat{w} \frac{\partial}{\partial \hat{z}} \right) \hat{w} = -\frac{\partial \hat{p}}{\partial \hat{z}} + \left(\epsilon^4 \left(\frac{\partial^2}{\partial \hat{x}^2} + \frac{\partial^2}{\partial \hat{y}^2} \right) + \epsilon^2 \frac{\partial^2}{\partial \hat{z}^2} \right) \hat{w}. \quad (4.11c)$$

Here, hatted symbols denote non-dimensionalized variables. The parameter $Re = \rho U_0 h / \mu$ denotes the Reynolds number, comparing the relative importance of inertia to viscous forces, and $St = L_0 / U_0 T_0$ denotes the Strouhal number, which represents the ratio between the advective time scale and the characteristic time scale. For the remainder of the derivation of the governing equations, it is assumed that the flow is dominated by viscosity, leading to

$$\epsilon Re \ll 1. \quad (4.12)$$

In order to determine the missing characteristic time scale of the problem, it is reasonable to choose the inverse oscillatory frequency $T_{osc} = 1/f_0$, and in the following, it is assumed that

$$\epsilon St Re = \frac{\rho h^2}{\mu T_{osc}} \ll 1. \quad (4.13)$$

This condition constitutes an upper limit for the oscillation frequency, such that inertia effects due to the oscillatory motion are negligible. Moreover, it is assumed that the electric field is uniform over the whole cell, without wall-normal component. Therefore, the surface conductivity has to be small compared to the bulk conductivity (Squires, 2008), and additionally, the dielectric permittivity of the liquid has to be larger than the wall.

4.3.2 Governing equations for the flow

In a next step, the leading order of the governing equations 4.11 is utilized. For readability, the hats denoting non-dimensional variables are dropped in the following derivation. Double integration of 4.11b with respect to z yields the local flow profile of a parabolic form as

$$\mathbf{u}_{\parallel} = \nabla_{\parallel} p \frac{z^2}{2} + \mathbf{f}z + \mathbf{g}, \quad (4.14)$$

where \mathbf{f} , \mathbf{g} are position- and time-dependent vector functions. They can be expressed by accounting for the boundary conditions at the upper and lower wall (eq. 4.8 and 4.9), resulting in

$$\mathbf{f} = \frac{\mu^U - \mu^L}{1 + \beta^U + \beta^L} \mathbf{E}_{\parallel} + \frac{-\frac{1}{2} - \beta^U}{1 + \beta^U + \beta^L} \nabla_{\parallel} p \quad (4.15)$$

and

$$\mathbf{g} = \mu^L \mathbf{E}_{\parallel} + \beta^L \frac{\mu^U - \mu^L}{1 + \beta^U + \beta^L} \mathbf{E}_{\parallel} + \beta^L \frac{-\frac{1}{2} - \beta^U}{1 + \beta^U + \beta^L} \nabla_{\parallel} p. \quad (4.16)$$

The local flow field depends both on the external electric field as well as the pressure field inside the cell, which may be due to an external pressure gradient or due to internal pressure gradients resulting from inhomogeneous EOF. Up to now, the pressure gradient $\nabla_{\parallel} p$ is not known and requires determination in subsequent steps.

In the following, the height-average is denoted by $\langle(\cdot)\rangle = \int_0^1(\cdot)dz$, and averaging the velocity field (eq. 4.14) gives the height-averaged velocity field

$$\langle\mathbf{u}_{\parallel}\rangle = -\frac{1}{12}\frac{1+4(\beta^U+\beta^L)+12\beta^U\beta^L}{1+\beta^U+\beta^L}\nabla_{\parallel}p + \frac{1}{2}\frac{\mu^U+\mu^L+2(\beta^U\mu^L+\beta^L\mu^U)}{1+\beta^U+\beta^L}\mathbf{E}_{\parallel}. \quad (4.17)$$

It is convenient to introduce the effective mobilities $\langle\mu^P\rangle$ and $\langle\mu^{\text{EOF}}\rangle$ as

$$\langle\mu^P\rangle = \frac{1+4(\beta^U+\beta^L)+12\beta^U\beta^L}{1+\beta^U+\beta^L} \quad (4.18)$$

and

$$\langle\mu^{\text{EOF}}\rangle = \frac{1}{2}\frac{\mu^U+\mu^L+2(\beta^U\mu^L+\beta^L\mu^U)}{1+\beta^U+\beta^L}. \quad (4.19)$$

Rewriting equation 4.17 demonstrates the similarity to Boyko et al. (2015)

$$\langle\mathbf{u}_{\parallel}\rangle = -\frac{1}{12}\langle\mu^P\rangle\nabla_{\parallel}p + \langle\mu^{\text{EOF}}\rangle\mathbf{E}_{\parallel}. \quad (4.20)$$

In chapter 5, information about the velocity deviation $\mathbf{u}_{\parallel} - \langle\mathbf{u}_{\parallel}\rangle$ will be required, which can be obtained by subtracting equation 4.20 from equation 4.14.

As discussed above, the pressure gradient $\nabla_{\parallel}p$ remains unknown up to now. By applying the two-dimensional divergence operator to equation 4.20 and by utilizing equation 4.11a as well as the no-flux boundary condition, a governing equation for the pressure is obtained as

$$\frac{1}{12}\nabla_{\parallel}\cdot(\langle\mu^P\rangle\nabla_{\parallel}p) = \nabla_{\parallel}\cdot\langle\mu^{\text{EOF}}\rangle\mathbf{E}_{\parallel}. \quad (4.21)$$

Both effective mobilities $\langle\mu^P\rangle$ and $\langle\mu^{\text{EOF}}\rangle$ are position-dependent. In combination with appropriate boundary conditions at the lateral edges of the flow domain, equation 4.21 can be solved for the pressure field, determining the velocity (eq. 4.20).

Alternatively, an equation for the stream function ψ , which is defined via $\mathbf{u}_{\parallel} = (\partial\psi/\partial y, -\partial\psi/\partial x)$ can be generated. Applying the z -component of the curl operator to equation 4.20 yields

$$(\nabla_{\parallel}\times\langle\mathbf{u}_{\parallel}\rangle)\cdot\mathbf{e}_z = -\nabla_{\parallel}^2\psi = -\frac{1}{12}(\nabla_{\parallel}\langle\mu^P\rangle\times\nabla_{\parallel}p)\cdot\mathbf{e}_z - (\mathbf{E}_{\parallel}\times\nabla_{\parallel}\langle\mu^{\text{EOF}}\rangle)\cdot\mathbf{e}_z, \quad (4.22)$$

where \mathbf{e}_z denotes the unit vector in z -direction. Physically, this equation describes the vorticity, which is defined by $\omega = -\nabla_{\parallel}^2\psi$. Following the source terms in eq. 4.22, vorticity results from gradients in the electro-osmotic mobility normal to the electric field or by pressure gradients normal to slip mobility gradients. If the slip mobility is constant throughout the domain, eq. 4.22 decouples from eq. 4.21.

Equations 4.21 and 4.22 are the governing equations of the leading order of the problem. As was shown by Boyko et al. (2015), this leading order solution allows to solve for the inverted problem, where a flow field is given, and the corresponding wall mobility is solved for. This property allows for designing specific flow fields, making it a useful tool to design microfluidic applications. While higher-order solutions can be obtained by analyzing the higher-order contributions in equations 4.11(a-c), solving for the inverse problem is not as straight-forward. Therefore, the solution is restricted to the leading order in the following.

Governing equations for the time-averaged fields

Equations 4.21 and 4.22 govern the problem, for arbitrary driving fields as well as electro-osmotic wall mobilities. As discussed, time-averaged flow fields can be induced by purely oscillatory functions, and in order to compute the resulting flow, it is assumed that the driving field and the wall mobilities consist of a time-averaged and an oscillatory component. Then, it is convenient to split equations 4.21 and 4.22 into their time-averaged and oscillatory components. Therefore, the time-average over one oscillation period is defined as

$$\overline{(\cdot)} = \frac{1}{T_{\text{osc}}} \int_{t_0}^{t_0+T_{\text{osc}}} (\cdot) dt, \quad (4.23)$$

where T_{osc} describes the period of oscillation and t_0 an arbitrary time. In order to compute the time-averages, the variables such as velocity, pressure, as well as electro-osmotic wall mobility are split into their time-averaged and oscillatory components as $a = \bar{a} + a'$.

Applying the time-average to eq. 4.21, the time-averaged pressure equation follows as

$$\frac{1}{12} \nabla_{\parallel} \cdot (\langle \mu^{\text{P}} \rangle \nabla_{\parallel} \bar{p}) = \nabla_{\parallel} \cdot \left(\overline{\langle \mu^{\text{EOF}} \rangle \bar{\mathbf{E}}_{\parallel}} + \overline{\langle \mu'^{\text{EOF}} \rangle \mathbf{E}'_{\parallel}} \right). \quad (4.24)$$

The resulting equation has a similar form as equation 4.21, with different source terms. A time-averaged flow field can either be driven by the interaction of a time-averaged mobility interacting with a time-averaged driving field, or by a non-zero time-average of the oscillatory components, such as two synchronized rectangular step functions. It is important to note that the temporal structure of the oscillatory components is of importance, as for example a phase shift between the signals leads to changing time-averages.

Similarly, the time-average applied to eq. 4.22 results in

$$-\nabla_{\parallel}^2 \bar{\psi} = -\frac{1}{12} (\nabla_{\parallel} \langle \mu^{\text{P}} \rangle \times \nabla_{\parallel} \bar{p}) \cdot \mathbf{e}_z - \left(\bar{\mathbf{E}}_{\parallel} \times \nabla_{\parallel} \overline{\langle \mu^{\text{EOF}} \rangle} \right) \cdot \mathbf{e}_z - \left(\mathbf{E}'_{\parallel} \times \nabla_{\parallel} \overline{\langle \mu'^{\text{EOF}} \rangle} \right) \cdot \mathbf{e}_z, \quad (4.25)$$

with additional source terms on the right-hand-side, containing the cross-product of time-averaged components, as well as the time-average of oscillatory components. The full time-averaged problem is defined by equations 4.24 and 4.25.

Governing equations for the oscillatory fields

While the time-averaged flow field suffices to determine the observed average flow field, in chapter 5, the oscillatory component of the flow field is required for determining the dispersion induced by the oscillatory fluid motion. Therefore, the oscillatory flow field components can be obtained by subtracting the time-averaged equation 4.24 from equation 4.21, leading to

$$\frac{1}{12} \nabla_{\parallel} \cdot (\langle \mu^{\text{P}} \rangle \nabla_{\parallel} p') = \nabla_{\parallel} \cdot \left(\langle \mu'^{\text{EOF}} \rangle \bar{\mathbf{E}}_{\parallel} + \overline{\langle \mu^{\text{EOF}} \rangle} \mathbf{E}'_{\parallel} + \langle \mu'^{\text{EOF}} \rangle \mathbf{E}'_{\parallel} - \overline{\langle \mu'^{\text{EOF}} \rangle} \mathbf{E}'_{\parallel} \right). \quad (4.26)$$

In order to generate insight into the expected oscillatory motion of the resulting flow field, it is instructive to discuss the forcing terms on the right hand side. The first two terms describe the interaction of the time-averaged wall mobility with the oscillatory component of the the driving field, and vice-versa. These terms exhibit an oscillatory motion similar to the driving field, as well as the wall mobility. The third and the fourth terms describe the interaction of the oscillatory components with each other, leading to higher-order frequencies. For example, if both the driving field as well as the wall mobility are forced according to a sinusoidal signal with frequency ω , the forcing terms will consist of frequencies with

ω and 2ω . If the oscillatory forcing of the wall mobility as well as the driving field consist of multiple frequencies, the resulting spectrum will consist of even more frequencies.

Continuing with the derivation of the stream function, the time-averaged equation 4.25 is subtracted from equation 4.22, resulting in

$$\begin{aligned} -\nabla_{\parallel}^2 \psi' = & -\frac{1}{12} (\nabla_{\parallel} \langle \mu^p \rangle \times \nabla_{\parallel} p') \cdot \mathbf{e}_z - \left(\mathbf{E}'_{\parallel} \times \nabla_{\parallel} \langle \overline{\mu^{\text{EOF}}} \rangle \right) \cdot \mathbf{e}_z \\ & - \left(\overline{\mathbf{E}}_{\parallel} \times \nabla_{\parallel} \langle \mu'^{\text{EOF}} \rangle \right) \cdot \mathbf{e}_z - \left(\mathbf{E}'_{\parallel} \times \nabla_{\parallel} \langle \mu'^{\text{EOF}} \rangle \right) \cdot \mathbf{e}_z + \left(\overline{\mathbf{E}'_{\parallel}} \times \nabla_{\parallel} \langle \mu'^{\text{EOF}} \rangle \right) \cdot \mathbf{e}_z. \end{aligned} \quad (4.27)$$

Similarly to the pressure equation, the additional coupling terms due to oscillatory components lead to multiple frequencies.

Ultimately, the governing equations of the problem are obtained, leading to equations 4.24 and 4.25 for the stationary part, and equations 4.26 and 4.27 for the oscillatory part. Then, one can construct the resulting time-averaged flow fields (\bar{u} , \bar{v} , \bar{w}), the height-averaged and time-averaged flow fields ($\langle \bar{u} \rangle$, $\langle \bar{v} \rangle$, $\langle \bar{w} \rangle$) as well as oscillatory flow fields (u' , v' , w'), depending on the requirement of the problem.

4.3.3 Flow field of a circular wall mobility

A specific flow field that is especially promising to test and validate the flow enhancement over superhydrophobic surfaces is the flow field due to a circular patch of a constant wall mobility $\langle \mu_{\text{EOF},0} \rangle$, with vanishing wall mobility at the outside. Since the resulting governing equations are similar to the resulting equations by Boyko et al. (2015), the mathematical treatment is analogous and thus only summarized in this section.

The corresponding wall mobility $\langle \mu_{\text{EOF},0} \rangle$ can be described as

$$\langle \mu^{\text{EOF}} \rangle = \langle \mu_{\text{EOF},0} \rangle H(r_0 - r), \quad (4.28)$$

where r_0 denotes the radius of the circular region, r the radial coordinate in a polar coordinate system fixed at the center of the disc, H the Heaviside step function, and $\langle \mu_{\text{EOF},0} \rangle$ the value of $\langle \mu^{\text{EOF}} \rangle$ above the electrode.

In the following, the electric field is directed along the x -direction and constant over time ($\mathbf{E}_{\parallel} = (E_0, 0)$). Solving equation 4.21 separately in the inner and outer region results in a pressure field in polar coordinates as

$$p(r, \Theta) = \begin{cases} \left(\frac{a_{\text{out}}}{r} + b_{\text{out}} r \right) \cos \Theta & r > r_0 \\ b_{\text{in}} r \cos \Theta & r < r_0. \end{cases} \quad (4.29a)$$

$$b_{\text{in}} r \cos \Theta \quad r < r_0. \quad (4.29b)$$

Then, the pressure can be inserted into equation 4.20, yielding the resulting velocity distribution as

$$\langle \mathbf{u}_{\parallel} \rangle(r, \Theta) = \begin{cases} \frac{1}{12} \langle \mu_{\text{p}}^{\text{out}} \rangle \left(\left(-b_{\text{out}} + \frac{a_{\text{out}}}{r^2} \right) \cos \Theta \mathbf{e}_r + \left(b_{\text{out}} + \frac{a_{\text{out}}}{r^2} \right) \sin \Theta \mathbf{e}_{\Theta} \right) & r > r_0 \\ \frac{1}{12} \langle \mu_{\text{p}}^{\text{in}} \rangle \left((-b_{\text{in}} + 12E_0 \langle \mu_{\text{EOF},0} \rangle) \cos \Theta \mathbf{e}_r + (b_{\text{in}} - 12E_0 \langle \mu_{\text{EOF},0} \rangle) \sin \Theta \mathbf{e}_{\Theta} \right) & r < r_0, \end{cases} \quad (4.30a)$$

$$\frac{1}{12} \langle \mu_{\text{p}}^{\text{in}} \rangle \left((-b_{\text{in}} + 12E_0 \langle \mu_{\text{EOF},0} \rangle) \cos \Theta \mathbf{e}_r + (b_{\text{in}} - 12E_0 \langle \mu_{\text{EOF},0} \rangle) \sin \Theta \mathbf{e}_{\Theta} \right) \quad r < r_0, \quad (4.30b)$$

where \mathbf{e}_r and \mathbf{e}_{Θ} are the unit vectors in polar coordinates, and the subscripts in and out denote the inner and outer region, respectively. Inside the inner region, the resulting flow field is uniform due to the constant pressure gradient, leading to

$$\langle \mathbf{u}_{\parallel} \rangle_{\text{in}} = -\frac{1}{12} \langle \mu_{\text{p}}^{\text{in}} \rangle b_{\text{in}} \mathbf{e}_x + E_0 \langle \mu_{\text{EOF},0} \rangle \mathbf{e}_x. \quad (4.31)$$

The resulting flow field resembles a dipole flow, with a uniform flow field above the electrode. Due to the uniformity, such a flow field is ideal to evaluate the effects of induced ζ potentials.

The remaining constants can be obtained by requiring that the flow field far away from the electrode vanishes, and that both the pressure as well as the radial velocity are continuous at $r = r_0$. The resulting coefficients then read

$$a_{\text{out}} = 12 \frac{E_0 \langle \mu_{\text{EOF},0} \rangle}{\langle \mu_{\text{p}}^{\text{in}} \rangle + \langle \mu_{\text{p}}^{\text{out}} \rangle} r_0^2. \quad (4.32)$$

$$b_{\text{in}} = 12 \frac{E_0 \langle \mu_{\text{EOF},0} \rangle}{\langle \mu_{\text{p}}^{\text{in}} \rangle + \langle \mu_{\text{p}}^{\text{out}} \rangle}, \quad (4.33)$$

$$b_{\text{out}} = 0. \quad (4.34)$$

Here, a_{out} represents the dipole strength, b_{in} the resulting pressure gradient in the direction of the electric field inside the circular region and b_{out} the externally applied pressure gradient, respectively. The resulting velocity in the inner region follows as

$$\langle \mathbf{u}_{\parallel} \rangle_{\text{in}} = E_0 \langle \mu_{\text{EOF},0} \rangle \left(\frac{\langle \mu_{\text{p}}^{\text{out}} \rangle}{\langle \mu_{\text{p}}^{\text{in}} \rangle + \langle \mu_{\text{p}}^{\text{out}} \rangle} \right) \mathbf{e}_x. \quad (4.35)$$

This result is valid for the theoretically predicted velocity in the central region of the dipole flow. It is important to keep in mind that this result is non-dimensional. Later on, its dimensional counterpart will be used to compare the experimentally observed velocity with the theoretically predicted velocity.

4.4 Characterization of electro-osmotic flow over superhydrophobic surfaces

4.4.1 Experimental setup

In order to characterize the electro-osmotic flow over superhydrophobic surfaces, the flow above a single disk-shaped gate electrode is characterized as a prototypical experiment. In Fig. 4.5, the experimental setup is depicted schematically. It consists of a superhydrophobic surface as the lower bounding wall of a Hele-Shaw cell with a size of 2 cm x 1 cm x 100 μm (length x width x depth). The surfaces utilized in the experiments correspond to the dual-scale surfaces presented in chapter 3, consisting of a PDMS-pillared surface with varying pillar pitch $p = 10, 15, 20,$ and $25 \mu\text{m}$ (see Table 3.1 for values of the geometric parameters). In addition, a secondary roughness consisting of PVC was applied to enhance the stability of the Cassie-Baxter wetting state. By variation of the pillar pitch, the effective slip length β was varied. The microfluidic device was created by producing several gate electrodes (chrome, diameter $d_{\text{disk}} = 500 \mu\text{m}$) on top of a glass wafer by vapor deposition (Balzers BAK 600) and a lift-off process using photoresist (AZ 9260). The resulting wafer was diced such that the remaining pieces have one electrode each. Then, the glass wafer as well as the back side of the microstructured PDMS was activated using oxygen plasma (*Diener Femto* plasma cleaner, 20 s, 50 W) and by placing the PDMS on the glass, a permanent bond was formed. The top part of the chip was created by glass slides cut to size, with drilled holes for liquid access. Both parts were sealed by UV-cured optical glue (*Thorlabs*, NOA68), with the lateral restriction of the PDMS posing as a spacer, creating the fluidic chamber. Reservoirs made from punched pieces of PDMS were placed on top of the holes of the chip.

The liquid domain was connected to a multichannel power source (*Labsmith HVS448-6000D*) via two platinum wire electrodes immersed into the channel reservoirs, as depicted in Fig. 4.5(b). In addition, the power source was connected to the gate electrode to provide the gate voltage. The EOF was driven by

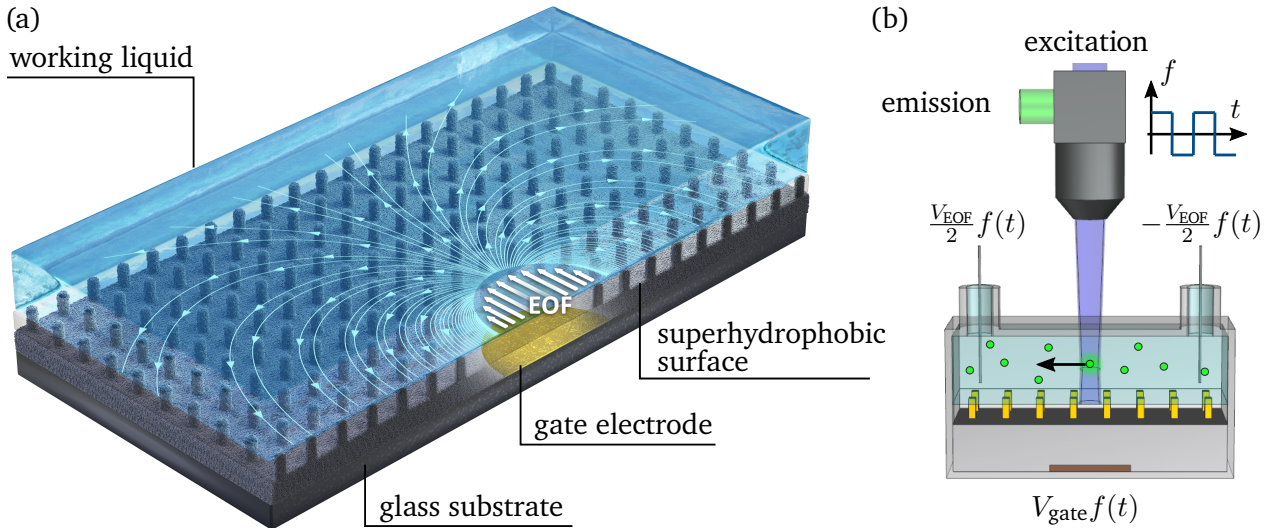


Figure 4.5: Schematic of the experimental setup. (a) Illustration of the resulting flow field induced by a circular gate electrode embedded below a microstructured, superhydrophobic surface. The fluidic cell is bound by a glass slide at the top (not shown). Inside the cell, a dipole flow field is induced. (b) Particle tracking velocimetry setup utilized to characterize the flow velocity using fluorescent tracer particles. The fluid motion is induced by two wire electrodes embedded into the reservoirs of the channel, actuated by a rectangular wave signal with a voltage difference V_{EOF} . At the synchronized gate electrode, a voltage amplitude of V_{gate} is applied. Adapted figure with permission from Sebastian Dehe, Baruch Rofman, Moran Bercovici, and Steffen Hardt, *Phys. Rev. Fluids*, 5(5), 053701, 2020. Copyright (2020) by the American Physical Society.

a rectangular AC voltage of alternating sign and zero mean, with a frequency of 5 Hz, thereby leading to a vanishing time-averaged motion due to the native ζ potential at the channel walls. The EOF above the electrode was driven by applying a synchronized AC signal with a rectangular waveform with a frequency of 5 Hz, and an amplitude V_{gate} , thus leading to a local flow.

By adding fluorescent polystyrene particles (diameter $d_{bead} = 2 \mu\text{m}$, *Thermofisher*, excitation 488 nm, emission 508 nm), the fluid flow was visualized through a *Nikon AZ-100* microscope with a magnification of 3x and a numerical aperture of $NA=0.1$, using a *Nikon intensilight* for illumination. Due to the low magnification and numerical aperture, particles over all z -positions of the fluidic domain were imaged simultaneously. An sCMOS camera (*ZWO ASI 178mm-cool*) captures the particle motion at a framerate of 100 fps. In order to match the solution's mass density to the particle density, a 50 vol-% D_2O / H_2O solution is used. Thus, the particles are homogeneously distributed over the channel depth. At standard conditions, an aqueous 4-(2-hydroxyethyl)-1-piperazineethanesulfonic acid (HEPES) buffer solution with an ionic strength of 10 mM at $pH = 7$ was used to run experiments. For variations of the pH value, buffer solutions between the pH values of 3 to 11 were used at a fixed ionic strength of 10 mM (see table 4.1 for detailed composition). In order to vary the ionic strength, a HEPES-NaOH buffer at an ionic strength of 1 mM was used, with additional KCl to adjust to the desired ionic strength. All experiments were performed at a laboratory temperature of 15 °C.

4.4.2 Flow velocity measurements

Before starting the experiments, the channels were filled with de-ionized water (DI-water, *Milli-Q*), and by optical inspection, the existence of a Cassie-Baxter wetting state was confirmed. As discussed in

Table 4.1: Buffer composition of the experiments. Aqueous solutions are used, based on a 50 % H₂O / D₂O mixture, with the ionic strength fixed to $I = 10$ mM. The pH value is changed by adding a weak base or acid and shifting the chemical equilibrium with a strong acid or base as titrant, respectively. The ionic strengths as well as buffer capacitance is calculated using *peakmaster* 5.3 (Gaš et al., 2005).

pH value	buffer (weak electrolyte)	concentration c_{buf} (mM)	titrant (strong acid / base)	concentration c_{tit} (mM)
3	Citric acid	20	NaOH	9
5	Creatinine	20	HCl	10
7	HEPES	42.85	NaOH	10
9	Histidine	26	NaOH	10
11	Histidine	9	NaOH	10

chapter 3, the Cassie-Baxter state exhibits a different reflectivity under epi-illumination than regions transitioned into a nano Cassie-Baxter state or Wenzel state. Continuing, the DI-water was flushed from the channel with the appropriate buffer solution. Each experimental series started at the lowest gate voltage amplitude, with each experiment performed at a fixed gate voltage amplitude for 60 s. In between experiments, a break of approximately 20 s was held, until the voltage was increased in steps of 250 V. As analyzed in chapter 3 (section 3.5), the wetting state transitions are partially irreversible. Therefore, the experimental data is only usable before such a transition occurs. This point is discussed in more detail in section 4.5.4. Also, from the previous chapter, it is known that initial transitions are confined to localized regions, due to surface inhomogeneities. Thereby, the effective slip length is reduced locally, leading to curved streamlines in the experiments, allowing assessment of the wetting state during experiments.

The flow velocity was obtained by using particle tracking velocimetry (PTV) provided by the *Matlab* toolbox *PTVLab* (Brevis et al., 2011). The recorded videos were imported and by computing and subtracting the median image from each image in the stack, the background illumination as well as stationary particles adhering to the surface are filtered out. The median image was used, since local intensity changes due to the particle motion do not propagate into the resulting image. Finally, only the fluorescent particle motion was processed without steady state background. From the evaluation, the particle positions as well as the velocities were obtained and saved. For one experimental condition, several tens of thousand particle velocities were obtained above the gate electrode during the experimental time of 60 s.

Due to the density matching between solution and particle and the large depth of field of the optical instrumentation, the PTV algorithm obtained particle velocities over the whole channel depth. Also, according to the governing equation (eq. 4.35), the averaged flow field above the electrode is position independent, thus allowing to ensemble-average all N measured particle velocities $\mathbf{u}_{\text{ROI},i}$ without loss of information. The region of interest is indicated in Fig. 4.6(a), and the resulting average velocity is obtained as

$$u_{\text{avg}} = \frac{1}{N} \sum_{i=1}^N \|\mathbf{u}_{\text{ROI},i}\|. \quad (4.36)$$

Effectively, a height-averaged measurement method is used to evaluate the height-averaged theory. In Fig. 4.6(b), the resulting averaged velocity is shown for different pillar pitches at pH= 7 and a driving field of 50 V cm⁻¹. The resulting velocity shows a linear dependence on the gate voltage in the range of -750 V to 750 V, and is antisymmetric upon reversing the sign of the gate voltage. As expected from equation 4.6, a higher pillar spacing leads to higher velocities due to the increased slip lengths. Upon

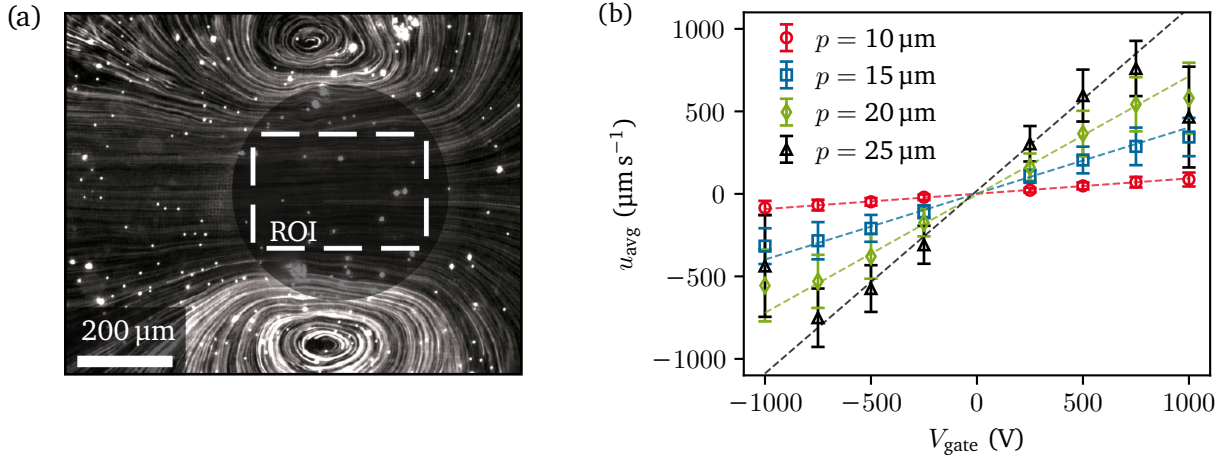


Figure 4.6: Measurement of EOF over superhydrophobic surfaces. (a) Particle streakline image showing the resulting flow field induced by a circular gate electrode (shown as dark overlay). The resulting flow field is obtained by ensemble-averaging the measured particle velocities according to eq. 4.36 within the region of interest (ROI). (b) Experimentally obtained flow velocity above the gate electrode for varying pillar pitches p with a driving field of 50 V cm^{-1} and a driving frequency of 5 Hz using a buffer solution with an ionic strength $I = 10 \text{ mM}$ at pH 7. The error bars represent the 95 %-confidence interval based on at least 6 independent measurements. The dashed lines represent linear fits for the range $V_{gate} = -750 \text{ V}$ to -750 V . Adapted figure with permission from Sebastian Dehe, Baruch Rofman, Moran Bercovici, and Steffen Hardt, Phys. Rev. Fluids, 5(5), 053701, 2020. Copyright (2020) by the American Physical Society.

further increase of the gate voltage, the velocity deviates from the linear scaling, leading to a reduction of the velocity. This is a direct result of the wetting state transitions, as will be discussed in section 4.5.4.

4.4.3 Rescaled flow velocity

In order to validate the theoretical model, the flow velocity can be rescaled according to equation 4.35, which requires information about the effective slip length β as well as the gas-liquid interface potential ζ_S . As discussed in section 4.2.2, an approximation for the slip length of a micropillared surface is given by Davis and Lauga (2010). For a flat gas-liquid interface, disregarding the viscous stress of the enclosed gas, and assuming a homogeneous surface, the isotropic slip length of an rectangular array of circular pillars can be approximated by equation 4.7. The geometric parameters of the utilized microstructure are described in Table 4.2. The surfaces exhibiting the smallest pillar pitch $p = 10 \text{ μm}$ have a sublayer thickness of 130 μm and a pillar height of 10 μm , and the other pillar pitches have a pillar height of 15 μm with a sublayer thickness of 120 μm . As discussed in the previous chapter, the pillars exhibit a square base shape with rounded edges. The additional PVC widens the pillars and lead to a more irregular shape. Based on the evaluation of SEM images, the pillars are approximated as circular pillars with a diameter of 6.5 μm . The resulting slip length predicted by Davis and Lauga (2010) are shown in Table 4.2, varying in the range between 1 μm and 25 μm .

In order to estimate the ζ_S potential at the gas-liquid interface, the system is modeled using an equivalent electric circuit, as shown in Fig. 4.7(a). A similar approach was reported in the context of AC field effect control (van der Wouden et al., 2005, 2006). Here, the capacitance C_{sub} represents the PDMS layer beneath the pillars and the air gaps, which is in series with two parallel branches. Each branch

Table 4.2: Geometric parameters of the superhydrophobic surface. The production of the surfaces is described in section 3.3. The solid interface fraction ϕ_{PVC} is computed for the PVC-coated hierarchical pillars. Based on SEM images, the resulting structures are approximated as circular pillars with a diameter $d = 6.5 \mu\text{m}$. The effective slip length follows from Davis and Lauga (2010) based on ϕ_{PVC} . The induced potential ζ_S is based on the equivalent electric circuit for a gate potential $V_{\text{gate}} = 500 \text{ V}$.

pillar pitch p (μm)	pillar height h_p (μm)	sublayer height h_{sub} (μm)	solid fraction without PVC ϕ (-)	solid fraction with PVC ϕ_{PVC} (-)	effective slip length β (μm)	induced potential for $V_{\text{gate}} = 500 \text{ V}$ ζ_S (mV)
10	10	130	0.2500	0.3318	1.6	0.2249
15	15	120	0.1111	0.1475	6.7	0.2701
20	15	120	0.0625	0.0830	14.7	0.2892
25	15	120	0.0400	0.0531	25.5	0.2990

represents the pillars, including their EDL, and the air gap including their EDL. Implicitly, it is assumed that the domains do not interact directly, such that no electric field lines cross the pillar side walls, and that the electric field is distributed uniformly inside the subdomains. The capacitance of a dielectric layer is modeled as parallel plate capacitors with $C_i = \epsilon_i A_i / h_i$, where A_i is the area of the capacitor, h_i the distance between its plates, and ϵ_i its electric permittivity. Here, air is assumed to exhibit a relative permittivity of $\epsilon_{\text{rel,air}} = 1$, and PDMS a relative permittivity of $\epsilon_{\text{rel,PDMS}} = 2.6$. The capacitance of the EDL can be calculated using the Guoy-Chapman framework with the differential capacitance $C_{\text{dif},i} = (\epsilon_0 \epsilon_{\text{rel},i} / \lambda_D) \cosh(e\zeta / 2k_B T) A_i$ (Butt et al., 2003, p. 50). Thereby, only the diffusive part of the double layer is accounted for, neglecting any Stern layer effects due to adsorption or surface chemistry. While in principle the solid-liquid interface can exhibit a Stern layer, no fixed layer is expected at the gas-liquid layer. Also, the observed velocity will depend mostly on the gas-liquid interface, since the induced ζ potentials will be of the same order of magnitude, but the gas-liquid contribution will be enhanced by a factor of β / λ_D . Solving the resulting implicit equation yields the induced potential ζ_S . Only the induced potential ζ_S is considered, since the contribution due to the native ζ potential averages out over one oscillation of the driving signal. The resulting potential ζ_S for a gate voltage $V_{\text{gate}} = 500 \text{ V}$ is shown in Table 4.2, and is on the order of $0.2 \text{ mV} - 0.3 \text{ mV}$. The potential ζ_S of the other gate potentials scales proportionally to the gate voltage.

The wall mobility above the electrode is assumed to be of the form described by Squires (2008), leading to

$$\mu^L = \hat{\zeta}_{\text{NS}} + \hat{\zeta}_S \frac{\beta}{\lambda}, \quad (4.37)$$

where it is important to remember that the hatted quantities are non-dimensionalized. The pressure mobility outside the electrode region (eq. 4.18) follows as

$$\langle \mu_p^{\text{out}} \rangle = \frac{1 + 4\hat{\beta}}{1 + \hat{\beta}}, \quad (4.38)$$

where the slip length $\hat{\beta} = \beta / h$ follows from equation 4.7. Inserting these equations into the solution of the flow field for a single electrode (eq. 4.35) and inserting the dimensional scales leads to a predicted flow velocity of

$$\langle u_{\parallel} \rangle = -\frac{\epsilon_0 \epsilon_{\text{rel}} E_0}{2\mu} \left(\frac{1 + 4\beta/h}{2 + 5\beta/h} \right) \left(\zeta_{\text{NS}} + \frac{\beta}{\lambda_D} \zeta_S \right) = -\frac{\epsilon_0 \epsilon_{\text{rel}} E_0}{\mu} a_{\text{disc}} \left(\zeta_{\text{NS}} + \frac{\beta}{\lambda_D} \zeta_S \right), \quad (4.39)$$

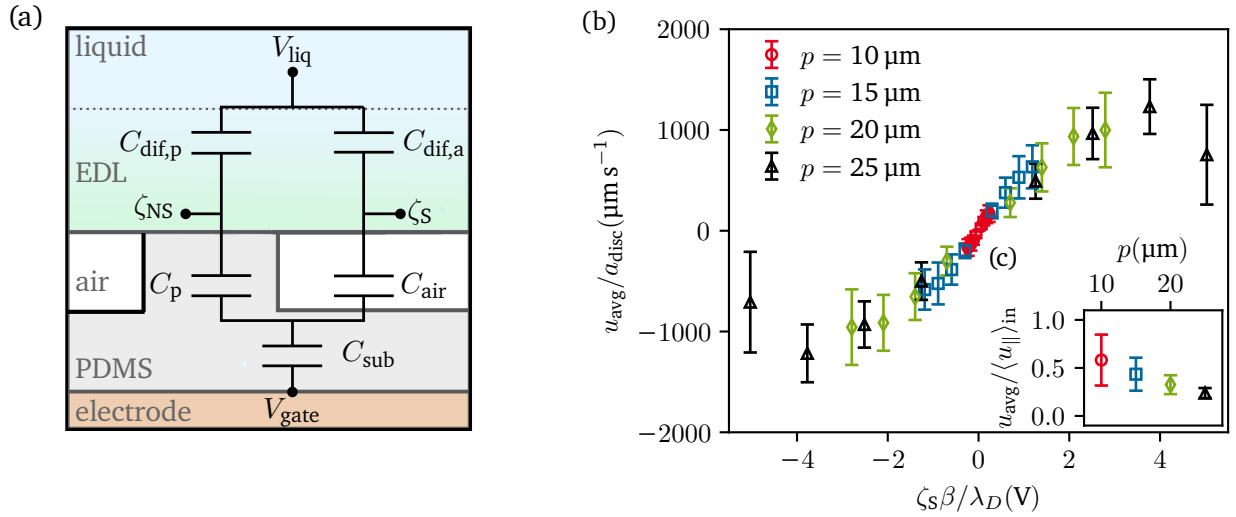


Figure 4.7: Scaling of flow velocity with theoretical predictions. (a) Electric circuit model used to calculate the resulting gas-liquid ζ_S potential. The EDL size is exaggerated for clarity. (b) The experimental results presented in Fig. 4.6 are rescaled according to eq. 4.39. Here, ζ_S is predicted using the equivalent circuit model, and β using eq. 4.7. The data collapses to one dataset, corroborating the theoretical modeling. Interestingly, induced ζ_S below mV (compare to Table 4.2) lead to an effective ζ potential $\zeta_S^{ind} \beta / \lambda_D$ of several V. (c, inset to b) The ratio of the experimentally observed velocity to the theoretically predicted velocity for different pillar pitches at a gate voltage of $V_{gate} = 750$ V. The experimentally measured velocities are about 50 % smaller than predicted. The error bars represent the 95 %-confidence interval based on at least 6 independent measurements. Subfigure (a): Adapted figure with permission from Sebastian Dehe, Baruch Rofman, Moran Bercovici, and Steffen Hardt, Phys. Rev. Fluids, 5(5), 053701, 2020. Copyright (2020) by the American Physical Society.

where the factor a_{disc} can be seen as a geometric factor of the specific flow field. If a different flow field induced by a disc-shaped electrode would be used, a different factor would emerge. In Fig. 4.7(b), the experimental velocity data is rescaled according to eq. 4.39, as a function of $\zeta_S \beta / \lambda_D$, with a vanishing contribution due to the solid-liquid interface ($\zeta_S \beta / \lambda_D \gg \zeta_{NS}$). Here, the velocity $\langle u_{||} \rangle / a_{disc}$ corresponds to the velocity which would be observed above a wall without pressure gradients. The data obtained for different pillar spacings and induced potentials collapse to a single curve, which indicates that the theoretical model captures the scaling of the flow velocity. The factor $\zeta_S \beta / \lambda_D$ can be interpreted as an effective ζ potential, and it is interesting that the small induced surface potentials (below 1 mV as shown in Table 4.2) lead to effective ζ potentials on the scale of several V.

In Fig. 4.7(c), the ratio of the measured velocity u_{avg} compared to the theoretically predicted dipole velocity $\langle u_{||} \rangle_{in}$ is presented for a gate voltage of 750 V. The measured velocities are smaller than the theoretically predicted velocities for all pillar pitches p , on the order of 50%. With increasing pillar pitch, the deviation becomes stronger. Possible explanations for the deviations include the curvature of the interface, surface conductivity effects as well as surfactants accumulating at the gas-liquid interface. The latter has been attributed to significant slip length reductions for pressure-driven flow over superhydrophobic surfaces, even if only trace amounts are present (Joly et al., 2014; Peaudcerf et al., 2017; Schäffel et al., 2016). In section 4.5.2, a more detailed discussion of surfactant effects can be found. Overall, however, the scaling of the experiments and theory agree well, especially considering the simplifications introduced for modeling the slip length as well as the induced potential ζ_S .

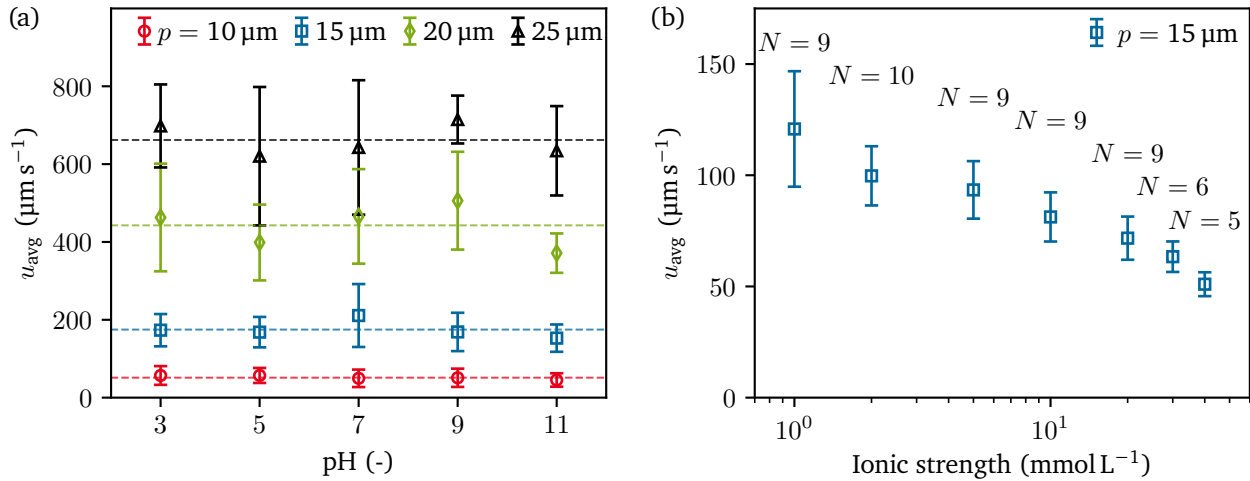


Figure 4.8: Dependency of the experimentally obtained velocity on the electrolyte properties. (a) Velocity as a function of pH for varying pillar pitch at an ionic strength of 10 mM and $V_{gate} = 500 \text{ V}$. The averages over all pH are represented by the dashed lines. Error bars represent the 90%-confidence interval based on 5 independent measurements. (b) Velocity as a function of ionic strength for a pillar pitch $p = 15 \mu\text{m}$, $\text{pH} = 7$, and $V_{gate} = 250 \text{ V}$. N denotes the number of independent measurements taken. Adapted figure with permission from Sebastian Dehe, Baruch Rofman, Moran Bercovici, and Steffen Hardt, Phys. Rev. Fluids, 5(5), 053701, 2020. Copyright (2020) by the American Physical Society.

4.4.4 Influence of the electrolyte

In Fig. 4.8(a), the flow velocity is shown versus the solution pH, with the different buffer compositions described in Table 4.1. The resulting flow velocity is independent of pH for the range between 3 and 11. This behavior contrasts the observations over no-slip surfaces, where a pH close to the isoelectric point of a surface eliminates surface charges and thus the EOF. Also, it contrasts the behavior observed for charge induction over flat surfaces: Here, the charge induction is counteracted by the surface chemistry, with increasing resistance the further the solution pH differs from the isoelectric point (Kirby and Hasselbrink, 2004a,b; van der Wouden et al., 2006).

In Fig. 4.8(b), the flow velocity is shown for varying ionic strength at a fixed pH of 7. The ionic strength is adjusted between $I = 1 \text{ mM}$ and 40 mM , as discussed in section 4.4.1. With increasing ionic strength, the flow velocity decreases. According to the electric circuit model presented in the previous section (Fig. 4.7(a)), no dependency on the ionic strength would be expected. A higher ionic strength increases both the double layer thickness as well as the surface potential ζ_S due to the change of the double layer capacitance C_{dif} . One potential explanation relates to the surfactant adsorption at the gas-liquid interface. Even at trace amounts the effective slip length can be decreased substantially. Since the adsorption of some surfactants increases with salt concentration (Tajima, 1971), an increase of ionic strength could lead to an increase of surfactants. However, this hypothesis has not been validated so far and requires exploration in future work.

4.5 Discussion

4.5.1 Comparison to no-slip surfaces

In order to compare the flow enhancement over superhydrophobic surfaces compared to no-slip surfaces, the flow velocity over flat surfaces in an equivalent dipole system can be used. Two test-cases exist: First, the flow velocity over flat surfaces with gate electrodes as reported in Paratore et al. (2019a) can be compared to the experimental velocities over superhydrophobic surfaces. Second, the velocity obtainable in a dipole flow field driven by native ζ potentials can be computed from literature data (Kirby and Hasselbrink, 2004a,b). For flat surfaces, the geometry dependent factor from eq. 4.39 results in $a_{\text{disc}} = 1/4$, thus allowing to calculate the equivalent height-averaged velocity over flat surfaces as

$$u_{\text{comp}} = \frac{1}{4} \mu_{\text{EOF}} E_0 = -\frac{1}{4} \frac{\epsilon}{\mu} \zeta_{\text{NS}} E_0. \quad (4.40)$$

Here, the viscosity of the electrolyte is taken as the viscosity of a mixture of H₂O and D₂O at a laboratory temperature of 15 °C, resulting in $\mu = 1.288$ mPa s. Using the experimental results from Paratore et al. (2019a), a maximum depth-averaged flow velocity of $u_{\text{comp}} = 25 \mu\text{m s}^{-1}$ would be observed for the electric field strength of 50 V cm^{-1} . Thus, EOF over superhydrophobic surfaces shows an enhancement of one order of magnitude compared to EOF over flat surfaces induced by gate electrodes.

Using the native ζ potentials for flat surfaces reported in Kirby and Hasselbrink (2004a,b), a high ζ potential of 100 mV is used to estimate the maximum achievable velocity using native ζ potentials. Inserting the native ζ potential into eq. 4.40 leads to a velocity of $u_{\text{comp}} = 69 \mu\text{m s}^{-1}$. Again, EOF over superhydrophobic surfaces shows an order of magnitude enhancement. Interestingly, this enhancement is independent of the pH value, as was discussed in the previous section. Therefore, EOF over superhydrophobic surfaces offers an alternative method of driving flows at a higher velocity magnitude in biological buffer systems.

4.5.2 Influence of surfactants

Surfactant accumulation at gas-liquid interfaces can significantly reduce the effective slip length, if the velocity along the interface leads to gradients in the surfactant concentrations. As was shown by Peaudecerf et al. (2017), even trace amounts can lead to Marangoni stresses, which transition the surface from a stress-free interface to a no-slip interface. This mechanism requires the accumulation of surfactants due to advective transport with the flow. It is unclear, however, how strongly surfactants influence the dipole flow field, since a backflow is present at all times, and in principle should counteract the accumulation.

In order to estimate whether surfactants can play a role in the test case presented here, a series of experiments with variations of the ionic strength similar to section 4.4.4 was conducted on a superhydrophobic surface with $p = 15 \mu\text{m}$. In one set of experiments, an anionic surfactant (sodium dodecyl sulfate, SDS) at a concentration of 0.2 mmol L^{-1} was added to the electrolyte, corresponding to 2.5 % of the critical micelle concentration (CMC). In Fig. 4.9(a), the averaged velocities measured are shown. It is important to stress that the experiments were performed only once per condition, and therefore no error bars are shown. It is visible that the velocities are reduced in the presence of SDS, compared to the electrolyte without additional surfactants. Surfactants can have at least a two-fold influence on the resulting flow velocity. First, they can reduce the effective slip lengths by Marangoni stress and thus suppress the enhancing effect of superhydrophobic surfaces. Secondly, they reduce the surface tension, leading to

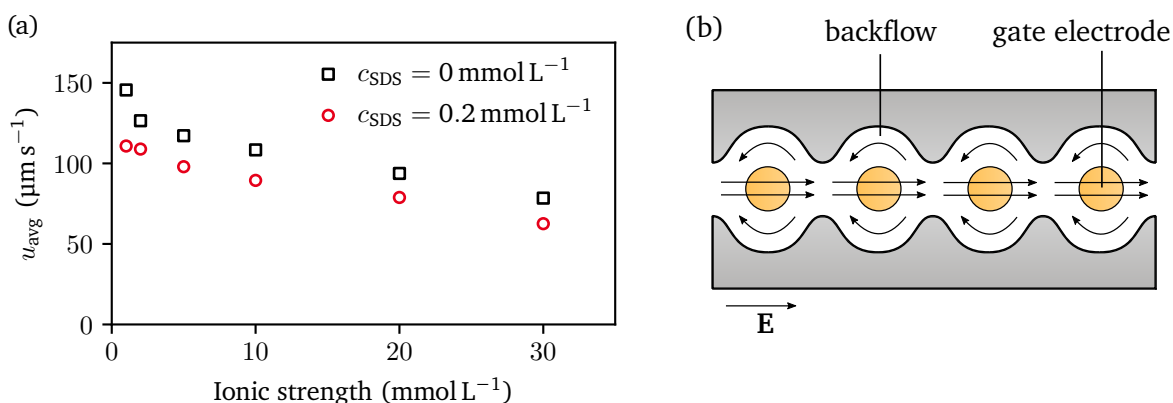


Figure 4.9: Surfactant effects on the EOF over superhydrophobic surfaces. (a) Experimentally obtained velocities for a channel with $p = 15 \mu\text{m}$, $\text{pH} = 7$, and $V_{\text{gate}} = 250 \text{ V}$. In order to analyze the influence of surfactants, the anionic surfactant SDS was added with a concentration of 0.2 mM , corresponding to 2.5% of the critical micelle concentration. (b) Top-view schematic of a pumping mechanism allowing for backflow, leading to a net transport from the left to the right. By allowing for controlled backflow, the build-up of a strong surfactant gradient immobilizing the interface could potentially be prevented, at the cost of diminished pumping rate.

wetting state transition as well as increased curvature of the interface. It is not clear which effect is responsible for the velocity reduction, warranting additional research effort in future work. However, it is also visible that even at non-negligible surfactant concentration, significant flow velocities are achieved.

This simple experiment emphasizes the importance of the channel design if EOF is driven over superhydrophobic surfaces. In order to enable EOF over superhydrophobic surfaces in technical applications, it is imperative to allow for backflow, so that surfactant accumulation is prevented. The flow field above a circular electrode shows constant backflow, and thus, surfactants can flow back as well, instead of immobilizing the gas-liquid interface. In Fig. 4.9(b), a potential system of electrodes is illustrated, allowing to drive EOF by placing several circular electrodes in series, and allowing for local backflow. By incorporating backflow into the design, it might be possible to leverage EOF over superhydrophobic surfaces even at moderate surfactant concentrations, as often present in biological systems. However, one has to keep in mind that backflow correlates to reduced pumping pressure head, and efficiency reduction. Thus, it remains to be explored how this alternative pumping performs compared to classical EOF pumps.

4.5.3 Demonstration of flow shaping by multiple electrodes

The main part of this chapter focuses on EOF over a single gate electrode, in order to characterize the achievable flow enhancement. Here, a demonstration of different flow patterns will be presented using additional gate electrodes that can be controlled independently. Especially the independence of pH makes EOF over superhydrophobic surfaces a promising technique for flow shaping applications in systems with varying pH, such as biological systems. In section 5.5.1, an additional demonstration of a mixer based on the blinking vortex principle will be presented.

In order to generate a vortex flow field, a system of two gate electrodes ($1000 \mu\text{m} \times 500 \mu\text{m}$ each, with an intermittent spacing of $100 \mu\text{m}$) was created in a similar channel configuration as the single circular electrode. The gate voltages on the electrodes had a similar driving frequency and magnitude (150 V , 5 Hz , rectangular signal), but with opposite signs. Thus, the resulting EOF is directed in opposite directions above each electrode, and an in-plane vortex was created. In Fig. 4.10(a), a streakline image

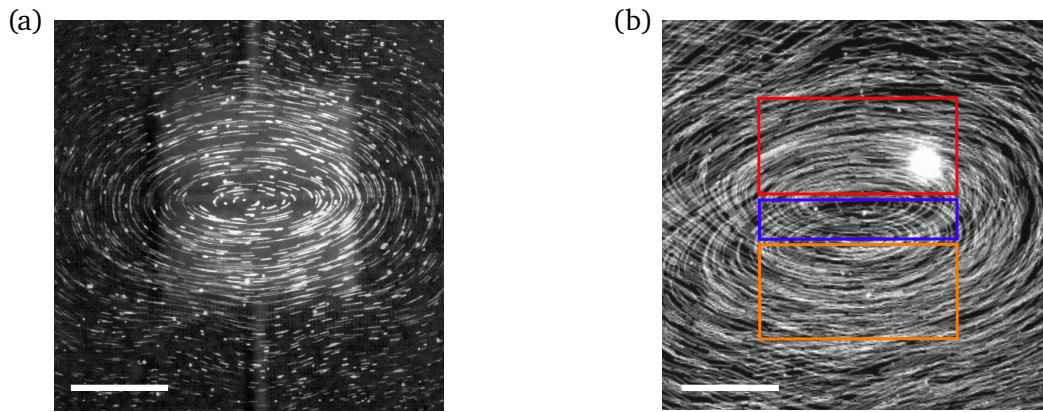


Figure 4.10: Demonstration of flow shaping using multiple gate electrodes. (a) Streakline image of a vortex flow created by two electrodes of size $1000 \mu\text{m} \times 500 \mu\text{m}$ each, with an intermittent spacing of $100 \mu\text{m}$. The streaklines were recorded above a microstructure with $p = 20 \mu\text{m}$ and a driving field of 50 V cm^{-1} using an exposure time of 1 s. The scale bar represents $500 \mu\text{m}$. (b) Demonstration of the blinking vortex principle. A superposition of two streakline images above three gate electrodes (marked in red, blue and orange) is shown. The upper and lower gate electrode (red and orange) exhibit a gate potential amplitudes of 150 V and -150 V , respectively. The gate voltage amplitude of the centered electrode changed its sign, so that the position of the resulting vortex shifted positions. The blinking frequency between the flow fields was set to 0.1 Hz . The scale bar represents $500 \mu\text{m}$.

recorded over the duration of 1 s above a microstructure with $p = 20 \mu\text{m}$ is shown. Clearly, the resulting flow field is circulatory, with the vortex center located between the electrodes. The electrodes are shown as an grayscale overlay.

In order to utilize a vortex flow for mixing, the well-known blinking vortex principle can be used (Aref, 1984). Therefore, two co-rotating vortices with a center offset are applied interchangeably, such that only one vortex is present at a time. For optimized parameters of the blinking frequency (the frequency at which the vortices change), a chaotic mixing region is created. In order to use this principle in Hele-Shaw cells, temporal control over the flow fields is required. In Fig. 4.10(b), two superposed streakline images are shown in a system where three electrodes were present, shown in different colors. The outer electrodes (red and blue) were driven by gate voltage amplitudes with opposing sign, and the center electrode was either driven with positive or negative sign of the gate voltage amplitude. Thereby, the center of the created vortex flow shifted in the vertical direction. The image was created by superposition of two streakline images of both vortex flows, which were blinking at a frequency of 0.1 Hz . This configuration illustrates that the flow field can be controlled spatially and over time. In Paratore et al. (2019a), other flow fields obtainable using gate electrodes were presented over flat surfaces, with more complex flow patterns. In principle, these flow fields can be created over superhydrophobic surfaces as well, with higher flow velocities.

4.5.4 Relation to electrowetting stability

The electro-osmotic velocity over superhydrophobic surfaces is limited by the electrowetting stability of the Cassie-Baxter wetting state. Especially for the high pillar pitches, the flow velocity deviates at higher gate voltages from the linear scaling with induced ζ_s . In chapter 3, the stability of the wetting state was characterized for the surfaces utilized in this section. In the following, the results of both chapters are related.

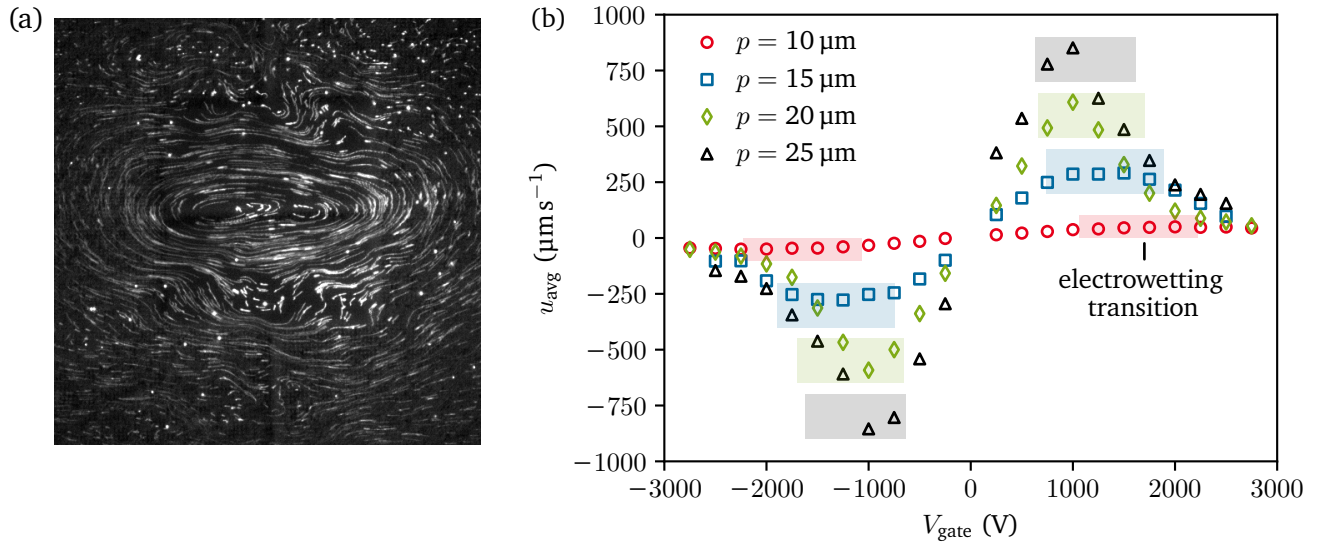


Figure 4.11: Influence of the electrowetting stability of the Cassie-Baxter state on the flow field. (a) Experimentally observed streaklines of the flow field presented in Fig. 4.10(a) after locally inducing wetting state transitions with an increased gate voltage. Due to local transitions, the streaklines are curved, leading to low-velocity regions embedded within high velocity regions. (b) Experimentally observed flow velocities for 4 specific measurements with varying pillar pitch at $\text{pH} = 7$. With increasing gate voltage magnitude, the resulting velocity deviates from the initial linear scaling with gate voltage, with diminishing velocities for increasing gate potentials. The colored boxes denote the wetting state stabilities determined experimentally in section 3.4. The edge with the lower magnitude of V_{gate} corresponds to the RST and the edge with the higher magnitude to the NCTP. The maximum velocity is observed in between these lower and upper limits, respectively.

Electrowetting transitions occur locally, and the liquid cannot slip over the interface. Local wetting state transitions lead to changes of the (local) slip length, and thus lead to curved streamlines. From the governing equations of the stream function (eq. 4.22), it is known that pressure gradients perpendicular to slip length gradients and electric fields perpendicular to electro-osmotic mobility gradients lead to vorticity, manifesting in curved streamlines. In Fig. 4.11(a), the vortex flow from Fig. 4.10(a) is shown, after local wetting state transitions were induced by high gate voltages. It is clearly visible that some regions with low velocity were present, which led to curved streaklines. Similarly, it is also visible that in the regions outside the transitioned regions significant flow was still present.

In order to characterize the influence of the electrowetting transition on the flow field, experiments with 4 channels of varying pillar pitch were performed at $\text{pH} = 7$, for higher gate voltage potentials than reported so far. It is important to keep in mind that the gate voltages were successively increased, starting with the lowest amplitude. In Fig. 4.11(b), the resulting flow velocities are depicted. It is visible that the initially observed linear dependency on the gate voltage flattens, and at some point an increase of the gate voltage led to smaller flow velocities. In order to relate the velocities to the electrowetting potentials observed in chapter 3, the regions of expected transition are depicted by the respective colored boxes. The edge corresponding to the lower absolute gate voltage corresponds to the RST from section 3.4, and the edge corresponding to the higher absolute gate voltage corresponds to the NCTP. The maximum of the observed velocity is located in between both limits, emphasizing the importance of the wetting state stability for the ability to induce flow. Also, well above the NCTP flow can be induced. This is due to the fact that the surface remains partially in the Cassie-Baxter wetting state, thus leading to some local flow. However, since the forcing is non-uniform over the surface, the streamlines become curved. Thus,

it depends on the specific application whether the flow can still be utilized.

4.6 Summary and Outlook

In this chapter, electro-osmotic flow over superhydrophobic surfaces was studied, with modifications of the surface charge using gate electrodes. A combination of a height-averaged theory based on the leading-order solution of electro-osmotic Hele-Shaw flows in conjunction with a height-averaged PTV measurement method was utilized to evaluate the resulting EOF. In order to average any flow due to the native ζ potential at the wall, a synchronized AC actuation of the driving field as well as the gate electrode voltage was utilized. In a single-electrode configuration, the dependence of the flow on the gate voltage and surface microstructure was characterized, exhibiting a linear dependency of the resulting flow on the gate voltage and effective slip length. By rescaling the data using an equivalent circuit model and slip-length predictions, a collapse of the data onto a single curve was shown, confirming the theoretical modeling. The induced flow is independent of the electrolyte pH value, and shows a decrease with increasing ionic strength. Interestingly, the resulting EOF over superhydrophobic surfaces shows an order of magnitude enhancement compared to no-slip surfaces, without the inherent dependency on the surface chemistry.

Electro-osmotic flow over superhydrophobic surfaces offers an alternative working point compared to classical EOF, with higher achievable velocities, but lower pressures due to the wetting state stability. Especially the independency of pH offers potential exploitation in a range of applications, including biological and chemical applications. In order to demonstrate the ability to utilize EOF over superhydrophobic surfaces in flow shaping applications, a demonstration of vortex flow created by multiple electrodes was shown in section 4.5.3. Also, the ability to drive EOF in the presence of surfactants due to the possibility of backflow was demonstrated, addressing a common pitfall in technical utilization of flow over superhydrophobic surfaces. Overall, driving electro-osmotic flow over superhydrophobic surfaces offers potential in a wide range of applications with benefits compared to classical EOF.

While this chapter lays the foundation of EOF over superhydrophobic surfaces, some questions have to be addressed in future work. First, the dependency on the ionic strength of the electrolyte remains to be explored. This open question is of importance for the utilization in biological buffer applications, where ionic strength exceed the ones explored in this chapter. Secondly, the role of surfactants could warrant additional modeling effort. For example, it might be beneficial to model the surfactant influence by solving an additional surfactant concentration equation, with coupling to the flow equations. Then, the effects of surfactant flow in geometries with backflow could be investigated further. Third, the microstructures used in this thesis could be varied. Especially by using alternative manufacturing techniques, e.g. 3D printing, alternative re-entrant structures could be produced, with higher wetting state stability and thus higher velocities. And lastly, it might be of interest to investigate the influence of the curvature of the interface on the EOF. Here, flat interfaces were assumed, which is an idealization of the real situation. The surface-normal electric field will lead to an interface curvature, which could be systematically investigated, as it might influence the EOF over superhydrophobic surfaces.

5 Dispersion in electrokinetic Hele-Shaw flows

In the previous chapter, the ability to induce height-averaged flow fields using electro-osmotic flow in a Hele-Shaw cell was discussed. In this chapter, the sample transport and dispersion within a Hele-Shaw cell geometry is investigated. Using a perturbation method, a reduced-order model is derived, where the sample dispersion due to velocity variations over the cell height is captured using a 2D model. The resulting reduced-order model is compared to full 3D simulations using Lagrangian particle simulations in three representative test cases. Also, the feasibility of mixing in a Hele-Shaw geometry is demonstrated experimentally. In addition, a possible strategy is outlined to create a desired dispersion field using oscillatory electro-osmotic flow.

The work presented in this chapter was funded by the *German-Israeli Foundation for Scientific Research and Development* (Grant No. I-1346-401.10/2016). An initial version of the dispersion model was derived by Imke-Sophie Lorenz as part of her Master's thesis using scaling arguments, accounting for steady-state flow fields (Lorenz, 2018). The model presented in this thesis is based on an alternative derivation using a multiple-scale perturbation method, extending the applicability to both stationary and oscillatory flow fields. The multiple-scale perturbation, the numerical computations, as well as the description of the inverted problem were distinct contributions of the author of the present thesis. For the experimental demonstration in section 5.5.1, the soft-lithography master structure was produced by Dr. Khaled Gommed and Baruch Rofman at the cleanroom facilities of the Micro-Nano-Fabrication & Printing Unit at Technion, Haifa. The gate electrodes were produced by Klaus-Dieter Voss at the clean-room facilities of the IMNS at TU Darmstadt. The production of the channels, conducting the experiments as well as the data evaluation were performed by the author of the present study. In his function as supervisor, Steffen Hardt provided valuable input during the whole process of this project, and helpful discussions with Baruch Rofman and Moran Bercovici are acknowledged. The main body of the work is published in Dehe et al. (2021b).

5.1 Introduction

The transport of a soluble species with a background flow is influenced by the velocity variations in the cross-stream direction. In his original works, Taylor discussed the dispersion of an initially confined distribution of a soluble species in a pressure-driven flow field through a circular tube (Taylor, 1953, 1954). The velocity profile exhibits non-uniformities over the radial coordinate, with a maximum located at the channel center. Over time, the initially confined distribution widens under the influence of both the molecular diffusion, as well as the velocity variation. The center of the distribution of the injected species travels with the mean velocity of the flow field, and the resulting distribution is symmetric around the center point. Taylor showed both analytically as well as experimentally that the spreading is governed by a 1D diffusion equation with an effective diffusion coefficient, which depends on the flow velocity U_0 , the cross-stream characteristic length scale a , as well as the molecular diffusion coefficient D as $\propto U_0^2 a^2 / D^2$. Subsequently, Aris extended Taylors analysis using the method of moments, showing that the resulting growth rate of the distribution is a sum of the molecular diffusion coefficient as well as the

effective diffusion coefficient derived by Taylor (Aris, 1956). Today, this effect is referred to as *Taylor-Aris dispersion*.

Dispersion due to velocity variations occurs in flow-shaping applications in Hele-Shaw cells as well. As discussed in chapter 4, height-averaged flow fields can be created by variations in electro-osmotic wall mobilities. However, as is known from the context of electro-osmosis in capillaries, inhomogeneous wall mobilities lead to internal pressure gradients, and thus height-induced variations and sample dispersion (Herr et al., 2000). Since the internal pressure gradients are essential for creating flow fields in Hele-Shaw cells, dispersion of soluble species is expected. Theoretical and experimental studies on this subject have focused on the ability to influence and control the resulting flow field (Bacheva et al., 2020; Boyko et al., 2015, 2021; Dehe et al., 2020; Paratore et al., 2019a,b). However, in order to utilize the principle for basic microfluidic functions such as mixing, an appropriate modeling of species transport is required as well. Effects which have to be considered to appropriately model sample dispersion include the electro-osmotic wall mobilities, slippage effects, as well as oscillatory motion of the fluid flow. In the following, it is assumed that the electro-osmotic mobility can exhibit a spatial and temporal distribution, whereas the effective slip at the wall exhibits solely a spatial variation. In order to complement the existing framework of flow shaping using 2D flow solutions, the species transport model describes the transport in the height-averaged velocity field, incorporating the effects over the channel height into an effective dispersion tensor field. As a result, the 3D scenario is captured by a 2D model, thus enabling further development of flow shaping applications in chemistry or bio-medical engineering.

In the previous chapter, the resulting flow field due to pressure-gradients and electro-osmotic flow inside a Hele-Shaw cell was discussed. In this chapter, the transport of a dissolved species in such a non-uniform flow field is studied, with a focus on sample dispersion due to velocity variations over the cell height. Specifically, the following questions are addressed: How can the sample transport be described in an effective macrotransport equation? Is the resulting macrotransport equation thermodynamically consistent? How well does the reduced-order model describe the flow transport? And can the resulting macrotransport equation be used to calculate the required electro-osmotic wall mobilities to create a required dispersion field? Therefore, the remainder of the chapter is organized as follows: In section 5.2, the basic mechanism of shear-induced sample dispersion is introduced, jointly with a literature overview. In section 5.3, the governing transport equation is derived, using a multiple-scale perturbation approach, and the thermodynamic consistency is discussed. In section 5.4, the reduced-order model is compared with 3D particle tracing simulations to assess the validity of the model. In section 5.5, an experimental demonstration of a micromixer in a Hele-Shaw geometry is provided (section 5.5.1), followed by a discussion addressing the inverted problem of dispersion shaping (section 5.5.2). A summary of the results is given in section 5.6.

5.2 Shear-induced sample dispersion

5.2.1 Dispersion in stationary pressure-driven flow through a capillary: Taylor-Aris dispersion

In this section, the mechanism of Taylor-Aris dispersion is outlined, using the classical solution obtained by Taylor, and the concept of an effective dispersion coefficient is summarized (Taylor, 1953). Therefore, the dispersion of a soluble species with an initially confined distribution is considered inside a pressure-driven flow through a circular capillary of radius a . In Fig. 5.1(a), a schematic of the respective flow field and initial distribution is shown.

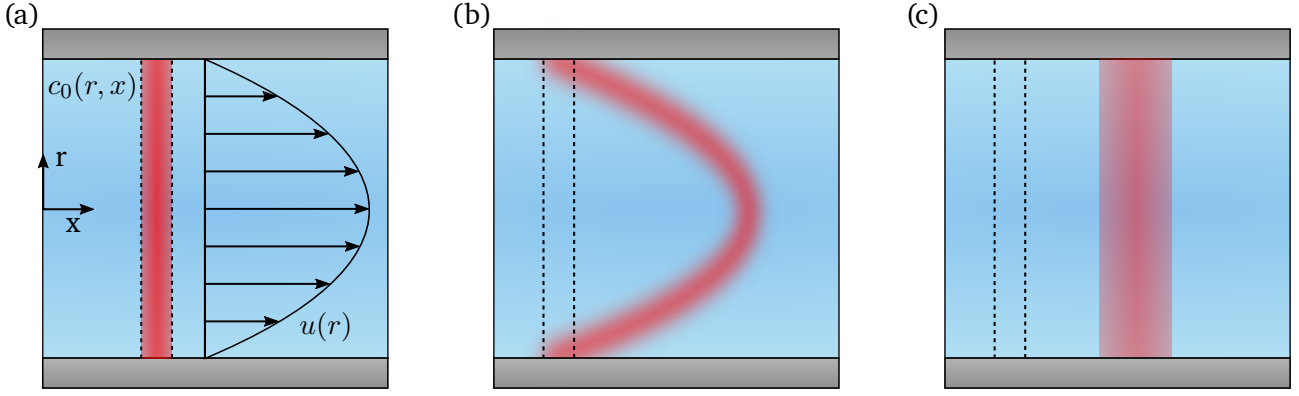


Figure 5.1: Taylor-Aris dispersion in a circular capillary. (a) An initially confined soluble species with concentration c_0 is released in a pressure-driven flow with velocity variations in the radial direction. (b) Without diffusion, only advection would lead to a variation of the concentration field, leading to a broad distribution in x -direction. (c) Molecular diffusion leads to a re-distribution in the radial direction, resulting in a height-averaged concentration distribution.

The transport process in such a capillary is governed by diffusion as well as advection, and occurs on different time scales. The radial diffusion is governed by a time scale on the order of $T_{\text{dif},a} = a^2/D$, where D represents the molecular diffusion constant. Similarly, axial diffusion occurs over time scales of $T_{\text{dif},L} = L_0^2/D$, where L_0 represents a typical axial length scale. Advection with the main flow along L_0 is governed by the time scale $T_{\text{adv}} = L_0/U_0$, where U_0 represents the mean flow velocity. In the following, it is assumed that radial diffusion is fast compared to axial advection and axial diffusion. Also, the axial diffusion is assumed to be slow compared to axial advection.

The flow velocity in a laminar flow results in a parabolic profile of the form

$$u = 2 \left(1 - \frac{r^2}{a^2} \right) U_0, \quad (5.1)$$

where U_0 represents the mean flow velocity over the capillary cross-section. The governing equation of the species transport is an advection-diffusion equation (eq. 2.69, without electrophoretic motion), and results for the given problem in radial coordinates in

$$\frac{\partial c}{\partial t} + u \frac{\partial c}{\partial x} = D \left(\frac{\partial^2 c}{\partial r^2} + \frac{1}{r} \frac{\partial c}{\partial r} + \frac{\partial^2 c}{\partial x^2} \right), \quad (5.2)$$

where the coefficient of molecular diffusion is assumed to be constant.

Since the transport in axial direction is governed by advection with the background flow, a coordinate transformation can be performed, such that the coordinate system moves with the mean velocity U_0 of the flow. Then, the axial coordinate as well as the velocity profile read

$$x_1 = x - U_0 t \quad \text{and} \quad u_1 = \left(1 - 2 \frac{r^2}{a^2} \right) U_0. \quad (5.3)$$

Now, the concentration profile is assumed to be stationary in the moving reference frame, and the axial gradient $\partial c / \partial x_1$ to be independent of r . Then, the transport problem results in

$$\left(1 - 2 \frac{r^2}{a^2} \right) U_0 \frac{\partial c}{\partial x_1} = D \left(\frac{\partial^2 c}{\partial r^2} + \frac{1}{r} \frac{\partial c}{\partial r} \right). \quad (5.4)$$

Equation 5.4 is subject to the boundary conditions of impermeable walls ($\partial c/\partial r = 0$ at $r = a$). A solution can be found as

$$c = c_0(x_1) + A \left(\frac{r^2}{a^2} - \frac{1}{2} \frac{r^4}{a^4} \right), \quad (5.5)$$

where $c_0(x_1)$ is the value of c at $r = 0$. By substitution into eq. 5.4, the coefficient A can be determined as

$$A = \frac{a^2 U_0^2}{4D} \frac{\partial c}{\partial x_1}. \quad (5.6)$$

In order to show the similarity to the diffusion process, the transport of mass over a plane located at x_1 can be computed as

$$J(x_1) = \frac{1}{\pi a^2} \int_0^a 2\pi r c(r, x_1) u_1(r) dr = -\frac{a^2 U_0^2}{48D} \frac{\partial c}{\partial x_1} = -D_{\text{eff}} \frac{\partial c}{\partial x_1}. \quad (5.7)$$

Equation 5.7 takes the same form as Fick's law, which describes molecular diffusion (see section 2.4), with an effective diffusion coefficient D_{eff} . It can be written as a dependency of the Péclet number $Pe = aU_0/D$, which denotes the relative importance of advective transport to diffusive transport, and results in the well-known quadratic dependency $D_{\text{eff}} = \frac{Pe^2}{48} D$. The numerical factor $1/48$ is a result of the flow field, and other numerical values are obtained in different channels geometries and flow fields.

According to eq. 5.7, the spreading of an initial distribution of solute can be described by an modified diffusion law, where the effective diffusion coefficient is determined by the flow, geometry and molecular diffusion coefficient. Also, the effects due to radial variations are incorporated into an one-dimensional representation of the system, leading to a reduced order model. While the above derivation by Taylor is strictly speaking only valid in the limit of dominant dispersion compared to diffusion, an alternative derivation by Aris (1956) using the method of moments demonstrated that the effects of dispersion and molecular diffusion can be described by

$$D_{\text{eff}} = \left(1 + \frac{Pe^2}{48} \right) D, \quad Pe \gg 1. \quad (5.8)$$

Dispersion enhances the effective diffusion coefficient compared to molecular diffusion.

While this classical framework of Taylor-Aris dispersion is known for over 60 years, it highlights some of the key-characteristics that will apply to the transport model derived in the following. First, it relies on the assumption that radial diffusion occurs over small time scales compared to other processes in the system. Thereby, the 2D transport process can be described by a 1D model. Second, it describes the dispersion in the limit of long times, as the diffusion process is required to equilibriate over the channel cross-section. Inversely, this restriction can be viewed as a limit on the change of the flow field. The characteristic length scale ΔL , over which the velocity profile changes, and the characteristic velocity scale U_0 define an advective time scale associated to the lateral change of the velocity profile. In order for Taylor-Aris dispersion to be applicable, the radial diffusive time scale has to be much smaller, thus resulting in the condition

$$\Delta L \gg \frac{aU_0}{D} a = Pe a. \quad (5.9)$$

If this condition is violated, a Taylor-Aris type of analysis is not applicable.

The early works on dispersion in capillary flow include Ananthakrishnan et al. (1965), where the authors present the regions of validity of the Taylor-Aris dispersion in a Péclet number - time space. Since then, various efforts have been focused on extending Taylor-Aris solution to short times (Barton, 1983; Gill et al., 1968, 1971), pulsating flow (Aris, 1960; Gill et al., 1968), and to generalize the dispersion theory

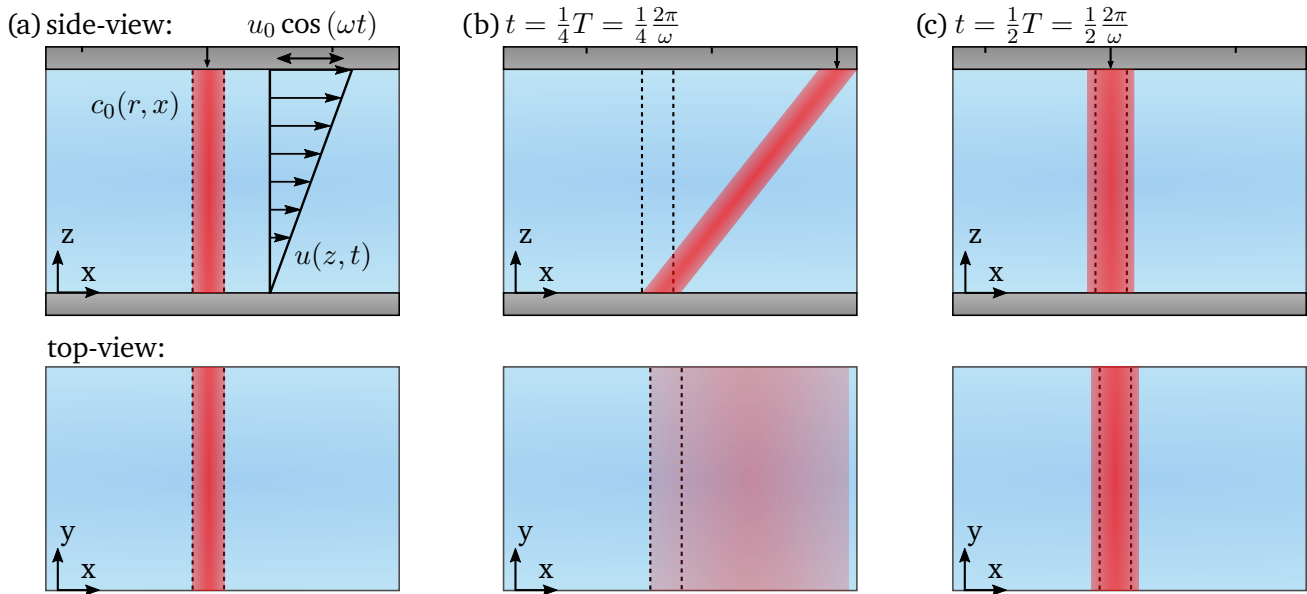


Figure 5.2: Shear-enhanced dispersion in an oscillatory flow field in a slit channel infinitely extending in y -direction. (a) An initially confined distribution of a soluble species is released in a shear-flow with a circular frequency ω . (b) If the oscillation frequency is much faster than the radial diffusion process, the soluble species is spread after one quarter of the oscillation period. In a height-averaged framework (top-view), the concentration field widens strongly. (c) After one half of the oscillation period, the concentration field returns to its initial concentration, with a slightly wider distribution width. In a height-averaged framework, the solution concentration contracts during the second quarter of the oscillation, corresponding to a negative dispersion coefficient.

to several transport processes in homogeneous and heterogeneous media (Brenner and Edwards, 1993). In the following, some of the research efforts related to this work will be summarized, focusing on the phenomenological description rather than the detailed mathematical treatment of each case.

5.2.2 Dispersion in oscillatory flow fields

Dispersion in oscillatory flow fields has attracted attention of the research community following the seminal work of Taylor and Aris. Oscillatory flow occurs naturally in geological flows such as coastal flow, and in technical applications, such as pumping with piston-type pumps. Chatwin (1975) focused on the dispersion due to an oscillatory pressure gradient. He showed that the mean distribution of a soluble contaminant satisfies a diffusion equation with an effective diffusion coefficient, that exhibits a harmonic time dependence based on twice the driving frequency. In the limit of slow oscillations compared to radial diffusion, the effective diffusion coefficient can be approximated by the corresponding steady-state dispersion coefficient. With increasing oscillation frequency, the dispersion coefficient decreases, since the cross-stream diffusion is unable to react to the changing flow field. Next, the influence of the channel geometry, frequency and Schmidt number was illuminated by Watson (1983). He provided exact solutions for slit and circular channel geometries, and showed that the effects of a superposed oscillatory and steady flow field are additive. Using the theoretical results by Watson, Joshi et al. (1983) confirmed experimentally the predicted theoretical scaling relations.

If the oscillatory period is smaller than the diffusive time scale in the cross-stream direction, dispersion modeling requires careful assessment of the modeling approach. For example, it is instructive to consider the situation depicted in Fig. 5.2 of an initially confined tracer distribution in an oscillatory shear flow.

During the first quarter of the oscillatory period, the initial distribution spreads, and the height-averaged distribution widens strongly. In a height-averaged framework, this corresponds to a positive dispersion coefficient. Since diffusion is assumed to be slow compared to the oscillation, the concentration will not equilibrate over the channel height, as shown in Fig. 5.2. In the second quarter of the oscillation period, the flow direction reverses, and the concentration tracer distribution returns into a more compressed form, with a slightly larger distribution width. In a height-averaged framework, the cloud of soluble is compressed. In the third and fourth quarter (not shown), the process occurs similarly with a widening of the distribution, followed by a compression. If the process would be modeled by an advection-diffusion equation, the compression of the tracer cloud would correspond to a negative effective diffusion coefficient. However, modeling diffusion with a negative diffusion coefficient leads to the accumulation of concentration and the formation of unphysical singularities. Smith addressed this issue by proposing the use of a delay-diffusion equation, incorporating a memory effect (Smith, 1982). Alternatively, in the limit of long times, the process can be modeled using a time-averaged diffusion coefficient. If the diffusion coefficient is evaluated at a specific instance in time, both expansion or compression of the soluble can be observed, corresponding to a positive or negative effective diffusion coefficient. However, after one period of oscillation, the distribution has returned to its initial state and will be widened slightly. Thus, by time-averaging over one period of oscillation, the unphysical behavior of singularity formation can be avoided. A downside of this approach is that transport effects on short time scales can only be included in the long-time limit. Other research efforts addressing oscillatory flows used adaptations to the method of moments to account for dispersion in a flow field consisting of a stationary and oscillatory component (Mukherjee and Mazumder, 1988). Also, combinations of oscillatory pressure-driven flow as well as wall oscillations in a parallel-plate channel were considered (Bandyopadhyay and Mazumder, 1999).

5.2.3 Dispersion in the context of microfluidics

The rise of microfluidics led to a revitalization of research on dispersion, focusing on flows on small scales. In a T-mixer, the variations of velocities close to the wall lead to varying residence times, as was discussed by (Kamholz et al., 1999). Thus, different shapes of the mixing zone can occur, either shaped as a butterfly, or as a flat profile. Experimental confirmation of the differently shaped zones due to the cross-stream variation was provided by Ismagilov et al. (2000). Stone and Brenner (1999) analyzed the dispersion due to the streamwise flow variations in a radially outflowing liquid between two plates. The cross-sectional shape of the fluidic domain influences the resulting flow field and induces variations in shallow microchannels, as was shown by Ajdari et al. (2006). Aside from the geometry, the walls can influence the dispersion as well if chemical reactions occur at the bounding walls, as was analyzed for oscillatory flow (Ng, 2006). Other research focused on the effects of a finite channel length (Giona et al., 2009) and the role of secondary flows (Adrover, 2013; Jiang et al., 2004; Zhao and Bau, 2007). Also, the role of time-dependent flow fields was discussed by Vedel and Bruus (2012) and Vedel et al. (2014), focusing on the interactions between external driving frequencies as well as internal time scales. As was elucidated, dispersion is enhanced by oscillations with timescales larger than the diffusion time scales of momentum and mass transport.

Next, the more specific situation of superposed pressure-driven flow and electro-osmotic flow was considered. In principle, electro-osmosis leads to a flat velocity profile, with shear confined to a small region close to the wall. However, if the wall mobilities exhibit non-uniformities, internal pressure gradients are induced by the EOF, leading to non-uniform flow profiles. In Fig. 5.3, a flow through a capillary with non-uniform wall mobilities is depicted, as for example considered by Herr et al. (2000). Here, due to non-uniform pressures, shear is induced. Early work on dispersion in EOF include Datta and Kotamarthi (1990), where a dispersion in capillary electrophoresis was studied, with both pressure

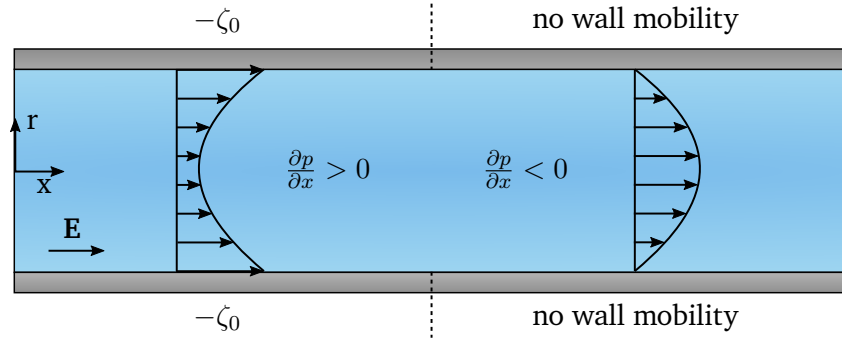


Figure 5.3: Schematic of internal pressure gradients in capillaries created by electro-osmosis with non-homogeneous wall mobilities. The region with wall mobility drives a flow field through the whole capillary. Due to the region without wall mobility, an internal pressure gradient builds up, which deforms the EOF profile. Due to the velocity changes in radial direction, sample dispersion increases.

and EOF, in the limit of small ζ potentials. Other research focused on large ζ potentials (Griffiths and Nilson, 2000), arbitrary cross sections (Zholkovskij and Masliyah, 2004; Zholkovskij et al., 2003), and overlapping EDL (Zholkovskij et al., 2010). The effects of non-uniform, randomized ζ potentials were explored by Gleeson and Stone (2004), and adsorption-desorption wall reactions were included by Datta and Ghosal (2008). Furthermore, Ng and Zhou (2012) studied the combined effects of variations in ζ potentials and wall slip, showing that slip effects can enhance dispersion. Bahga et al. (2012) modeled dispersion in channels with variations of the cross-section, accounting both for multispecies transport as well as chemical reactions at equilibrium. Recent work on dispersion was performed by Vargas et al. (2017), who accounted for magnetohydrodynamic forces, and Muñoz et al. (2018), who accounted for pulsating EOF and slip. Chu et al. (2019) discussed both stationary and oscillatory flow fields, and re-visited the problem of apparent negative dispersion coefficients.

One of the key differences between the flow field considered in chapter 4 and the work presented above is the directionality of the flow. In flow through capillaries, the fluid velocity is directed mainly along a specific direction, e.g., the channel axis, due to uniformly applied pressure gradients and a constant direction of the electric field. Inhomogeneous flows in Hele-Shaw cells due to electro-osmosis, on the other hand, lead to internal pressure gradients and strong variations in the flow direction. Notably, Lin et al. (2008) considered electro-osmotic flow in a shallow-channel geometry, with the flow direction determined by the spatio-temporal evolution of the conductivity. Both the direction and magnitude of the velocity was determined by the electric field and ζ potential, that in turn depended on the local conductivity. From the analysis, a dispersion tensor emerged, describing the non-isotropic dispersion within the fluidic domain. The main difference between the model of Lin et al. and the present work is due to the nature of the wall mobility. Lin et al. determined the wall velocity based on the internal dynamics of the ion transport, whereas in this work, the dispersion due to externally imposed wall boundary conditions is considered. Other work on dispersion in Hele-Shaw cell exists, especially for pressure-driven flow. For example, Zimmerman and Homsy (1991) proposed a model in the context of viscous fingering of miscible fluids. However, since implicitly a constant form of the local flow profile for a given average velocity was assumed, it is inapplicable for the specific situation of superposed EOF and pressure-driven flow considered here. Other works consider dispersion in Hele-Shaw geometries in uniformly applied pressure fields, as for example in the experiments of Roht et al. (2015). To summarize, while dispersion has been considered in a variety of situations, the dispersion in inhomogeneous Hele-Shaw flows due to externally imposed oscillatory and stationary wall boundary effects requires additional modeling effort, which will be pursued in the following.

5.3 Species transport in inhomogeneous Hele-Shaw flows

5.3.1 Introduction

In this section, the transport equation for a dissolved species in a background fluid flow in a Hele-Shaw cell is derived. The dissolved species is passive (no influence on the flow) and electro-neutral (no migration in the electric field). In Fig. 5.4, a schematic of the considered fluidic domain is shown. While the governing equations of the flow have been derived in section 4.3, the dispersion model will be derived without assuming a specific flow field, rendering it applicable to a variety of flow problems. Only in section 5.4, specific flow fields will be introduced. In accordance with the derivation of the flow equations, a Newtonian, incompressible fluid is considered, with the fluidic domain bound by two parallel plates located at $z = 0$ and $z = h$, respectively. Following, the z -direction will be denoted as cross-stream, and the x - y -direction as in-plane. The side-length of the cell is denoted by L . In the following, the three-dimensional flow field is assumed to take the form

$$u(x, y, z, t) = \bar{u}(x, y, z) + u'(x, y, z, t) \quad (5.10a)$$

$$v(x, y, z, t) = \bar{v}(x, y, z) + v'(x, y, z, t) \quad (5.10b)$$

$$w(x, y, z, t) = \bar{w}(x, y, z) + w'(x, y, z, t), \quad (5.10c)$$

where u and v represent the in-plane velocity components, and w the cross-stream component. Following the notation outlined in section 4.3, each velocity component is decomposed into a steady-state and fluctuating part, denoted by $\bar{(\cdot)}$ and $(\cdot)'$, respectively. In the following, it is assumed that the fluctuating component is oscillatory with a period $T_{\text{osc}} = 1/f$, where f denotes a characteristic frequency. It is important to note that the oscillatory component can be composed of multiple frequencies, resulting for example from the interaction of an AC driving field with a mixed DC-AC electro-osmotic wall mobility (see section 4.3.2 for details).

Two processes contribute to the transport of a dissolved, electrically neutral species: The background flow field transports the species by advection, and Brownian motion of the molecules leads to molecular diffusion. An illustration of the transport mechanisms is shown in Fig. 5.4(b). In the present problem, it is assumed that no sources or sinks of species are present, e.g. due to chemical reactions or wall adsorption. Further, the molecular concentration is assumed to be sufficiently small, leading to the advection-diffusion equation

$$\frac{\partial c}{\partial t} + u \frac{\partial c}{\partial x} + v \frac{\partial c}{\partial y} + w \frac{\partial c}{\partial z} = D \left(\frac{\partial^2 c}{\partial x^2} + \frac{\partial^2 c}{\partial y^2} + \frac{\partial^2 c}{\partial z^2} \right), \quad (5.11)$$

where D represents the molecular diffusion coefficient of the species, and c the molecular concentration. In order to provide the problem with appropriate boundary conditions, the upper and lower wall are assumed to be impermeable, leading to

$$\frac{\partial c}{\partial z} = 0 \quad \text{at} \quad z = 0, h. \quad (5.12)$$

At the perimeter of the cell, no specific boundary conditions are imposed as of now, since they strongly depend on the specific problem under investigation and are not required to continue with the derivation.

Equations 5.11 and 5.12 describe the full three-dimensional species transport. However, since all three dimensions need to be resolved such that the processes occurring over the smallest scales are resolved, obtaining a numerical solution can become computationally demanding. Especially transient problems might be impractical to solve for in a reasonable time. To overcome these limitations, a reduced order

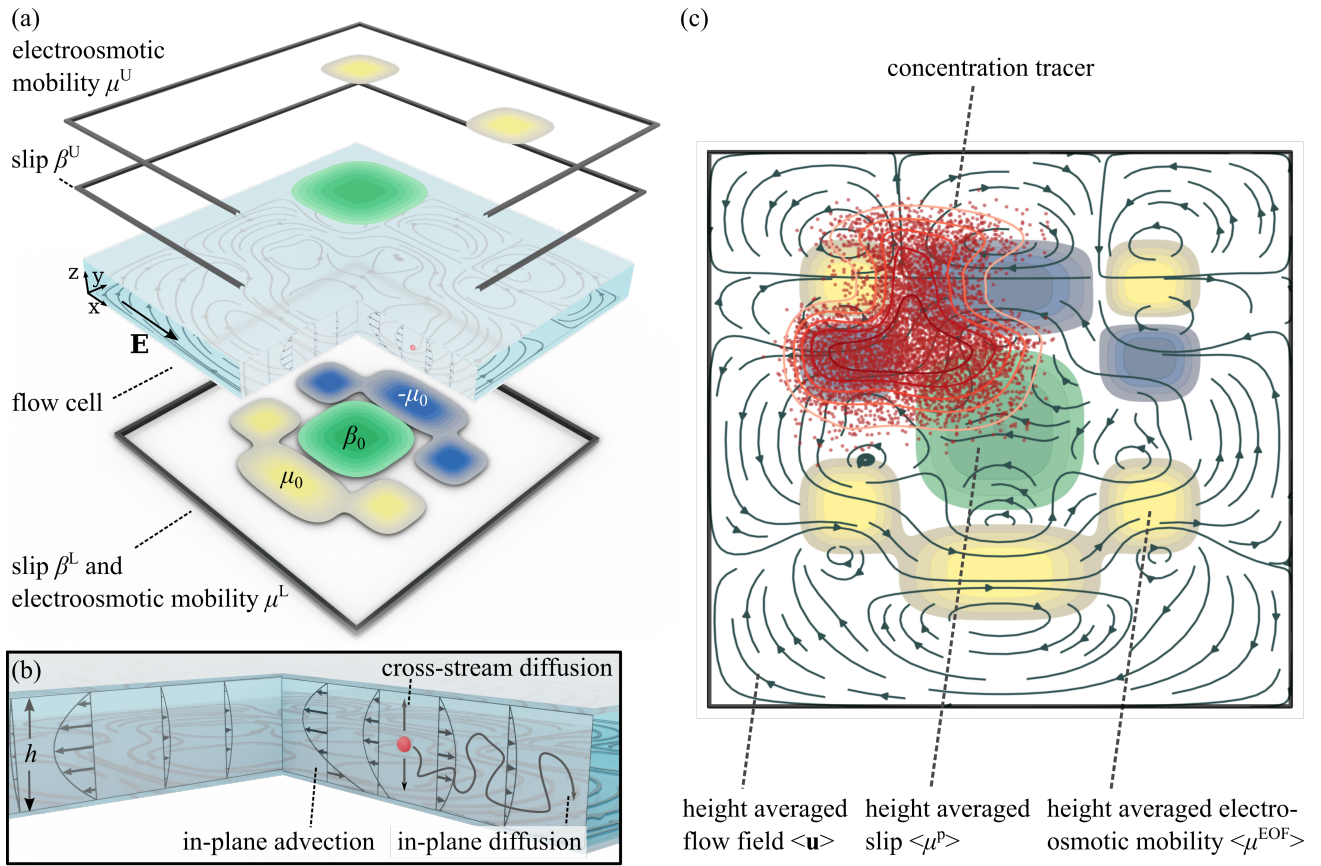


Figure 5.4: Illustration of species transport in a Hele-Shaw cell geometry under electric field actuation. (a) The upper and lower fluidic walls can both exhibit a non-uniform slip length as well as electroosmotic mobility, and are separated by a gap width h . As a result, a non-uniform flow field develops. (b) The dissolved species is transported by different mechanisms, including advection and diffusion. (c) Reduced-order representation of the system. The concentration field (red) is redistributed due to advection, dispersion and molecular diffusion. The species transport processes occurring over the cross-stream direction are incorporated into the transport coefficients of the two-dimensional model. Reprinted with permission from Cambridge University Press, *J. Fluid Mech.* 925, 2021, Dehe et al. (2021b).

model is derived, which captures the transport processes on the small scale (cross-stream direction), such that only the large scales have to be resolved (in-plane direction). A schematic of such a representative reduced-order model of Fig. 5.4(a) is shown in Fig. 5.4(c).

In the following, the multiple-scale perturbation approach is utilized to separate the micro- and macroscales (Mei and Vernescu, 2010). Based on the derivation of the flow equations in section 4.3, the typical length scale in the in-plane direction is identified as L_0 and much larger than the channel height h . As before, it is important to note that the scale L_0 denotes a typical scale of inhomogeneity of the flow field, which can differ from the side length of the domain L . In the following, the small parameter

$$\epsilon = \frac{h}{L_0} \ll 1, \quad (5.13)$$

will be used in the perturbation analysis.

Considering the different length-scales of the problem in combination with the transport mechanisms, three distinct time scales emerge. The shortest time scale is due to cross-stream diffusion, in analogy to

Taylor-Aris dispersion. It results in

$$T_{\text{dif,h}} = O\left(\frac{h^2}{D}\right) = O(T_{\text{osc}}). \quad (5.14)$$

Here, the additional assumption is introduced that the oscillation time scale is of similar order as the cross-stream diffusion timescale, in analogy to Chu et al. (2019). This assumption can be supported by using the channel geometries reported in recent flow-shaping applications (Bacheva et al., 2020; Boyko et al., 2021; Paratore et al., 2019a). Channel heights on the order of 10^{-5} m, in conjunction with diffusion coefficients of $10^{-9} \text{ m}^2 \text{ s}^{-1}$ lead to $T_{\text{dif,h}} = O(10^{-1} \text{ s})$, which coincides with the order of magnitude of the reported oscillatory frequencies.

Next, the time scale of the advection along the in-plane inhomogeneity scale L_0 follows as

$$T_{\text{adv}} = O\left(\frac{L_0}{U_0}\right) = O\left(\frac{h}{W_0}\right) = \frac{T_{\text{dif,h}}}{\epsilon}, \quad (5.15)$$

where U_0 and W_0 are the in-plane and cross-stream velocity scales identified in section 4.3, and their relation followed from an order-of-magnitude analysis of the continuity eq. 2.17. In the following, it is assumed that the advective time scale occurs on a scale $T_{\text{dif,h}}/\epsilon$.

The third time scale of the system can be identified as the in-plane diffusion time scale, resulting in

$$T_{\text{dif,L}} = O\left(\frac{L_0^2}{D}\right) = \frac{T_{\text{dif,h}}}{\epsilon^2}, \quad (5.16)$$

assumed to occur over an even longer time scale. After identifying all time scales of the problem, a hierarchy of time variables can be introduced for use in the perturbation analysis, leading to

$$t_0 = t, \quad t_1 = \epsilon t, \quad t_2 = \epsilon^2 t. \quad (5.17)$$

Subsequently, the advection-diffusion equation 5.11 is non-dimensionalized using the respective length and velocity scales, as well as a molar concentration scale c_0 and the diffusive time scale $T_{\text{dif,h}}$. The non-dimensional transport equation then reads

$$\frac{\partial \hat{c}}{\partial \hat{t}} + \epsilon Pe \left(u \frac{\partial \hat{c}}{\partial \hat{x}} + v \frac{\partial \hat{c}}{\partial \hat{y}} + w \frac{\partial \hat{c}}{\partial \hat{z}} \right) = \epsilon^2 \left(\frac{\partial^2 \hat{c}}{\partial \hat{x}^2} + \frac{\partial^2 \hat{c}}{\partial \hat{y}^2} \right) + \frac{\partial^2 \hat{c}}{\partial \hat{z}^2}, \quad (5.18)$$

subject to the respective boundary conditions

$$\frac{\partial \hat{c}}{\partial \hat{z}} = 0 \quad \text{at} \quad \hat{z} = 0, 1. \quad (5.19)$$

In analogy to chapter 4, non-dimensionalized quantities are denoted by hatted variables, and Pe denotes the Péclet number $Pe = U_0 h / D$. In order to reduce the three-dimensional problem to an effective two-dimensional model, the approach outlined by Chu et al. (2019) will be followed, resulting in the long-time limit of eq. 5.18.

In the following, the multiple scale perturbation approach is used to expand the problem into the different orders in ϵ . First, the concentration field is expanded in ϵ , including the dependency on the different time scales, resulting in (Fife and Nicholes, 1975)

$$c(x, y, z, t) = c^{(0)}(x, y, z, t_0, t_1, t_2) + \epsilon c^{(1)}(x, y, z, t_0, t_1, t_2) + \epsilon^2 c^{(2)}(x, y, z, t_0, t_1, t_2) + O(\epsilon^3). \quad (5.20)$$

For readability, the hats are dropped in the following derivation, keeping the variables non-dimensional. Next, the time scales in eq. 5.17 are used to expand the time-derivative using the chain rule, leading to

$$\frac{\partial}{\partial t} = \frac{\partial}{\partial t_0} + \epsilon \frac{\partial}{\partial t_1} + \epsilon^2 \frac{\partial}{\partial t_2}. \quad (5.21)$$

In the following derivation, the expanded time-derivative as well as concentration field will be used to split the governing equation 5.18 and boundary conditions 5.19 into a set of equations of varying orders in ϵ . Then, considering the equations in increasing order, the macroscale transport equation is constructed.

At this point, it is instructive to discuss the physical interpretations of the concentrations $c^{(0)}$, $c^{(1)}$ and $c^{(2)}$. As will be justified during the derivation of the macrotransport equation, the component $c^{(0)}$ represents the concentration, averaged over the channel height and one period of oscillation. Thus, the components $c^{(1)}$ and $c^{(2)}$ are fluctuating in nature, with vanishing average over the channel height and one period of oscillation. The macrotransport equation can be derived without introducing this assumption a priori, and in section 5.3.4, the changes during the derivation are sketched. It is instructive, however, to utilize this assumption, since it enables a clearer interpretation of the intermediate results.

5.3.2 Leading order perturbation: $O = (\epsilon^0)$

The leading-order in ϵ of eq. 5.18 results in

$$\frac{\partial c^{(0)}}{\partial t_0} = \frac{\partial^2 c^{(0)}}{\partial z^2}, \quad (5.22)$$

subject to the boundary condition

$$\frac{\partial c^{(0)}}{\partial z} = 0 \quad \text{at } z = 0, 1. \quad (5.23)$$

A solution to eq. 5.22 which satisfies the respective boundary condition (eq. 5.23) follows as an infinite series of the form

$$c^{(0)} = c_0^{(0)}(x, y, t_1, t_2) + \sum_{n=1}^{\infty} c_n^{(0)}(x, y, t_1, t_2) e^{-n^2 \pi^2 t_0} \cos(n\pi z). \quad (5.24)$$

From eq. 5.24, it is visible that any initial dependence of the concentration distribution on z decays exponentially over a timescale t_0 due to the factor $e^{-n^2 \pi^2 t_0}$. Since it is irrelevant for the long-term solution, the dependency of $c^{(0)}$ on t_0 can be dropped, resulting in

$$c^{(0)} = c_0^{(0)}(x, y, t_1, t_2). \quad (5.25)$$

Physically, the independence of $c^{(0)}$ on t_0 and z corroborates the assumption introduced above that $c^{(0)}$ represents the cross-stream and short-time average.

5.3.3 First-order perturbation: $O = (\epsilon^1)$

Continuing with the next order in ϵ , the first-order perturbation of eq. 5.18 leads to

$$\frac{\partial c^{(0)}}{\partial t_1} + \frac{\partial c^{(1)}}{\partial t_0} + Pe u \frac{\partial c^{(0)}}{\partial x} + Pe v \frac{\partial c^{(0)}}{\partial y} = \frac{\partial^2 c^{(1)}}{\partial z^2}, \quad (5.26)$$

subject to the boundary conditions

$$\frac{\partial c^{(1)}}{\partial z} = 0 \quad \text{at } z = 0, 1. \quad (5.27)$$

In analogy to chapter 4, it is useful to define the time-average over the oscillation period (on the short time scale t_0) as

$$\overline{(\cdot)} = \frac{1}{T_{\text{osc}}} \int_{t_0}^{t_0+T_{\text{osc}}} (\cdot) dt_0, \quad (5.28)$$

and the cross-stream average as

$$\langle (\cdot) \rangle = \int_0^1 (\cdot) dz. \quad (5.29)$$

In order to obtain an expression for $c^{(0)}$ on the time scale t_1 , applying both the time- and cross-stream average to eq. 5.26 yields

$$\frac{\partial c^{(0)}}{\partial t_1} + Pe \langle \bar{u} \rangle \frac{\partial c^{(0)}}{\partial x} + Pe \langle \bar{v} \rangle \frac{\partial c^{(0)}}{\partial y} = 0. \quad (5.30)$$

Here, the right-hand side vanishes due to the boundary condition 5.27, similarly the time- and cross-stream average of the second term on the left-hand side, as it represents a fluctuating component. Physically, eq. 5.30 shows that the transient development of the average concentration $c^{(0)}$ results from advection with the mean flow.

In a next step, an equation for $c^{(1)}$ can be constructed, by subtracting eq. 5.30 from eq. 5.26, and inserting the velocity definitions (eq. 5.10) leads to

$$\frac{\partial c^{(1)}}{\partial t_0} + Pe ((\bar{u} - \langle \bar{u} \rangle) + u') \frac{\partial c^{(0)}}{\partial x} + Pe ((\bar{v} - \langle \bar{v} \rangle) + v') \frac{\partial c^{(0)}}{\partial y} = \frac{\partial^2 c^{(1)}}{\partial z^2}. \quad (5.31)$$

Physically, eq. 5.31 shows that the cross-stream concentration variation $c^{(1)}$ is driven by the velocity variations over the channel height. Two contributions drive the system: One stems from the time-averaged velocity difference over the channel cross-section $(\bar{u} - \langle \bar{u} \rangle, \bar{v} - \langle \bar{v} \rangle)$, and the other one due to the oscillatory velocity variation (u', v') . As eq. 5.31 is linear, the solution to $c^{(1)}$ is assumed to be composed of a stationary as well as an oscillatory part of the form

$$c^{(1)} = Pe (\mathbf{a}(x, y, z) + \mathbf{b}(x, y, z, t_0)) \cdot \nabla_{\parallel} c^{(0)}. \quad (5.32)$$

In analogy to chapter 4, the in-plane gradient is denoted by $\nabla_{\parallel} = (\partial/\partial x, \partial/\partial y)$ for better readability. As discussed above, $c^{(1)}$ represents a fluctuating quantity, and thus contributions from the general solution of the homogeneous equation were neglected in the above ansatz.

Obtaining the stationary solution \mathbf{a} and the oscillatory solution \mathbf{b} is at the center of generating the reduced-order model. The governing problems for both can be generated by inserting eq. 5.32 into eq. 5.31, and separating the stationary and the oscillatory problem. In order to retrieve the boundary conditions, eq. 5.32 can be inserted into the boundary condition 5.27. The governing problem of the steady-state term \mathbf{a} follows as

$$\begin{pmatrix} \bar{u} - \langle \bar{u} \rangle \\ \bar{v} - \langle \bar{v} \rangle \end{pmatrix} = \frac{\partial^2 \mathbf{a}}{\partial z^2}, \quad \text{with} \quad \frac{\partial \mathbf{a}}{\partial z} = 0 \quad \text{at } z = 0, 1. \quad (5.33)$$

Due to the structure of eq. 5.33, the solution is not unique. For every solution $\mathbf{a}^{(1)}$, additional solutions of the form $\mathbf{a}^{(1)} + \mathbf{C}(x, y)$ can be constructed, where $\mathbf{C}(x, y)$ is an arbitrary function depending on x, y only. An additional constraint to render the solution unique can be defined as $\langle \mathbf{a} \rangle = \mathbf{0}$. This condition justifies our initial assumption that $c^{(1)}$ is expected to be a fluctuating quantity.

Similarly, the governing problem of the unsteady solution component \mathbf{b} can be obtained as

$$\frac{\partial \mathbf{b}}{\partial t_0} + \begin{pmatrix} u' \\ v' \end{pmatrix} = \frac{\partial^2 \mathbf{b}}{\partial z^2}, \quad \text{with} \quad \frac{\partial \mathbf{b}}{\partial z} = 0 \quad \text{at} \quad z = 0, 1. \quad (5.34)$$

Analogous to the stationary component, eq. 5.34 does not uniquely define \mathbf{b} . For any solution $\mathbf{b}^{(1)}$, additional solutions of the form then $\mathbf{b}^{(1)} + \mathbf{D}(x, y)$ can be obtained, with $\mathbf{D}(x, y)$ denoting an arbitrary function depending on x and y only. Here, the additional condition $\langle \bar{\mathbf{b}} \rangle = \mathbf{0}$ is imposed to render the solution unique. As a result, the oscillatory component of $c^{(1)}$ satisfies the initial assumption that $c^{(1)}$ is a fluctuating component. Both boundary value problems 5.33 and 5.34 can be solved for specific flow fields, either analytically or numerically. A specific solution will be discussed in section 5.3.7. For the remainder of the derivation of the macrotransport equation, the general form is kept, assuming that the solutions \mathbf{a} and \mathbf{b} were obtained. Then, $c^{(1)}$ is defined and the second-order perturbation can be approached.

5.3.4 Second-order perturbation: $O = (\epsilon^2)$

The second-order governing equation reads

$$\frac{\partial c^{(0)}}{\partial t_2} + \frac{\partial c^{(1)}}{\partial t_1} + \frac{\partial c^{(2)}}{\partial t_0} + Pe \left(u \frac{\partial c^{(1)}}{\partial x} + v \frac{\partial c^{(1)}}{\partial y} + w \frac{\partial c^{(1)}}{\partial z} \right) = \frac{\partial^2 c^{(0)}}{\partial x^2} + \frac{\partial^2 c^{(0)}}{\partial y^2} + \frac{\partial^2 c^{(2)}}{\partial z^2}, \quad (5.35)$$

subject to the boundary conditions

$$\frac{\partial c^{(2)}}{\partial z} = 0 \quad \text{at} \quad z = 0, 1. \quad (5.36)$$

In order to obtain the solution to the second-order perturbation, eq. 5.35 is averaged over time and the cross-channel direction. In the following, each term will be discussed separately. The second term on the left-hand side can be simplified using eq. 5.30 and eq. 5.32, leading to

$$\frac{\partial c^{(1)}}{\partial t_1} = -Pe^2 (\mathbf{a} + \mathbf{b}) \cdot \nabla_{\parallel} \left(\langle \bar{u} \rangle \frac{\partial}{\partial x} c^{(0)} + \langle \bar{v} \rangle \frac{\partial}{\partial y} c^{(0)} \right). \quad (5.37)$$

As discussed above, the averages $\langle \mathbf{a} \rangle = \langle \bar{\mathbf{b}} \rangle = \mathbf{0}$ vanish, and thus this term vanishes.

In order to simplify the third term on the left-hand side, it is important to note that eq. 5.35 does not define $c^{(2)}$ uniquely. Therefore, in analogy to \mathbf{a} and \mathbf{b} , the additional condition $\langle \bar{c}^{(2)} \rangle = 0$ is imposed to render the solution unique. This is in line with the assumption that $c^{(2)}$ represents a fluctuating quantity. Therefore, the time- and height-average of the third term on the left-hand side disappears.

In retrospect, the initial assumptions of the choice of $c^{(1)}$ and $c^{(2)}$ being fluctuating quantities is supported by the choice of additional conditions. As a result, $c^{(0)}$ represents the cross-stream average of the concentration distribution in the long-time limit, in line with other works utilizing multiple-scale perturbation methods (Chu et al., 2019; Mei et al., 1996). In principle, other conditions could have been chosen to render the solutions of \mathbf{a} , \mathbf{b} , and $c^{(2)}$ unique, with non-vanishing time- and cross-stream averages. Then, $c^{(0)}$ would not represent the long-time and height average, but instead it would be required to use $\langle \bar{c} \rangle = \langle \bar{c}^{(0)} \rangle + \epsilon \langle \bar{c}^{(1)} \rangle + \epsilon^2 \langle \bar{c}^{(2)} \rangle$ to rewrite the final transport equation. However, with the current choice of constraints, the macrotransport equation is obtained in terms of $c^{(0)}$, simplifying it significantly.

The fourth term on the left-hand side of eq. 5.35 can be rewritten by utilizing the solution of $c^{(1)}$ (eq. 5.32) and time-averaging over one period of oscillation. Then, the term can be expressed as

$$Pe \left\langle u \frac{\partial c^{(1)}}{\partial x} \right\rangle = Pe^2 \left(\left\langle \bar{u} \frac{\partial \mathbf{a}}{\partial x} \right\rangle \cdot \nabla_{\parallel} c^{(0)} + \bar{u} \mathbf{a} \cdot \frac{\partial \nabla_{\parallel} c^{(0)}}{\partial x} \right) + Pe^2 \left(\left\langle u' \frac{\partial \mathbf{b}}{\partial x} \right\rangle \cdot \nabla_{\parallel} c^{(0)} + \overline{u' \mathbf{b}} \cdot \frac{\partial \nabla_{\parallel} c^{(0)}}{\partial x} \right). \quad (5.38)$$

Invoking the cross-stream average, the term simplifies to

$$Pe \left\langle u \frac{\partial c^{(1)}}{\partial x} \right\rangle = Pe^2 \left(\left(\left\langle \bar{u} \frac{\partial \mathbf{a}}{\partial x} \right\rangle + \left\langle u' \frac{\partial \mathbf{b}}{\partial x} \right\rangle \right) \cdot \nabla_{\parallel} c^{(0)} + (\langle \bar{u} \mathbf{a} \rangle + \langle u' \mathbf{b} \rangle) \cdot \frac{\partial \nabla_{\parallel} c^{(0)}}{\partial x} \right). \quad (5.39)$$

Similarly, the fifth term on the left-hand side of eq. 5.35 yields

$$Pe \left\langle v \frac{\partial c^{(1)}}{\partial y} \right\rangle = Pe^2 \left(\left(\left\langle \bar{v} \frac{\partial \mathbf{a}}{\partial y} \right\rangle + \left\langle v' \frac{\partial \mathbf{b}}{\partial y} \right\rangle \right) \cdot \nabla_{\parallel} c^{(0)} + (\langle \bar{v} \mathbf{a} \rangle + \langle v' \mathbf{b} \rangle) \cdot \frac{\partial \nabla_{\parallel} c^{(0)}}{\partial y} \right), \quad (5.40)$$

and the sixth term results in

$$Pe \left\langle w \frac{\partial c^{(1)}}{\partial z} \right\rangle = Pe^2 \left(\left\langle \bar{w} \frac{\partial \mathbf{a}}{\partial z} \right\rangle \cdot \nabla_{\parallel} c^{(0)} + \left\langle w' \frac{\partial \mathbf{b}}{\partial z} \right\rangle \cdot \nabla_{\parallel} c^{(0)} \right). \quad (5.41)$$

Finally, the third term on the right-hand side of eq. 5.35 vanishes due to the boundary condition 5.36.

The resulting governing equation of the second-order problem can be constructed by collecting the terms from eq. 5.39, 5.40 and 5.41 and inserting them into equation 5.35, yielding

$$\begin{aligned} \frac{\partial c^{(0)}}{\partial t_2} + Pe^2 \left(\left\langle \bar{u} \frac{\partial \mathbf{a}}{\partial x} \right\rangle + \left\langle \bar{v} \frac{\partial \mathbf{a}}{\partial y} \right\rangle + \left\langle \bar{w} \frac{\partial \mathbf{a}}{\partial z} \right\rangle + \left\langle u' \frac{\partial \mathbf{b}}{\partial x} \right\rangle + \left\langle v' \frac{\partial \mathbf{b}}{\partial y} \right\rangle + \left\langle w' \frac{\partial \mathbf{b}}{\partial z} \right\rangle \right) \cdot \nabla_{\parallel} c^{(0)} \\ + Pe^2 \left(\langle \bar{u} \mathbf{a} \rangle \cdot \frac{\partial \nabla_{\parallel} c^{(0)}}{\partial x} + \langle \bar{v} \mathbf{a} \rangle \cdot \frac{\partial \nabla_{\parallel} c^{(0)}}{\partial y} + \langle u' \mathbf{b} \rangle \cdot \frac{\partial \nabla_{\parallel} c^{(0)}}{\partial x} + \langle v' \mathbf{b} \rangle \cdot \frac{\partial \nabla_{\parallel} c^{(0)}}{\partial y} \right) = \nabla_{\parallel}^2 c^{(0)}. \end{aligned} \quad (5.42)$$

This equation describes the time-evolution of the concentration field $c^{(0)}$ on the time scale t_2 .

5.3.5 Resulting macrotransport equation

In order to obtain the resulting macrotransport equation, eq. 5.42 is multiplied by ϵ^2 , eq. 5.30 multiplied by ϵ and both added to eq. 5.22. Then, the hierarchy of time-coordinates $t_i = \epsilon^i t$ is reduced to a single time-coordinate, resulting in

$$\frac{\partial c^{(0)}}{\partial t} + (\epsilon Pe \langle \bar{u}_{\parallel} \rangle + \epsilon^2 Pe^2 (\mathbf{k}_{\text{stat}} + \mathbf{k}_{\text{osc}})) \cdot \nabla_{\parallel} c^{(0)} = \epsilon^2 \left(\nabla_{\parallel} \cdot \left[(\mathbf{I} - Pe^2 \mathbf{D}) \cdot \nabla_{\parallel} c^{(0)} \right] \right), \quad (5.43)$$

with the in-plane velocity components expressed as $\bar{\mathbf{u}}_{\parallel} = (\bar{u}, \bar{v})$. The vector fields \mathbf{k}_{stat} and \mathbf{k}_{osc} represent advection correction terms resulting from the stationary and oscillatory component of the flow field, \mathbf{I} represents the identity tensor, and \mathbf{D} the dispersion tensor. Here, the advection correction terms are defined as

$$\mathbf{k}_{\text{stat}} = - \left\langle \frac{\partial \bar{u}}{\partial x} \mathbf{a} \right\rangle - \left\langle \frac{\partial \bar{v}}{\partial y} \mathbf{a} \right\rangle + \left\langle \bar{w} \frac{\partial \mathbf{a}}{\partial z} \right\rangle \quad (5.44)$$

and

$$\mathbf{k}_{\text{osc}} = - \left\langle \frac{\partial u'}{\partial x} \mathbf{b} \right\rangle - \left\langle \frac{\partial v'}{\partial y} \mathbf{b} \right\rangle + \left\langle w' \frac{\partial \mathbf{b}}{\partial z} \right\rangle, \quad (5.45)$$

and the dispersion tensor follows as

$$\mathbf{D} = \mathbf{D}_{\text{stat}} + \mathbf{D}_{\text{osc}} = \begin{bmatrix} \langle \bar{u}a_x \rangle & \langle \bar{v}a_x \rangle \\ \langle \bar{u}a_y \rangle & \langle \bar{v}a_y \rangle \end{bmatrix} + \begin{bmatrix} \langle u'b_x \rangle & \langle v'b_x \rangle \\ \langle u'b_y \rangle & \langle v'b_y \rangle \end{bmatrix}. \quad (5.46)$$

It is important to note that the subscripts x, y in eq. 5.46 represent vector components of \mathbf{a} and \mathbf{b} .

At this point, it is instructive to discuss the structure and physical interpretation of the macrotransport equation 5.43. Only the in-plane coordinates x and y enter the final equation, as they represent the macroscales of the problem. The time-averaged transport effects due to cross-stream transport are included into the coefficient fields (equations 5.44 - 5.46). They are defined by solving the micro-scale problems (eq. 5.33 and eq. 5.34). Physically, the second term on the left-hand side of eq. 5.43 represents advection with the mean flow, and the third term an advection-correction term due to velocity variations in z of the stationary (\mathbf{k}_{stat}) and oscillatory flow field (\mathbf{k}_{osc}). The first term on the right-hand side represents molecular diffusion and Taylor-Aris dispersion due to stationary (\mathbf{D}_{stat}) and oscillatory (\mathbf{D}_{osc}) flow. Similarly to previous work on dispersion, the effects of the stationary and oscillatory flow components are additive (Watson, 1983). Also, the classical Pe^2 dependency of the dispersion is retrieved, but here with a negative sign due to the definition of \mathbf{a}, \mathbf{b} . Due to the variations of the flow field in different directions, the dispersion is represented by a tensor field, which can be non-isotropic. Overall, eq. 5.43 represents the long-time, height-averaged limit of the three-dimensional problem, thus reducing the problem to an equivalent two-dimensional problem. For a given flow field, the transport coefficients are determined. While the motivation of the dispersion model was given by electro-osmotic flow shaping, it is important to note that the dispersion of all flow fields satisfying the underlying conditions, i.e., the large lateral length scale compared to the channel height h , can be modeled. For example, flow shaping due to pressure-driven flow in a Hele-Shaw cell with variations of the wall slip can be modeled as well. Also, the model is not restricted to flow fields derived in chapter 4. Higher-order solutions of the flow field in Hele-Shaw cells can readily be implemented into the dispersion model.

5.3.6 Thermodynamic consistency of the dispersion tensor

As discussed in section 5.2.2, the dispersion tensor $\mathbf{I} - Pe^2 \mathbf{D}$ (eq. 5.46) has to be positive definite. Otherwise, modeling dispersion using an advection-diffusion equation is not possible, since negative eigenvalues of the matrix would lead to the formation of singularities within the concentration field (Smith, 1982). As the dispersion tensor represents the time- and z -averaged concentration transport, a compression of the concentration field would violate the second law of thermodynamics.

In order to prove that the dispersion matrix is positive definite, the mathematical properties of positive-definite tensors can be used. A positive definite tensor A_{ij} satisfies $\chi_i A_{ij} \chi_j > 0$ (in index-notation, using the Einstein summation convention), where χ represents an arbitrary vector, which is not the null vector. Then, the condition

$$\chi_i (\delta_{ij} - Pe^2 (D_{\text{stat},ij} + D_{\text{osc},ij})) \chi_j > 0 \quad (5.47)$$

has to be satisfied, where the identity tensor is expressed using the Kronecker delta δ_{ij} . The first term of eq. 5.47 is positive definite, as $\chi_i \delta_{ij} \chi_j = (\chi_i)^2 > 0$.

The stationary component can be evaluated by rewriting \mathbf{D}_{stat} as

$$D_{\text{stat},ij} = \langle \bar{u}_i a_j \rangle = \langle a_j (\bar{u}_i - \langle \bar{u}_i \rangle) \rangle = \left\langle a_j \frac{\partial^2 a_i}{\partial z^2} \right\rangle, \quad (5.48)$$

using the governing equation 5.33 of a_i . Then, integration by parts and utilization of the boundary condition of eq. 5.33 yields

$$\left\langle a_j \frac{\partial^2 a_i}{\partial z^2} \right\rangle = \left[\frac{\partial a_i}{\partial z} a_j \right]_{z=0}^1 - \left\langle \frac{\partial a_j}{\partial z} \frac{\partial a_i}{\partial z} \right\rangle = - \left\langle \frac{\partial a_j}{\partial z} \frac{\partial a_i}{\partial z} \right\rangle. \quad (5.49)$$

Using this alternative expression of the stationary component, it is possible to show that it is positive semi-definite, since

$$\chi_i (-Pe^2 D_{\text{stat},ij}) \chi_j = Pe^2 \chi_i \left\langle \frac{\partial a_i}{\partial z} \frac{\partial a_j}{\partial z} \right\rangle \chi_j = Pe^2 \left\langle \chi_i \frac{\partial a_i}{\partial z} \chi_j \frac{\partial a_j}{\partial z} \right\rangle = Pe^2 \left\langle \left(\frac{\partial a_k}{\partial z} \chi_k \right)^2 \right\rangle \geq 0, \quad (5.50)$$

becomes zero only if \mathbf{a} vanishes everywhere. Then, no dispersion due to the stationary flow field occurs.

Turning the attention towards the oscillatory component, it can be rewritten using eq. 5.34, resulting in

$$D_{\text{osc},ij} = \left\langle \overline{b_i u_j'} \right\rangle = \left\langle b_i \left(-\frac{\partial b_j}{\partial t_0} + \frac{\partial^2 b_j}{\partial z^2} \right) \right\rangle = - \left\langle b_i \frac{\partial b_j}{\partial t_0} \right\rangle + \left\langle b_i \frac{\partial^2 b_j}{\partial z^2} \right\rangle. \quad (5.51)$$

The second term on the right-hand side is positive semi-definite, following the line of arguments presented for the stationary component. The first term of eq. 5.51 utilized in eq. 5.47 vanishes, since

$$\begin{aligned} \chi_i \left\langle -b_i \frac{\partial b_j}{\partial t_0} \right\rangle \chi_j &= - \left\langle \frac{1}{2} \chi_x^2 \frac{\partial b_x^2}{\partial t_0} \right\rangle - \left\langle \frac{1}{2} \chi_y^2 \frac{\partial b_y^2}{\partial t_0} \right\rangle - \left\langle \chi_x \chi_y \frac{\partial b_x}{\partial t_0} b_y + \chi_x \chi_y \frac{\partial b_y}{\partial t_0} b_x \right\rangle \\ &= - \left\langle \frac{1}{2} \chi_x^2 \frac{\partial b_x^2}{\partial t_0} \right\rangle - \left\langle \frac{1}{2} \chi_y^2 \frac{\partial b_y^2}{\partial t_0} \right\rangle - \left\langle \chi_x \chi_y \left(\frac{1}{T_{\text{osc}}} [b_x b_y]_{t_0}^{t_0+T_{\text{osc}}} - \frac{\partial b_y}{\partial t_0} b_x + \frac{\partial b_y}{\partial t_0} b_x \right) \right\rangle = 0. \end{aligned} \quad (5.52)$$

Here, the definition of \mathbf{b} as an oscillatory function (see eq. 5.34) leads to a vanishing time-average. Considering all contributions, it follows that the condition 5.47 is satisfied, proving that the dispersion tensor is indeed positive-definite and thus thermodynamically consistent. Also, it is visible that the resulting dispersion tensor $\mathbf{I} - Pe^2 \mathbf{D}$ is symmetric.

5.3.7 Resulting dispersion tensor for a parametrized flow field

From the derivation of the governing equations of the flow field in section 4.3, it follows that the flow field takes the form of a quadratic polynomial over the z -coordinate. In the following, the dispersion tensor is shown for a parametric stationary velocity field of the form

$$u(x, y, z) = A_1(x, y)z^2 + A_2(x, y)z + A_3(x, y) \quad (5.53a)$$

$$v(x, y, z) = B_1(x, y)z^2 + B_2(x, y)z + B_3(x, y). \quad (5.53b)$$

Then, eq. 5.33 can be solved for the parametrized flow field. The stationary dispersion tensor can be obtained from eq. 5.46 as

$$\mathbf{D}_{\text{stat}} = \begin{bmatrix} -\frac{8A_1^2}{945} - \frac{A_1 A_2}{60} - \frac{A_2^2}{120} & -\frac{8A_1 B_1}{945} - \frac{A_2 B_1}{120} - \frac{A_1 B_2}{120} - \frac{A_2 B_2}{120} \\ -\frac{8A_1 B_1}{945} - \frac{A_2 B_1}{120} - \frac{A_1 B_2}{120} - \frac{A_2 B_2}{120} & -\frac{8B_1^2}{945} - \frac{B_1 B_2}{60} - \frac{B_2^2}{120} \end{bmatrix}, \quad (5.54)$$

and the advection correction term from eq. 5.44 as

$$\mathbf{k}_{\text{stat}} = \begin{bmatrix} \frac{1}{2160} (16A_1 + 15A_2) \left(2\frac{\partial A_1}{\partial x} + 3\frac{\partial A_2}{\partial x} + 6\frac{\partial A_3}{\partial x} + 2\frac{\partial B_1}{\partial y} + 3\frac{\partial B_2}{\partial y} + 6\frac{\partial B_3}{\partial y} \right) \\ \frac{1}{2160} (16B_1 + 15B_2) \left(2\frac{\partial A_1}{\partial x} + 3\frac{\partial A_2}{\partial x} + 6\frac{\partial A_3}{\partial x} + 2\frac{\partial B_1}{\partial y} + 3\frac{\partial B_2}{\partial y} + 6\frac{\partial B_3}{\partial y} \right) \end{bmatrix}. \quad (5.55)$$

Here, it is visible that the components D_{xx} and D_{yy} can only take negative values, due to the quadratic terms. The off-diagonal components, however, can take both positive and negative values. Also, the constant parts of the flow field A_3, B_3 have no effect on the dispersion, as they introduce no shear. A corresponding parametrization of an oscillatory flow field is not straight-forward, since in principle an infinite series of oscillatory frequencies can occur, and thus is not provided explicitly in this framework.

5.4 Comparison between 3D and 2D numerical computations

In the following, a comparison between the reduced-order transport model and three-dimensional numerical simulations will be performed for several Hele-Shaw flow fields. For the full three-dimensional transport problem, a particle tracking approach is utilized. A first and second test case include stationary and oscillatory flow fields in a Hele-Shaw cell. In a third test case, the species transport in a circulatory flow field, reminiscent of the blinking-vortex principle (Aref, 1984), is analyzed.

5.4.1 Numerical methods

Implementation of the particle-tracking method

In order to solve the three-dimensional problem, the particle tracking model implemented in Comsol Multiphysics 5.5 is utilized. In the following, the information on the implementation of the particle simulations are summarized, where settings specific to Comsol are indicated in *italic*. More details can be found in the Comsol Multiphysics reference guide (COMSOL, 2019). The particle motion is defined by the Brownian motion as well as the drag force of the surrounding fluid acting on the particle (COMSOL, 2019; Kim and Zydney, 2004). The equation of motion for each particle reads

$$\frac{d}{dt} (m_p \mathbf{u}_p) = \frac{1}{\tau_p} m_p (\mathbf{u} - \mathbf{u}_p) + \alpha \sqrt{\frac{6\pi k_B \mu T d_p}{\Delta t}}, \quad (5.56)$$

where m_p represents the particle mass, \mathbf{u}_p the particle velocity, \mathbf{u} the surrounding fluid's velocity, τ_p the particle's response time discussed below, k_B the Boltzmann constant, μ the dynamic viscosity of the surrounding fluid, T the absolute temperature, and d_p the particle diameter. The vector α contains normally distributed random numbers and defines the direction of the Brownian force acting on the particle. At each time step Δt , the vector is evaluated, and the random numbers change the direction of the Brownian motion. The numbers are independent and exhibit a zero mean and a unit standard deviation (COMSOL, 2019). The response time of a particle follows from Stokes drag as

$$\tau_p = \frac{\rho_p d_p^2}{18\mu}, \quad (5.57)$$

where ρ_p denotes the particle mass density. The coefficient of molecular diffusion results from the parameters as

$$D = \frac{k_B T}{3\pi\mu d_p}. \quad (5.58)$$

The parameters used in the particle-tracking simulations are listed in Table 5.1, yielding a generic diffusion coefficient of $D = 1 \times 10^{-10} \text{ m}^2\text{s}^{-1}$. The response time of the particle follows as $\tau_p = 1.02 \text{ ps}$,

Table 5.1: Parameter values used in the particle-tracking simulations. The values were chosen specifically to yield a molecular diffusion coefficient of $1 \times 10^{-10} \text{ m}^2 \text{ s}^{-1}$.

parameter	description	value
ρ_p	particle density	$1 \times 10^3 \text{ kg m}^{-3}$
d_p	particle diameter	$4.29 \times 10^{-9} \text{ m}$
D	molecular diffusion coefficient	$1 \times 10^{-10} \text{ m}^2 \text{ s}^{-1}$
μ	dynamic viscosity of water	$1 \times 10^{-3} \text{ Pa s}$
T	temperature in the fluid	293.15 K
k_B	Boltzmann constant	$1.38 \times 10^{-23} \text{ m}^2 \text{ kg s}^{-2} \text{ K}^{-1}$

indicating that the particle follows the motion of the surrounding fluid. At the domain boundaries, a specular reflection condition was utilized, defined as

$$\mathbf{u} = \mathbf{u}_c - 2(\mathbf{n} \cdot \mathbf{u}_c) \mathbf{n}, \quad (5.59)$$

where \mathbf{n} denotes the wall normal and \mathbf{u}_c the particle velocity when hitting the wall. To ensure accuracy of the simulations, the time-stepping has to be small compared to the diffusive time scale, such that wall interactions are limited to a small fraction of the time steps.

The initial conditions for the particle simulations are obtained by releasing particles from a uniformly spaced grid. The grid point occupation is set proportional to a provided concentration distribution. Then, the particles are equilibrated for times much longer than the diffusive timescale $T_{\text{dif,h}}$ using molecular diffusion only, to ensure that the influence of the particle release positions has decayed. Thereby, artifacts and sharp concentration gradients are diminished, which can lead to unphysical results. Additionally to the particle distribution, a fluid flow has to be provided to model particle dispersion. The flow field is supplied following from the corresponding 2D model, in order to ensure that potential differences between two-dimensional and three-dimensional simulations are due to the dispersion model only.

In order to compare the results between 3D and 2D simulations, it is useful to create a normalized concentration distribution, averaged over the cell height. Therefore, an x - y -mesh is defined in the computational domain, and the particle numbers per mesh cell are retrieved. Then, the particle count is normalized using the initial particle count in regions of maximum concentration, as defined by the initial distribution. As a result, a normalized concentration distribution comparable to the two-dimensional simulations is obtained. In the following, the distribution is shown without additional smoothing, in order to preserve the extend of mixing zones between high-concentration and low concentration regions. The number of used particles per simulation varies between the test cases and is described in the respective sections.

From eq. 5.56 it follows that the time step size is a crucial parameter influencing the random force acting on the particles. The time step has to be chosen sufficiently small, such that the particles react sufficiently often to the random force in order to reproduce molecular diffusion. Therefore, the condition $\Delta t \ll T_{\text{dif,h}}$ has to be satisfied. In order to ensure sufficient time step resolution, a convergence study was performed within a flow field similar to test case C, which is described in detail in section 5.4.4. Here, the cell height was set to $h = 100 \mu\text{m}$, and the maximum wall velocity to $500 \mu\text{m s}^{-1}$. Then, the time step size was varied, using the *Generalized alpha* solver, which is an implicit, second-order accurate time-stepping scheme with less numerical damping of high-frequency components than comparable implicit solvers (COMSOL, 2019). The *High frequency amplification factor* was set to 0.75, and a *relative tolerance* of 10^{-3} was used.

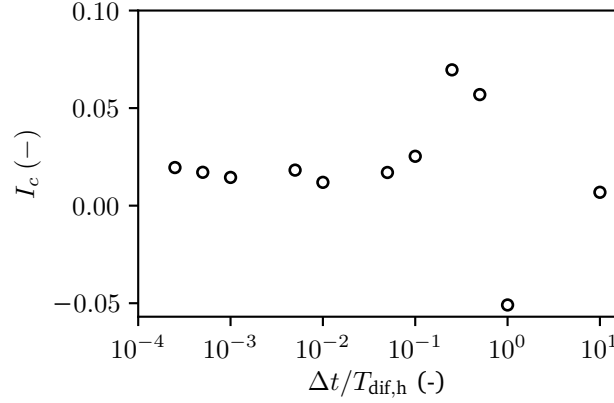


Figure 5.5: Convergence study of the time-stepping in the particle-tracking simulations. The mixing intensity (eq. 5.60) is evaluated after $t = 872.9 T_{\text{dif,h}}$. Reprinted with permission from Cambridge University Press, J. Fluid Mech. 925, 2021, Dehe et al. (2021b).

As a global measure for the convergence study, the mixing intensity is introduced as

$$I_c = 1 - \frac{\int |c(t) - c_{\text{avg}}| dV}{\int |c(0) - c_{\text{avg}}| dV}, \quad (5.60)$$

where c_{avg} represents the concentration averaged over the computational domain, and c the concentration at a specific location and time. At $I = 0$, the system is in its initial state, and at $I = 1$, the system exhibits a homogeneous concentration everywhere. In Fig. 5.5, the resulting mixing intensity is shown versus the maximum time step size. If the time step is on the order of the diffusive timescale $T_{\text{dif,h}}$, unphysical results are obtained, characterized by a strong oscillation and de-mixing. For decreasing time steps, the resulting mixing intensity converges to an asymptotic value, with no significant change for smaller time steps. As a final value for the time-step size $\Delta t = 2.5 \times 10^{-4} T_{\text{dif,h}}$ was chosen, assuring a sufficient time-resolution of the diffusion process.

Implementation of the 2D dispersion model

In order to utilize the two-dimensional reduced-order model, the fluid velocity has to be computed. The governing equations from section 4.3 are used for this purpose (eq. 4.24 and 4.25 for the stationary component, eq. 4.26 and eq. 4.27 for the oscillatory flow). Then, from the flow field solutions ($\nabla_{\parallel} \bar{p}$, $\nabla_{\parallel} p'$, $\bar{\mathbf{u}}_{\parallel}$, \mathbf{u}'_{\parallel}), the dispersion coefficients in the macrotransport equation can be obtained. The solutions are computed using *Comsol Multiphysics 5.5*.

In order to solve the flow equations, additional boundary conditions at the perimeter of the cell have to be defined. For the pressure, either a Dirichlet boundary condition is used ($p = p_0$), or a no-penetration boundary condition. The latter can be obtained from $\langle \mathbf{u}_{\parallel} \rangle \cdot \mathbf{n} = 0$, where \mathbf{n} defines the boundary normal vector. Then, by inserting eq. 4.20 the boundary condition reads

$$\mathbf{n} \cdot \left(-\frac{1}{12} \langle \mu^{\text{p}} \rangle \nabla_{\parallel} p + \langle \mu^{\text{EOF}} \rangle \mathbf{E}_{\parallel} \right) = 0. \quad (5.61)$$

If only no-penetration conditions are utilized, it is required to fix the pressure at one point such that the overall pressure scale is fixed. Furthermore, the in-built stabilization scheme (*consistent stabilization with streamline and crosswind diffusion*) is used for that purpose (COMSOL, 2019). The equations are solved using the *MUMPS* solver using a *relative tolerance* of 1×10^{-3} . Other numerical settings include

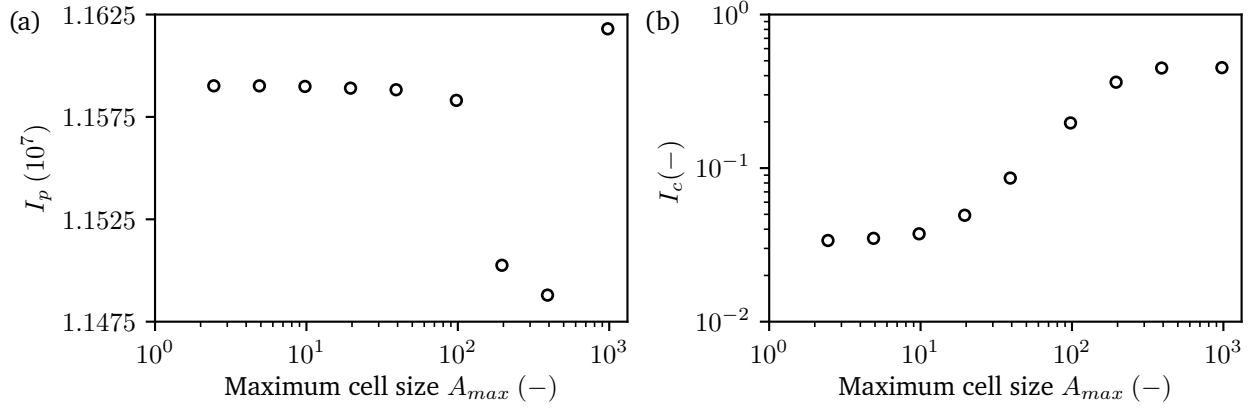


Figure 5.6: Convergence study of the maximum element size of the 2D model. (a) The global measure I_p (eq. 5.62) for the flow field convergence shows an asymptotic behavior for decreasing cell size. (b) The mixing intensity I_c (eq. 5.60) converges for small cell sizes at the final time step $t = 918 T_{\text{dif,h}}$. The second-finest mesh size was utilized in the final computations. Reprinted with permission from Cambridge University Press, J. Fluid Mech. 925, 2021, Dehe et al. (2021b).

the discretization of the variables, where the pressure is discretized using elements of quartic order to reach sufficient resolution at the level of individual cells. The domain is meshed using the automatic meshing function with triangular cells, with a restriction on the maximum cell size. The maximum cell size was determined using a convergence study, as presented below. The final mesh in test case C consists of 3138 cells with a *minimum element quality* of 0.666 and an *average element quality* of 0.9698.

From the determined velocity field, the coefficients of the macrotransport equation 5.43 are computed. Here, the stationary and oscillatory solutions **a** and **b** are computed via the respective governing equations (eq. 5.33 and eq. 5.34) based on the local flow field. The transport coefficients are then implemented into the advection-diffusion equation, solving for c . The concentration field was discretized using quadratic element functions. At the boundaries, either no-flux conditions ($\nabla_{\parallel} c \cdot \mathbf{n} = 0$) or Dirichlet-conditions ($c = c_0$) are prescribed. The time-evolution of the concentration field is solved on the same mesh as the flow field, and the convergence study is presented below. The initial conditions of the concentration are denoted in the respective test cases. For solving the transient advection-diffusion equation, the direct solver *MUMPS*, and the implicit time stepping solver *generalized alpha* are utilized. Here, the solver settings include the *amplification factor for high frequencies* as 0.75, the *relative tolerance* of 1×10^{-3} , and the maximum time step of $\Delta t_{\text{max}} = 23.5 T_{\text{dif,h}}$ of the *intermediate time stepping* method.

In order to ensure sufficient resolution of the problem, convergence studies for both the flow field as well as the concentration field with respect to the maximum cell size were performed. As shown in Fig. 5.6(a), the *maximum cell size* A_{max} was varied, and the convergence was assessed using an integral of the local pressure deviation from the mean, defined as

$$I_p = \int_A (p - p_{\text{avg}}) dA, \quad (5.62)$$

with p_{avg} denoting the average pressure in the Hele-Shaw cell, and A denoting the area of the 2D domain. Similarly, the convergence of the concentration field is analyzed, which is shown in Fig. 5.6(b). Here, the mixing intensity I_c is used to evaluate convergence, which is defined analogous to eq. 5.60. Both the flow equations as well as the concentration equation show convergence for small cell sizes, thus indicating that the cell sizes are sufficiently refined. In the following, the second-finest mesh resolution with a maximum cell size $A_{\text{max}} = 5$ was used.

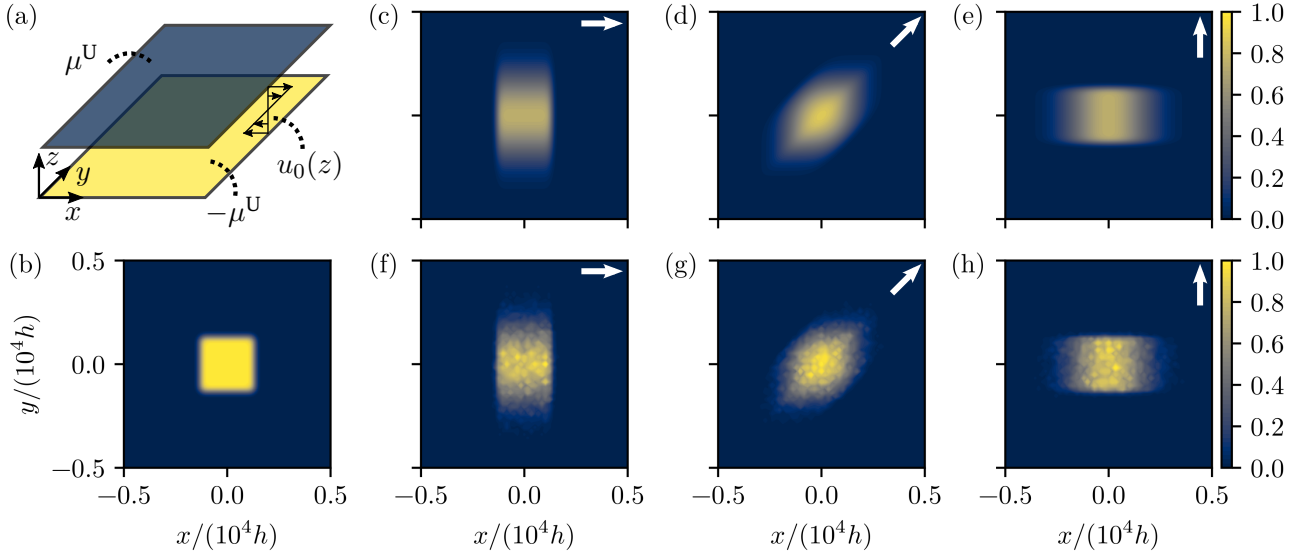


Figure 5.7: Test case A: Hydrodynamic dispersion inside a Hele-Shaw cell for a stationary flow field, as obtained using the 2D model (c-e) as well as the 3D particle tracking simulations (f-h). (a) A shear flow with zero height-averaged flow is created due to wall mobilities of similar magnitude, but varying sign in a Hele-Shaw configuration. (b) Initial distribution of the soluble species. (c-h) Resulting flow field for a simulation time of $t = 70.59 T_{\text{dif},h}$, with the direction of the electric field indicated in the top-right corner of each panel. Reprinted with permission from Cambridge University Press, *J. Fluid Mech.* 925, 2021, Dehe et al. (2021b).

5.4.2 Test case A: Dispersion in steady flow

The first test case concerns the stationary part of the transport model. Here, the distribution of an initial tracer distribution in a steady-state shear flow with vanishing average velocity is considered. The flow field is created by imposing constant wall mobilities of opposite signs at the bounding plates ($\mu^U = -\mu^L$), and no external pressure gradients, as indicated in Fig. 5.7(a). Due to the absence of a height-averaged flow velocity, solely the time-derivative of the concentration field as well as the dispersion tensor are left in eq. 5.43.

The simulation parameters are listed in Table 5.2. In the following, three variations are considered, with similar electric field magnitude, but changing direction, while maintaining the wall mobilities as well as the initial concentration distribution. Thereby, the off-diagonal components of the dispersion tensor can be probed. The initial concentration distribution is defined as a square shape with smoothed edges using the functional dependency

$$c_0(t=0) = \frac{1}{4} \left[1 + \operatorname{erf} \left(\frac{x - y_{\text{off}}}{L_{c,\text{ini}}} \right) \operatorname{erf} \left(\frac{-x - y_{\text{off}}}{L_{c,\text{ini}}} \right) \right] \left[1 + \operatorname{erf} \left(\frac{y - y_{\text{off}}}{L_{c,\text{ini}}} \right) \operatorname{erf} \left(\frac{-y - y_{\text{off}}}{L_{c,\text{ini}}} \right) \right], \quad (5.63)$$

where $\operatorname{erf}()$ denotes the error function.

In Fig. 5.7, the comparison between the reduced-order model (c-e) and the 3D particle simulations (f-h) are shown. The electric field direction is indicated in the upper right corner of each image. It is visible that the three-dimensional data is less smooth than the two-dimensional data. The concentration field is extracted using the method described in section 5.4.1 on a mesh of 60x60 cells. The initial concentration corresponds to 142 particles per cell. Despite the local inhomogeneities, it is not smoothed, in order to prevent artificial broadening of mixing zones. Qualitatively, the agreement between both models is

Table 5.2: Parameter values as used in test cases A and B (see Fig. 5.7 and Fig. 5.8).

parameter	description	value
h	cell height	$1 \times 10^{-4} \text{ m}$
L_0	cell edge length	$1 \times 10^4 h$
$ \mu^U \mathbf{E}_{\parallel} $	wall velocity	$5 \times 10^{-4} \text{ m s}^{-1}$
D	molecular diffusion coefficient	$1 \times 10^{-10} \text{ m}^2 \text{ s}^{-1}$
t_{final}	simulation time span	$70.59 T_{\text{dif,h}}$
$Pe = U_{\text{wall}} h / D$	Péclet number	500
N_p	number of particles	30, 976
y_{off}	initial distribution side length parameter	$1250 h$
$L_{c,\text{ini}}$	initial distribution transition region size parameter	$200 h$

evident, and the dispersion is enhanced in the direction of the electric field. In order to quantify the agreement between 2D and 3D data, the case of the electric field in the x -direction is used as an example (Fig. 5.7(c,f)) and the extend of the regions with non-zero concentration is compared. Therefore, the boundary of the distribution is defined as the value x_0 , for which $c(x_0) = 0.1$ is satisfied. For the 2D data, the size is denoted by $x_{0,2D}$, and for the 3D particle simulations by $x_{0,3D}$, respectively. Comparing both regions yields a relative error of the distribution size as $(x_{0,2D} - x_{0,3D})/x_{0,3D} = 7.4\%$, averaged over the central region ($|y| < 0.1$). Perpendicular to the electric field direction, the relative error yields 2.5%, averaged over the central region ($|x| < 0.1$). The enhanced transport due to dispersion in the direction of the electric field is reproduced by the 2D dispersion model, while similarly preserving concentration gradients perpendicular to the electric field direction. These results show that the stationary dispersion effects can be captured adequately using the reduced-order model.

5.4.3 Test case B: Dispersion in oscillatory flow

The second test case concerns the oscillatory part of the dispersion model. Here, a similar shear flow field as in test case A is utilized, with zero average flow velocity. However, the velocity is modified by a factor $\sin(2\pi ft)$, leading to a purely oscillatory flow field, as indicated in Fig. 5.8(a). Both the time-averaged velocity $\bar{\mathbf{u}}$ as well as the cross-stream averaged velocity $\langle \mathbf{u} \rangle$ vanish. Since the effect of the electric field direction on the dispersion tensor was analyzed in test case A, in this test case solely the influence of the oscillation frequency is analyzed, with the electric field directed in the x -direction in all cases.

At this point, it is instructive to point out some of the analogies between dispersion due to an oscillatory flow field and a stationary flow field. In the macroscale transport equation (eq. 5.43), for each stationary term, denoted as some function of the time averaged flow field \mathbf{u} and \mathbf{a} , an analogous term due to the oscillatory flow field exists, indicated as some function of the oscillatory flow field \mathbf{u}' and \mathbf{b} . It shows that dispersion is driven by inhomogeneities of the flow field, either occurring over z in a stationary flow field, or over both t and z for an oscillatory flow.

In order to determine the the transport coefficients in eq. 5.43, the boundary value problem for \mathbf{b} has to be solved (eq. 5.34). While obtaining a solution is more complex than for the analogous problem governing \mathbf{a} , as \mathbf{b} is time-dependent, it is straightforward and can be done numerically. In Fig. 5.9, the resulting dispersion coefficient $\langle \mathbf{u}' \mathbf{b} \rangle$ is shown for varying oscillation frequencies, non-dimensionalized by the diffusive time scale as $\hat{f} = f T_{\text{dif,h}}$. The dispersion coefficient shows a similar asymptotic behavior for small and large oscillatory frequencies, as reported previously (Chatwin, 1975; Chu et al., 2019; Vedel

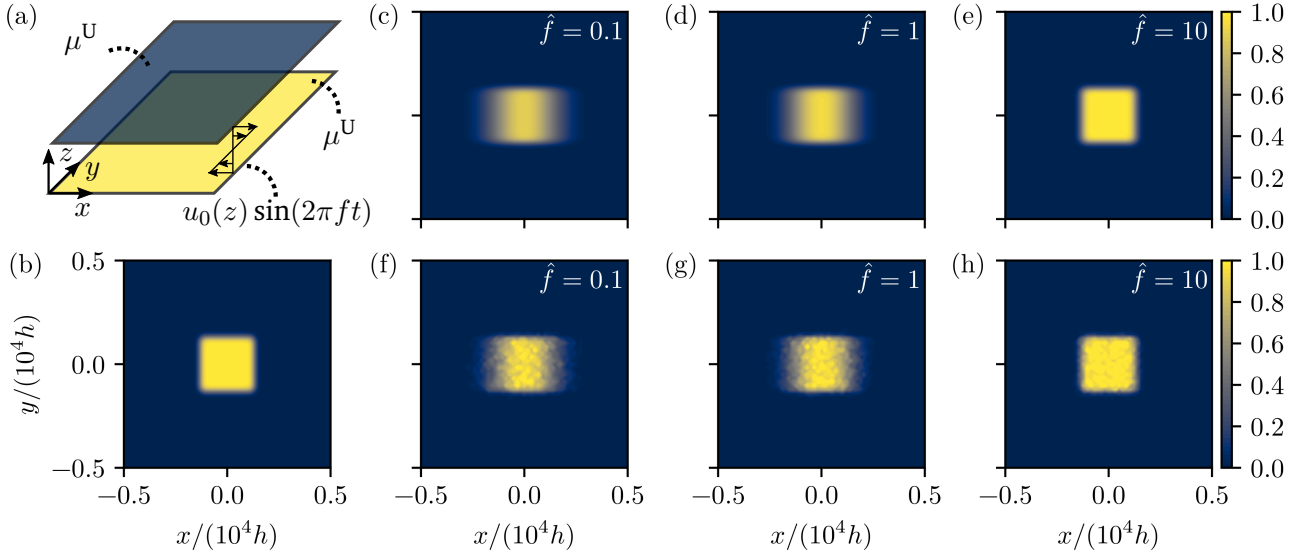


Figure 5.8: Test case B: Hydrodynamic dispersion inside a Hele-Shaw cell for an oscillatory flow field, as obtained using the 2D model (c-e) as well as the 3D particle tracking simulations (f-h). (a) A shear flow with vanishing height- and time-averaged flow is created due to wall mobilities of similar magnitude, but varying sign in a Hele-Shaw configuration, and an oscillatory driving field in the x -direction. (b) Initial distribution of the soluble species. (c-h) Resulting flow field for a simulation time of $t = 70.59 T_{\text{dif},h}$, with the non-dimensional oscillation frequency of the electric field $\hat{f} = f T_{\text{dif},h}$ indicated in the top-right corner of each panel. Reprinted with permission from Cambridge University Press, *J. Fluid Mech.* 925, 2021, Dehe et al. (2021b).

and Bruus, 2012). In case of slow oscillations ($\hat{f} \rightarrow 0$), the dispersion coefficient can be approximated by the dispersion coefficient obtained for stationary flow. It approaches half of the value obtained in test case A. Mathematically, this limit is determined by the integral over one period of oscillation of the product of two sine-functions, as both \mathbf{u}' and \mathbf{b} exhibit a functional form similar to the wall oscillations. Thus, the resulting numerical factor results in $1/2$. If a multitude of different frequencies would occur in the flow field, e.g., due to both oscillating wall mobilities as well as driving fields, the numerical pre-factor would differ from $1/2$. In case of fast oscillations ($\hat{f} \gg 1$), the dispersion coefficient asymptotically approaches zero. If the flow oscillations occur on timescales much faster than the diffusive time scale, the diffusion cannot react to the the flow oscillations.

In Fig. 5.8, the resulting concentration fields for three different oscillatory frequencies ($\hat{f} = 0.1, 1, 10$) are depicted, with the initial concentration corresponding to the concentration field described in test case A. With decreasing frequency, the dispersion increases, with the dispersion most pronounced at $\hat{f} = 0.1$. At $\hat{f} = 10$, it is on the same order as molecular diffusion, as can be seen from the size of the concentration distribution in x and y direction. In order to quantify the relative error between the two-dimensional and three-dimensional simulations, the same relative error as in test case A is utilized, characterizing the extend of the concentration distribution in x -direction. For $\hat{f} = 0.1$, the relative error results in 7.6%, for $\hat{f} = 1$ in 3.9%, and for $\hat{f} = 10$ in 7.9%, respectively. Similarly to test case A, the agreement between the reduced-order model and the three-dimensional simulations is good, apart from the local inhomogeneities of the particle simulations. The dispersion in the limiting cases of high and low oscillation frequencies as well as the intermediate region is reproduced adequately.

Apart from the agreement between the numerical approaches, additional physical interpretations can be drawn from the results. Two conditions have to be fulfilled, such that the dispersion due to oscillations can dominate: First, the amplitude of \mathbf{u}' has to exceed the steady-state component of a corresponding

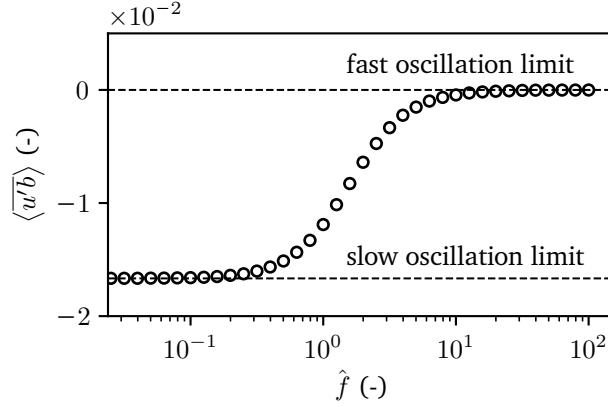


Figure 5.9: Test case B: Resulting non-zero entry of the dispersion matrix, shown for varying oscillation frequencies. In the limit of fast oscillations, the dispersion asymptotically approaches zero, and in the limit of slow oscillations, it approaches one half of the value obtained for a stationary flow field of same magnitude. Reprinted with permission from Cambridge University Press, *J. Fluid Mech.* 925, 2021, Dehe et al. (2021b).

stationary flow field. Additionally, the oscillation period has to be of the order of the diffusive time scale or larger. Otherwise, steady-state dispersion dominates.

5.4.4 Test case C: Dispersion in circulatory flow field

The third test case concerns the ability to model dispersion in a complex flow field. The research is motivated by the ability to reconfigure flow fields within a microfluidic platform, such that standard operations can be run consecutively by inducing different flow fields. Therefore, one specific fluidic operation is considered here, namely mixing. A fluidic domain is considered, where only one half is filled by a dissolved species ($y > 0$), and a rotational flow field is applied to mix the two regions. This procedure is inspired by the blinking-vortex principle (Aref, 1984), and an experimental demonstration will be given in section 5.5.1. However, due to computational constraints on the three-dimensional computations, only the initial phase distorting the lamella is computed. The numerical parameters of test case C are summarized in Table 5.3.

An overview over the fluidic domain, including the wall mobility, is given in Fig. 5.10(a,b). At the lower wall, two patches of non-zero wall mobility μ^L are given, which are antisymmetric with respect to the y -axis. The exact distribution is given as

$$\begin{aligned} \mu^L = & \mu_0 S(x/2, L_{\text{patch}} L_{\text{smooth},x}) S\left(y - \frac{L_{\text{patch}} - L_{\text{smooth},y}}{2}, L_{\text{patch}}, L_{\text{smooth},y}\right) \\ & - \mu_0 S(x/2, L_{\text{patch}}, L_{\text{smooth},x}) S\left(y + \frac{L_{\text{patch}} + L_{\text{smooth},y}}{2}, L_{\text{patch}}, L_{\text{smooth},y}\right), \end{aligned} \quad (5.64)$$

where S is a smoothed step function, defined as $S(x, L_{\text{patch}}, L_{\text{smooth}}) = H(x + L_{\text{patch}}/2, L_{\text{smooth}}) - H(x - L_{\text{patch}}/2, L_{\text{smooth}})$. Here, $H(x, d)$ is a smoothed Heaviside function with a continuous second derivative, implemented in *Comsol* as (COMSOL, 2019)

$$H(x, d) = \begin{cases} 0 & \text{if } x < -d \\ 0.5 + 0.9375 \frac{x}{d} - 0.625 \left(\frac{x}{d}\right)^3 + 0.1875 \left(\frac{x}{d}\right)^5 & \text{if } -d < x < d \\ 1 & \text{if } x > d. \end{cases} \quad (5.65)$$

Table 5.3: Numerical parameters utilized in test case C (see Fig. 5.10).

parameter	description	value
h	cell height	$1 \times 10^{-4} \text{ m}$
L	aspect ratio side length x -direction to channel height	$4.2 \times 10^4 h$
W	aspect ratio side length y -direction to channel height	$1.05 \times 10^4 h$
L_{smooth}	initial diffusion zone size	$5.5 \times 10^2 h$
$L_{\text{patch},x}$	size of the zeta-potential patch, x -direction	$11,000 h$
$L_{\text{patch},y}$	size of the zeta-potential patch, y -direction	$L_{\text{patch},x}/2$
$L_{\text{smooth},x}$	size of the smoothing zone patch, x -direction	$10,000 h$
$L_{\text{smooth},y}$	size of the smoothing zone patch, y -direction	$L_{\text{smooth},x}/2$
$ \mu^L \mathbf{E}_{\parallel} $	wall velocity	$5 \times 10^{-4} \text{ m s}^{-1}$
D	molecular diffusion coefficient	$1 \times 10^{-10} \text{ m}^2 \text{ s}^{-1}$
t_{final}	simulation time span	$917.67 T_{\text{dif},h}$
$Pe = U_{\text{wall}} h / D$	Péclet number	500
N_p	number of particles	239,769
$N_{\text{bins},x}$	number of bins, x -direction	200
$N_{\text{bins},y}$	number of bins, y -direction	50
$L_{c,\text{ini}}$	initial concentration distribution width	$550 h$

At the upper wall, the mobility is of opposite sign, with a magnitude of 0.75 ($\mu^U = -0.75\mu^L$) compared to the lower wall. The driving electric field is pointed into the x -direction, leading to an circulatory flow field. The streamlines are shown in Fig. 5.10(b). Differently to test cases A and B, the aspect ratio of the cell is now fixed to 4:1 in the x - y -plane. At the perimeter of the cell, the boundaries are assumed to be periodic in the y -direction, and no-penetration boundary conditions are assumed in the x -direction. The initial concentration of the soluble species is provided as

$$c_0(t = 0) = \frac{1}{2} + \frac{1}{2} \operatorname{erf} \left(\frac{y}{L_{c,\text{ini}}} \right). \quad (5.66)$$

Solving the governing equations of the flow and the transport coefficients in the macrotransport equation, the dispersion tensor components depicted in Fig. 5.10 are obtained. In x -direction, a strong enhancement of the dispersion is seen in the regions of non-zero wall mobility, as the shear flow is most pronounced in this region. Outside, molecular diffusion dominates. The off-axis components exhibit values smaller than molecular diffusion, thus having negligible effect on the concentration distribution. The dispersion tensor component in y -direction experiences a slight increase, as pressure gradients created by the wall mobility lead to the re-circulation. However, due to the small flow velocity magnitude, the dispersion is comparable to molecular diffusion.

In Fig. 5.11, the time evolution of the concentration field is depicted, computed using the three-dimensional particle simulations, the reduced-order transport model accounting for dispersion, and a 2D advection-diffusion equation, only accounting for molecular diffusion. The concentration fields are shown for three points in time. Considering the global structure of the concentration fields, all three approaches yield comparable results, with the lamella being deformed in the rotary flow field. This is due to the dominant effect of advection with the mean flow. However, certain differences between the concentration fields become apparent when considering the mixing regions between high-concentration and low-concentration regions. Initially, before the lamella enters the regions of large wall mobility, the mixing regions are nearly identical, since the dispersion is comparable to molecular diffusion. At later

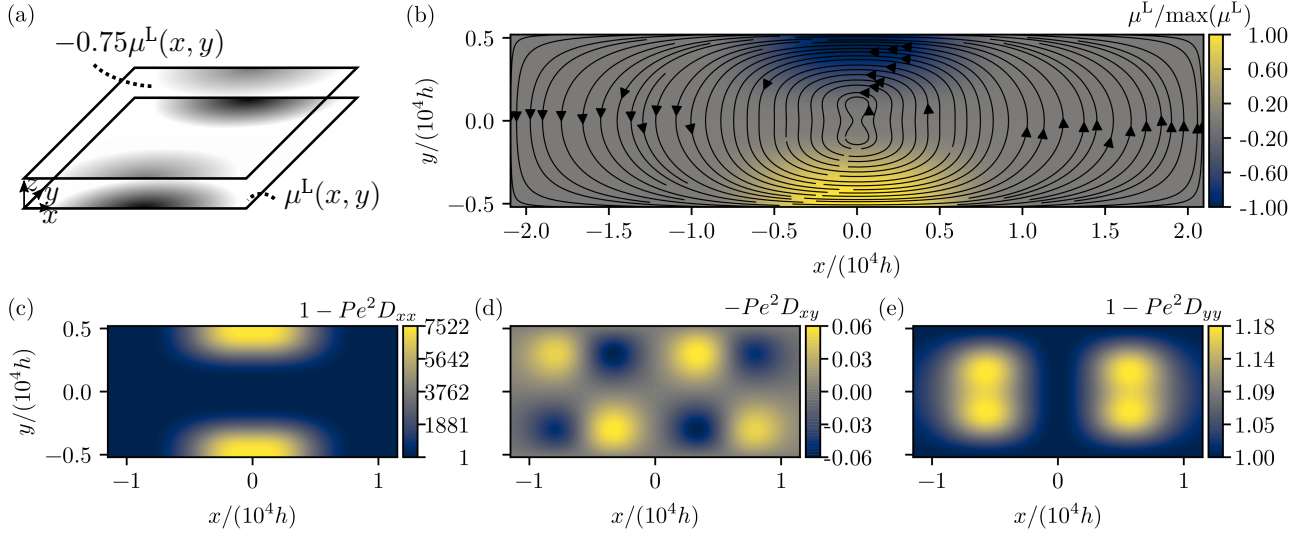


Figure 5.10: Test case C: Dispersion in a circulatory flow field. (a) The flow field is induced by a wall mobility distribution on the upper and the lower bounding plate, where the mobilities exhibit opposing signs. Additionally, the mobility at the upper plate has a magnitude of 75 % of the lower wall mobility. The electric field is directed into the x -direction. (b) Streamlines of the average flow velocity, resulting in a circulating flow field. The normalized wall mobility distribution is shown as the colormap. (c-e) Resulting dispersion tensor components. In x -direction, the dispersion is enhanced in the regions of the mobility patches, and in the y -direction, it is comparable to molecular diffusion. Reprinted with permission from Cambridge University Press, *J. Fluid Mech.* 925, 2021, Dehe et al. (2021b).

time steps, when the mixing regions passed the shear flow, the extend of the mixing region changes, with larger mixing regions in the models accounting for dispersion. At later times, the effect becomes more pronounced. In order to assess the ability of the reduced-order model to reproduce the growth of the mixing zones with time, the projected area of the mixing zones is computed for each time step. In order to prevent any errors due to the inhomogeneities present in the bulk of the particle simulations (visible in Fig. 5.11(d,g,j)) to enter this global measure, only mixing regions with comparatively small concentrations are considered ($0.1 < c < 0.5$). The area in the central region of the cell is evaluated, corresponding to the region shown in Fig. 5.11. For the time steps shown in Fig. 5.11, the macrotransport model overpredicts the dispersion, leading to an increase of the mixing zone regions of 6.1 %, 4.4 %, and 2.1 %, respectively. When only molecular diffusion is considered, the size of the mixing regions is underpredicted by 2.1 %, 23.6 %, and 26.9 %, respectively. For longer times, an even stronger deviation between the three-dimensional simulations and the reduced-order model is expected, as the deviations at initial times accumulate at later times. Overall, the effects of dispersion are represented more accurately by the model accounting for dispersion compared to the model accounting for molecular diffusion only, and good agreement is shown between the full simulations and the reduced order model.

To conclude this section, an exemplary flow field is used to compute the concentration development, where dispersion plays a crucial role. The flow within the same cell as before is considered, but with the wall mobility magnitude at the upper wall taking 95 % of the lower wall ($\mu^U = -0.95\mu^L$). Thereby, the averaged flow velocity is decreased, and the shear is increased. Due to restrictions on the existing hardware, only the results of the dispersion model and the advection-diffusion model accounting for molecular diffusion only could be computed. In Fig. 5.12(b-c), the resulting concentration fields after $t = 4693 T_{\text{dif,h}}$ are shown. As is prominently visible, the dispersion has a strong influence on the size of the mixing regions even after the first rotation. These results emphasize that modeling dispersion can be crucial in flow shaping applications. Also, the fact that the three-dimensional particle simulations

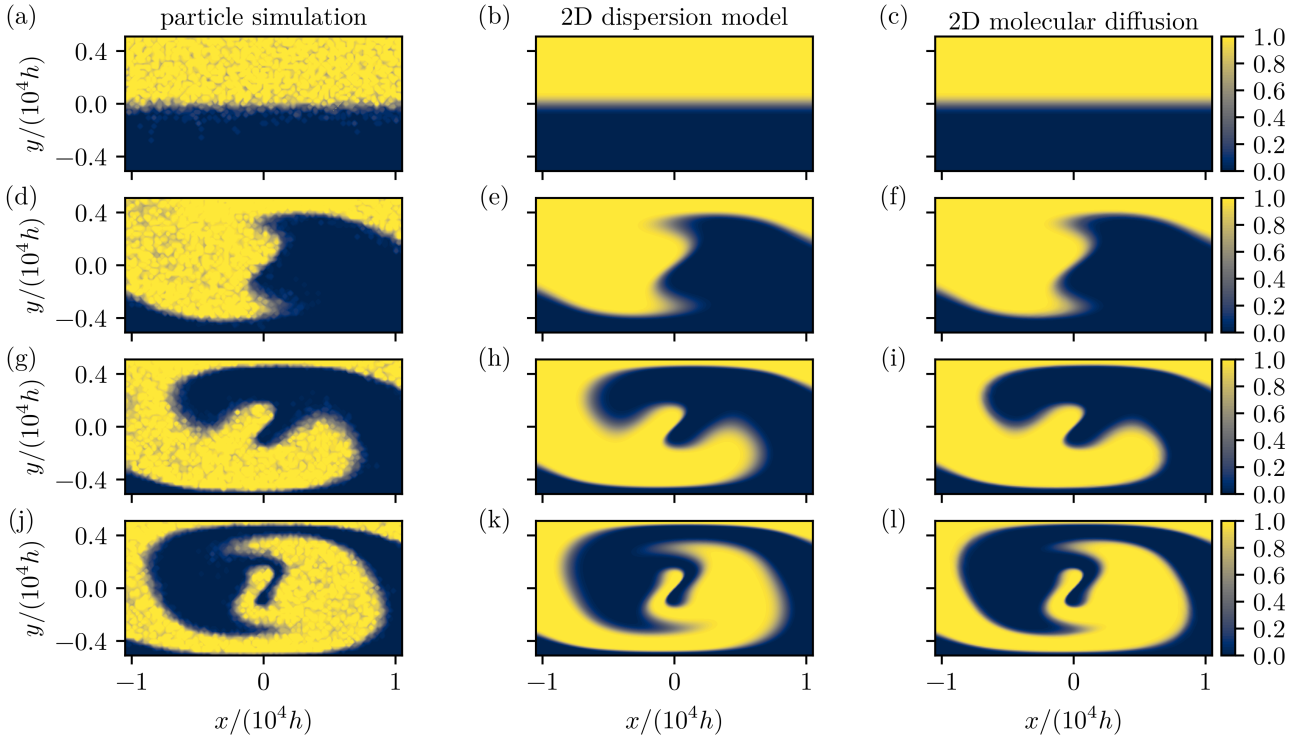


Figure 5.11: Test case C: Resulting concentration distributions as computed with 3D particle simulations (a,d,g,j), the 2D dispersion model (b,e,h,k) and purely 2D molecular diffusion (c,f,i,l). The concentration field is shown for the three time steps $t = 0 T_{\text{dif}}$ (a-c), $t = 306 T_{\text{dif}}$ (d-f), $t = 612 T_{\text{dif}}$ (g-i) and $t = 918 T_{\text{dif}}$ (j-l). Since advection dominates the species transport, the structure of the concentration field is the same in all three cases. Once the lamella passes the regions with enhanced dispersion, the size of the mixing zones, as obtained for molecular diffusion only, is smaller compared to the 3D simulations and the reduced order model. Reprinted with permission from Cambridge University Press, *J. Fluid Mech.* 925, 2021, Dehe et al. (2021b).

were too demanding to generate results in acceptable time scales outlines the necessity of accurate reduced-order models.

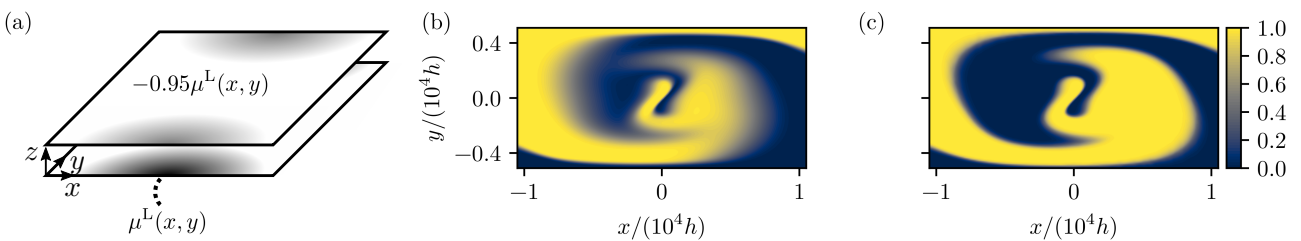


Figure 5.12: Variation of test case C with an upper wall mobility of $\mu^U = -0.95\mu^L$. The resulting concentration distribution as obtained from the dispersion model (b) and the molecular diffusion model (c) at $t = 4693 T_{\text{dif,h}}$. As is visible, dispersion can have a strong influence on the flow field. Reprinted with permission from Cambridge University Press, *J. Fluid Mech.* 925, 2021, Dehe et al. (2021b).

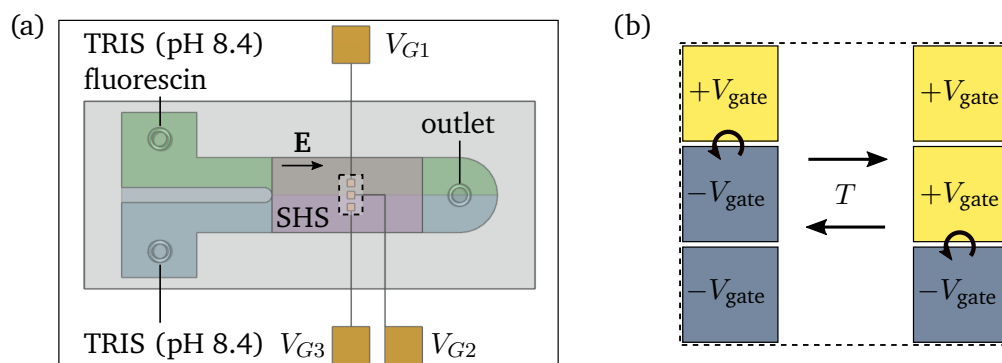


Figure 5.13: Experimental setup for the blinking vortex demonstration. (a) Layout of the microfluidic chip. A superhydrophobic surface (SHS) with side lengths $2\text{ cm} \times 1\text{ cm}$ is positioned above three gate electrodes that can be controlled individually. A fluidic lamella of different fluorescein concentrations is created by pressure-driven flow at the inlet. The driving electric field is applied by wire electrodes inside the reservoirs. Once the lamella is created, the pressure-driven flow is stopped, and the experiments are performed. (b) Control schematic of the gate electrodes. By changing the sign of the central gate electrode after each $T = 60\text{ s}$, the center of the circulatory flow field shifts, while maintaining the rotation direction. Both the driving field as well as the gate potentials are driven using a rectangular waveform with a frequency of 5 Hz .

5.5 Discussion

5.5.1 Experimental demonstration of the blinking vortex principle

In this section, an experimental demonstration of the mixing in a Hele-Shaw geometry is provided, in order to underline the ability to use flow shaping for fluidic mixing. It is important to note, however, that this section is not meant for quantitative assessment of the dispersion model.

In Fig. 5.13, a schematic of the experimental setup is depicted. A superhydrophobic surface (marked as SHS) of size $2\text{ cm} \times 1\text{ cm}$ with a pillar pitch of $p = 20\text{ }\mu\text{m}$ was placed at the bottom of a fluidic domain with height $h = 150\text{ }\mu\text{m}$. Two fluidic inlets were positioned upstream of the superhydrophobic surface, allowing to introduce two different liquids into the cell. Both streams were joined just before the superhydrophobic surface. By providing a pressure-driven flow to the cell, a fluidic lamella with a defined mixing region was provided. Downstream of the superhydrophobic surface, an outlet was placed at the center of the chip, in order to dispose of the excess liquid. Three gate electrodes ($1\text{ mm} \times 1\text{ mm}$ side lengths) were positioned at the center of the superhydrophobic surface, with individual contact pads allowing to control the gate voltage individually. At the inlet and outlet, the fluid was contacted electrically using platinum wire electrodes. At each inlet, a TRIS buffer (pH 8.4) of ionic strength 10 mmol L^{-1} was provided, where the liquid at one port additionally contained fluorescein with a molar concentration of 1 mmol L^{-1} . By imaging the fluorescent signal emitted from the liquid, the presence of the fluorescein was detected. In principle, from the signal intensity, the molar concentration of the tracer can be computed, but since no quantitative comparison to the theory is possible, only the raw experimental images are shown in the following.

The experiments were carried out as follows: First, the channel was filled with DI-water and the presence of a Cassie-Baxter wetting state was confirmed. Then, by using a syringe pump, the TRIS buffer solutions were pumped through the liquid domain, and thus a mixing region between the two streams was formed above the superhydrophobic surface. After creating a stable mixing region, the pressure-driven flow

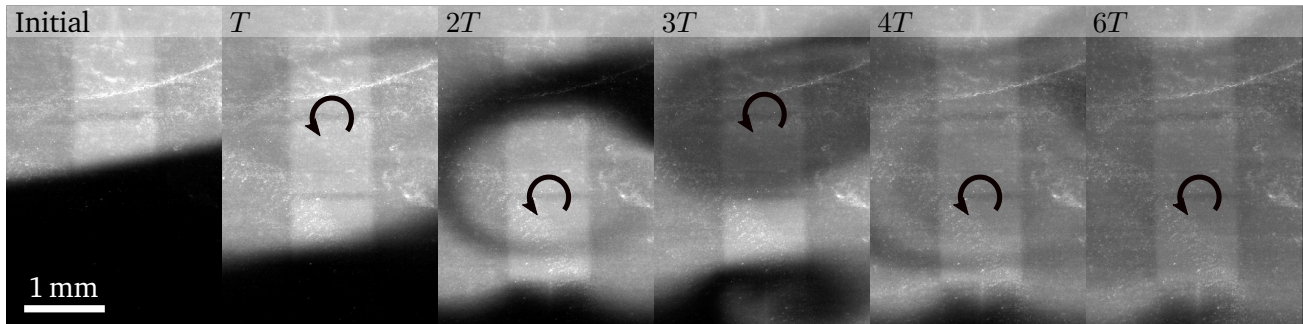


Figure 5.14: Experimentally obtained fluorescence images. The initially created lamella with a confined mixing region is deformed using a circulatory flow field. The depicted time steps are denoted in the upper left corner of each panel. The center of the past $T = 60$ s is denoted by the arrow. Over time, a homogeneous mixing region is achieved, occurring on timescales much shorter than molecular diffusion ($(3 \text{ mm})^2/D \approx 6.25 \text{ h}$).

was stopped, and electro-osmotic flow was induced above the electrodes using an AC driving field with amplitude 50 V cm^{-1} and a rectangular wave-form with a frequency of $f = 5 \text{ Hz}$, and a synchronized potential difference to the liquid with an amplitude of 250 V . As indicated in Fig. 5.13(b), the gate potentials of the outer electrodes had different signs, and the sign of the central electrode switched every $T = 60 \text{ s}$. Thereby, a circulatory flow field was induced, with variations of the vortex center. The development of the concentration distribution was imaged every 1 s .

In Fig. 5.14, the experimentally obtained fluorescent signals are presented at different times. The initial concentration distribution shows a clear distinction between both streams. However, as is evident, the lamella exhibits a rotation compared to the gate electrodes of approximately 10.5° . This is due to misalignment during the manufacturing process. During the assembly process, the PDMS cast of 5 cm length has to be bonded on top of the microscope slide with the electrodes, which resulted in a large number of defective chips either due to bubble enclosure, or leakage due to uneven bonding. For future implementations, the chip layout has to be redesigned to simplify alignment of the different layers and to yield reproducible results. Due to the misalignment, the electric field direction was rotated as well. Nevertheless, a rotational flow field was induced. The concentration fields after several time steps are presented, where the time is denoted at the upper corner. Also, the center of rotation for the past 60 s is shown by the arrow. As is visible, the blinking vortex principle leads to effective mixing in the central region of the chip over time.

While the experiments can be used to provide a proof-of-principle demonstration of the mixing procedure, they can not be compared to the macroscale dispersion model. Fluorescein exhibits a molecular diffusion constant of approximately $D = 0.4 \times 10^{-9} \text{ m}^2 \text{ s}^{-1}$ (Casalini et al., 2011), which leads in combination with the present channel height to a cross-stream diffusion time scale of 56.2 s . As discussed in section 5.2.1, the underlying assumption of Taylor-Aris dispersion is the ability of the soluble species to equilibrate over the cross-stream direction on time scales shorter than changes of the velocity occur. The condition $\Delta L \gg hU_0h/D$ is violated for the channel heights and velocities utilized in this section, as $\Delta L \gg 5 \text{ mm}$ for $U_0 = 100 \mu\text{m s}^{-1}$. If the channel height was reduced to $20 \mu\text{m}$, the condition would change to a more realistic $\Delta L \gg 100 \mu\text{m}$.

To summarize, the flow shaping using EOF over superhydrophobic surfaces is suitable for enhancing the mixing of a fluidic lamella. Compared to molecular diffusion ($(3 \text{ mm})^2/D \approx 6.25 \text{ h}$), mixing is achieved on much smaller time scales. While an experimental proof-of-principle is provided, future implementations face two challenges: First, the design of the fluidic domain has to allow for higher yield of usable channels, for example by fabricating stacked channels with smaller single pieces allowing for

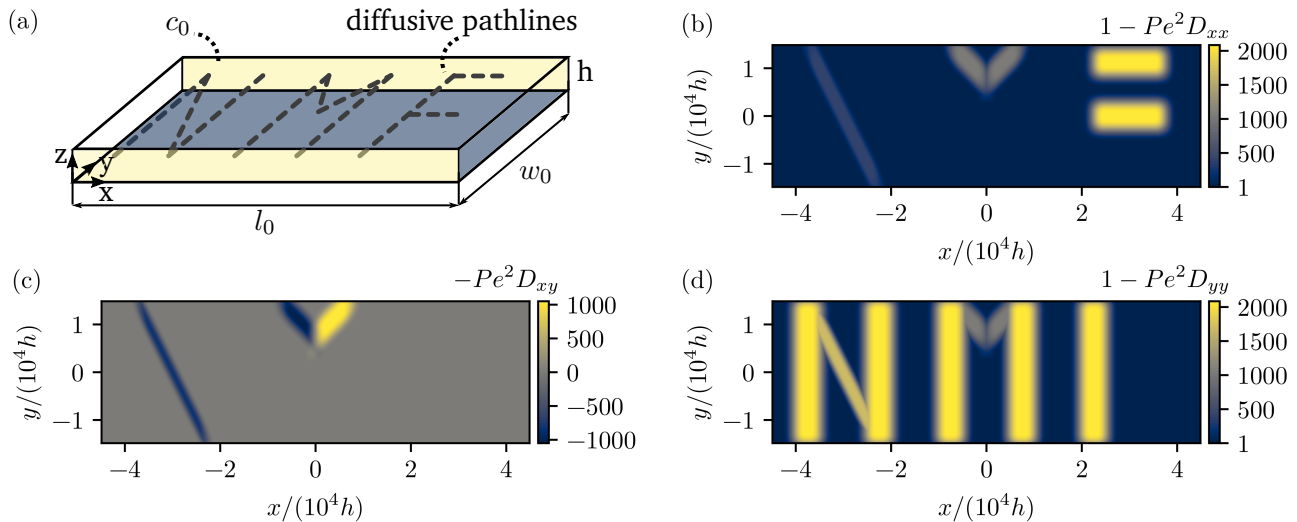


Figure 5.15: Dispersion shaping by flow fields used to enhance dispersion along defined pathlines. (a) Within a Hele-Shaw cell, the dispersion is enhanced along arbitrary pathlines, here forming the letters *NMF*. The effective diffusivity is much higher than in the surrounding liquid. (b-d) Components of the symmetric dispersion tensor ($D_{xy} = D_{yx}$).

better alignment. Second, it has to be verified that the underlying assumptions of the macrotransport equation are satisfied, if the mixing process should be computed using the reduced-order model. In this context, it might be instructive to investigate how local deviations of the flow field from the theoretical description, e.g., due to jumps in boundary conditions, propagate into the flow field and thus into the concentration field.

5.5.2 The inverse problem: Dispersion shaping

In the main part of this chapter, the dispersion of a soluble species in a given flow field was considered. For some problems, however, the inverse problem can be of interest: Instead of shaping the flow and computing the resulting dispersion, a desired dispersion field can be created by providing the required flow field. For example, a wide variety of applications require stable concentration gradients, which can be created by connecting two reservoirs of different concentrations by a region of strong effective diffusivity, e.g., in the context of migration of organisms due to chemical stimuli (chemotaxis) (Diao et al., 2006; Li and Lin, 2011). In this section, the outline of a specific solution methodology for this class of problems is provided, jointly with a discussion of general solutions of the problem.

In order to generate a required spatial distribution of the dispersion tensor $\mathbf{D} = (D_{xx}, D_{xy}; D_{yx}, D_{yy})$ as a function of both space and time, it is important to remember that dispersion can be created either by stationary or oscillatory flow fields. Both effects are additive, as follows from the macrotransport equation 5.43. As given by the definition of the transport coefficients, various flow fields can lead to the same dispersion tensor, which requires the introduction of additional constraints. Usually, these constraints are posed by the level of control over the magnitude, frequency and shape of driving electric field and wall mobilities. Additionally, a cost function can be introduced, for example minimizing the energy input. In the following, the problem will be vastly simplified by assuming that the upper and lower wall mobilities exhibit locally the same magnitude, but different signs. Then, no average flow field will be introduced, and only a local shear flow will be present. While this simplification is convenient for

Table 5.4: Parameters utilized in the calculations of the dispersion shaping, as indicated in Fig. 5.15.

parameter	description	value
h	cell height	1×10^{-4} m
L_x	cell side length x -direction	9×10^4 h
L_y	cell side length y -direction	3×10^4 h
d_{path}	path width	7500 h
$d_{\text{transition}}$	path transition zone	5000 h
$u_{\text{wall}} = \mu_0^{\text{U}} E_0$	reference wall velocity	500 m s^{-1}
D	molecular diffusion coefficient	$1 \times 10^{-10} \text{ m}^2 \text{ s}^{-1}$
t_{final}	simulation duration	$44 \times 10^3 T_{\text{dif,h}}$
$Pe = u_{\text{wall}} h / D$	Péclet number	500

the following treatment of the problem, such a large amount of control over the flow field is rare, as it requires for example gate electrodes at both bounding plates.

To outline the concept of shaping dispersion, a flow cell is considered in the following, with enhanced dispersion along arbitrary pathlines. A schematic is shown in Fig. 5.15. Here, the pathlines form the three letters *NMF*, but other configurations can be considered accordingly. Outside of these pathlines, the dispersion is supposed to vanish, with only molecular diffusion acting on the soluble species. By defining Dirichlet wall conditions at the bounding walls in y -direction, corresponding to infinite reservoirs, the concentration tracer is transported by an effective diffusion along the defined pathlines. At the center lines of the paths, the dispersion is set to correspond to a shear flow between two plates, with a velocity of $125 \mu\text{m s}^{-1}$ at the upper and the lower plate pointing in opposite directions. The transport is supposed to be enhanced along the pathlines, and perpendicular to the paths, no enhanced transport should occur. The width of the regions around the center lines is defined as a smoothed step function $S(x, d_{\text{path}}, d_{\text{transition}})$, as defined in eq. 5.64 and eq. 5.65. In Table 5.4, the numerical parameters utilized within the model are depicted. The corresponding dispersion tensor components are shown in Fig. 5.15(b-d).

The required dispersion tensor field can be created using only local shear flow, if any wall mobility fields $\mu^{\text{U}}(x, y, t)$, $\mu^{\text{L}}(x, y, t)$ can be applied at the upper and the lower wall, and if the direction of the driving electric field can be controlled arbitrarily. One specific strategy to obtain the desired dispersion field is to vary the electric field direction periodically in time. In the following, the electric field direction is adjusted such that it points into the directions $(1, 0)$, $(0, 1)$, $(1, 1)$, or $(1, -1)$ over one quarter of the oscillation period. In addition, a time-periodic square wave $h(t)$, oscillating between 1 and -1 , is applied on the electric field direction, with a period length of $T_{\text{osc}}/4$. As a result, the electric field points into the direction $(1, 0)$ between $t = 0$ and $t = 1/8 T_{\text{osc}}$, into the direction $(-1, 0)$ between $t = 1/8 T_{\text{osc}}$ and $t = 2/8 T_{\text{osc}}$, and analogously for the following time-intervals. Then, the resulting flow field takes the form

$$\mathbf{u} = \begin{cases} (2z - 1) \mu_1^{\text{U}} E_0 h(t) \mathbf{e}_x & \text{for } 0 \leq t < \frac{1}{4} T_{\text{osc}} \\ (2z - 1) \mu_2^{\text{U}} E_0 h(t) \mathbf{e}_y & \text{for } \frac{1}{4} T_{\text{osc}} \leq t < \frac{2}{4} T_{\text{osc}} \\ (2z - 1) \mu_3^{\text{U}} E_0 h(t) \left(\frac{1}{\sqrt{2}} \mathbf{e}_x + \frac{1}{\sqrt{2}} \mathbf{e}_y \right) & \text{for } \frac{2}{4} T_{\text{osc}} \leq t < \frac{3}{4} T_{\text{osc}} \\ (2z - 1) \mu_4^{\text{U}} E_0 h(t) \left(\frac{1}{\sqrt{2}} \mathbf{e}_x - \frac{1}{\sqrt{2}} \mathbf{e}_y \right) & \text{for } \frac{3}{4} T_{\text{osc}} \leq t < T_{\text{osc}}. \end{cases} \quad (5.67)$$

Here, $\mu_i^{\text{U}}(x, y)$ denotes the local wall mobility at the upper wall during the four sub-intervals and E_0 the electric field magnitude. Basically, the problem is divided into four sub-problems, each with a time

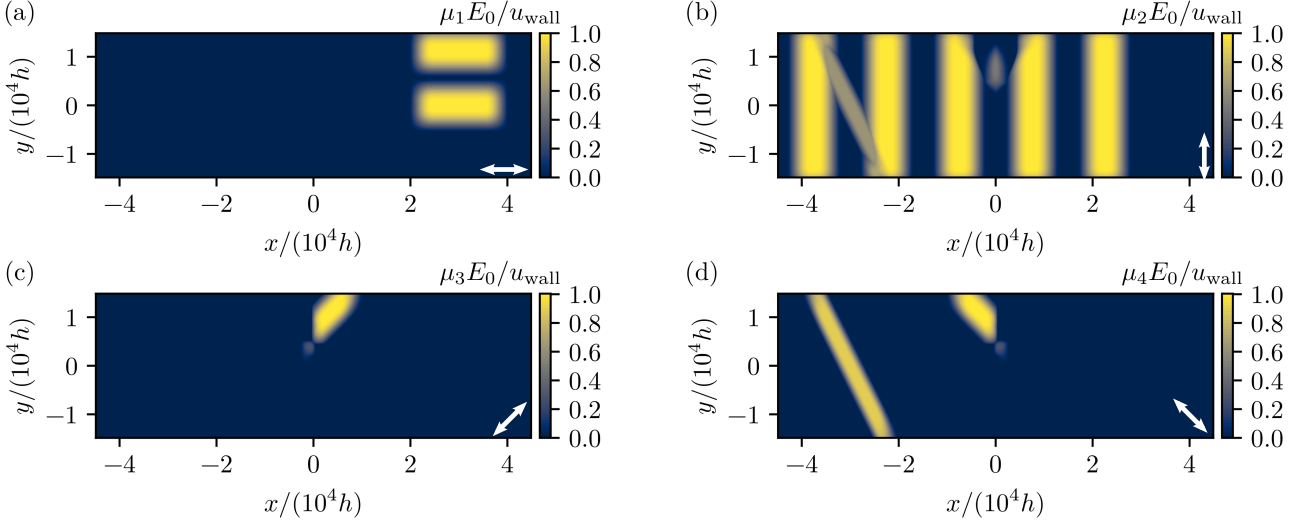


Figure 5.16: Wall mobilities required to create the dispersion tensor fields shown in Fig. 5.15, during each of the time-intervals $i = 1, \dots, 4$. The directions of the electric field during the time-interval i is indicated in the lower right corner of each panel. The upper and lower wall mobility have the same spatial distribution, but opposing signs.

length of $T_{\text{osc}}/4$, contributing to the effective time-averaged dispersion. In the following, the appropriate choice of $\mu_i^{\text{U}}(x, y)$ leads to the desired dispersion field.

The defining problem 5.34 for \mathbf{b} decomposes into four sub-problems, with both the height-averaged and the time-averaged flow field vanishing. Under the assumption that the flow field adjusts immediately to the driving electric field, the time-derivative in eq. 5.34 becomes negligible, and the problem is quasistatic. During each of the intervals $i = 1, \dots, 4$, the flow field induces the dispersion of a shear-flow in different directions, and the resulting dispersion tensor follows as the time-average of each of the subproblems. For example, the component D_{xx} is computed as

$$\langle \overline{u'b_x} \rangle = \frac{1}{4} \left(\left\langle \int_0^{\frac{1}{4}T_{\text{osc}}} u'b_x dt_0 \right\rangle + \left\langle \int_{\frac{1}{4}T_{\text{osc}}}^{\frac{2}{4}T_{\text{osc}}} u'b_x dt_0 \right\rangle + \left\langle \int_{\frac{2}{4}T_{\text{osc}}}^{\frac{3}{4}T_{\text{osc}}} u'b_x dt_0 \right\rangle + \left\langle \int_{\frac{3}{4}T_{\text{osc}}}^{T_{\text{osc}}} u'b_x dt_0 \right\rangle \right), \quad (5.68)$$

and the other components of the dispersion tensor follow analogously. For the given flow field (eq. 5.67), the expressions of the dispersion tensor result in

$$D_{xx} = \frac{1}{120} \left((\mu_1^{\text{U}} E_0)^2 + \frac{1}{2} (\mu_3^{\text{U}} E_0)^2 + \frac{1}{2} (\mu_4^{\text{U}} E_0)^2 \right), \quad (5.69a)$$

$$D_{xy} = D_{yx} = \frac{1}{120} \left(\frac{1}{2} (\mu_3^{\text{U}} E_0)^2 - \frac{1}{2} (\mu_4^{\text{U}} E_0)^2 \right), \quad (5.69b)$$

$$D_{yy} = \frac{1}{120} \left((\mu_2^{\text{U}} E_0)^2 + \frac{1}{2} (\mu_3^{\text{U}} E_0)^2 + \frac{1}{2} (\mu_4^{\text{U}} E_0)^2 \right). \quad (5.69c)$$

Now it becomes clear that a wide class of symmetric dispersion field can be created using the outlined principle. The off-diagonal components are adjusted during intervals $i = 3, 4$ and the diagonal elements are then adjusted using the wall mobilities during $i = 1, 2$. With the right parametrization of $\mu_i^{\text{U}}(x, y)$, arbitrary symmetric dispersion tensors can be defined, with dispersion coefficients larger than molecular diffusion, where the off-axis components can either be positive or negative.

Following the parametrization of the wall mobilities outlined above, equations 5.69 lead to wall mobilities as provided in Fig. 5.16. In the lower right corner of each image, the directions of the electric field are

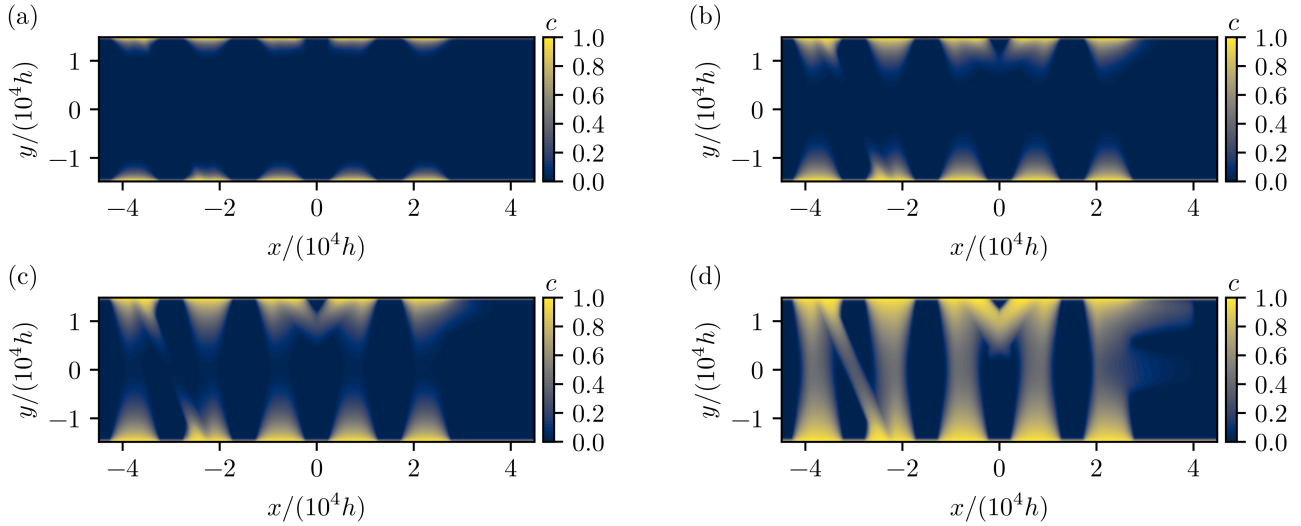


Figure 5.17: Resulting concentration fields created by the dispersion shaping outlined in Fig. 5.15 for the time steps $t/T_{\text{dif},h} = 1 \times 10^3, 5 \times 10^3, 1 \times 10^4, 4 \times 10^4$. The bounding walls in y -direction are connected to reservoirs of concentration $c = 1$. Along the pathlines, transport is enhanced, and outside, molecular diffusion leads to a much smaller concentration change.

indicated during the respective time interval. As is visible for Fig. 5.16(a,b), the pathlines in the direction of the axes require wall mobilities during the time intervals $i = 1, 2$. For the pathlines in directions other than the principal axis, wall mobilities during the intervals $i = 3, 4$ follow accordingly.

The resulting concentration field is depicted in Fig. 5.17 for different time steps, where the bounding walls in the y -direction are connected to infinite reservoirs ($c = 1$). The concentration of the soluble is confined to regions around the paths, and become more uniform with increasing times. While the dispersion field distribution demonstrated here is not motivated physically, it underlines that the dispersion can be controlled using the fluid flow, given that the degree of control over the flow field is sufficient.

In the example above, it was assumed that the wall mobility as well as the electric field direction can be controlled arbitrarily. In real-world applications, this is usually not the case. For example, gate electrodes exhibit a finite size, with usually a uniform gate potential. Thus, the wall mobilities are usually discretized in space. Also, it is uncommon that both wall mobilities can be controlled, since often an optical access into the fluidic domain is required. Then, the outlined methodology has to be adapted, by solving both for the flow field and the dispersion field, incorporating the underlying constraints placed on wall mobilities and electric field. Especially if the pressure is non-uniform and flow fields emerge, advective transport has to be accounted for. However, analyzing these more complicated cases is beyond the scope of this work and requires additional modeling effort and optimization strategies. Nevertheless, this section outlines the potential of shaping the dispersion by flow fields. For an implementation, it is conceivable to replace the upper bounding plate by a permeable membrane or hydrogel, with a second domain of interest positioned above. Then, the Hele-Shaw cell can be used to generate spatial and temporal distributions of concentrations, which are diffusing in the upper domain, in which for example cell culture experiments can be run. Then, one can provide concentration gradients in the x - y -direction in the upper domain without the cells being exposed to flow and electric fields. A large variety of experiments are conceivable that involve spatial concentration gradients, which are not easily implemented otherwise, such as the migration of microorganisms in temporally changing concentration fields, as well as the reactions of cell growth to temporally changing concentration gradients.

5.6 Summary and conclusion

In this chapter, the transport of a soluble species in a electro-osmotically driven Hele-Shaw cell was studied, with focus on the sample dispersion. Starting with an overview over previous work on dispersion, the principle mechanism of shear-enhanced dispersion in stationary and oscillatory flow fields was introduced. Then, a height-averaged species transport equation was derived, accounting both for stationary and oscillatory flow fields, using a multiple-scale perturbation approach. Here, the time- and cross-stream average of the transport problem is obtained, and the species transport processes in the cross-channel direction are incorporated into effective transport coefficients. The resulting dispersion tensor exhibits only positive eigenvalues and is thus thermodynamically consistent. Next, a comparison between numerical simulations using a full three-dimensional model with a particle tracking method and the reduced-order macrotransport equation was performed, showing good agreement between both approaches in three test cases, considering stationary, oscillatory and circulatory flow. Also, an experimental demonstration of a microfluidic mixer was presented in order to emphasize that flow shaping enables standard microfluidic operations involving mass transport. Lastly, the inverse problem of shaping dispersion using flow fields was discussed, showing that depending on the level of control over the wall boundary conditions, arbitrary path lines of high dispersion can be embedded in an otherwise low dispersion region, mimicking species transport in biological systems.

The derived reduced-order model supplements the existing framework of flow-shaping with an appropriate species transport model. Therefore, it provides the required tool to design bio-chemical processes in Hele-Shaw cells. By reducing the problem to an equivalent two-dimensional problem, the computational costs associated with transient computations in complex flow fields is significantly reduced, enabling the study of complex transport processes with widely-available hardware. Furthermore, the influence of sample dispersion can be systematically studied using the reduced-order model, since the contributions due to stationary and oscillatory flow fields follow accordingly. Thereby, it allows to determine in which conditions dispersion is of importance, and when it might be negligible.

In future work, a more general description of the solution mechanism for the dispersion shaping is desirable, specifically considering the situation of non-vanishing height-averaged flow fields. Also, a comparison to experiments is feasible and should be pursued. And finally, a systematic assessment of the influence of non-idealities in the flow would be beneficial, e.g. with the flow field locally violating the underlying assumption of small changes in the lateral direction. While the deviations in the flow field is usually confined to small regions around such a jump in boundary conditions, the concentration field exhibits an inherent memory-effect. Small deviations of concentration fields at early times can lead to large differences with increasing times, and the extend of this deviation might be interesting to characterize. Also, mitigation strategies could be explored, such as active feedback of the concentration field into the theoretical modeling, with an in-situ control of the flow.

6 Instabilities at liquid-liquid interfaces under homogeneous AC fields

In the previous chapters, the influence of electric fields on gas-liquid interfaces, which were stabilized by a surface microstructure, were explored. In this chapter, the instability of a liquid-liquid interface actuated by a spatially homogeneous, but harmonically oscillating electric field is investigated, representing the analogy to the mechanically actuated Faraday instability. Using high-speed imaging in combination with an algorithm to evaluate refraction at the liquid-liquid interface, the dominant instability wavelengths and modes are extracted, and the influence of the liquid viscosity on both the onset voltage as well as instability wavelength is investigated. The experimentally obtained interfacial wavelengths show good agreement to theoretical predictions. In addition, the instability shows either boundary-independent patterns or discrete modes of the surface harmonics, depending on the boundary influence of the circular domain.

The work presented in this chapter was funded by the German Research Foundation (DFG, Grant No. HA 2696/45-1). An initial version of the experimental setup was built by Julian Keller as part of his Bachelor's thesis, supported by Jörg Bültemann (Keller, 2020). Distinct contributions of the author of the present work include the adaptation of the experimental cell to facilitate optical access from the bottom, the implementation of the refraction-based surface reconstruction algorithm and the wavelength extraction from the experimental data based on Fourier power spectra. The instability experiments were performed jointly with Maximilian Hartmann. The liquid properties presented in section 6.3.4 were measured by Maximilian Hartmann. The theoretical predictions used for comparison are based on the work by Bandopadhyay and Hardt (2017), with modifications provided in private communication by Aditya Bandopadhyay. In his function as supervisor, Steffen Hardt provided valuable input during the whole process of this project. The main body of this work is considered for publication (Dehe et al., 2021a).

6.1 Introduction

Resonance can lead to the formation of various patterns at the interface of liquid films when deposited on a vibrating Chladni plate, which has been systematically investigated by Faraday (1831). In order to visualize the patterns, Faraday used various methods such as adding particles to the liquid, observing light reflections from various incident angles, as well as observing the light adsorption of a dyed liquid as a measure of the local film thickness. In his investigation with various liquids, the typical wavelength of the pattern (or *crispations* as Faraday describes them) exhibits a dependency on both the vibration frequency as well as amplitude, and Faraday reported the interface to oscillate with half the driving frequency of the excitation. Later on, this result was strongly opposed by Matthiessen (1868, 1870), who reported interface oscillations isochronous with the actuation frequency. The different observations lead Lord Rayleigh (1883) to reproduce the original experiments of Faraday and by utilizing several techniques, including stroboscopic observation, determined the interface to oscillate with half the driving

frequency. An theoretical explanation for the different observations was provided by the description of Benjamin and Ursell (1954), who showed that the instability of an ideal fluidic layer under harmonic oscillation results in a Mathieu's equation, which will be discussed in section 6.2.1. The stability analysis of the equation shows that oscillations isochronous with the forcing frequency (harmonic response) or with half the forcing frequency (subharmonic) are observed, depending on the forcing parameter. However, utilizing this inviscid theory, unstable wavenumbers exist even at negligible forcing amplitudes, contradicting physical observations. Including the effects of viscosity in the stability analysis, Kumar and Tuckerman (1994) showed that finite forcing amplitudes are required to trigger an instability, and with increasing viscosity, the onset amplitude shifts to higher values. Both the critical forcing amplitude as well as the dominant pattern wavelength showed good agreement to experimental observations.

Similar to mechanical forcing, the Maxwell stress due to electric fields can lead to a deformation and ultimately disintegration of a fluidic interface. An interface between a dielectric and a conducting liquid exposed to a spatially uniform, but harmonically oscillating electric field poses the electrostatic analogy to the mechanically induced Faraday instability (Yih, 1968). Similarly to the work by Benjamin and Ursell, the stability analysis of ideal fluids results in a Mathieu's equation, with the difference that the base-frequency is double the frequency of the applied AC field, as the Maxwell stress at the interface is proportional to the electric field squared. Thus, the interface oscillations occur either isochronous or with double the driving frequency of the applied forcing. Other types of electrohydrodynamic (EHD) instabilities due to electric fields acting on interfaces were heavily researched in the past decades. For example, Taylor and McEwan (1965) investigated the response of a fluidic interface to a normal, time-constant electric field, and Briskman and Shaidurov (1968) analyzed the parametric forcing in an AC field. Other research involving electric fields and interfacial flows were studied by Melcher (1966) in the context of traveling waves, tangential electric fields (Melcher and Schwarz, 1968) and the formation of liquid columns between conducting lines due to electric fields (Jones and Melcher, 1973). Technically, the resonant actuation inside a container was exploited by Iino et al. (1985), who used electrical actuation to excite resonant waves in a circular domain for determining the surface tension of liquid helium. Other technical investigations include the work of Robinson et al. (2000, 2001, 2002), who analyzed actuation of a fluidic layer in an AC field within an ozone generator. Furthermore, a thin liquid film can form pillaring instabilities upon DC actuation, and Roberts and Kumar (2009) used a superposed AC field to control the resulting pillar size and spacing. Recent research involved the instability of a dielectric-dielectric interface (Gambhire and Thaokar, 2010), conductivity effects therein (Gambhire and Thaokar, 2012), and Debye-layer effects at a dielectric-conductor interface (Gambhire and Thaokar, 2014). The saturation of electrostatically actuated Faraday instabilities to finite instability amplitudes due to nonlinear effects was studied by Pillai and Narayanan (2018) at a dielectric-conductor interface in the long-wavelength limit.

Despite the extensive research effort in the past decades on electrically induced instabilities, only recently two extensions to the theory of Yih (1968) were provided to account for viscosity, similar to the extension of Kumar and Tuckerman (1994) to the original work of Benjamin and Ursell (1954). The first work by Bandopadhyay and Hardt (2017) considered the interface between a perfect dielectric and a perfectly conducting fluid theoretically, studying the stability curve which relates the critical voltage and instability wavenumber for a given actuation signal. For the electric fields, both single frequency harmonic actuation as well as the superposition of multiple harmonic signals of varying driving frequency were studied. A second work extended the model by replacing the assumptions of a perfect-dielectric and perfect-conductor using the leaky dielectric model (Ward et al., 2019). The results of Bandopadhyay and Hardt (2017) were reproduced when the conductivities of both liquids showed a sufficiently high contrast. Additionally to the theoretical considerations, the onset voltage of the instability for varying driving frequencies was measured for two test cases. While the onset voltage showed good agreement to theory, the instability wavelengths could not be measured, due to the observation mode from the side through a

curved glass cylinder. However, Ward et al. made two notions with respect to the wavelengths: First, they noted that the fluidic domain was sufficiently sized to act as an unbound domain (diameter of 127 mm for an upper fluidic layer of ≈ 5 mm) such that no discrete modes were obtained during the experiments. Second, they noted that a multitude of wavelengths emerged for all unstable driving amplitudes and frequencies. These two observations are of importance for this chapter, and will be further studied. Especially the second observation warrants additional exploration, as for mechanically actuated Faraday instabilities, usually one dominant wavelength is observed (see section 6.2.1). Therefore, in this chapter, an extension of the experimental exploration of electrostatically actuated Faraday instabilities is provided, with specific focus on the emerging wavelengths and spatial structure of the instability.

In the previous chapter, the influence of normal and tangential electric fields on gas-liquid interfaces, which were stabilized by a surface microstructure, were explored. In this chapter, the electrostatically induced instability at a liquid-liquid interface without a specific support is studied, posing the electrostatic analogy to the mechanically induced Faraday instability. Specifically, the following questions are addressed: How can the instability pattern be measured and the dominant wavelength be extracted? Can the instability be described using the perfect-dielectric / perfect-conductor model or are conductivity effects in the dielectric of importance (leaky dielectric model)? How well does the theoretical description fit the experimentally observed interfacial wavelengths? And what spatial structure does the instability exhibit? Therefore, the remainder of the chapter is organized as follows: In section 6.2, the general principle and relevant phenomena of the Faraday instability and its characterization are introduced with a literature overview over the relevant effects. Also, a short summary of the theoretical approach by Bandopadhyay and Hardt (2017) is provided as a background for the remaining work. In section 6.3, the experimental setup and surface reconstruction algorithm are introduced. In section 6.4, the resulting critical voltages and pattern wavelengths are presented upon variation of the salt concentration as well as the liquid viscosities. Also, the spatial structure of the instability is examined. In section 6.5, the results are briefly discussed, and section 6.6 provides a summary.

6.2 Fundamentals

6.2.1 Faraday instability

The Faraday instability describes the resonant response of a fluidic interface to oscillatory excitation. Originally, it was described for mechanically actuated films at a gas-liquid interface. However, it can be viewed as the specific case of the interface between two fluidic layers, in which the upper layer is composed of gas. In Fig. 6.1, three systems exhibiting Faraday instabilities are depicted. In Fig. 6.1(a), the electrostatically actuated Faraday instability is visible. An interface between a conducting liquid and a dielectric liquid is actuated by a harmonically oscillating electric field by applying an oscillating potential between the upper and the lower electrode. Similarly, in a closed container, which is vibrated vertically, an instability can be triggered at the liquid-liquid interface (Fig. 6.1(b)). A special case of this situation is depicted in Fig. 6.1(c): Here, the container is not closed off, but instead the lower liquid is in contact with the surrounding gaseous environment. The viscosity of the upper phase is negligible compared to the lower liquid. Due to its simplicity and experimental accessibility, the latter case has received wide attention in literature, and a large body of work exists.

In order to discuss the physics of the instability, it is instructive to summarize the stability analysis for inviscid fluids for both the mechanical as well as the electrostatic actuation. The goal of this section is to motivate the experiments, not to repeat the full mathematical treatment of the problems, which can be obtained from the original works (Benjamin and Ursell, 1954; Kumar and Tuckerman, 1994; Yih, 1968). The mathematical treatment is similar in both cases and follows classical stability analysis.

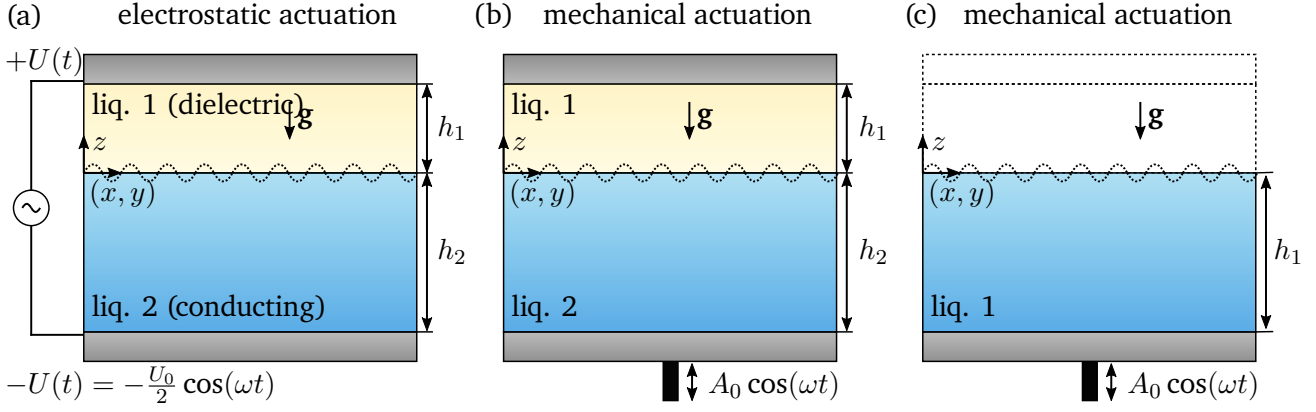


Figure 6.1: Faraday instability due to different actuations. (a) Electrostatically induced Faraday instability. An interface between a dielectric liquid and a conducting liquid is excited by a harmonically oscillating electric field. (b) Mechanically induced Faraday instability between two liquids. A container is mechanically vibrated in the direction normal to the interface. Due to the mechanical actuation, an instability is induced at the interface. (c) Mechanically induced Faraday instability of a fluidic layer in contact with air. The upper layer can be viewed as a fluid with negligible viscosity.

First, the governing equations are formulated, which are the continuity equation and the equation of motion for inviscid fluids in case of mechanical actuation. Here, the gravitational force is directed in $-z$ -direction, and the total gravitational force term is of the form $g - a_g \cos(\omega t)$. For electrostatic actuation, additionally the electric potential distribution in the dielectric liquid is accounted for by utilizing Laplace's equation (eq. 2.3 without space charge). Then, the boundary conditions are assembled at the container walls, which enforce vanishing normal velocity components. At the liquid-liquid interface, a kinematic boundary condition ensures immiscibility of the liquids, and a dynamic surface condition governs the stress balance at the interface. In case of electrostatic actuation, it includes the Maxwell stress at the interface. The stability problem is formulated by expanding the surface coordinate into a series of eigenfunctions $S_m(x, y)$ at the interface. The eigenfunctions or surface harmonics satisfy the impermeability at the side-walls, which is represented by a condition $(\partial^2/\partial x^2 + \partial^2/\partial y^2 + k_m^2)S_m(x, y) = 0$, where k_m denotes the corresponding eigenvalues. Then, the z -coordinate of the interface, ζ , can be extended into $\zeta(x, y, t) = \sum_0^\infty a_m(t)S_m(x, y)$, where $a_m(t)$ denote the time-dependent oscillations. In both actuation modes, the dynamic stress condition at the interface results in a Mathieu's equation of the form

$$\frac{d^2 a_m}{d\tau^2} + (p - 2q \cos(2\tau)) a_m = 0 \quad (6.1)$$

Table 6.1: Parameters of eq. 6.1 for electrostatic and mechanical forcing.

parameter	electrostatic actuation (Yih, 1968)	mechanical actuation (Benjamin and Ursell, 1954; Kumar and Tuckerman, 1994)
τ	ωt	$\frac{1}{2}\omega t$
p	$\frac{\omega_0^2 - \beta}{\omega^2}$	$\frac{\omega_0^2}{(\omega/2)^2}$
q	$\frac{1}{2\omega^2}\beta$	$\frac{1}{2(\omega/2)^2}\beta$
ω_0^2	$\frac{(\rho_1 - \rho_2)gk_m + \sigma k_m^3}{(\rho_1 \coth(k_m h_1) + \rho_2 \coth(k_m h_2))}$	$\frac{(\rho_1 - \rho_2)gk_m + \sigma k_m^3}{(\rho_1 \coth(k_m h_1) + \rho_2 \coth(k_m h_2))}$
β	$\frac{2\epsilon V_0^2 k_m^2 \coth(k_m h_1)}{h_1^2 (\rho_1 \coth(k_m h_1) + \rho_2 \coth(k_m h_2))}$	$\frac{(\rho_1 - \rho_2)a_g k_m}{(\rho_1 \coth(k_m h_1) + \rho_2 \coth(k_m h_2))}$

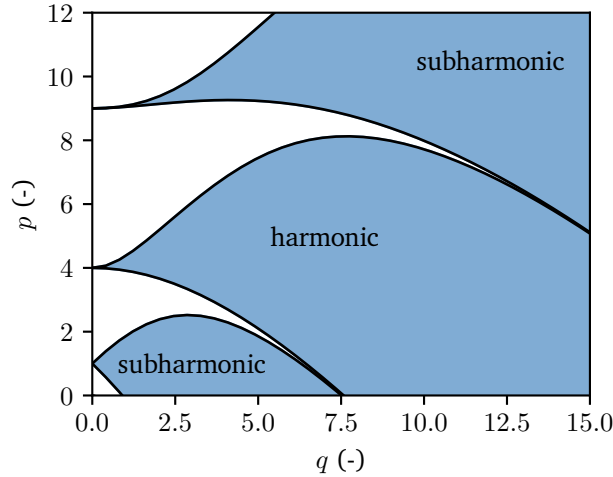


Figure 6.2: Stability of Mathieu's equation in the p - q -space. A point located in the white region is stable, a point located in the blue region is unstable. The black line denotes the marginal stability curves. Even at small forcing q , unstable values of p exist. Depending on the specific point (p, q) , the solution is either harmonic or subharmonic with the characteristic frequency of the normalized time scale τ .

upon correct parametrization of the problem. In Table 6.1, the corresponding parameters for both situations are given, emphasizing the similarity between the actuations. In eq. 6.1, the parameter p represents the restoring term which results from gravitational, capillary, and, if present, an electrostatic component. The parameter q denotes the forcing term, which depends on the acceleration or the electrostatic forcing. From the normalization of τ it is visible that the base frequency of electrostatic forcing is doubled compared to mechanical forcing, which is important for the possible oscillation frequencies of the interface. As is visible from Table 6.1, the forcing and restoring terms depend on the wavenumber k_m of the interface oscillation.

Independent of the forcing, eq. 6.1 can be analyzed to determine whether a coefficient $a_m(t)$ grows exponentially (unstable) or decays (stable) over time. The solutions $a_m(t)$ exhibit a periodicity of either 2π or π in τ (Benjamin and Ursell, 1954), with an additional exponential component. For a more detailed discussion of the equation, see the works by Benjamin and Ursell (1954). For a given q , only specific p result in periodic solutions which are not growing or decaying. In the p - q -space, these characteristic values of p for a given q denote the marginal stability curves, as shown as black lines in Fig. 6.2. If a point (p, q) is located in the white area of the graph (at smaller q), the solution a_m is stable, if it is located in the blue region (at higher q) it is unstable. Depending on the region in which (p, q) is located, also the periodicity is defined. The values are tabulated and can be obtained for example by using the *Python* toolbox *scipy* functions *special.mathieu_a* and *special.mathieu_b*. As is visible from Fig. 6.2, even for small q unstable solutions exist. This behavior is unphysical, but is rectified with the introduction of viscosity, as the marginal stability curves are shifted to the right (Bandopadhyay and Hardt, 2017). While the p - q -space is instructive for the discussion of the stability, in the remainder of the work the stability is represented as marginal stability curves in the V_0 over k space. It represents the voltage amplitude at a given frequency ω at which an interface perturbation with a given wavenumber k becomes unstable, and will be discussed in more detail in the following section.

Electrically driven instability

The effects of viscosity were incorporated by Bandopadhyay and Hardt (2017) and Ward et al. (2019) for the electrostatically actuated Faraday instability. In this section, the principle methodology of the stability analysis is summarized, without detailing the involved mathematics, in order to provide the reader with an idea of the underlying assumptions. For the mathematical treatment, the reader is referred to the original works.

The system under investigation in Bandopadhyay and Hardt (2017) consists of two immiscible fluid layers with thickness h_1, h_2 between two plate electrodes, as depicted in Fig. 6.1(a). Both fluids $i = 1, 2$ exhibit a density ρ_i , a dynamic viscosity η_i , and the dielectric fluid has a permittivity ϵ_1 . The interface coordinate perpendicular to the fluid is denoted as z , with the origin located at the interface in the unperturbed state, pointing into the upper liquid. The gravitational force is pointed into negative z direction, and the interface location is denoted as $\zeta(\mathbf{x}_s, t)$, where \mathbf{x}_s denotes the x, y -position of the unperturbed interface. It is important to note that the governing equations in Bandopadhyay and Hardt (2017) are non-dimensionalized, but since only the key results are shown here, the non-dimensionalization of the equations is skipped and the equations are shown in dimensional form for brevity.

The governing equations of the problem are the continuity equation and the Navier-Stokes equation for the hydrodynamics, as well as the Laplace equation for the electrostatics, since the dielectric nature of the upper liquid leads to vanishing space charge. The hydrodynamic equations are solved in both liquids, and the electric potential is solved in the upper liquid only. Since the lower liquid is perfectly conducting, the liquid-liquid interface is assumed to be isopotential. The equations are complemented with no-slip and no-penetration conditions at the upper and lower electrode surface, and at the interface, a kinematic boundary condition as well as a normal and tangential stress balance are enforced. Both equations are solved for the base state with no superposed fluid flow and unperturbed interface.

Next, a domain perturbation approach is utilized for the stability analysis, by assuming a perturbation of the interface of the form

$$\zeta(\mathbf{x}_s, t) = \hat{\zeta} \sin(\mathbf{k} \cdot \mathbf{x}_s), \quad (6.2)$$

where \mathbf{k} denotes the wavenumber vector, and $\hat{\zeta}$ the transient interface amplitude. Then, the electrostatic potential, pressure and flow velocities are expanded in terms of $\hat{\zeta}$, and inserted into the governing equations as well as boundary conditions. Following Floquet-theory, the z -velocity in the liquid phases i and interface coordinate ζ are expressed for the normal stress interface condition as

$$(w_j, \zeta) = (\hat{w}_j(z, t), \hat{\zeta}(z, t)) \sin(\mathbf{k} \cdot \mathbf{x}_s), \quad (6.3)$$

and the amplitudes are expanded into infinite series of the form

$$\hat{w}_j = \exp(st + i\alpha t) \sum_{n=-\infty}^{n=+\infty} W_{j,n}(z) \exp(int), \quad (6.4)$$

$$\hat{\zeta} = \exp(st + i\alpha t) \sum_{n=-\infty}^{n=+\infty} Z_n(z) \exp(int). \quad (6.5)$$

Here, if s is positive, the system is unstable, and if $s = 0$, the solution is oscillatory, corresponding to the marginal stability curve. These coefficients are inserted into the governing equations and boundary conditions, and a set of equations is obtained, which allows to express all unknown parameter in terms of Z_n . The normal stress balance at the interface can then be expressed in the form of a generalized eigenvalue problem as

$$\mathbf{AZ} = \text{MaBZ}, \quad (6.6)$$

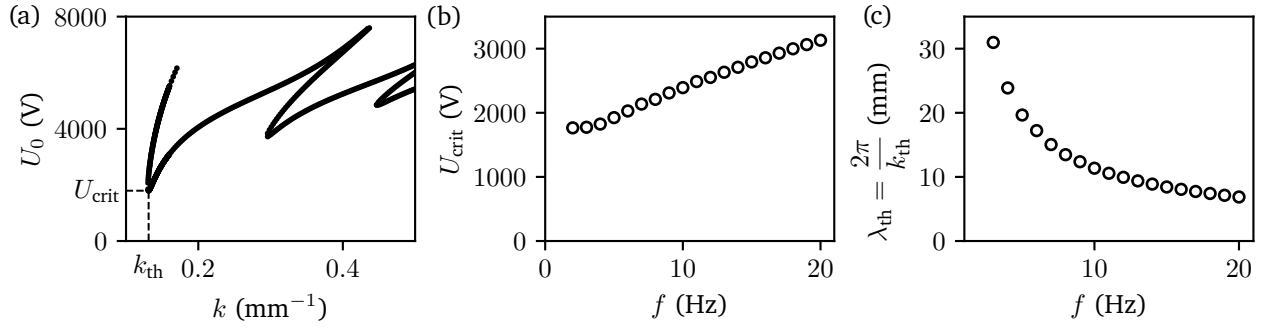


Figure 6.3: Theoretically obtained stability curve for the fluid pair of silicone oil of 0.65 cSt and 0 wt% glycerol (described in section 6.3.4). (a) Marginal stability curve for a driving frequency of $f = 2$ Hz. The wavenumbers become unstable at different voltages, and the lowest critical voltage U_{crit} represents the onset voltage of instability. (b) Stability map. For otherwise constant parameters, the lowest critical voltage can be plotted versus the driving frequency, and represents the experimentally measurable stability curve. (c) Corresponding critical wavelength for the given onset voltage. The wavelengths are expected to be observed for instabilities close to the onset voltage.

where the matrices A and B follow from the set of equations, and the vector Z contains the components Z_n . The remaining parameter Ma , the Mason-number, is given as

$$\text{Ma} = \frac{\epsilon_1 U_0^2}{4\eta_1 \omega h_1^2}, \quad (6.7)$$

where ω denotes the circulatory frequency of the driving electric field. While in principle infinite modes Z_n are introduced into the problem, in practice, the eigenvalues converge for a discrete number of modes n and thus the problem can be truncated following a convergence study (Bandopadhyay and Hardt, 2017). In order to obtain the marginal stability curve for a given set of parameters, the growth parameter is set to $s = 0$, the wavenumber k is varied, and the eigenvalue problem is solved numerically to yield the corresponding Mason-number at which the problem becomes unstable. The lowest resulting Mason-number corresponds to the experimentally observable onset voltage. Compared to the method presented by Bandopadhyay and Hardt (2017), additionally the assumption of a thin upper layer compared to the lower layer is used ($h_2 \gg h_1$), resulting in the vanishing of the terms $S_{2,n}$, $Q_{2,n}$ in the aforementioned work.

A similar analysis was performed by Ward et al. (2019), who relaxed the assumption of a perfect-dielectric and a perfect-conductor to the leaky dielectric model. Then, the electric potential has to be solved in both phases, and the interfacial charges are governed by a charge transport equation. Also, tangential electric stresses have to be accounted for, which vanish in case of a perfect conductor. After introducing these changes, a more complex eigenvalue problem emerges, which can be solved analogously, and the marginal stability curve can be obtained by varying the wavenumber k and solving the eigenvalue problem. As was shown by Ward et al. (2019), the solutions obtained by the model of Bandopadhyay and Hardt (2017) are recovered upon a sufficient conductivity ratio between the liquids. In the following, the theory by Bandopadhyay and Hardt (2017) is used to determine the theoretical comparison to the experiments, and in section 6.4.1, the validity of this assumption is tested experimentally by varying the salt concentration of the conducting liquid.

Figure 6.3(a) shows an exemplary marginal stability curve for a given set of driving parameters, which are given in the figure caption. Here, the typical tongues of the marginal stability curve are visible, where small changes of k lead to strong changes of the critical voltage. The lowest critical voltage U_{crit} corresponds to the most unstable wavenumber k_{th} , which is expected to be observed in the experiments

close to the onset of instability. With increasing voltage, more wavenumbers become unstable. In order to take the domain size into account, the lower limit of allowable wavenumbers is on the order of $2\pi/d$, where d is the domain diameter. In this case, the wavelengths of the resulting instability are on the order of the domain size. Upon varying the driving frequency, a stability map is created, as is shown in Fig. 6.3(b), which can be measured experimentally. Here, the onset voltage of instability is plotted in dependency of the driving frequency $f = \omega/2\pi$. Simultaneously, the expected wavelengths at the onset of instability follow readily as $\lambda_{\text{th}} = 2\pi/k_{\text{th}}$, and are shown in Fig. 6.3(c).

Mechanical instability

From inviscid theory, it is apparent that both mechanically and electrostatically actuated Faraday instabilities are closely related. While the experimental work on electrically actuated Faraday instabilities is limited, a large body of work exists on mechanically actuated Faraday instabilities. For comprehensive reviews on Faraday instabilities, the reader is referred to the dedicated reviews of Nevolin (1984), Miles (1990), Perlin and Schultz (2000) and Müller et al. (2011). In the following, an emphasis is placed on pattern formation in single-frequency actuation, and the relevant literature is summarized. In the stability analysis by Benjamin and Ursell (1954), the surface instability is expressed as a series of eigenfunctions $S_m(x, y)$ with the eigenvalues k_m . For a circular domain of radius R , these eigenfunctions are of the form

$$S_{l,n} = J_l(k_{l,n}r) \cos(l\theta), \quad (6.8)$$

where J_l denotes the Bessel function of the first kind and $k_{l,n}$ the n -th zero of $J'_l(k_{l,n}R)$. It is important to note that the indexing of the eigenfunctions changes from m to l, n in order to facilitate their specific structure. In Fig. 6.4, the surface harmonics for the first combinations (l, n) are shown. Here, it becomes apparent that increasing l increases the number of azimuthal nodes, and larger n lead to more radial nodes. In their work, Benjamin and Ursell used the (2,1) mode for experimental validations. Following, Dodge et al. (1965) reported experimental observations of modes with similar form, with good agreement to the inviscid theory. Continuing, Gollub and Meyer (1983) reported secondary instabilities triggered by increasing driving amplitudes of initially ordered modes, which lead to transition to a spatially disordered system. While discrete modes exhibit distinct wavenumbers $k_{l,n}$, adjacent modes of similar wavenumber can interact and lead to periodic and chaotic fluctuations between modes, as well as superpositions of their patterns (Ciliberto and Gollub, 1984). The Faraday instability in a square container was studied by Douady and Fauve (1988), resulting in rectangular patterns, and the role of the boundary meniscus was discussed. In the presence of a meniscus, side-waves can penetrate into the domain and influence the pattern selection, which was further studied by Douady (1990). Here, it was reported that the absence of a meniscus due to using a brimful container suppresses edge-waves, and enables the observation of pure modes, and conversely, that edge-waves couple to the parametric excitation. Next, Gluckman et al. (1993) showed that a chaotic pattern can exhibit a highly ordered time-average, since the boundaries can have a long-range interaction with the instability. A different technique to reduce meniscus effects other than pinning the contact line was reported by Batson et al. (2013a), who used a liquid-liquid combination that resulted in a wetting film at the boundary, resembling a freely moving contact line. Thereby, the large-scale fluid flow mimicked the stress-free boundary condition, which allowed comparison to theory. Also, it emphasized the effect of contact line dissipation, which can dominate the overall energy dissipation in the system. In a recent work, Shao et al. (2021) re-employed the brimful-container approach and combined it with theoretical modeling. Their experiments resulted in the observation of the first 50 resonant modes, and by actively introducing a meniscus, complex mode mixing was observed.

With increasing container size, the Faraday instability becomes independent of the boundary and forms patterns distinctly different than the discrete modes of the surface harmonics. At the onset of instability, rectangular patterns were observed by Tuffillaro et al. (1989) with subsequent transitions into a disordered

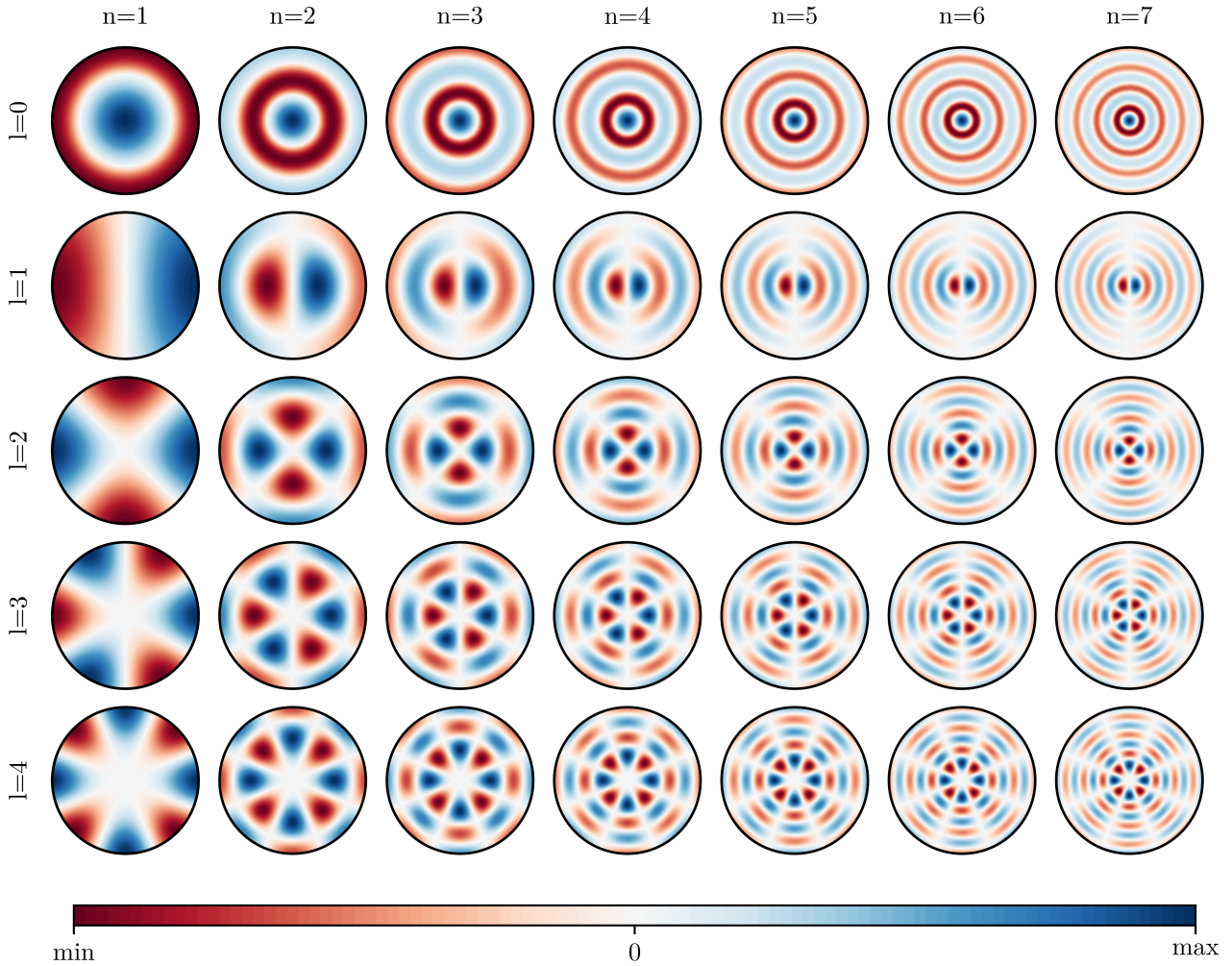


Figure 6.4: Surface harmonics of the form $S_{l,n} = J_l(k_{l,n}r) \cos(l\theta)$ for a circular domain, where J_l denotes the Bessel function of the first kind and $k_{l,n}$ the n -th zero of $J_l'(k_{l,n}R)$ (Benjamin and Ursell, 1954). The data is normalized, with red denoting the maximum and blue denoting the minimum value.

system at higher driving amplitudes. Edwards and Fauve (1994) reported instability patterns of lines, squares, circles, and spirals at single frequency forcing. Specifically, they explored the transition to boundary independent patterns at higher viscosities, larger driving frequencies and domain sizes. More detailed measurements of the hexagonal and square structure were performed by Kityk et al. (2005) using light adsorption, resolving both amplitude and phase of the interface. While more complex modes with several distinct wavelengths can occur upon of multi-frequency actuation, single frequency actuation is usually restricted to specific patterns with a dominant wavelength, especially close to the onset of instability. This brief overview over the existing literature on mechanically induced Faraday instabilities shows that the remarks made by Ward et al. (2019) with respect to the wavelengths for electrostatic actuation, i.e, boundary independence and a multitude of wavelengths for all unstable configurations, contrast the observations made for mechanical actuation. In light of the apparent analogies between both driving mechanisms, they deserve further exploration.

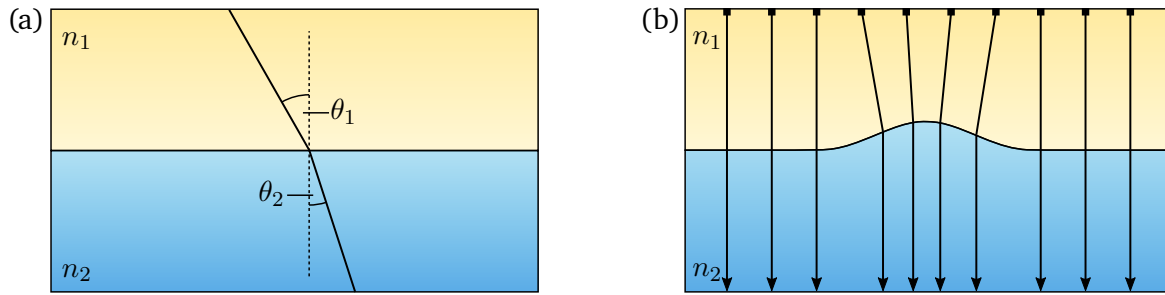


Figure 6.5: Refraction at an interface of two media with different refractive indices ($n_1 < n_2$). (a) Refraction of a single optical path at a flat interface. (b) Refraction of a regular grid (black rectangles) immersed in medium 1 at a non-flat interface. The regularly spaced grid appears to be non-regularly spaced if projected on a screen far away from the interface, as can be seen from the varying distances of the light paths.

6.2.2 Refraction

The measurement technique utilized in this chapter is based on refraction, which describes the change of optical paths due to changes of the optical properties of a material. Light travels with different velocities in media of different composition. In vacuum, the speed of light c_0 is approximately $c_0 \approx 2.9979 \times 10^8 \text{ m s}^{-1}$ (Möller, 2003). A measure of the speed of light in different materials is given by the index of refraction, which is defined as

$$n_i = c_0/v_i, \quad (6.9)$$

where v_i denotes the speed of light in the medium i . With increasing refractive index, the speed of light decreases. At interfaces of two media with different refractive indices, this leads to refraction of optical paths. A light ray satisfies the *law of refraction* (also referred to as *Snell's law*), which is defined as

$$n_1 \sin(\theta_1) = n_2 \sin(\theta_2), \quad (6.10)$$

where n_i denote the refractive indices of the materials, and θ_i the incident angles with the surface normal (see Fig. 6.5(a) for a schematic).

Similarly, refraction occurs at non-flat interfaces, and the law of refraction is satisfied locally. In Fig. 6.5(b), an exemplary situation is depicted, where a regularly spaced grid, which is immersed in liquid 1, is imaged through an interface with a dimple. If the grid is projected onto a screen far away from the interface, it appears as unevenly spaced. As will be illustrated in section 6.3, this principle can be used to identify the interface position by comparison between a recorded image distorted by refraction, and the original image.

6.3 Methods

6.3.1 Experimental setup

Figure 6.6 shows the experimental setup, in which the electrostatically forced Faraday instability was analyzed. The fluidic cell is depicted in Fig. 6.6(a) and consists of a glass cylinder (inner diameter $d = 125 \text{ mm}$, height $h = 35 \text{ mm}$), which is clamped between two stainless steel electrodes. The setup represents a modification of the setup used by Ward et al. (2019). In order to prevent leakage between the glass cylinder and the electrodes, gaskets are placed in between, which are sealed by mounting

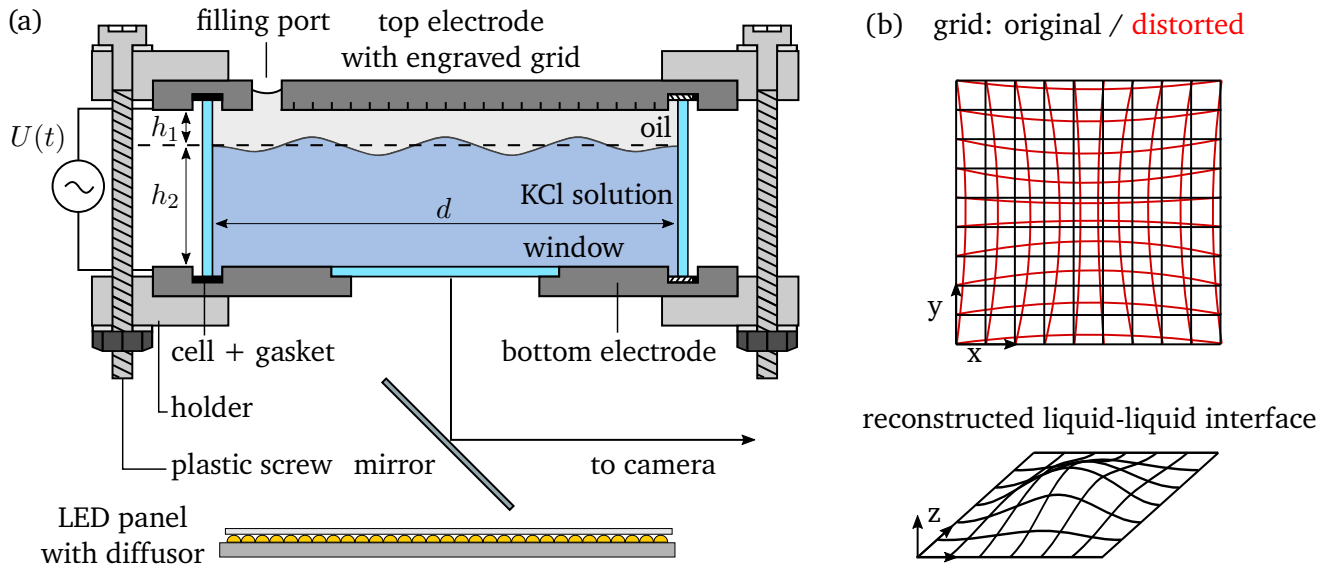


Figure 6.6: Schematic of the experimental measurement setup. (a) Experimental setup cell. A glass cylinder is clamped in between two metal electrodes by using a plastic holder. At the upper electrode, a grid with a line-spacing of 0.5 mm is engraved. The grid is imaged through a glass at the bottom electrode. A high-voltage power source provides a time-dependent potential difference between the electrodes and induces the instability at the interface. (b) Schematic of the interface reconstruction algorithm. The grid at the upper electrode is imaged through the interface and appears distorted. For known refractive indices, the 3D interface can be reconstructed from the 2D images, yielding information about the third dimension.

pressure. At the upper electrode, an eccentrically located filling port (diameter 1 cm) allows filling of the chamber. Also, a grid of known line-distance of 0.5 mm is engraved into the upper electrode by laser-ablation. The optical access into the cell is provided via a rectangular glass window, which was glued using UV adhesive above a rectangular cut-out of the lower electrode (4.6 cm \times 4.6 cm), forming a planar bottom surface with the electrode. The outer holding clamp was fabricated such that the electrodes can be changed, and made from non-conductive material to prevent any electrical connection between the electrodes. The upper and lower part of the plastic holder were connected using up to twelve plastic screws to ensure a uniform mounting pressure. The grid was imaged using a high-speed CMOS camera (*FASTCAM Mini AX*, *Photron*, Japan) with a macro objective (*SWM VR ED IF Micro 1:1*, *Nikon*, Japan) via a mirror placed below the cell. The mirror allows the placement of the camera aside the cell, so that in case of potential leakage no liquid penetrates the camera. It is positioned using a goniometer (*OWIS*, Germany), allowing fine-adjustment of the optical path. The illumination was provided by an LED panel (*NL480*, *NEEWER*, China) placed below the window, resulting in an image of a dark grid on a bright background due to reflection on the upper electrode. When the grid was imaged through the liquid-liquid interface, it is distorted if the optical paths form a non-zero incident angle with the interface. As is shown schematically in Fig. 6.6(b), the image of the distorted grid allows to reconstruct the interface position using an algorithm described in section 6.3.3. The time-dependent electric potential difference $U(t)$ between the electrodes was provided by a high voltage power source (*HVS448 6000D*, *LabSmith*, USA), which was connected to one channel per electrode each. At both electrodes, voltage signals of similar time-dependent signal, but opposing sign were applied, with the maximum voltage difference accumulating to 6000 V. Both the power source as well as the camera were operated using the appropriate software of the manufacturer (*Photron Fastcam Viewer* and *LabSmith Sequence*).

6.3.2 Experimental procedure

Before assembly and filling with the working liquids, all parts of the fluidic cell were cleaned thoroughly using isopropanol and DI water, and dried under a stream of nitrogen. Thereby, contamination and pollutants such as dust particles were removed, and the cell was assembled, with the opening ports covered. Next, it was positioned onto a holder on top of an air-dampened optical table, and horizontally aligned. Then, the optical path was aligned using the goniometer to ensure a distortion-free imaging of the upper electrode. The alignment of the cell can be verified quickly by opening the aperture of the camera to a wide setting, reducing the depth of field significantly. If the upper electrode appears sharp over the whole imaging region ($\approx 35 \text{ mm} \times 35 \text{ mm}$), the alignment was successful. Before adding the liquids to the chamber, they were degassed in a desiccator for 30 min to avoid gas bubbles forming later in the experiment. Afterwards, the liquids were added to the chamber through the filling port using a pipette to avoid splashing and bubble capture. The upper liquid was filled until the overflow port was brimful and then the port was covered to avoid evaporation of the liquids, or dust entering the upper phase. After filling, the electrodes were connected to the power source using clamps, and the focus on the grid was rechecked by adjusting the working distance of the objective.

In order to determine the onset voltage of instability for a defined liquid-liquid combination and a constant driving frequency f , a driving voltage difference of the form $U(t) = U_0 \sin(2\pi ft)$ was set in the software, where the initial driving amplitude was chosen sufficiently below the theoretically predicted onset voltage. Next, the voltage signal was applied, such that each electrode exhibits the same voltage with opposing sign ($U(t)/2$). Following, the interface oscillations were observed for a duration of 3 min. If the interface exhibited a specific motion, e.g., edge-waves or distinct patterns, it was noted for later evaluation. Continuing, the excitation amplitude was increased over subsequent experiments. Typically, above a specific voltage amplitude, the interface response changes qualitatively, both in amplitude and spatial structure, with a clear distinction between edge-waves occurring below the threshold and the Faraday-patterns appearing above. The edge-waves are a result of the meniscus changing under the influence of the applied electric field, and occur with a driving frequency of $2f$. They are induced at the wall, and move inwards into the liquid domain, thus forming a circular pattern. The Faraday waves oscillate with a frequency of f , and are thus clearly distinguishable from the edge waves. In case of Faraday patterns appearing or unclear responses, the interface motion was recorded for 1 s at a framerate of 1000 fps, with the recording starting ≈ 150 s after the voltage has been started. Thus, the developed instability is analyzed, without specific information how the transition to this quasi-steady state occurred. The interface was only recorded for (near-)critical responses and the experiments well below the instability threshold were not recorded. Thereby, the data overhead was reduced, and the observations during the experiments were confirmed later on using the postprocessing algorithm. In case of strongly growing instabilities, the experiments need to be stopped prematurely to prevent the lower phase to touch the upper electrode. If the interface touched the upper electrode, the liquid adhering to the upper electrode necessitates the disassembly and cleaning of the fluidic cell. If the lower liquid touched the electrode, the response is noted as critical and shown for the critical voltage, but excluded from the wavelength determination, as the instability is highly transient.

6.3.3 Data evaluation algorithm

The refraction at the interface is used to determine the dominant wavelength of the instability pattern. As shown in Fig. 6.7(a), a reference grid (black) was imaged through the interface, and the distorted image (red) was recorded. Where the optical paths pass the interface perpendicularly, no change of the light paths occur, thus an unchanged grid correspond to local maxima and minima of the interface $h(x, y)$. On the other hand, regions with strong interfacial gradients ∇h lead to strong refraction and

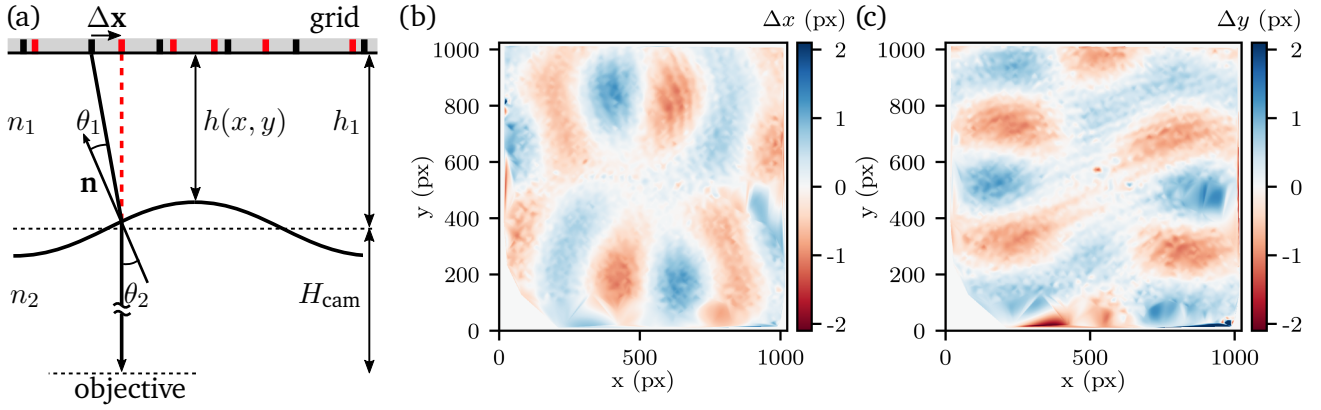


Figure 6.7: Displacement field detection. (a) Schematic of the measurement method with the respective relevant properties. (b,c) Exemplary displacement field in x - and y -direction, as obtained from the measurements. The displacement field is linearly proportional to the surface gradient ∇h .

thus to larger deviations from the reference grid. In the following, the difference between the undistorted grid and the recorded grid is denoted as displacement field $\Delta \mathbf{x}$, which is a property relating both images. In order to transform the displacement field to the physical gradients at the interface, the framework by Moisy et al. (2009) is utilized, who derived the relation between the displacement field $\Delta \mathbf{x}$ and the surface gradient ∇h under the following assumptions: First, it is assumed that the optics are paraxial. This condition is satisfied if the observation field is small compared to the camera-image distance (here: image side length of ≈ 3.5 cm vs. camera-image distance of ≈ 35 cm). Furthermore, they assumed small interfacial gradients ∇h , translating to the condition of small angles between the interface normal \mathbf{n} and the unit vector in z -direction. Also, it is assumed that the interface amplitudes are small, which can be expressed as $(h_1 - h)/h_1 \approx 0$. If all three conditions are satisfied, the surface gradient is linearly proportional to the displacement field $\Delta \mathbf{x}$ and can be computed as

$$\nabla h = -\frac{a_{cal}}{h^*} \Delta \mathbf{x}, \quad (6.11)$$

where a_{cal} denotes the image calibration factor in mm/px and h^* an effective height resulting from the optical path as

$$h^* = \left(\frac{1}{\alpha h_1} - \frac{1}{H_{cam} + h_1} \right)^{-1}. \quad (6.12)$$

The parameters in eq. 6.12 are the ratio of the refractive indices ($\alpha = 1 - n_2/n_1$), and the distance between the objective and the interface (H_{cam}). Due to the large ratio $H_{cam}/h_1 \ll 1$, the second term is negligible.

Before further detailing each step of the image evaluation, it is instructive to discuss eq. 6.11. For a constant surface gradient ∇h , the displacement field will increase with h_1 and stronger difference of the refractive indices. Also, in case of matching refractive indices, no refraction will occur. Before continuing, it is important to point out that the surface coordinate $h(x, y)$, which is reconstructed from the measurements, is sensitive to deviations of ∇h and h^* resulting from deviations of the refractive indices as well as the layer thickness. However, the wavelength evaluation does not depend on the absolute amplitudes of the interfacial patterns. In section 6.5.2, the sensitivity to errors is analyzed using artificial data, emphasizing the robustness of the measurement method. In the following, the evaluation is structured into three distinctive steps: First, the surface gradient $\nabla h(x, y)$ is obtained from the displacement field $\Delta \mathbf{x}$ of the experiments, relating image data to physical data. Second, the surface gradients $\nabla h(x, y)$ are used to reconstruct the interface $h(x, y)$. Third, the dominant pattern wavelength is extracted from the reconstructed interface using a Fourier transform of the image.

Measurement of the surface gradient

The detection of the surface gradient $\nabla h(x, y)$ is based on the relative motion of the cross-points of the reference grid (points at which perpendicular lines intersect). Additional information could be retrieved if the grid line deformations were taken into account, however, the cross-point detection is relatively simple and robust, with a subpixel accuracy. First, the cross-points are extracted from the images by inverting the grey-scale values of the images, such that the grid appears as a bright grid in front of a dark background. Then, the illumination is homogenized by subtracting the local mean value measured in a $60 \text{ px} \times 60 \text{ px}$ region around each image point. Subsequently, the line thickness is further reduced by the morphological closing and erosion operations, using the *Python* toolbox *skimage.morphology*. This processed image serves to generate initial guesses for each cross-point, and a Harris corner-detection algorithm (*Python* toolbox *Skimage, feature.corner_peak*) is applied. These initial guesses are used for a subpixel-detection of the grid-points using a statistics based algorithm (*feature.corner_subpix*) as described by Förstner and Gülch (1987). The resulting cross-points in each image are saved for further processing, and for perturbed interfaces the spacing is inhomogeneous.

In order to obtain the time-development of the displacement field, the motion of each cross-point is tracked over subsequent images, so that the traces over time of the cross-points are generated. The time-dependent motion of the cross-points is resolved sufficiently by using at least 50 images for each oscillation period. Since the videos were recorded at a constant framerate (1000 fps) with varying driving frequencies (2 Hz - 20 Hz), the number of images corresponding to one period of oscillation varies. In order to limit computational costs, not every frame is used at lower oscillation frequencies (every second frame for 4 Hz – 7 Hz driving frequency, every third for 3 Hz, and every fifth for 2 Hz). Also, the points are tracked for one period of oscillation. The tracking is performed using a nearest neighbor method with a maximum movement between images of 5 px. After this processing, the movement of the cross-points over time is known, with $\mathbf{x}_i(t)$ denoting the position of the i -th grid-point at time step t .

The displacement field $\Delta \mathbf{x}_i(t)$ of each point i at time step t can be calculated using

$$\Delta \mathbf{x}_i(t) = \mathbf{x}_i(t) - \frac{1}{N} \sum_{t=1}^N \mathbf{x}_i, \quad (6.13)$$

with N denoting the number of images during one period of oscillation. The resulting deviation field is spline-interpolated onto a regular grid ($M \times M = 51 \times 51$ grid points, 20 px spacing between points) to smoothen the uneven spacing, which is important for the next processing step. Then, by using eq. 6.11 and eq. 6.12, the surface gradient $\nabla h(x, y)$ is obtained from the displacement field at the time steps t . Figure 6.7(b,c) show the components of an exemplary displacement field obtained from the experiments.

Reconstruction of the surface

The surface gradient $\nabla h(x, y)$ can be used to determine the interface coordinate $h(x, y)$ using different approaches. For example, it is possible to integrate directly, starting from one point at a boundary and integrate over the surface gradients to obtain the position at each other point with respect to this reference point. While it is technically possible, direct integration works best with data in the absence of noise. If noise is present in the image, for example due to measurement errors, the results accumulate more of the noise the further away a point is from the reference point. A different approach was outlined by Moisy et al. (2009), which is based on an optimization problem, and will be described in the following. For the reconstruction, the previously defined grid points ($M \times M = 51 \times 51$) are used, at which the surface gradients are known. Due to the regular spacing of the grid, the gradients can be expressed in terms of h using a centered difference approximation. Each grid point can be identified by an index j ,

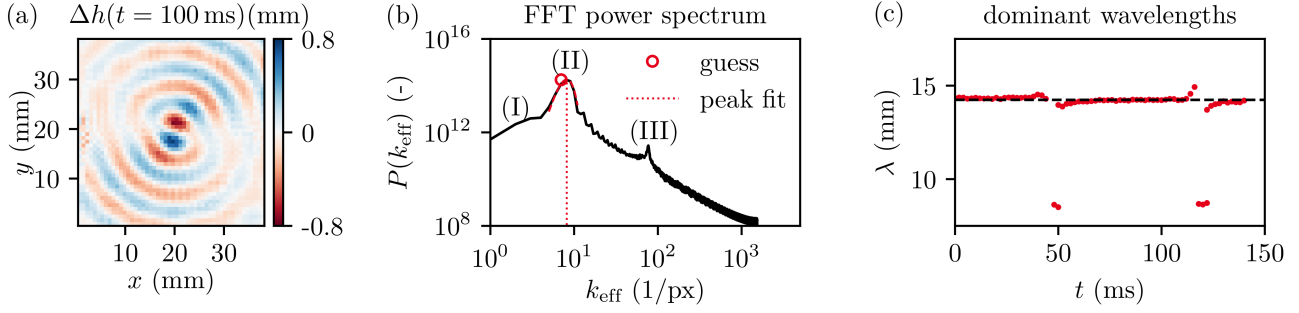


Figure 6.8: Pattern wavelength extraction. (a) Reconstructed interface for the displacement field shown in Fig. 6.7(b,c). (b) Resulting FFT power spectrum. The power spectrum exhibits peaks due to the Fourier-transform (I), the physical interface pattern (II) and due to the interface reconstruction (III). The detected value of k_{eff} is used for further processing and can be transformed into a respective wavelength (eq. 6.18). (c) Measured dominant wavelengths for one period of oscillation (7 Hz, 143 ms period length). As is visible, the dominant pattern wavelength persists over the majority of the measurement, resulting in an average value of 14.23 mm (shown as a dashed line). During parts of the oscillation, the Faraday instability has small amplitudes. Then, a different wavelength is obtained, which can be attributed to the edge-waves of the system.

denoting the j -th grid point in x -direction and an index l , denoting the l -th grid point in y -direction. Then, the gradient at point (j, l) can be expressed as

$$\frac{\partial h(j, l)}{\partial x} = \frac{h(j+1, l) - h(j-1, l)}{2L} \quad (6.14)$$

$$\frac{\partial h(j, l)}{\partial y} = \frac{h(j, l+1) - h(j, l-1)}{2L}, \quad (6.15)$$

with L denoting the spacing between two adjacent grid points. At the grid boundary, the central difference scheme has to be replaced by a forward or backward difference scheme to obtain the gradients. Expressing the gradients at each grid point results in a set of $2M^2$ equations, which can be written as two sets of linear systems. First, the height h at the grid points is sorted into a vector \mathbf{h} of dimension $(M^2, 1)$ and the gradients in x - and y -direction are sorted into two vectors $\mathbf{p}_x, \mathbf{p}_y$ of dimension $(M^2, 1)$. Then, the systems $\mathbf{G}_x \mathbf{h} = \mathbf{p}_x$ and $\mathbf{G}_y \mathbf{h} = \mathbf{p}_y$ follow, where the matrices $\mathbf{G}_x, \mathbf{G}_y$ of dimension (M^2, M^2) result from the difference approximation schemes (eq. 6.14 and eq. 6.15). Both systems can be combined into one linear system as

$$\begin{pmatrix} \mathbf{G}_x \\ \mathbf{G}_y \end{pmatrix} \cdot \mathbf{h} = \begin{pmatrix} \mathbf{p}_x \\ \mathbf{p}_y \end{pmatrix}, \quad (6.16)$$

with $2M^2$ equations for M^2 points. Here, both the vectors $\mathbf{p}_x, \mathbf{p}_y$ and the matrices $\mathbf{G}_x, \mathbf{G}_y$ are known, and the system has to be solved for \mathbf{h} . This over-determined system can be solved by formulating it as a minimization problem of the form $\min |(\mathbf{G}_x, \mathbf{G}_y)^T \mathbf{h} - (\mathbf{p}_x, \mathbf{p}_y)^T|^2$ and solving it using a standard algorithm (here function `lsq_linear` of the *Python* toolbox *scipy*). As was noted before, the optimization approach minimizes the global error and is thus less sensitive to measurement outliers. As a last step, the points of the vector \mathbf{h} are interpolated onto the original image of dimension $N \times N = 1024 \text{ px} \times 1024 \text{ px}$, and for further processing the deviation between the unperturbed interface and the reconstructed interface is noted as $\Delta h(x, y) = h(x, y) - h_1$. An exemplary reconstructed interface is shown in Fig. 6.8(a), obtained from the surface gradients presented in Fig. 6.7(b,c).

Dominant pattern wavelength

The dominant instability pattern wavelength λ is extracted by computing a discrete Fourier transform (DFT) from the reconstructed interface $\Delta h(x, y)$ and extracting the dominant wavelength from the Fourier power spectrum. First, the reconstructed interface Δh is placed at the center of a $3N \times 3N$ image, with other values set to zero. The matrix entries are addressed using the indices j and l for the x - and y direction. The two-dimensional discrete Fourier transform H is defined as

$$H(k_x, k_y) = \frac{1}{(3N)^2} \sum_{j=0}^{3N-1} \sum_{l=0}^{3N-1} \Delta h(j, l) e^{-i2\pi \left(\frac{j k_x}{3N} + \frac{l k_y}{3N} \right)}, \quad (6.17)$$

where k_x, k_y denote the wavenumbers in x - and y -direction, respectively. Next, the two-dimensional image information of $H(k_x, k_y)$ is reduced to a one-dimensional power spectrum dependent on an effective wavenumber k_{eff} . The equivalent one-dimensional wavenumber $k_{\text{eff}}(k_x, k_y)$ corresponding to a two-dimensional wavenumber pair k_x, k_y can be computed using $k_{\text{eff}}(k_x, k_y) = (k_x^2 + k_y^2)^{0.5}$. Also, the amplitudes at a wavenumber k_x, k_y are computed as $A(k_x, k_y) = |H(k_x, k_y)|^2$. Then, the average values of the amplitudes $A(k_x, k_y)$ of the equivalent one-dimensional wavenumber $k_{\text{eff}}(k_x, k_y)$ are computed, binning them into bins of the size of $dk_{\text{bin}} = 1$ px. The lower bin edges range from 0 px to $3N/2$ px. Next, the bin values are normalized using the area of each bin in the DFT $H(k_x, k_y)$ as $\pi (k_{\text{bin}} + dk_{\text{bin}})^2 - \pi k_{\text{bin}}^2$. Ultimately, the power spectrum is obtained in terms of the one dimensional wavenumber k_{eff} .

The resulting power spectrum exhibits some distinct properties, and in Fig. 6.8(b), an exemplary power spectrum corresponding to the reconstructed interface is shown. During some experiments, a local maximum at small wavenumbers (equivalent to large wavelengths) is visible, with the region marked by (I). This local maximum is a numerical artifact following from the placement of $\Delta h(x, y)$ in the center of a domain of dimension $3N \times 3N$. With increasing wavenumber, the spectrum shows decreasing values on average, with a localized peak (II). This peak corresponds to the observed interface pattern in the reconstructed interface. A third peak is visible at even larger wavenumbers (III). This is a numerical artifact of the reconstruction, which was computed at a reduced grid size. Here, the typical wavelengths L and $2L$ resulting from the central difference scheme are visible as the peak (III). Thus, solely peak (II) is relevant for further processing, as its corresponding wavenumber k_{max} corresponds to the dominant wavelength λ of the instability, which can be computed as

$$\lambda = (3N)a_{\text{cal}}/k_{\text{max}}. \quad (6.18)$$

Here, a_{cal} denotes the calibration factor already introduced in eq. 6.11. For each experiment, the peaks of all power spectra over one period of oscillation are detected (*Python* toolbox *scipy*, function *signal.find_peaks*). Since the power spectrum was obtained using a bin size of 1 px, the accuracy of the processing is enhanced by fitting a Gaussian distribution to the peak, with the detected peak as an initial guess. Then, the fitted mean value of the Gaussian is used as the dominant wavenumber for further processing, as is shown in Fig. 6.8(b).

In each experiment, not every image exhibits a dominant wavelength, since the instability oscillates and exhibits a small amplitude during parts of the period. The dominant wavelength for an experiment is obtained by using all dominant wavelengths detected in all images. Usually, each image exhibits only one physically relevant peak per image, but in principle, multiple peaks can be detected if edge-waves are prominently visible. In Fig. 6.8(c), the dominant wavelengths over the duration of one oscillation period are shown. Over the majority of images, the wavelength is constant, with a few exceptions when the instability has small amplitudes. Here, the edge-waves lead to smaller wavelengths. The multiple peaks of the experiments can be treated by using the histogram of the wavelengths over all experiments. Then, the average over each distinct peak corresponds to each physical process. In case of multiple wavelengths

Table 6.2: Substance properties of the used liquids. Values are composed of mean and standard deviation. In case of the dynamic viscosity, the measured density and kinematic viscosity from the data sheet are used (c), and for the dielectric permittivity, the values taken from the respective data sheet (l) (Wacker-Chemie GmbH, 2002). The values are composed of mean and standard deviation of five individual measurements.

liquid	density (g ml ⁻¹)	viscosity (mPa s)	relative permittivity (-)	refractive index (-)
0.65 cSt	0.746 ± 0.015	0.48 ± 0.01 (c)	2.18 (l)	1.376
1 cSt	0.810 ± 0.005	0.81 ± 0.01 (c)	2.31 (l)	1.383
5 cSt	0.911 ± 0.000	4.55 ± 0.00 (c)	2.49 (l)	1.397
0 wt%	0.996 ± 0.010	1.00 (l)	-	1.333
60 wt%	1.153 ± 0.004	9.38 ± 0.43	-	1.412
70 wt%	1.185 ± 0.022	19.69 ± 0.29	-	1.427

present in the system, the wavelength which is found in the most images is referred to as *dominant*, and other wavelengths are denoted as *secondary*. In section 6.4, the error bars shown for the wavelength measurements correspond to the standard deviation over the measurements including only the dominant peak, not the secondary wavelengths. It therefore represents a measure of the measurement error in one experiment.

6.3.4 Fluid data

For the investigation of the instability, specific liquid-liquid combinations were utilized. As the dielectric liquids, silicone oils of varying viscosity (*Silikonöl AK 0.65*, *Silikonöl B1*, and *Silikonöl B5*, *Silikon Profis*, Germany) were used, due to their immiscibility with water. In the following, they are identified using their respective kinematic viscosities (0.65 cSt, 1 cSt, and 5 cSt). As the conducting liquid, three different mixtures of DI-water (*Milli-Q Integral 3*, *Millipore*) and glycerol ($\geq 99.5\%$ water free, *Sigma-Aldrich* and *Carl Roth*, Germany) were prepared. For brevity, they are identified in the following by their glycerol mass fraction. In order to adjust the viscosity of the lower phase, three mixtures 0 wt%, 60 wt% and 70 wt% glycerol were used. The conductivity was adjusted using potassium chloride (KCl, Quality: ACS Reagent, *Sigma-Aldrich*, Germany), with a concentration of $c_{\text{KCl}} = 1 \text{ mmol L}^{-1}$ unless otherwise noted. Before use, the glycerol-mixtures were thoroughly stirred for a minimum of 24 h to ensure a homogeneous, dispersion free mixture.

In order to compare the measurements to the theoretical predictions, the relevant substance data has to be known. For the pure substances, the liquid properties are summarized in Table 6.2, obtained at a laboratory temperature of 20 °C. The dynamic viscosity of the water-glycerol mixture was determined using a digital rotation rheometer (*DV-III-Ultra*, spindle *CPE-40* with coefficient $\gamma = 307$, *Brookfield*, USA) by relating the torque M to the dynamic viscosity η as $\eta = \omega\gamma/M$. The reported value was obtained by at least 5 independent measurements. The density was measured by deposition of droplets of known volume on a precision scale (*NewClassic MF / MS 105DU*, *Mettler Toledo*, Switzerland) and measurement of the mass directly after deposition. Again, the reported values represent the mean of at least five individual measurements. The refractive indices were measured using an Abbe refractometer (*Carl Zeiss*,

Table 6.3: Interfacial tensions for the used liquid-liquid combinations. The values are composed of mean and standard deviation of five individual measurements.

lower phase	upper phase	interfacial tension (mN m ⁻¹)
0 wt%	0.65 cSt	39.6 ± 0.4
	1 cSt	42.0 ± 0.1
	5 cSt	35.9 ± 0.1
60 wt%	0.65 cSt	27.4 ± 0.1
70 wt%	0.65 cSt	25.7 ± 0.4

West Germany). The viscosities of the silicone oils as well as the dielectric constants are obtained from their data sheet.

The interfacial tensions of the relevant liquid-liquid combinations are summarized in Table 6.3. They were determined using a ring tensiometer (*DCAT 25*, ring *RG 11*, *DataPhysics Instruments*, Germany). The measurements were performed following the recommendations of the manual, with the first measurement determined using the *pull 2 step* method as implemented in the manufacturer’s software, with subsequently four measurements using the *push/pull lamella* method.

6.4 Results

In the following, the experimental results with respect to the critical voltage and the observed interfacial patterns are presented. In all experiments, the upper layer thickness was held constant at 5 mm. For one driving frequency and a fixed set of fluids, the instability shows a distinct behavior with increasing excitation amplitudes. First, the edge-waves induced by the meniscus penetrate from the side to the center of the domain due to the electrostatic actuation near the three-phase contact line. Since the Maxwell stress is proportional to the electric field squared, an oscillatory signal of frequency ω results in edge-waves with a frequency of 2ω . Second, with increasing amplitude, the Faraday instability starts to occur above a critical voltage, with oscillations of frequency ω . Near the onset voltage, the instability develops slowly and reaches a meta-stable state, in which the interface oscillation amplitude does not grow further. A similar effect was investigated numerically by Pillai and Narayanan (2018) and attributed to nonlinear effects. This effect persists for a certain range of voltage amplitudes above the onset voltage. Upon further increase of the driving amplitude, the amplitude of oscillation grows until it touches the electrode. As discussed in section 6.3.2, the analysis is restricted to the instabilities close to the onset voltage, which show a meta-stable behavior. In the following, all experiments which lead to Faraday waves are denoted as critical, since the voltage exceeds the onset voltage. All other experiments are summarized as subcritical, if no Faraday instability is observed, independent of other interface motions such as edge-waves. In the following, at each data point one experiment was performed and evaluated. As denoted in section 6.3.3, the error bars denote the observed standard deviation in one experiment.

6.4.1 Influence of the salt concentration

The theoretical model of Bandopadhyay and Hardt (2017) used to determine the instability threshold and pattern wavelength relies on the perfect-dielectric / perfect-conductor assumption (see section 6.2.1). The results by Ward et al. (2019) recover similar results, if the conductivity ratio between the upper and

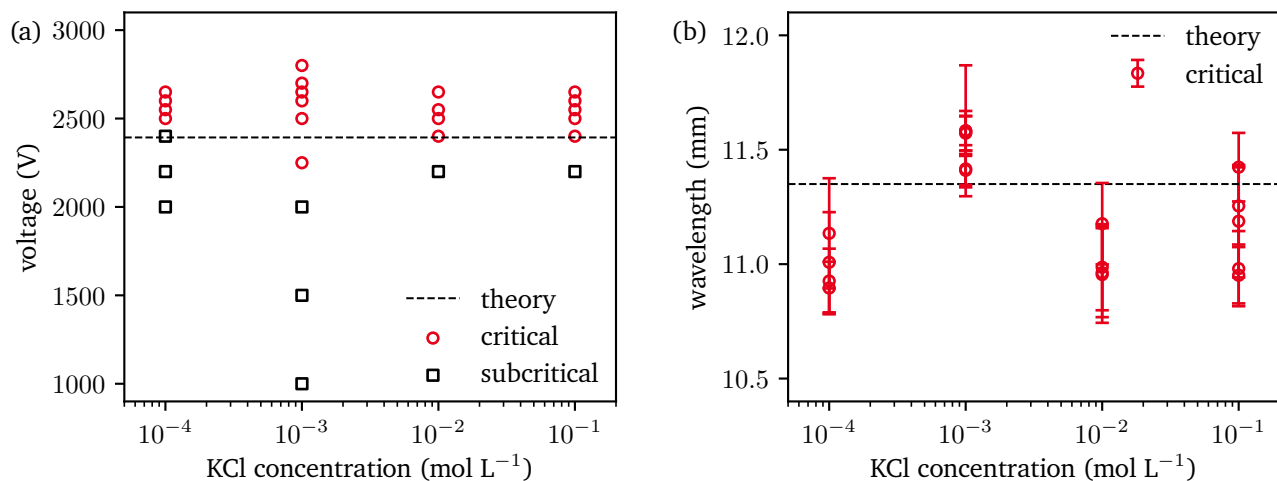


Figure 6.9: Influence of the salt concentration on the instability. (a) Comparison between the experimental stability map and theoretical predicted onset voltage amplitude $U_{\text{crit}} = 2393$ V obtained from the perfect-dielectric / perfect-conductor model. (b) Comparison between dominant pattern wavelength and theoretical predicted dominant wavelength $\lambda_{\text{th}} = 11.35$ mm obtained from the perfect-dielectric / perfect-conductor model. Error bars denote the standard deviation for the determined patterns within one experiment.

the lower phase is large. In order to verify that the conductivity of the lower phase has no influence on the results and that the perfect-dielectric / perfect-conductor assumption is applicable, the KCl-concentration is varied between 1×10^{-4} mol L⁻¹ and 1×10^{-1} mol L⁻¹. Then, experiments are performed using the silicone oil of 0.65 cSt, the lower liquid with 0 wt% glycerol, an upper layer thickness of 5 mm and a driving frequency of 10 Hz.

Figure 6.9(a) shows the stability map as the voltage over the ionic concentration, with the colors denoting whether the experiments were critical or subcritical. The theoretical predictions are shown as a dashed line corresponding to 2393 V. The experimentally observed critical voltage is not strongly affected by the salt concentration. While it appears to be slightly increased at $c_{\text{KCl}} = 1 \times 10^{-4}$ mol L⁻¹, it decreases slightly at $c_{\text{KCl}} = 1 \times 10^{-3}$ mol L⁻¹, overall indicating that it is rather the measurement uncertainty than a physical trend. Also, since the measurement principle relies on the interfacial gradients, it is possible that the onset of instability is not clearly distinguishable for small Faraday amplitudes, rendering the measurements less accurate in terms of the onset voltage. Nonetheless, the experimental data fits the theoretically predicted onset voltage reasonably well.

Figure 6.9(b) shows the dominant pattern wavelengths for critical experiments exhibiting Faraday instabilities compared to the theoretical predictions of $\lambda_{\text{th}} = 11.35$ mm. It is visible that the experiments yield results close to the theoretical predictions, and that the change of wavelengths for one driving amplitude is of similar magnitude as the difference of the average values for varying salt concentrations. Overall, the salt concentration shows no clear influence on the experimental results in the range of the studied molar concentrations, as would be expected if the perfect-conductor model was violated. Thus, the conductivity ratio of both liquids is sufficiently high to model the instability using the perfect-dielectric / perfect-conductor model.

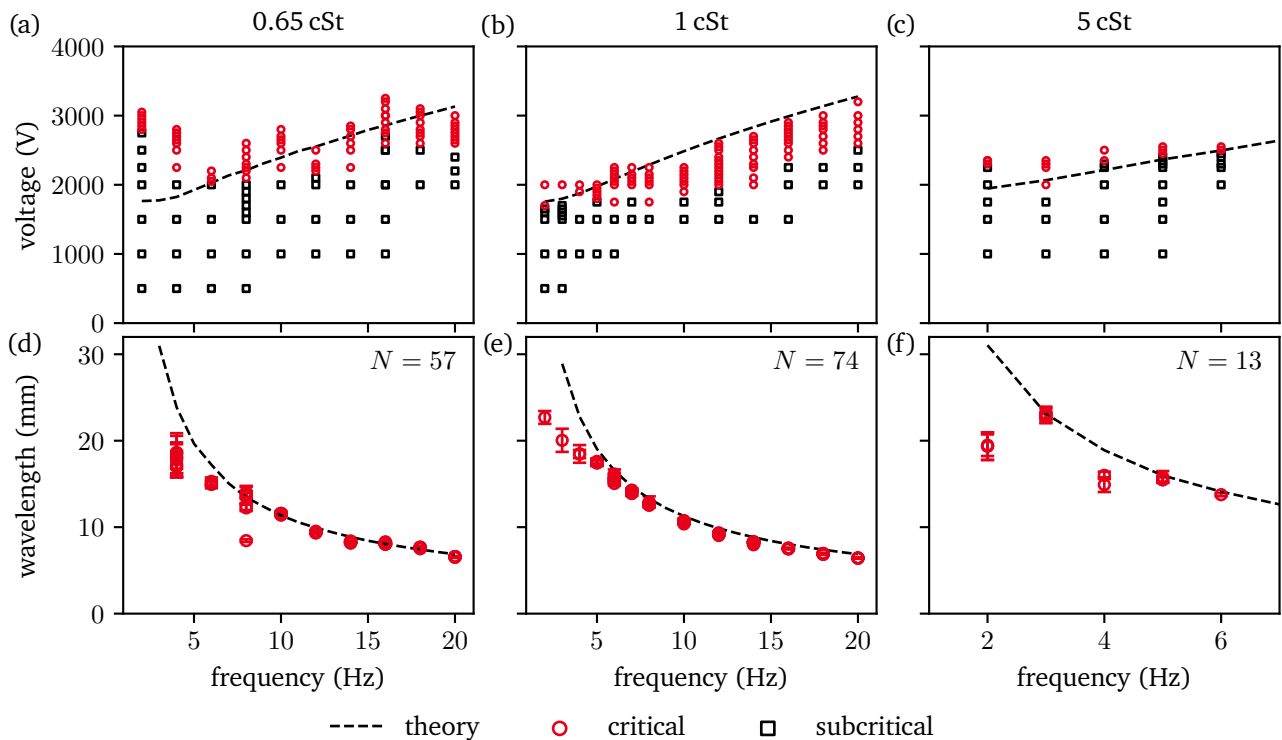


Figure 6.10: Influence of the dielectric's viscosity. The dielectric liquid is varied, while using DI-water with a KCl concentration of $c = 1 \text{ mmol L}^{-1}$. The theoretical results are shown as a dashed line. (a-c) Experimentally obtained stability maps. (d-f) Dominant pattern wavelengths. Error bars represent the standard deviation in each experiment. In the upper right corner, the number of critical experiments shown in the respective panel is shown.

6.4.2 Influence of the dielectric's viscosity

In this section, the influence of the viscosity is studied by changing the dielectric liquid, while simultaneously keeping the 0 wt% glycerol mixture as the electrolyte. By changing the upper liquid, other parameters than the viscosity are changed as well, e.g. the interfacial tension (see Table 6.2 and Table 6.3), however, the fluid data is used as input parameter of the theoretical model. Figure 6.10 shows the experimentally obtained stability map (critical / subcritical) as a function of the applied voltage amplitude U_0 and driving frequency, as well as the pattern wavelengths of the instability. For the 0.65 cSt oil (Fig. 6.10(a)), the stability shows partial agreement with the theoretical predicted onset voltage. Especially at low driving frequencies, a qualitatively different behavior is observed, with the voltage increasing for decreasing frequencies. At higher driving frequencies, the voltage shows better qualitative agreement, with Faraday instabilities setting in at lower voltage amplitudes than predicted. In addition, it is noteworthy that a large range of amplitudes exhibit Faraday patterns without exponentially growing instability amplitudes. In Fig. 6.10(d), the corresponding wavelengths are shown, which show good agreement to theory, especially at larger driving frequencies. Only at low driving frequencies, the experimentally obtained values are smaller than theoretical predictions. Here, the theoretically predicted wavelengths are of the same order as the size to the observation window, which is expected to lead to an underprediction of the wavelength. Also, it is visible that the dominant wavelengths are approximately constant for one driving frequency above the onset voltage.

Figures 6.10(b,e) show the results for the oil viscosity of 1 cSt. Similarly, the Faraday instabilities are observed for lower voltages than predicted by theory, with better qualitative agreement than in the

case of 0.65 cSt. Partially, the deviation of the absolute value of the onset voltage might be attributed to an inaccuracy of the upper layer thickness. Since the Maxwell-stress depends on the square of the electric field, it is strongly influenced by the layer thickness, and a decrease of the layer thickness by 0.25 mm leads to an increase of the resulting Maxwell stress by 10.8 %. The instability wavelength shows better agreement to theory than the voltage, with slightly smaller wavelengths than expected over the whole range of driving frequencies. At low driving frequencies, the wavelengths deviate from the theoretical predictions, similarly to the results with 0.65 cSt. Again, this can be rationalized by the wavelengths being on the order of the size of the region of observation. Overall, the wavelengths show good agreement to theory.

Figures 6.10(c,f) depict the results for an oil viscosity of 5 cSt, where it is important to note that the range of driving frequencies is much more restricted than for the other oils. At higher driving frequencies, no Faraday instabilities were obtainable, since the lower liquid made contact to the upper electrode without exhibiting Faraday waves by forming local Taylor cones. The reason for this behavior is unknown, but it suggests that a different instability mechanism became relevant. In the range of the obtained stability and wavelengths, good agreement is observed to theory, with deviations at the lowest driving frequency. Notably, fewer voltage amplitudes exhibited a Faraday instability without indefinitely growing instability amplitudes compared to lower viscosities.

Overall, the obtained pattern wavelengths match the theoretical predictions well, with notable exception at low driving voltages. Also, an increase of the driving voltage above the onset voltage had little influence on the observed pattern wavelengths. In terms of onset voltage, the agreement was less accurate, with qualitative differences occurring for the lowest driving frequencies.

6.4.3 Influence of the conducting liquid viscosity

The viscosity of the conducting liquid is varied by adding glycerol, which leads to a dynamic viscosity of 9.38 mPa s and 19.69 mPa s for 60 wt% and 70 wt% glycerol, respectively. As the dielectric liquid, the silicone oil with 0.65 cSt viscosity is used.

Figure 6.11 shows the resulting stability maps and wavelengths, with the data of 0 wt% glycerol corresponding to Fig. 6.10(a,d). At 60 wt%, the onset voltage shows good agreement to the theoretically predicted critical voltage. Notably, the range of Faraday patterns without growing amplitude decreases compared to 0 wt%. Also, with increasing viscosity, both the absolute onset voltage as well as the slope between onset voltage and driving frequency increase. As can be seen from Fig. 6.11(e), the pattern wavelengths show good agreement to theoretical predictions, with slightly lower experimental values on average, compared to theory.

A further increase of viscosity with 70 wt% glycerol leads to higher onset voltages, as is visible from Fig. 6.11(c). Similarly, the slope of the onset voltage with driving frequency steepens, which corresponds well to theory. Furthermore, the voltage range in which Faraday patterns can be observed without infinitely growing amplitudes becomes even smaller. The resulting wavelengths of the instability pattern match theory well, as can be seen in Fig. 6.11(f). Overall, the increasing viscosity leads to higher onset voltages required to drive the instability, and to smaller wavelengths at a constant driving frequency, consistent with theory.

6.4.4 Spatial structure of the instability pattern

The dominant pattern wavelength yields no information about the spatial structure of the instability, as the two-dimensional wave structures were reduced to a one-dimensional effective wavenumber k_{eff} . In

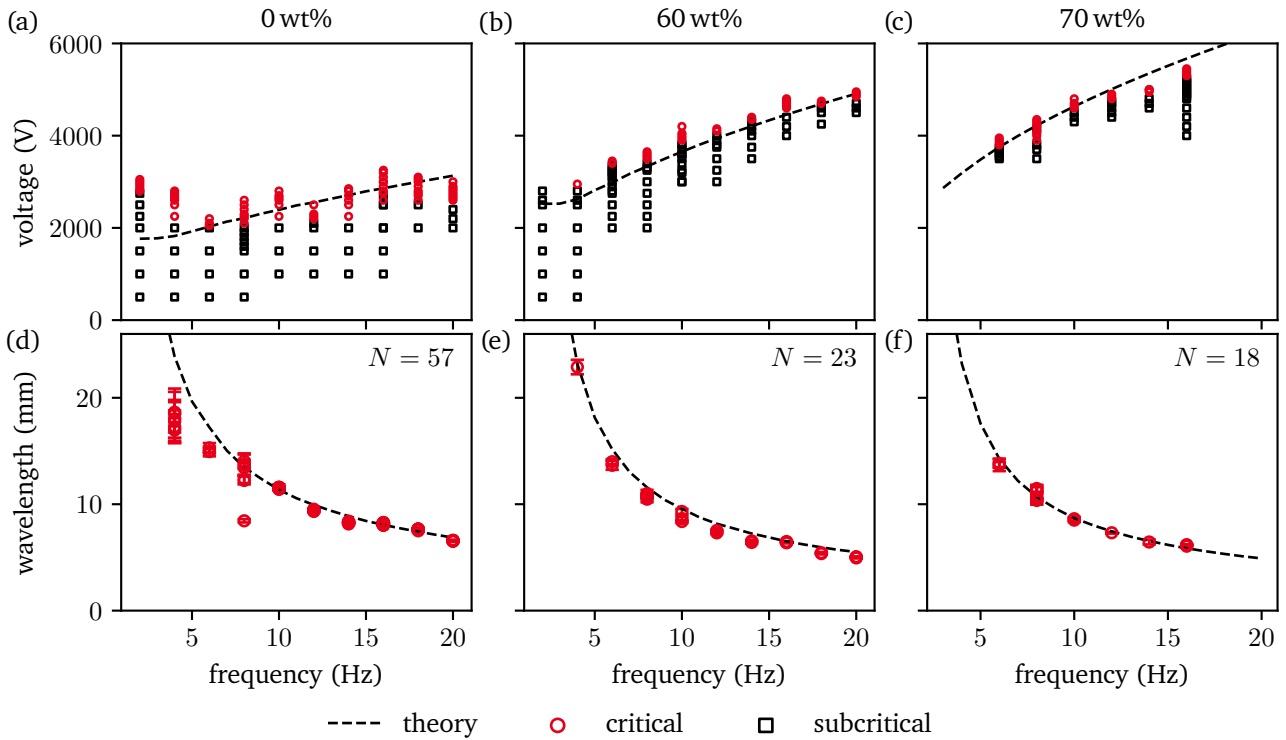


Figure 6.11: Influence of the electrolyte's viscosity. The viscosity of the conducting liquid is varied by changing the wt% glycerol, while using silicone oil with 0.65 cSt as the dielectric, and retaining the KCl concentration of $c = 1 \text{ mmol L}^{-1}$. The theoretical results are shown as a dashed line. (a-c) Experimentally obtained stability maps. (d-f) Dominant pattern wavelengths. Error bars represent the standard deviation in each experiment. In the upper right corner, the number of critical experiments shown in the respective panel is shown.

the following, the spatial structures of the instability patterns are analyzed, to supplement the theoretical validation of the wavelengths. The theory summarized in section 6.2.1 considers an infinite domain without lateral boundaries, with the influence of the domain represented by a restriction of lowest allowed wavenumbers. As is shown in the previous sections, theory and experiments agree with respect to observed pattern wavelengths nonetheless. As was discussed initially, the experiments of this chapter were also motivated by the results of Ward et al. (2019), who noted that no discrete modes were observed, and that for all unstable experiments, a multitude of wavelengths was observed. These results are investigated in the present section, with a domain of similar size as was used by Ward et al. (2019). Also, comparisons to observations made for mechanical actuation, as summarized in section 6.2.1, are drawn.

Before continuing to the experimental results, it is helpful to repeat the form of the surface harmonics shown in Fig. 6.4. For a circular cylinder, they follow the form of eq. 6.8, with an azimuthal node number l and a radial mode number n . The azimuthal mode number defines how many sectors in circumferential direction are present, as is visible in Fig. 6.4. An increase in l leads to an increase of waves in circumferential direction. The radial number n denotes how many waves are present in radial direction, increasing with n . A mode is associated with a typical wavenumber $k_{l,n}$, with different combinations of (l, n) potentially leading to nearly identical wavenumbers. The numerical order of wavenumbers (and their associated wavelengths) is not directly sorted by (l, n) , for example, the mode $(l = 6, n = 10)$ results in a wavelength $\lambda_{6,10} = 10.33 \text{ mm}$, and $(l = 6, n = 11)$ in $\lambda_{6,11} = 9.54 \text{ mm}$, whereas $(l = 2, n = 12)$ results in a much closer value of $\lambda_{2,12} = 10.22 \text{ mm}$. Thus, in the following discussion, the adjacency of

modes refers to wavelengths being nearly identical, and not to the adjacency in (l, n) . However, if one of the mode numbers is held constant while the other number is increased, the resulting wavelength decreases. Thus, especially at large wavelengths, only a discrete number of modes is attainable. The spectrum of available wavenumbers becomes more continuous for smaller wavelengths and increasing mode-numbers. For example, between 40 mm and 50 mm, only five discrete wavelengths are available, whereas between 30 mm and 40 mm already 11 discrete wavelengths are obtained.

In the following, the instability patterns with the largest amplitude are shown during the experimental dataset. They represent the instability at one given moment in time and contain no information about the long-time behavior and longevity of a pattern. Gluckman et al. (1993) showed that even instantaneously unordered systems can exhibit a highly-ordered long-time average, but in the following, only instantaneous patterns are analyzed. The interfaces are shown normalized, without the reconstructed amplitudes, since the information of the instability is contained in the spatial structure, not in the absolute amplitudes. Also, it allows much more compact representation. When comparing the experimental results to the surface harmonics, it is important to keep in mind that the observation region is restricted to the central region of the domain, with an approximate size of $3.5 \text{ cm} \times 3.5 \text{ cm}$. In the following, not for all experimental conditions the resulting patterns are shown, but only selected, representative modes. Other experimental conditions show qualitatively similar behavior.

Figure 6.12 depicts the instability patterns for the combination of silicone oil with 0.65 cSt and 0 wt% glycerol. At the top of each column, the theoretically expected wavelength λ_{th} for the given driving frequency is shown, and below each panel, the voltage amplitude as well as the measured pattern wavelength are noted. In each column, the patterns are sorted with increasing driving voltage amplitude. The instability patterns at a driving frequency of 8 Hz and 10 Hz show a mode form with an azimuthal mode number $l = 7$ and $l = 8$, respectively. Here, a circular structure of waves encloses an inner region of negligible amplitude. Identifying l is straight forward, but due to the restricted view at the center of the instability, the mode number n is not readily identified. For the driving frequency of 10 Hz, it is most likely the mode corresponding to $n = 8$, since the theoretically predicted wavelength $\lambda_{8,8} = 11.42 \text{ mm}$ is close to experimental observations, but since this value is only inferred from theory and not directly measured, no further identification of n is attempted. Also, these modes exemplify why the measurements of the wavelengths at low driving frequencies could potentially deviate from theory: Since the central region shows no significant amplitudes, the wavelength identification becomes less accurate. For lower n (larger wavelengths), the ring-like structure moves further to the boundary of the observation region, obscuring the measurement. Interestingly, the observed modes are a strong indication for the boundary influence, while simultaneously, the experimentally obtained wavelengths are accurately predicted by theory assuming an unbounded domain. Next, comparing the instability patterns for one fixed driving amplitude shows that the patterns can change strongly while only small changes of wavelength occur. For example, at 10 Hz, the increase of amplitude from 2600 V to 2700 V leads to a different spatial structure that is not well represented by the pure modes, but the wavelength remains similar. Another interesting observation is the fact that not all modes correspond to the pure boundary-dominated modes, as is illustrated by the mode at 18 Hz and 3000 V. Similarly, it is not a clear order-disorder transition, since for a higher driving amplitude, a boundary dominated oscillation is again visible. Overall, the spatial structures of the instability at 0.65 cSt and 0 wt% glycerol show a strong influence of the boundary over the whole range of studied driving frequencies.

Figure 6.13 shows the instability patterns for the combination of silicone oil with 1 cSt and 0 wt% glycerol. Again, with slightly increased viscosity of the dielectric phase, the boundary influence is still strongly visible, resulting in instabilities of the form of surface harmonics, e.g., at 6 Hz and 2000 V, at 8 Hz and 2150 V, and at 14 Hz and 2500 V. Also, in addition to single surface harmonics, other highly ordered patterns can be observed. At 8 Hz and 2100 V, the pattern shows an anti-symmetry with respect to an axis that is tilted approximately 30° with respect to the vertical direction. This can be explained by

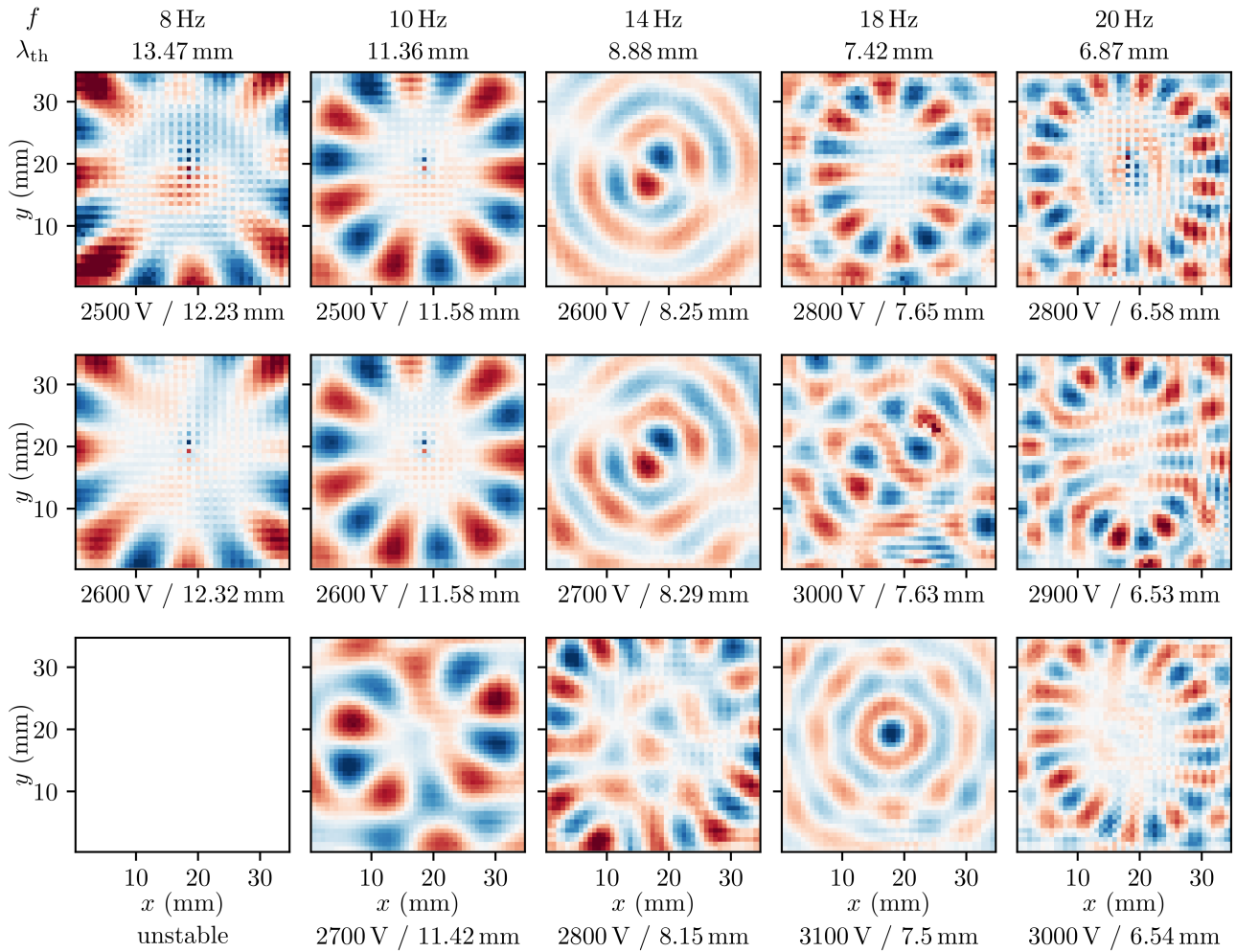


Figure 6.12: Reconstructed spatial structure of the instability using silicone oil with a viscosity of 0.65 cSt and 0 wt% glycerol. The interface deviation Δh is normalized, with blue denoting negative interface deflections and red positive deflections. The theoretical prediction of the wavelength for the given driving frequency is shown at the top of each row. Below each panel, the respective driving amplitude as well as the measured pattern wavelengths are shown.

mode-mixing of adjacent modes with similar wavelength. For example, if the modes with $(l = 7, n = 7)$ with $\lambda_{7,7} = 13.18$ mm and $(l = 5, n = 8)$ with $\lambda_{5,8} = 13.0$ mm are superposed, a similar instability pattern can be observed. Thus, it is likely that both modes were actuated by the driving voltage and frequency and lead to a mixed surface response. Other examples of potentially superposed modes can be seen at 6 Hz and 2100 V, 8 Hz and 2250 V as well as 18 Hz and 2600 V. In principle, a systematic classification of all modes could be attempted, but in practice, one has to account for rotation of the modes with respect to each other. Therefore, the evaluation becomes computationally straining, with little additional information. As a result, a systematic classification of mixed modes is not attempted, and it is left off with the notion that superposition of modes can occur, if their wavelengths are similar, allowing simultaneous excitation. Overall, the patterns at 1 cSt and 0 wt% glycerol show good agreement to theoretical predicted wavelengths. The boundary influence is clearly visible, as both single surface harmonics as well as superpositions are observed over the whole range of the driving frequencies.

Figure 6.14 shows the resulting patterns for the combination of silicone oil with 0.65 cSt and 60 wt% glycerol. First, it is important to note that the voltage range of Faraday instabilities with meta-stable

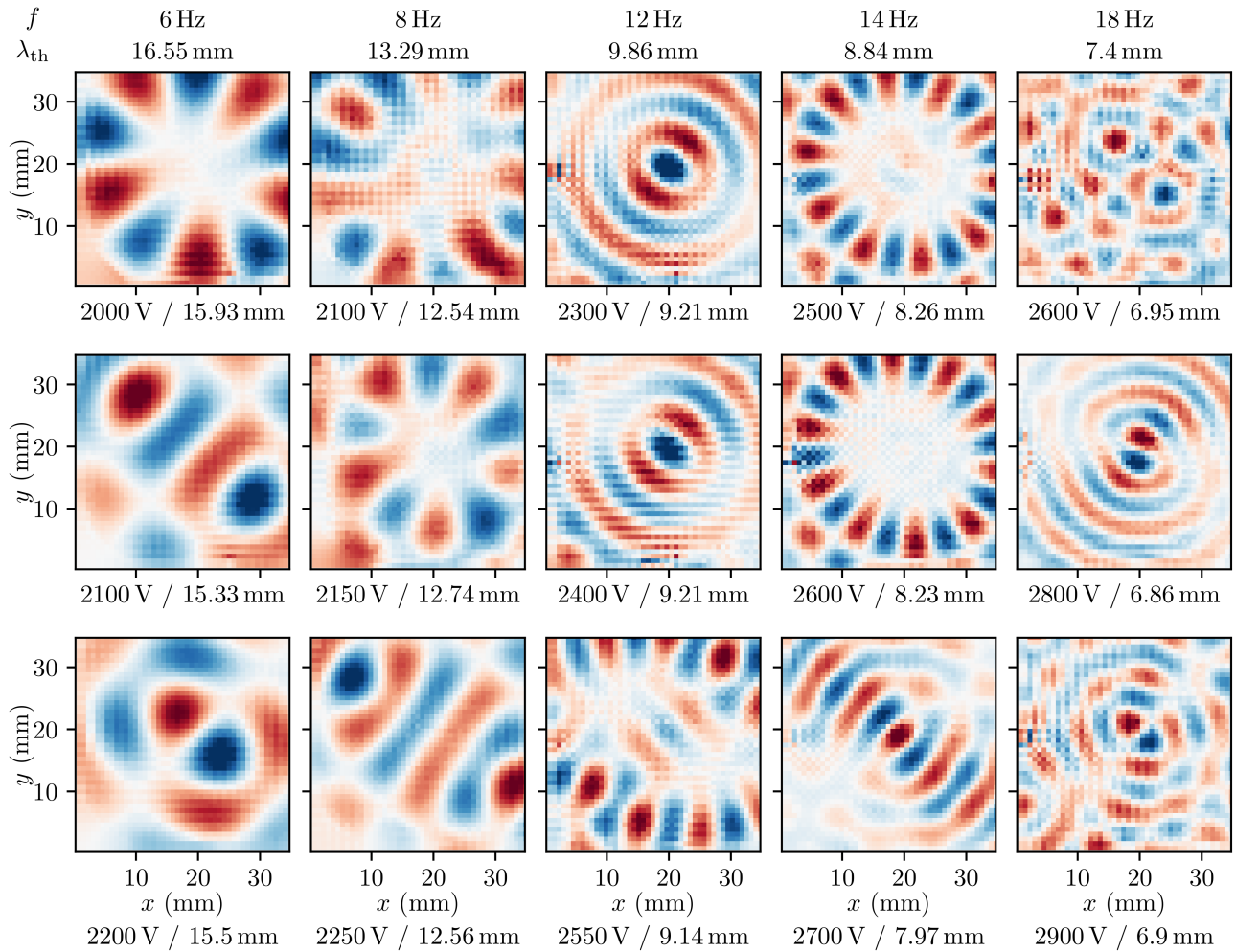


Figure 6.13: Reconstructed spatial structure of the instability using silicone oil with a viscosity of 1 cSt and 0 wt% glycerol. The interface deviation Δh is normalized, with blue denoting negative interface deflections and red positive deflections. The theoretical prediction of the wavelength for the given driving frequency is shown at the top of each row. Below each panel, the respective driving amplitude as well as the measured pattern wavelengths are shown.

amplitude is reduced, and therefore only two patterns per driving frequency are shown. Up to 10 Hz driving frequency, the instability pattern shows distinct boundary influence, as is visible from the pattern symmetry. At higher driving frequencies, the patterns show no boundary influence, and resemble patterns observed for mechanically induced Faraday instabilities (Edwards and Fauve, 1994). At 12 Hz, 18 Hz, and 20 Hz, a hexagonal structure is visible, and at 16 Hz an initially structured system becomes chaotic. Overall, the increase of driving frequency as well as lower-liquid viscosity renders the instability boundary independent, as edge-effects are dampened out more quickly. A similar trend was observed by Edwards and Fauve (1994) for mechanically actuated Faraday waves.

To summarize, the instability is boundary dominated for nearly the whole range of investigated conditions, with exceptions at higher viscosities and driving frequencies. Both for boundary-dominated and boundary-independent conditions, the agreement of the wavelengths to unbound theory is good. Also, the electrostatically forced Faraday instability exhibits patterns similar to those observed for mechanically actuated Faraday instabilities. In addition to the patterns which were observed here, it is likely that other effects might be relevant for electrostatic actuation as well, including different spatial structures, such

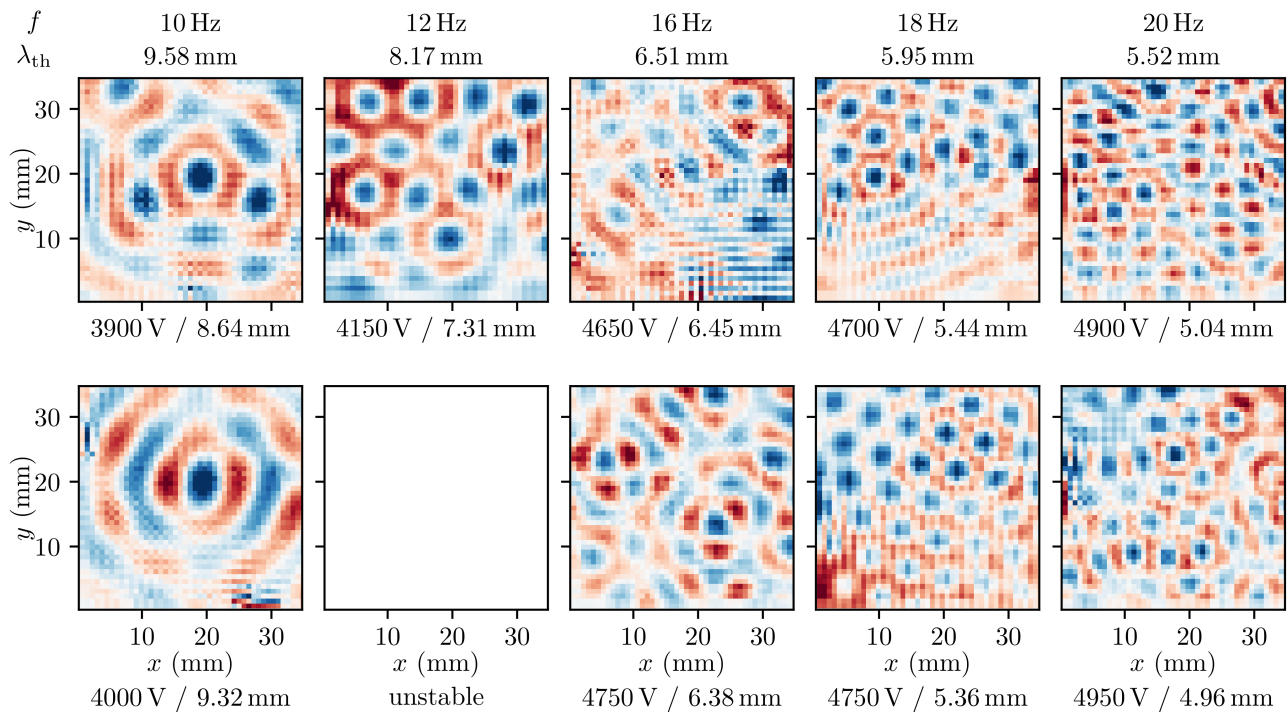


Figure 6.14: Reconstructed spatial structure of the instability using silicone oil with a viscosity of 0.65 cSt and 60 wt% glycerol. The interface deviation Δh is normalized, with blue denoting negative interface deflections and red positive deflections. The theoretical prediction of the wavelength for the given driving frequency is shown at the top of each row. Below each panel, the respective driving amplitude as well as the measured pattern wavelengths are shown.

as rectangular patterns, quasi-patterns (Edwards and Fauve, 1994) and superlattices (Douady, 1990; Kahouadji et al., 2015). These might be especially interesting for applications such as thin film patterning (Zhao et al., 2019) and creating defined patterns of tracer in the lower phase (Serpooshan et al., 2017).

6.5 Discussion

6.5.1 Comparison to observations of Ward et al.

The observations made by Ward et al. (2019) motivated parts of this work, as the authors noted the absence of discrete modes in their experiments, and the existence of a multitude of wavelengths simultaneously in all Faraday experiments. Since our experimental setup adapts their experimental cell, both the radial and height-dimensions are similar in both experiments. Also, the silicone oil with a viscosity of 1.5 cSt used by Ward et al. as a dielectric liquid is closely matched by the viscosities of 1 cSt and 5 cSt in the present experiments. Deviating from the observations by Ward et al., the experiments presented here showed a significant influence of the boundary, leading to the existence of discrete modes. Also, independent of the boundary influence, a dominant wavelength could be observed, as the systems were spatially highly organized.

The first potential reason for the different observations relates to the mode of excitations of the waves. The experimental procedure described here induced waves at a constant driving amplitude, and if the Faraday instability did not form within 3 min, the experiment were taken to be stable. In the case of

Ward et al. (2019), the Faraday instability was induced by using a driving amplitude well above the critical voltage, and the critical voltage was found by decreasing the amplitude until the Faraday waves vanished. In principle, it is possible that the latter mechanism induces a wider spectrum of wavelengths if the excitation occurs far above the critical voltage. Then, the patterns could exhibit the described multitude of wavelengths. However, as is visible from the experiments reported here, the wavelengths show only a small change for different driving voltages above the critical voltage, and remain nearly constant for a constant driving frequency. If the Faraday waves induced well above the critical voltage would result in a multitude of pattern wavelengths, similar observations should be made in the setup used in this work. Thus, it is unlikely that this variation of the experimental protocol resulted in the different observations.

A second potential reason relates to the observation mode of Ward et al. from the side. As was noted by the authors, the observation of the instability through a curved cylinder leads to refraction, additionally obscuring the interface. As was additionally noted, they could not discern the wavelengths to any accuracy. However, as is visible from the experiments presented in this chapter, it is very likely that the experiments by Ward et al. were still showing significant boundary influence, and exhibited discrete modes. If one of the discrete modes described in Fig. 6.4 was superposed by edge-waves and additionally obscured by refraction, it might have appeared to be a chaotic system, with a multitude of wavelengths present in the system. While Ward et al. could not observe the discrete modes, their agreement between theoretically predicted onset voltage and experimental measurements is evident and exceeds the agreement observed in the experiments presented here. The experiments by Ward et al. and from this work focus each on different aspects of the instability, and combined they provide a solid verification of the theory accounting for viscous effects.

6.5.2 Robustness analysis of wavelength determination algorithm versus measurement uncertainty

The extraction of the dominant wavelengths relies on the reconstruction of the interface from experimental data of the interface gradients, which is inherently noisy. As is visible for example in the experimental data of Fig. 6.7(b,c), the displacement field exhibits maximum values on the order of a few pixel. This is due to the small difference of the refractive indices, and the thin layer thickness of the upper layer of 5 mm. While the grid point detection implements a subpixel-detection, a measurement error of a single pixel is already on the order of the displacement field amplitude, and can even exceed locally the measured displacement field. Therefore, it is important to test the robustness of the extraction algorithm versus measurement error.

In order to control the noise, an artificial data set is created and random noise of a defined maximum value is introduced. The original interface is chosen as

$$\Delta h = A_0 \left(\cos \left(\frac{2\pi k_0}{1024 \text{ px}} x \right) + \cos \left(\frac{2\pi k_0}{1024 \text{ px}} y \right) \right), \quad (6.19)$$

where the amplitude was set to $A_0 = \frac{1 \text{ mm}}{36 \text{ mm}} \times 1024 \text{ px}$, the wavenumber as $k_0 = 5$, corresponding to experimental observations made on a $1024 \text{ px} \times 1024 \text{ px}$ domain. The original interface is shown in Fig. 6.15(a). The gradient of the interface is obtainable analytically, and additionally, noise is added as

$$\nabla h = -\frac{2\pi A_0 k_0}{1024 \text{ px}} \left(\begin{pmatrix} \sin \left(\frac{2\pi k_0}{1024 \text{ px}} x \right) \\ \sin \left(\frac{2\pi k_0}{1024 \text{ px}} y \right) \end{pmatrix} + \gamma_{\text{rel}} \begin{pmatrix} R \\ R \end{pmatrix} \right), \quad (6.20)$$

where γ_{rel} is the amplitude of the random noise, and the function R results in a random number in the interval $[-1, 1]$ with an equal probability of all values. The noise amplitude γ_{rel} denotes how large the

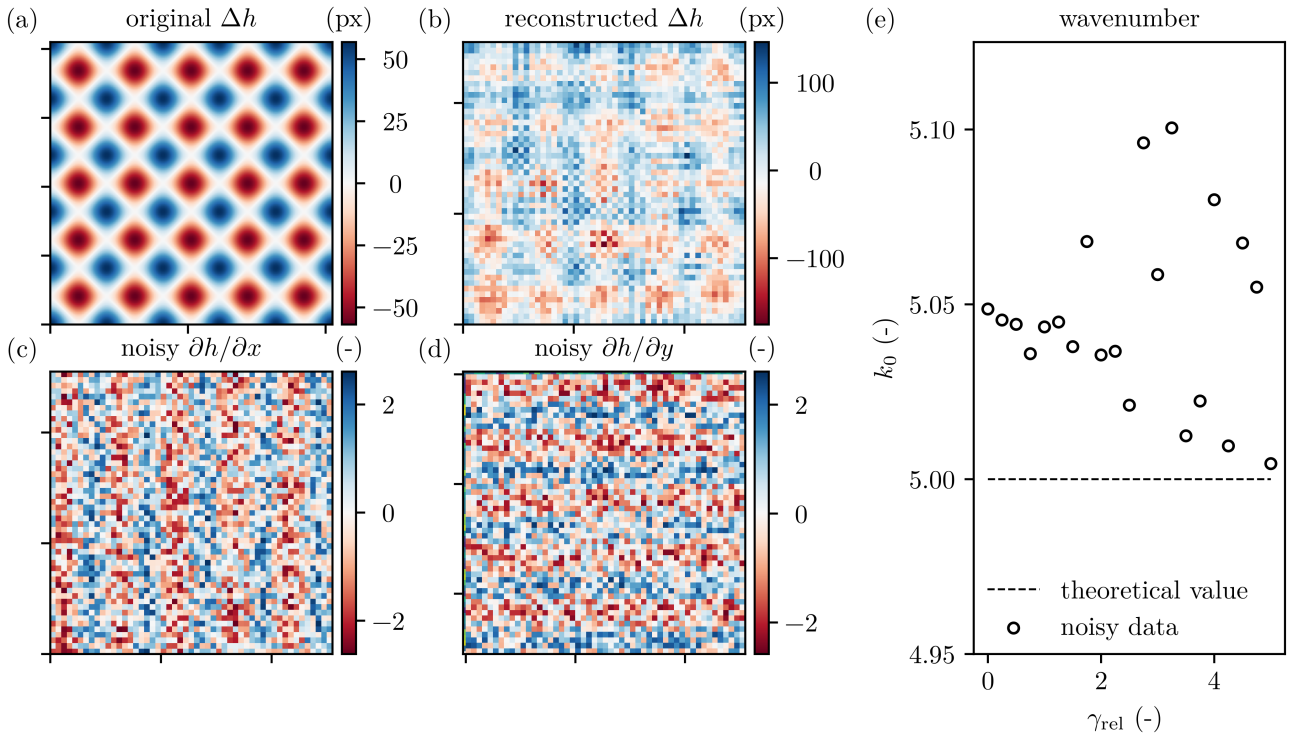


Figure 6.15: Robustness of wavelength extraction algorithm versus noise. (a) Artificial interface in a $1024 \text{ px} \times 1024 \text{ px}$ domain. (b) Reconstructed interface on a reduced grid of 51×51 grid points, for the relative error amplitude of $\gamma_{\text{rel}} = 2$. As is visible, the reconstructed interface becomes noisy, with locally strong deviations from the original data. (c,d) Corresponding gradients from which the interface in (b) is reconstructed. The noise corresponds to $\gamma_{\text{rel}} = 2$. (e) Variation of the extracted wavenumber with relative error amplitude γ_{rel} .

noise is compared to the gradient, with values $\gamma_{\text{rel}} > 1$ denoting that the noise can exceed the maximum value of the gradient. Exemplary noisy gradients are shown in Fig. 6.15(c,d) for a specific value of $\gamma_{\text{rel}} = 2$. Then, on the noisy data, the algorithm outlined in section 6.3.3 is applied, leading to a reconstructed interface as shown in Fig. 6.15(b). Here, it is visible that the absolute values of the interface are strongly influenced by the noise, and show locally strong deviations from the original interface. Nevertheless, the qualitative structure of the interface is recovered, even for large noise-levels.

Figure 6.15(e) shows the resulting wavenumbers for varying noise amplitudes γ_{rel} . Here, two effects are noteworthy: First, the reconstructed wavenumber shows no large variation even for noise levels exceeding the original surface gradient. While the reconstructed interface shows strong deviations, the detected wavenumbers are robustly reproduced. Second, even for low noise, a deviation from the original wavenumber is visible, on the order of 1%. This is probably due to the fitting of the wavelength to the power spectrum. As outlined, a fit is performed to the peak of the power-spectrum using a Gaussian distribution, and since the peak-width is only a few wavenumbers large, the small sampling size leads to the deviation of the wavenumber. Nevertheless, the algorithm shows robust wavenumber detection despite noise, and allows the evaluation of images even with small displacement fields.

A second potential reason for inaccurate wavelength prediction stems from the nature of Fourier-transforms. The terms $k_x/3N$, $k_y/3N$ in eq. 6.17 represent how often a wave fits into the domain of observation. Thus, the image is separated into discrete spectra of harmonic functions which fit between one time and up to $3N - 1$ times into the domain of side length $3N$, and an additional constant offset. Thus, at low wavenumbers, the difference of a dominant wave fitting n or $n + 1$ into the domain

Table 6.4: Mode numbers, corresponding wavelengths and critical voltage in the range between 40 mm and 48 mm for a container diameter of 125 mm, sorted by wavelength.

l	n	$\lambda_{l,n}$ (mm)	U_{crit} (V)
8	1	40.71	2883 V
4	2	42.31	2663 V
7	1	45.78	2091 V
1	3	46.00	2044 V

corresponds to a large change of wavelength. At high wavenumbers on the other hand, the change of wavelengths is small. Typically, in the experiments presented here, the waves fit only a few times into the domain, and thus the resolution at large wavelengths is smaller. Therefore, small errors in wavenumbers might lead to more pronounced errors in wavelength. However, as seen in Fig. 6.15(e), the detection of the wavenumbers yields reasonable results, even at a small wavenumber $k_0 = 5$.

6.5.3 Potential influence of the discrete modes on the stability map

If the boundary influence of the domain dominates the spatial pattern, not every wavelength is accessible by the instability, since the modes exhibit discrete wavenumbers with corresponding wavelengths. The theoretical values obtained for the dominant pattern instability, however, are obtained assuming that every wavenumber can be achieved by the system. Revisiting the instability for 0.65 cSt and 0 wt% glycerol, a qualitative deviation of the stability map is visible at 2 Hz. The stability range of the voltage versus wavenumber is shown in Fig. 6.3(a). Theoretically, the instability is assumed to show a dominant wavelength of 46.52 mm. In Table 6.4, the modes and their corresponding wavelengths between 40 mm and 48 mm are shown, emphasizing the discrete nature of the accessible wavelengths. The closest wavelength to the theoretical prediction corresponds to the mode ($l = 1, n = 3$) with a wavelength of $\lambda_{1,3} = 46$ mm. The linear stability analysis shows that the critical voltage corresponding to a wavelength of 46.0 mm results in 2044 V, instead of 1765 V for 46.65 mm. Thus, it is possible that the shift to higher onset voltages at the small driving frequencies can be partially attributed to the discretized nature of the accessible wavelengths. However, comparison to Fig. 6.10(a) also shows that a much larger shift is observed than would be expected from Table 6.4. Thus, it is likely that a different mechanism has an additional influence on the deviation from theory. As with increasing driving frequency the wavelengths decrease, more modes become accessible per wavelength range, as outlined in section 6.4.4, and thus the effect is expected to become negligible.

In order to experimentally validate that a wavelength selection process can have an influence on the stability, it would be beneficial to select an appropriate mode, which is sufficiently isolated in terms of wavelengths. For example, the ($l = 4, n = 2$) mode could be used. Then, one has to identify which driving frequency f corresponds to the wavelength of the mode using the stability theory, and vary the driving frequency closely around this value. If the onset voltage of instability shows a local minimum at the corresponding frequency, the discrete nature of the modes has an influence onto the onset voltage. As a similar influence has been observed for mechanical actuation (e.g. Batson et al. (2013b)), it is likely that it will be visible for electrostatic actuation as well.

6.6 Summary and conclusion

In this chapter, the instability at an interface of a dielectric and a conducting liquid, that is induced by a spatially homogeneous, but harmonically oscillating electric field perpendicular to the interface, was studied, and a focus was placed on the observed wavelengths and spatial structure. First, the analogy between electrostatic and mechanical actuation was shown by repeating the key results of the stability analysis assuming inviscid media. Then, the theoretical results of Bandopadhyay and Hardt (2017) were summarized, as they provide the theoretical background for comparison. Also, the observations made for mechanical actuation with respect to the spatial distribution of the instability patterns were summarized. Next, the experimental setup based on light refraction was introduced, jointly with the data evaluation algorithm. Using the refracted image of a known grid, the interface gradients were measured, and using the fluid data as well as system parameters, the interface was reconstructed. From the reconstructed images, the dominant wavelengths were obtained by identifying peaks of the Fourier power spectrum. Following, the onset voltage and dominant wavelengths were measured for varying salt concentrations in the conducting liquid, varying dielectric liquids, and varying glycerol mass fractions in the conducting liquid. The theory showed fair agreement with the onset voltage of instability, and good agreement with respect to the wavelengths. Also, the existence of discrete instability modes was shown, and the superposition of different modes of similar wavelengths was observed. Only for the larger viscosities of the lower phase and larger driving frequencies, the instability showed a boundary independent behavior. These results were compared to the findings of Ward et al. (2019), and potential reasons for the differences of observations were presented. Finally, the robustness of the wavelength detection algorithm was analyzed versus measurement errors, and the potential influence of the discrete modes at large wavelengths on the stability map was studied.

In future work, more complex excitation frequency signals can be investigated. So far, only purely harmonic signals with one driving frequency were applied. Upon excitation with superpositions of different frequencies as well as superpositions of DC and AC signals, more complex mode-mixing is expected, and a variation of the interface oscillation should occur, accompanied by a wavelength change. In that context, phenomena such as superlattices and quasi-patterns are expected, as they occur for mechanical oscillations (Edwards and Fauve, 1994). Also, it might be interesting to investigate the potential influence of the discrete instability modes, as outlined in section 6.5.3 and study the response of one discrete mode to excitation variations in more detail. Furthermore, phenomena which are only loosely related to Faraday-instabilities might be interesting to study. For example, in mechanically vibrated domains, it has been found that droplets deposited on the interface are not coalescing, and exhibit a walking behavior for specific parameters (Couder et al., 2005). In a recent work by Fernández-Mateo and Pérez (2021), the phenomena of walking droplets on both electrostatically and mechanically actuated baths was analyzed theoretically, and its transition to experiments might be worthwhile.

7 Instabilities at liquid-liquid interfaces under inhomogeneous DC fields

In the previous chapter, the instability of a liquid-liquid interface actuated by a spatially homogeneous, harmonically oscillating electric field was studied. In this chapter, the instability of a liquid-liquid interface actuated by a time-constant, but spatially inhomogeneous electric field is investigated, where a pin electrode is placed inside a dielectric liquid, above an electrically contacted interface. Aside the classical Taylor cone, an alternative breakdown mode exists, where the surface moves away from the pin electrode and forms a surface depression, with cones emerging from the rim of the dip. Relating optical imaging of the surface depression and electric current measurements of an submerged electrospray above the liquid-liquid interface, the impinging background flow of the dielectric is identified as the governing mechanism. Finally, by modeling the charge transport numerically, the surface depression is reproduced, and the role of the space charge as a regulatory mechanism is identified.

The work presented in this chapter was funded by the German Research Foundation (DFG, Grant No. HA 2696/45-1). The liquid properties presented in section 7.3.2 were measured by Maximilian Hartmann and Frank Plückebaum. The replacement cell presented in section 7.3.1 is a modification of a setup implemented by Julian Keller as part of his Bachelor's thesis, supported by Jörg Bültemann (Keller, 2020). All other work presented in this chapter represent distinct contribution of the author, including the experimental measurements, data evaluation, and the numeric modeling. Helpful discussions with Maximilian Schür regarding the numerical implementation are acknowledged. In his function as supervisor, Steffen Hardt provided valuable input during the whole process of this project. The main body of this work is published in Dehe and Hardt (2021).

7.1 Introduction

Electric fields acting on fluidic interfaces can lead to deformation and ultimately, above a certain critical field strength, to disintegration, which has been studied for more than a century (Zeleny, 1917). The electric field leads to a Maxwell stress at fluidic interfaces, and in order to maintain the stress balance, the interface deforms and capillary forces counteract the electrostatic force. At the interface between a dielectric and a conducting fluid, a conical cusp forms, which is initially stationary. Upon increase of the electric field strength, the cusp tip radius decreases in order for capillary forces to increase. The tip forms a singularity, which would be stable for liquids of infinite conductivity. However, due to the tangential electric stress at the interface, the surface charges are set into motion, and the surface convection current is balanced by conduction through the central part of the cusp. In case that the conductivity is unable to balance the tangential movement of the interface, a fine jet or droplets are issued from the tip of the cusp, leading to electrohydrodynamic (EHD) tip streaming. Today, the conical cusp is referred to as *Taylor cone*, due to the seminal work by Taylor (1964). Since then, EHD tip streaming has been utilized in a wide range of technical applications, such as liquid atomization (Grace and Marijnissen, 1994), electrospinning (Teo and Ramakrishna, 2006) and printing (Park et al., 2007). Potentially, the

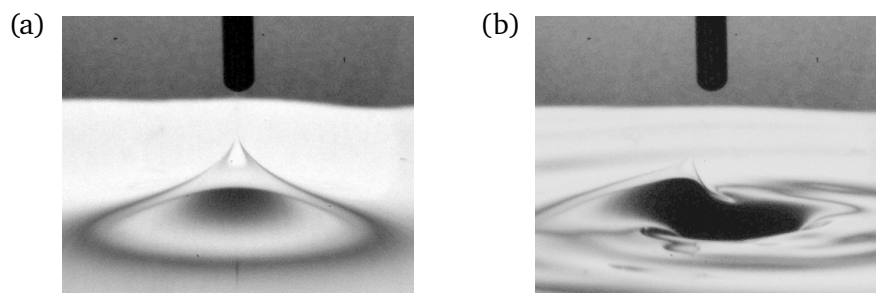


Figure 7.1: Exemplary instability modes of a liquid-liquid interface due to a pin electrode positioned above the interface. The upper dielectric liquid is a silicone oil of 0.65 cSt viscosity, the lower liquid is a grounded aqueous KCl solution with an ionic concentration of 10 mmol L^{-1} . Additionally, the non-ionic surfactant Triton-X100 was added to the conducting liquid ($6 \mu\text{mol L}^{-1}$). (a) The system forms a Taylor cone, and a fine jet of droplets is issued from its tip. (b) The system forms a surface depression below the electrode, and from its rim, a Taylor cone emerges towards the electrode. This image corresponds to Fig. 7.4(b). Adapted figure with permission from Sebastian Dehe, and Steffen Hardt, *Phys. Rev. Fluids*, 6(12), 123702, 2021. Copyright (2021) by the American Physical Society.

largest impact was made in mass spectrometry (Fenn et al., 1989), enabling the fast characterization of biological molecules. John Fenn was awarded a share of the Nobel Prize in Chemistry in 2002 for the electrospray ionization in mass spectroscopy.

Since EHD tip streaming is wide-spread in technical applications, a thorough understanding of the underlying physics is crucial. Therefore, simple prototypical experiments can be used, with easily controllable parameters. One example of such prototypical experiments involves a pin electrode, placed above a fluidic interface, where between the pin electrode and the lower conducting fluid an electric potential difference is applied. Such a system was used in a numeric investigation of the instability of a liquid film by Collins et al. (2008), revealing the existence of a scaling for the droplet charge after pinch-off. Similar scaling laws were observed in a corresponding numerical setup for liquid-liquid systems by Pillai et al. (2016). This chapter is motivated by peculiar observations made by Aditya Bandopadhyay in an experimental setup, where a pin electrode was placed within a dielectric liquid, above a conducting liquid connected to a second electrode. Upon application of a voltage difference, in some situations, a Taylor cone formed at the liquid-liquid interface, as would be expected from theoretical considerations. However, in the same setup, the system sometimes exhibited a different instability mechanism, with the interface moving away from the electrode, forming a localized depression. At later stages of the break-down mechanism, one or multiple cones emerged from the rim of this depression, ejecting droplets towards the electrode. An illustrative breakdown is shown in Fig. 7.1, where the system exhibits under similar conditions two alternative breakdown modes. As the appearance of the surface depression (or dimple) was observed predominantly in systems with additional surfactants, the initial hypothesis for the formation of the surface dimples related to surfactant effects, but further investigations were required to supplement these initial observations. In the following chapter, the underlying mechanism of the surface depression is investigated, demonstrating that charged droplets in the dielectric liquid lead to a background flow, which can significantly alter the breakdown mode.

In the previous chapter, the instability at a liquid-liquid interface induced by a spatially homogeneous, time-dependent electric field was studied. In this chapter, the instability at a liquid-liquid interface due to a time-constant, but spatially inhomogeneous electric field is analyzed, with a specific focus on the viscous effects in the background fluid. Specifically, the following questions are addressed: What is the governing mechanism of the formation of the surface depression below the electrode? What is

the influence of the disperse droplets on the instability? How can the surface depression be studied in a more systematic manner? And can the formation of the depression be reproduced using simple order-of-magnitude estimates? Therefore, the remainder of the chapter is organized as follows: In section 7.2, the fundamental principle of EHD instabilities at fluidic interfaces is reviewed qualitatively. In section 7.3, the experimental setup and evaluation algorithm is presented. In section 7.4, EHD tip streaming experiments are presented to highlight the different breakdown modes. Then, in section 7.5, the influence of parameter variations on the surface depression are studied, using a submerged electrospray to controllably introduce charged droplets into the system. Following, in section 7.6 a simple numerical approach is used to reproduce the size of the surface depression, confirming the working hypothesis of the governing mechanism. Finally, a summary and outlook are provided in section 7.7.

7.2 Fundamentals of electrohydrodynamic tip streaming

Electrohydrodynamic tip streaming describes the ejection of a fine jet or stream of droplets from the tip of a conical structure, which is induced by electric fields acting on the interface. For a perfectly conducting liquid, the electric field is directed perpendicular to the interface. The electrostatic solution of the electric potential in the vicinity of an equipotential cone was first described by Taylor (1964), assuming a balance between electrostatic and capillary stress at the interface of an spheroid (water droplet) immersed in a dielectric medium. A schematic of the cone-tip is shown in Fig. 7.2(a), and it describes the stable configuration of a cone with an equipotential surface. In short, requiring that the capillary stress, Maxwell stress and pressure jump at the interface of a cone balance each other, the electrostatic potential results in (Fernández de la Mora, 2007; Taylor, 1964)

$$\phi(r, \theta) = a_0 r^{0.5} P_{1/2}(\cos \theta), \quad (7.1)$$

where $P_{1/2}$ denotes the Legendre function of order $1/2$, and the constant a_0 follows as

$$a_0 = 0.552 (\epsilon_0 / \gamma)^{0.5}. \quad (7.2)$$

Here, ϵ_0 denotes the dielectric permittivity of the surrounding fluid, and γ the interfacial tension between the liquids. As it is required that the cone-surface is an equipotential surface, only one possible angle θ_T exists, where $P_{1/2}(\cos \theta_T) = 0$, which results in the well-known conical angle of $360^\circ - 2\theta_T = 98.6^\circ$. Experimentally, its validity was observed by Taylor. The analysis of Taylor is based on the assumption that the liquid from which the cone forms is perfectly conducting, and that the cone itself is stationary. While the electric potential at the cone surface results in an equipotential interface, the resulting electric field becomes singular at the tip of the cone (Fernández de la Mora, 2007), thus leading to droplet ejection. Thus, the electrostatic solution is an approximation of the real situation close to the emission of droplets or a jet from the interface. As the stationary solution yields no information about the dynamics of the surface disintegration, different emission modes of EHD tip streaming will be discussed below.

In a more recent work, the onset of EHD tip streaming from a liquid film subjected to a perpendicular electric field was studied using numerical simulations of both perfect conductors and leaky dielectrics (Collins et al., 2008). Its findings are noteworthy, because the effects of conduction and tangential shear stress become apparent in the results. Upon the formation of a cusp, the tip curvature increases, until a singularity is formed. In case of a perfectly conducting liquid, the increasing capillary pressure is balanced instantaneously by additional charges introduced by conduction, and no emission of droplets is observed. If the liquid is assumed to exhibit a finite conductivity, the cusp forms as well, but the acceleration by tangential electric stress leads to an increase of convective charge transport along the surface of the cone, overcoming conduction. The strong tangential electric shear stress leads to an acceleration of the fluid

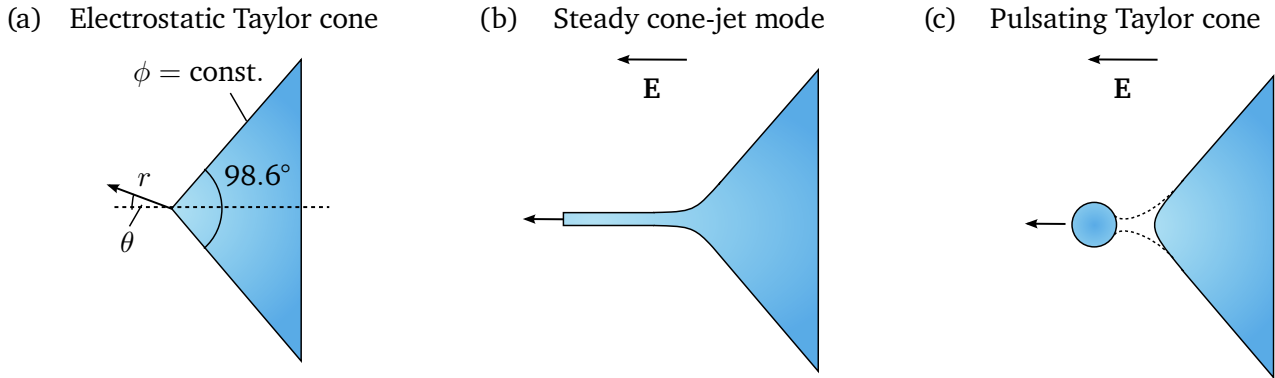


Figure 7.2: Schematic of different operating modes of a Taylor cone. A conducting liquid (blue) is emitted into a second liquid or gas by means of an electric field. The principle direction of the electric field is indicated at the top of the sketch, denoting the initial electric field direction, without considering the changes introduced by the presence of the cone. (a) Stationary Taylor cone of a liquid with infinite conductivity following Taylor (1964). The cone takes the characteristic cone-angle of 98.6° , and no emission of liquid occurs. (b) EHD tip streaming in the steady cone-jet mode. A small jet is emitted from the tip of the Taylor cone, since the tangential electrostatic stress cannot be balanced by conduction. Further downstream, the jet can undergo Rayleigh-Plateau instabilities and break-up into droplets. (c) Pulsating Taylor cone. The Taylor cone emits droplets in a pulsating mode, with an advancing and receding cone-tip.

close to the tip, and a formation of a jet emerging from the cone. In the absence of tangential electric stresses, no EHD tip streaming was observed. This role of the shear stress is important in a variety of research conducted on EHD tip streaming, and the underlying argument that the conduction current and convective current are balancing each other up are found in many scaling arguments. In the following, some of the potential emission modes are discussed, where the emphasis is placed on the ejection, once the initial instability has already formed.

7.2.1 Steady cone-jet mode

The steady cone-jet mode describes the electro spraying mode, in which a small jet is issued from the tip of the cone in a stationary fashion. A schematic of this process is shown in Fig. 7.2(b). In typical setups, the liquid which undergoes EHD tip streaming is supplied through a small capillary of radius R_n with a fixed volume flow rate Q , held at a constant electric potential ϕ_n . The EHD tip streaming is induced by a second electrode, typically of ring-shape, placed further away from the capillary. Under proper tuning of the parameters, a fine jet is emitted, with a typical diameter d_j , which can breakup further downstream into small droplets, forming an electro spray. The stable cone-jet mode has two major advantages: First, it can be operated continuously, leading to a defined jet current. Second, the resulting electro spray can exhibit highly monodisperse droplet distributions, with typical droplet sizes on smaller length scales than the stabilizing capillary. Due to its simplicity and degree of control, a lot of work has focused on the steady-cone jet, and in the following, the most important results are summarized.

A steady cone-jet emitted into air carries a specific current I_j , and Fernández de la Mora and Loscertales (1994) derived a scaling law for the jet current and diameter for liquids exhibiting a non-negligible conductivity. The idea behind the scaling law is to describe the cone by Taylor's electrostatic solution, up to a point near the tip, at which the surface convection current reaches the order of the electrical

relaxation time (the time scale of conduction), defined as $K/\epsilon_0\epsilon_{\text{rel}}$, where K denotes the conductivity of the liquid. Then, the conduction is unable to balance the convective current, the cone interface forms the jet, and the current transported scales as

$$I_j = g(\epsilon) (\gamma K Q)^{0.5}, \quad (7.3)$$

where the coefficient $g(\epsilon)$ depends on the dielectric constant (Fernández de la Mora, 2007), γ denotes the interfacial tension, K the liquid conductivity and Q the volume flow rate. The jet radius scales as

$$d_j = G(\epsilon)(Q\epsilon_0/K)^{1/3}, \quad (7.4)$$

where the function $G(\epsilon)$ depends on the dielectric constant as well (Fernández de la Mora, 2007). As follows from equations 7.3 and 7.4, both the emitted current as well as the diameter are independent of the externally applied electric field, and depend only on the local properties of the fluid. This result assumes that the externally applied electric field suffices to form the steady cone-jet, but once it is formed and stabilized, the scalings (eq. 7.3 and eq. 7.4) applies. Also, the resulting jet diameter is independent of the capillary radius used to stabilize the meniscus. For the experimental discussion in section 7.5, it is instructive to summarize the qualitative effects the parameters have on the current and jet. With increasing flow rate, the jet current increases, as well as with the conductivity and interfacial tension of the liquid, with all parameters exhibiting the same influence. The externally applied electric field, on the other hand, has no influence on the current. The jet diameter decreases with the conductivity, as a higher conductivity decreases the charge relaxation time, and thus higher convective velocities (and thus smaller diameters) are required to overcome conduction. Contrary, the volume flow increases the jet diameter. Experimentally, the scaling of eq. 7.3 without the specific form of g has been confirmed by Fernández de la Mora and Loscertales (1994), Hartman et al. (1999), and also has been extended to submerged electrosprays (Higuera, 2010). For completeness, it is also important to mention that a minimum volume flow rate exists, below which the steady cone-jet mode cannot be stabilized (Fernández de la Mora, 2007).

7.2.2 Alternative operating modes of electrohydrodynamic tip streaming

While the steady cone-jet mode is probably the most studied due to its controllable droplet size distribution and stable operating conditions, a variety of different operating modes exist for EHD tip streaming (also termed EHD spraying / electrospraying) (Fernández de la Mora, 2007; Jaworek and Krupa, 1998). The first operating mode, which can be observed for a liquid that is supplied to a needle, is the formation of droplets, which drip of the needle via gravity, without requiring additional electric fields. If an electric field is applied, the droplets dripping from the needle decrease their size with increasing electric field (Guerrero et al., 2019; Marginean et al., 2006b). The ejection is an intricate interplay between capillary effects, electrostatics, gravitational forces and viscosity. Next, upon further increase of the voltage, but below the onset voltage of the steady cone-jet, a pulsating cone can be observed (Marginean et al., 2006a). Here, the cone emits liquid in bursts, often accompanied by a characteristic frequency. A schematic of this unsteady process is shown in Fig. 7.2(c). As was shown by Bober and Chen (2011), the resulting frequency depends strongly on the flow rate, if the minimum flow rate to maintain a stable cone-jet is not reached, and becomes nearly independent of the flow rate above this threshold.

In addition to the variations of a single liquid sprayed using EHD tip streaming, variations of the operating modes can be introduced by using multiple liquids. Loscertales et al. (2002) showed that either one of the immiscible liquids supplied to two concentric capillaries can be actuated by the electric field, leading to a composite electric spray with one liquid encapsulating the other. Variations of the supplied flow rates leads to different ratios of the inner-to-outer liquid volumes in the resulting droplets. Subsequently,

López-Herrera et al. (2003) derived the relevant scaling laws for the current and the jet diameter. Also, Marín et al. (2007) used a similar approach to form emulsions in liquid media. By replacing the inner liquid with an ionic liquid, Larriba-Andaluz and Fernández de la Mora (2010) injected charges into an insulating liquid and were able to form an electro spray with monodisperse droplet distributions.

Further variations of EHD tip streaming exists, for example in combination with flow focusing (Gañán-Calvo et al., 2006; Kim et al., 2007) and multiple Taylor cones (Bocanegra et al., 2005). However, a comprehensive review of all modes is beyond the scope of this thesis, and the reader is referred to dedicated reviews, e.g., by Fernández de la Mora (2007) and Gañán-Calvo et al. (2018).

7.2.3 Submerged electro sprays

In this section, some effects related to submerged electro sprays are summarized. In contrast to electro sprays in gaseous environments, the spray is dispersed into a liquid bath. Then, additional parameters, such as a non-negligible outer liquid viscosity, change the electro spray. As was shown by Barrero et al. (2004), a conducting liquid can be electro sprayed using the steady cone-jet regime into a dielectric liquid, and the jet current exhibited the $Q^{0.5}$ dependency observed for electro spray in air. As was noted by the authors, the droplets of the electro spray exhibited a much smaller velocity than in air, leading to a widening of the electro spray, and an additional screening of the cone from the electric field by the charged spray. A similar screening effect was found by Larriba-Andaluz and Fernández de la Mora (2010), when an ionic liquid was electro sprayed into a dielectric liquid, resulting in a negligible dependence on the flow rate, and a strong dependence on the externally applied electric field. Larriba-Andaluz and Fernández de la Mora attribute these dependencies on space charge effects, as the resulting droplets are very small, and thus are only slowly moving through the dielectric. Thereby, the cone is screened off the electric field and the ejected current is balanced. In a microfluidic implementation of an electro spray by Gundabala et al. (2010), a similar weak dependency of the spray current on the flow rate was observed, with a linear influence of the external voltage on the current. They attributed these observations to the small distance from the capillary, at which the jet breaks into droplets, and argue, that convection by the externally imposed field play a dominant role in contrast to electro sprays with longer jets.

The differences of the current scaling were addressed by Higuera (2010), who used order-of-magnitude estimates to determine the resulting current scaling law of a steady cone-jet in a dielectric bath. For a wide range of different operating conditions, the scaling of the current with the volume flow rate emerges in the form of eq. 7.3, however, above a critical flow rate, the scaling is not recovered. Then, no stable jet is expected to exist, if the outer phase viscosity plays a role, and an alternative scaling is predicted, independent of the flow rate Q . Riboux et al. (2011) studied a glycerine jet in a hexane-bath and characterized the whipping instability of the jet, with the jet exhibiting a spiraling motion before break-up into droplets. Here, the jet current exhibited only a weak dependency on the flow rate of $I_j \propto Q^{1/5}$ and a strong dependency on the externally applied electric field as $E^{4/3}$. Also, different regimes of whipping were identified. The influence of surfactants on the electro spray was analyzed by Marín et al. (2012), where the surfactant concentration of a liquid bath was varied, and an electro spray was immersed. Among other observations, the authors showed the existence of satellite droplets in the electro spray, once a critical flow rate was exceeded. Also, Marín et al. attributed the weak dependence of the current on the flow rate above a critical surfactant concentration to space charge effects. While their study is restricted to the case of a high-viscosity liquid dispersed in a low viscosity bath, they noted that in the case of a low-viscosity fluid dispersed in a high-viscosity bath, space charge effects are expected to dominate. On a side note, the authors also mention that the external bath exhibits large velocities due to the electro spray exhibiting a viscous drag on the liquid. Overall, this short overview over some of the relevant literature of submerged electro sprays illustrates that the bath viscosity can play a significant role on the dynamics of the EHD tip streaming.

7.2.4 Properties of the electrospray

So far, an emphasis was placed on the EHD tip streaming and its dynamics. Resulting from the tip streaming, an electrospray is formed, and for the remainder of the chapter, it is important to discuss some of its properties. A single spherical droplet can only hold a finite amount of (surface) charge. If it is charged above this limit, it undergoes Coulombic fission and emits small charged progeny droplets. This mechanism was first described by Lord Rayleigh (1882), and the value of this limiting *Rayleigh charge* results in

$$q_R = 8\pi\sqrt{\epsilon_0\gamma R^3}, \quad (7.5)$$

where γ denotes the interfacial tension, and R the droplet radius. Hunter and Ray (2009) showed that the resulting progeny droplets carry 50% of the Rayleigh charge, and experimentally determined that the radius of the progeny droplets scale with the conductivity of the mother droplet as $K^{-2/3}$. Thus, the resulting charge of a progeny droplet scales as $q \propto R_d^{3/2}$, where R_d denotes the progeny drop radius. These results were obtained for liquid in air. A similar scaling law was obtained by Collins et al. (2013) for the charge of the emitted droplets from a droplet in air at onset of EHD tip streaming as $q_d \propto R_d^{3/2}$ depending on their resulting progeny droplet radius. A different scaling was obtained by Pillai et al. (2016), for droplets in liquid environments, resulting in $q/q_R \propto (R_d/R)^{5/2}$, where R_d denotes the progeny droplet size and R the mother droplet size. As Coulombic fission is a special case of EHD tip streaming from the tip of pointed droplets, the decrease of the progeny droplet size with increasing conductivity is in line with the observations made for steady cone-jetting.

Turning now the attention from the individual droplets towards the whole electrospray emitted from EHD tip streaming, a few notes can be made with respect to the spray structure. Gañán-Calvo et al. (1994) used both experimental measurements and numerical modeling to study the spray structure of an electrospray in gas. The droplet motion was modeled using a Lagrangian approach, accounting for Coulombic interactions between individual droplets, electric fields and drag forces on the droplets. The droplet charge was assumed to be proportional to the droplet volume, and the numerics were initialized using experimental conditions. Especially noteworthy is the observation that the electrospray showed a larger homogeneity of the droplet size with increasing deviation from the center line. Also, in their experiments, they observed a surrounding cloud of satellite droplets around the core of the electrospray. Tang and Gomez (1994) studied an electrospray in steady cone-jet mode, and observed a bi-disperse droplet size distributions, with larger sized droplets within the spray core, and smaller satellite droplets surrounding it. The droplet charge was inferred from measurements, showing that the main portion of the current ($\approx 85\%$) and the mass ($\approx 97\%$) were transported by the spray core. The radial motion of the droplets was mainly governed by space charge effects, where the charge of the electrospray pushed droplets radially outwards. Also, the gas flow showed entrainment with the electrospray, but was significantly slower than the droplets. Rosell-Llompарт and Fernández de la Mora (1994) showed that the bi-disperse distributions transitioned into distributions with a larger number of monodisperse droplet classes (up to 6 in their measurements) upon increase of the supplied flow rate. While the aforementioned studies were conducted for electrosprays in gaseous environments, a similar bi-disperse droplet size distribution was observed by Marín et al. (2012) for submerged electrosprays. The droplet size measurement showed that the primary droplet size depended on the supplied flow rate, whereas the size of the satellite droplets remained nearly constant. Overall, the trend shown in the experiments is that the droplet distributions lose their mono-disperse distribution, when the flow rate is increased well above the minimum flow rate required to form a stable cone-jet.

7.3 Experimental methods

7.3.1 Experimental setup

Figure 7.3 depicts two distinct experimental setups used to study EHD tip streaming at a liquid-liquid interface between a dielectric and a conducting liquid. In the first setup, a pin electrode (diameter D_e) was placed above the liquid-liquid interface in a rectangular glass container (*Kruess*) with inner side length $a = 36$ mm, as shown in Fig. 7.3(a). The distance between the needle and the interface was adjusted using a 3D-printed lid with a clamping mechanism, which additionally allows to change the electrode geometry. The lower, conducting liquid was electrically contacted by a second wire electrode, which was passed through a glass tube from the top of the container. Thereby, current flowing between the electrodes could only pass through the lower conducting liquid, and not through the dielectric phase via droplets. The liquids were added through an additional filling-port using a pipette, with the filled volumes adjusting the layer thicknesses h_o , h_w of both the upper and the lower liquid, respectively.

The dynamic of the EHD tip streaming was recorded from the side, using a high-speed camera (*FASTCAM Mini AX200*, *Photron*) equipped with either a DSLR objective (*AF-S Micro NIKKOR 105mm 1:2,8G VR*, *Nikon*) or a long working distance microscope ($6\times$ magnification, *Navitar*). Both the camera position and incident angle relative to the glass container were controlled using a mount (not shown in Fig. 7.3). Since the interface forms a meniscus at the glass side-wall, observations close to the interface were only possible if the camera was slightly tilted. The camera was connected to a computer using an ethernet connection and controlled via the proprietary software *Photron Fastcam Viewer 4*. The illumination of the cell was provided by an LED panel of adjustable brightness with a diffusor sheet. Figure 7.3(c) shows the layout of the peripheral equipment, including the high-voltage power source (*Heinzinger PNC-series 6 kV* or *Labsmith HVS448 – 6000D*, depending on the experiment) used to apply the electric potential difference between the electrodes.

As will be explored in sections 7.4 and 7.5, controlling the droplets of the conducting phase in the dielectric liquid is crucial for explaining the dimple formation at the liquid-liquid interface. Therefore, a second experimental cell was designed, as schematically shown in Fig. 7.3(b), while the peripheral equipment and optical system were maintained. The underlying idea is to decouple the occurrence of EHD tip streaming at the liquid-liquid interface from the existence of electrified droplets in the measurement cell. The upper pin electrode was replaced by a hollow metallic needle (inner diameter 0.58 mm, outer diameter 0.91 mm, length 3.81 cm, *Vieweg*), and a conducting liquid was electro sprayed into the dielectric liquid. Thereby, the amount of droplets was controlled independently of the EHD breakdown process at the interface. The cell was formed by a glass cylinder of inner diameter $D_c = 12.4$ cm, which was clamped between two plates and sealed tight by additional gaskets using a plastic holder and plastic screws, to avoid electrical contact to the environment. In order to ensure the suppression of wall effects, the cell size was significantly increased compared to the first setup. The lower plate served as the bottom electrode, and the upper plate had a square opening for filling and electrode placement. The hollow needle was positioned using a plastic holder with a clamping mechanism, and it was connected to the power source for applying the electric potential difference. The conducting liquid was supplied to the needle using a syringe pump (*KD-Scientific KDS-210-CE*) and plastic tubing. Thus, the flow rate of the submerged electro spray and the applied voltage difference were controlled independently. The current at the bottom electrode was monitored using a pico-ammeter (*Keithley 6485*), which was protected by a safety mechanism (Eifert, 2015) versus overvoltage, that occurs if the lower liquid contacts the needle electrode. The current measurement was not influenced by the safety mechanism, which was tested by comparing the measured current of the electro spray for some conditions with and without the safety mechanism at otherwise unchanged conditions. The optical system was supplied with an additional

Table 7.1: Conductivity data for KCl solutions computed from reference data (Shreiner and Pratt, 2004).

KCl concentration c_{KCl} (mol/m ³)	relative conductivity Λ (mS m ² mol ⁻¹)	Absolute conductivity K (mS m ⁻¹)
0.1	95.6	9.6
1	93.4	93.4
10	86.6	866.5
20	82.5	1650.5

dark background, thus enhancing the contrast significantly. More details are given in Fig. 7.5.

7.3.2 Fluid data

For the experiments in this chapter, aqueous KCl solutions with varying salt concentrations in the range between 0.1 mmol L⁻¹ and 20 mmol L⁻¹ were used as the conducting liquid. The variation of the salt concentration adjusts the electric conductivity of the solution, which is calculated from reference data (Shreiner and Pratt, 2004). First, the relative conductivity Λ , which denotes the conductivity per molar concentration, is calculated at $T = 20^\circ\text{C}$ according to Kohlrausch's law as (Job and R uffler, 2011)

$$\Lambda = \Lambda^0 - A\sqrt{c}. \quad (7.6)$$

Here, Λ^0 represents the relative conductivity at infinite dilution, and A a fitting parameter. The resulting conductivity data is summarized in Table 7.1.

Due to their immiscibility with water, silicone oils with varying viscosity were used as the dielectric liquid, with kinematic viscosities ranging from 0.65 cSt to 10 cSt (*Silikon l AK 0.65*, *Silikon l B1*, *Silikon l B5*, and *Silikon l B10*, *Silikon Profis*, Germany). In the following, they are identified using their respective kinematic viscosities (0.65 cSt, 1 cSt, 5 cSt, and 10 cSt). The measurement of the relevant fluid properties was described in section 6.3.4, and the resulting fluid properties are summarized in Table 7.2. For the EHD tip streaming experiments with a pin electrode, additionally n-dodecane (CAS: 112-40-3, *Merck Millipore*, Germany) was used as a dielectric. Since no quantitative evaluation was made using n-dodecane, the fluid properties were not measured systematically, and the density (0.749 g mL⁻¹) and kinematic viscosity (1.97 cSt) are reported from literature (Cooper and Asfour, 1991).

Table 7.2: Fluid properties of the silicone oils as obtained from the data sheets and interfacial tension measurements. The data is obtained according to section 6.3.4.

kinematic viscosity ν (cSt)	relative permittivity ϵ_r (-)	density ρ_o (g mL ⁻¹)	interfacial tension to water γ (mN m ⁻¹)
0.65	2.18	0.76	39.6
1	2.31	0.92	42.0
5	2.49	0.92	35.9
10	2.67	0.94	36.4

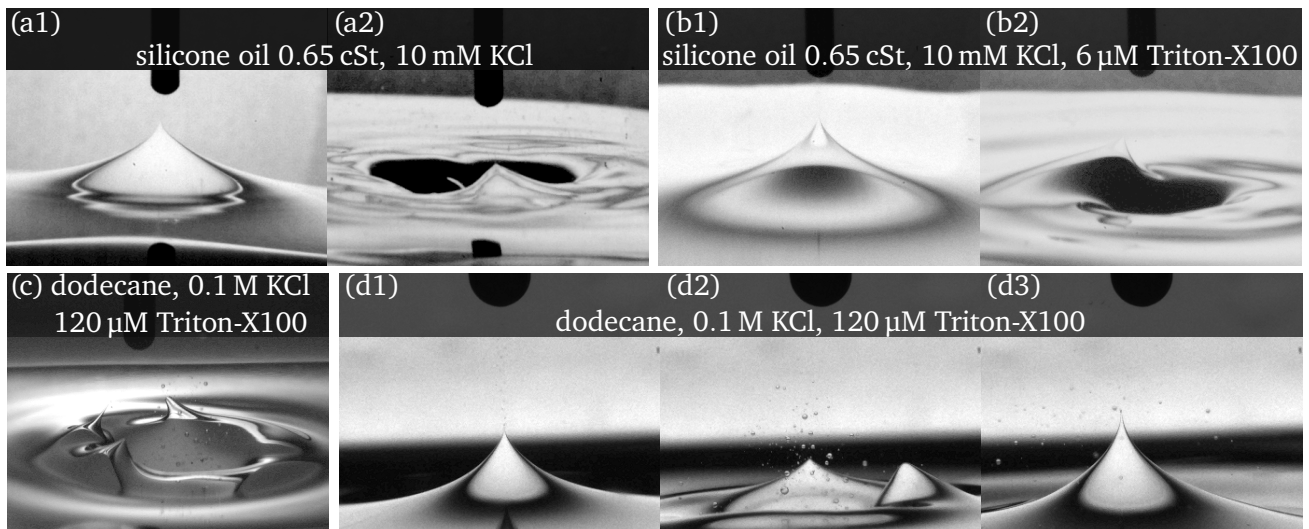


Figure 7.4: EHD tip streaming at a liquid-liquid interface induced by a pin electrode, close to the time of surface disintegration. Images with the same letter denote experiments performed for the same liquid-liquid combination at comparable experimental conditions. (a) Interface between silicone oil (0.65 cSt) and a 10 mM KCl solution, resulting in the formation of a classical Taylor cone (a1) or a surface dimple with a cone emerging from the rim (a2). (b) Interface between silicone oil (0.65 cSt) and a 10 mM KCl solution with additional non-ionic surfactant (Triton-X100), resulting in the formation of a classical Taylor cone (b1) or a surface dimple with a cone emerging from the rim (b2). (c) Interface between n-dodecane and a KCl solution with a concentration of 0.1 M and additional surfactant Triton-X100, resulting in a dimple with multiple cones forming from the rim. (d) Image sequence of the interface between dodecane and a KCl solution with a concentration of 0.1 M and additional surfactant Triton-X100. First, a Taylor-cone is formed and droplets are ejected (d1), then the interface forms a dimple (d2), and subsequently a cone is formed again (d3). Adapted figure with permission from Sebastian Dehe, and Steffen Hardt, *Phys. Rev. Fluids*, 6(12), 123702, 2021. Copyright (2021) by the American Physical Society.

7.4 EHD tip streaming induced by a pin electrode

First, the EHD instability at the liquid-liquid interface is studied experimentally in a pin electrode/interface configuration. The experiments were conducted in the square glass container shown in Fig. 7.3(a), and the interface was observed under a slight incidence angle through the top phase using the DSLR objective. The electric potential difference between the pin electrode and the conducting liquid was controlled manually with the high-voltage sequencer from *Labsmith*, and gradually increased over time. As soon as the interface became unstable, the high-speed camera recording was stopped using an end-trigger, keeping the video of the instability in memory. As these results are intended for a qualitative overview over the EHD instability modes, no further processing of the images was performed, and in the following, some representative results are shown. The main goal of this section is to highlight the different instability modes observed in the pin electrode / interface configuration, whose governing mechanism is of interest.

Figure 7.4 shows some illustrative results of EHD streaming induced by a pin electrode positioned above a liquid-liquid interface. The panels are grouped by their corresponding experimental conditions, where equal letters of the subfigure notation indicate that the experiments were performed for a similar liquid-liquid combination under similar experimental conditions. As is visible, the system can exhibit strongly deviating results under similar external conditions. In Fig. 7.4(a), the EHD instability at an

interface between a silicone oil with a kinematic viscosity of 0.65 cSt and an aqueous KCl solution with a salt concentration of 10 mM is shown. The electrode with a diameter 0.75 mm is positioned 4 mm above the interface. During the initial experiment, the classical tip streaming is observed at an applied pin electrode potential of $\phi_n = 5$ kV, where the bottom liquid is connected to ground (Fig. 7.4(a1)). The EHD tip streaming leads to the ejection of droplets towards the pin electrode, ultimately leading to a conducting connection, resulting in an automatic shutdown of the applied potential difference. Upon repetition of the experiment in the same setup, the observations change drastically: A surface dimple is formed, where the interface is moving away from the electrode, and at a potential of $\phi_n = 4.5$ kV, a cone emerges from the rim of the dimple. It is visible in Fig. 7.4(a2) as the bright cone at the location of the rim closest to the camera, in front of the dark dimple. Subsequently, droplets are ejected towards the electrode. These results illustrate that under very similar experimental conditions, strongly deviating interface deformations can be observed.

In Fig. 7.4(b), the EHD instability at an interface of a silicone oil with a kinematic viscosity of 0.65 cSt and an aqueous KCl solution with a salt concentration of 10 mM is shown, where additionally the non-ionic surfactant Triton-X100 (*Sigma Aldrich*) was added to the conducting phase. The surfactant concentration resulted in a concentration of approximately $6 \mu\text{mol L}^{-1}$, corresponding to 2.7% of the critical micelle concentration. Surface-active substances can change the properties of interfaces strongly, for example immobilize gas-liquid interfaces at superhydrophobic surfaces (Peaudecerf et al., 2017). Regardless, the experimental results are qualitatively comparable to the results without additional surfactants: During the first experiment, a Taylor cone forms and emits droplets towards the electrode. Upon repetition in the same system, a surface dimple forms, with a single cone emerging from its rim. The similarity to the results presented in Fig. 7.4(a) show that surfactant play no critical role in the formation of the dimple.

The dimple formation can be observed for a large variety of dielectric liquids and conductivities of the electrolyte. During initial tests, dimples were observed as well in corn oil and canola oil, which are more viscous than the silicone oils used in this work, as well as with n-dodecane, which has a viscosity of approximately 1.974 cSt. The details of the instability vary, e.g., the breakdown voltage, but qualitatively, the dimples are still observed. For example, in Fig. 7.4(c) the EHD instability with n-dodecane, a KCl solution with a concentration of 100 mM and an additional surfactant concentration of $120 \mu\text{mol L}^{-1}$ is shown. Here, several cones are emitted from the rim of the dimple. A wide range of phenomena can be observed, with variations of number and form of the cones emerging from the rim, but in this work, it is not attempted to map the different regimes in the parameter space. Instead, the emphasis is placed on the governing mechanism behind the dimple formation.

Figure 7.4(d) shows a series of three images from the same experiment, where an interface of n-dodecane and an aqueous KCl-solution with additional Triton-X100 is subjected to a voltage difference of 4920 V with an electrode spacing of 5 mm. First, the interface forms a Taylor cone, and droplets are ejected towards the electrode (Fig. 7.4(d1)), where they change direction upon contact with the electrode. Then, they move from the electrode back to the liquid-liquid interface, and shortly after the initial droplets touched the upper electrode, the liquid-liquid interface forms a dimple with cones emerging from the rim (Fig. 7.4(d2)). Subsequently, the dimple vanishes and a cone is formed again, as shown in Fig. 7.4(d3). Here, the dimple appearance is triggered by the existence of charged droplets of the electrolyte in the dielectric phase. In the presence of droplets, the dimple appears, and when they have merged with the main phase, the cone is observed again. Revisiting the previous experiments show immediately the presence of droplets in Fig. 7.4(c), whereas in Fig. 7.4(a,b) no droplets can be seen with the magnification used. Since in those experiments the dimple was triggered only after the initial experiments were performed, it is reasonable to assume that some electrolyte was deposited at the pin electrode during the first instability. Upon repetition of the experiment in the same system, the electrolyte residue at the upper electrode provides a reservoir of liquid for the formation of additional droplets. It is plausible that their size is well below the resolution limit of the macro lens. These observations point

towards a strong memory effect of the system, as the EHD instability would depend on both past and present evolution of the system.

Hypothesis formulation: The experiments indicate that charged electrolyte droplets in the dielectric phase play a fundamental role in the creation of the surface dimple, and thus it is necessary to understand how exactly they influence the system. Also, it is important to differentiate between the governing mechanism, and the influence of secondary parameter on the instability. For example, while surfactants might not be causing the surface dimple, their reduction of the interfacial tension might lead to a more pronounced surface depression. Droplets can influence the interface deformation in several ways, and in the following, the potential mechanisms are summarized:

(i) **Inverted Maxwell stress:** The effect of charged droplets in the dielectric phase can be interpreted as an increase of the conductivity of the oil phase (domain 1). If the charge transport in the system is assumed to be of steady state and dominated by conduction, the charge conservation at the interface leads to a ratio of the electric fields at the interface as $\mathbf{E}_1 \cdot \mathbf{n} = K_2/K_1 \mathbf{E}_2 \cdot \mathbf{n}$, where K_i denotes the conductivity of the upper or lower phase, and \mathbf{n} the surface normal (eq. 2.11). Then, if the electric field is assumed to be normal to the interface, the normal component of the Maxwell stress can be computed as (eq. 2.31, and see e.g., (Saville, 1997))

$$[\sigma^{\text{el}} \cdot \mathbf{n}] \cdot \mathbf{n} = \frac{1}{2} \epsilon_0 \left[\epsilon_{\text{rel}} \left((\mathbf{E} \cdot \mathbf{n})^2 - (\mathbf{E} \cdot \mathbf{t}_1)^2 - (\mathbf{E} \cdot \mathbf{t}_2)^2 \right) \right] = \frac{1}{2} \epsilon_0 \left(\epsilon_{\text{rel},1} - \epsilon_{\text{rel},2} \left(\frac{K_1}{K_2} \right)^2 \right) (\mathbf{E}_1 \cdot \mathbf{n})^2. \quad (7.7)$$

In case of droplets in the oil phase, charge is transported between the upper electrode and the liquid-liquid interface, and with increasing number of droplets, the conductivity increases. If the (effective) conductivity K_1 is sufficiently large, the sign of the Maxwell stress at the interface (eq. 7.7) could change relative to a system with negligible conductivity K_1 . As a result, the interface would be repelled from the electrode, leading to a depression rather than a Taylor cone.

(ii) **Droplet impact:** The charged droplets traveling through the dielectric liquid are accelerated by the electrostatic force. Upon impact of the droplets with the interface, their momentum could lead to a deformation of the interface, pushing it away from the electrode. If the transported momentum is sufficiently large, it could overcome the Maxwell stress at the interface.

(iii) **Viscous momentum transfer:** While the droplets move through the viscous dielectric liquid, they transfer momentum to the surrounding liquid. If the drag of the droplets on the surrounding phase is sufficiently large, the dielectric liquid could develop a background flow which impinges on the liquid-liquid interface, leading to a surface depression.

All of the above hypothesis require conducting droplets to be dispersed within the dielectric liquid, in order to induce the surface depression. In the pin electrode system, the droplets are introduced upon EHD tip streaming of the conducting phase, which ultimately leads to the formation of a conducting bridge between the electrode and the conducting phase. Thus, the presence of droplets is hardly controllable, as it occurs close to interface breakdown. The ability to study the governing mechanism is limited by highly dynamic processes coupled to breakdown, e.g., secondary breakup and coalescence as well as strong interface dynamics. In the following, the emission of charged droplets in the dielectric liquid is decoupled from EHD tip streaming by replacing the pin electrode with a hollow metallic needle, as is shown in Fig. 7.3(b). The volume flow of the dispersed liquid introduced into the dielectric phase is controlled by a syringe pump, and the submerged electro spray emits droplets at lower potential differences than are required for the formation of EHD tip streaming at the interface. Thus, droplets can be introduced and their influence on the interface can be studied at conditions further away from interface breakdown. The droplets which are introduced by the submerged electro spray mimic the droplets that occur during EHD tip streaming due to a pin electrode. In the latter case, they move upwards to the electrode, change their charge, and travel downwards to the interface, and in the former case, only the motion of the droplets

from the upper electrode towards the lower interface is present. Overall, this replacement system allows a more systematic investigation of the role of the droplets and their influence on the surface depression under well-controlled conditions.

7.5 Dimple formation by a submerged electro spray

By replacing the pin electrode with a hollow needle, a submerged electro spray introduces charged droplets into the system, leading to a surface depression below the needle. In the following, the effect of the spray parameters on the depression are studied, and thus the governing mechanism is identified. The experiments were performed in the cylindrical cell described in Fig. 7.3(b), with the *Heinzinger* high voltage source for supplying the electric potential difference. Figure 7.5 summarizes the key parameters of the setup. Both the needle dimensions (outer diameter $D_n = 0.91$ mm, inner diameter $D_i = 0.58$ mm) and the distance to the interface $L_0 = 5$ mm were held constant during the different experiments. As the dielectric liquid, the silicone oils described in section 7.3.2 were used, and as the conducting liquid, an aqueous KCl solution with a concentration of $c_{\text{KCl}} = 0.1$ mM was used. By holding the concentration and the filling height $h_w = 20$ mm of the lower phase constant, the electric conduction time scale of the lower phase remained constant. Due to the large container size and small spray volume flows, the submerged electro spray does not significantly change the distance of the needle and the interface over time.

Submerged electro spray operation mode

For the submerged electro spray, both the flow rate as well as the conductivity were varied during the experiments, in order to change the spray properties. The range of flow rates and conductivities were determined in preliminary studies, with the goal to achieve a stable interface deflection. The applied potential difference was varied between 2500 V and 4000 V, as this was the voltage range slightly below the onset of EHD tip streaming in the pin electrode system. Then, the volume flow of the electro spray was adjusted correspondingly. The minimum flow rate at which a stable depression was observed was identified as $20 \mu\text{L min}^{-1}$, and for the purpose of studying the flow rate influence, Q was increased up to $80 \mu\text{L min}^{-1}$. The conductivity of the dispersed liquid was chosen such that a comparatively high conductivity was present, in the range of 10 mS m^{-1} to 1.65 S m^{-1} . It is important to note that it was not attempted to reach a specific electro spray regime such as the stable cone-jet mode, instead, the parameters were chosen to fix the surface deformation mode. Nevertheless, the resulting electro spray regime can be compared to the regimes described by Higuera (2010) for submerged electro sprays. While in principle only applicable to steady cone-jets, it is possible to gain some insight into the spray regime. As was described by Higuera, the viscosity of the outer liquid becomes important compared to inertia and axial viscous forces, if the dimensionless parameters $\Pi = \mu_o K^{1/3} / (\rho_w \epsilon_o \gamma^2)^{1/3}$ and $\Pi R^{1/4}$ with $R = \rho_w^{4/3} K^{2/3} Q / (\epsilon^{2/3} \mu_w \gamma^{1/3})$ are of the order of unity. For the specific case of the silicone oil with 1 cSt viscosity, a spray flow rate of $20 \mu\text{L min}^{-1}$ and a KCl concentration of 1 mmol L^{-1} , they result in $\Pi = 1.26$ and $\Pi R^{1/4} = 16.1$, indicating that the outer liquid viscosity has a strong effect on the spray. Also, a second estimate was given with respect to the flow rate: If the flow rate is of order $Q_m = \epsilon_o \gamma^2 D_i / (3m \nu_o^2 K)$ or larger, and if viscosity of the outer liquid is important, no stable jet configuration can exist. For the given parameters, Q_m follows as $Q_m = 7.9 \mu\text{L min}^{-1} < Q$. Thus, the electro spray is expected to exhibit instabilities in close proximity to the needle, breaking up immediately into droplets. As a result, the current is expected to scale approximately as $I_j \propto \epsilon_o^{1/2} \gamma^{3/2} (D_i/2)^{1/2} / \mu_o$, independent of Q . The experimental observations show that the Taylor cone at the needle is oscillatory, and breaks up into droplets very closely to the needle, thus being in qualitative agreement with the scaling relations of Higuera. Overall, the electro spray is expected to be influenced by the viscosity of the dielectric liquid,

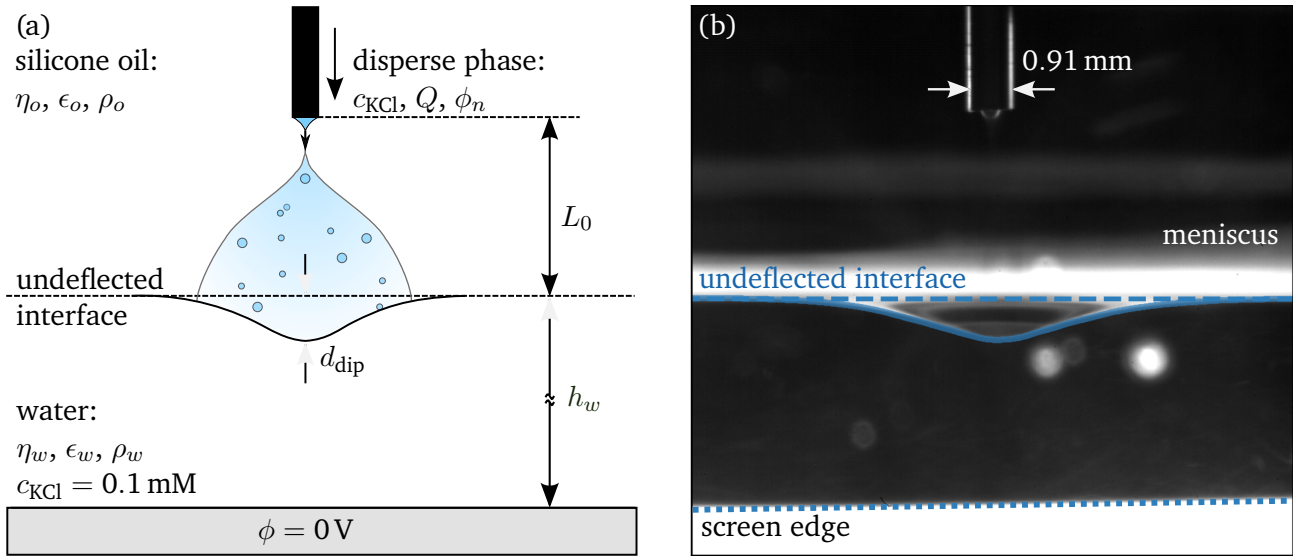


Figure 7.5: Interface deflection characterization. (a) Schematic of the system with a submerged electro spray. As the dielectric liquid, silicone oils with varying dynamic viscosity η_o , dielectric permittivity ϵ_o , and mass density ρ_o were used. As the conducting liquid, an aqueous KCl solution with a concentration of $c_{\text{KCl}} = 0.1 \text{ mM}$ was used. A second conducting liquid was emitted from the hollow needle, with a supplied volume flow rate Q and a KCl concentration c_{KCl} , which were both varied in the experiments. The electro spray was formed by supplying an electric potential ϕ_n to the metallic needle, and the lower electrode was held constant at 0 V . The submerged electro spray (blue region) was dispersed in the dielectric and finally merged with the lower phase. (b) Representative interface deflection as observed in sideview. The averaged image was created from the recorded video (see main text for details), with the interface appearing as a bright line in front of a dark screen. The surface depression was extracted via postprocessing (solid blue line) and compared to the undeflected interface (dashed line). The meniscus at the side-wall of the glass cylinder is visible as a bright region above the undistorted interface position. The dark background results from a matte screen, which is placed outside the cell and prevented the illumination to enter directly the region of interest, whereas the interface reflects the light entering from outside the field of view, thus creating a strong contrast for the postprocessing. The screen boundary is visible at the bottom (dotted line). Adapted figure with permission from Sebastian Dehe, and Steffen Hardt, *Phys. Rev. Fluids*, 6(12), 123702, 2021. Copyright (2021) by the American Physical Society.

being in a regime of high flow rates, where the resulting droplet diameter distribution is expected to be poly-disperse.

Experimental procedure

In the following, the system response to the submerged electro spray is characterized by two observables, the measured current at the lower electrode I and the interface deflection. Here, the depth of the deflection of the dip d_{dip} is used as the characterizing quantity, denoting the difference between the lowest point of the interface and the unperturbed interface. Since the electro spray parameters were chosen such that the surface dimple was approximately stationary, transient effects were excluded from the analysis, simplifying the subsequent evaluation. Within each experiment, the flow rate Q , the disperse phase KCl concentration c_{KCl} and the applied voltage ϕ_n were held constant. Using the pico-ammeter, the current was monitored, where the built-in averaging function was used (moving average with 100

readings, with a measurement period of 1/60 s) to minimize measurement uncertainties. First, the voltage and the flow rate were applied, and then it was waited until the averaged current stabilized. Usually, this occurred over a time scale of a few seconds. Then, a video of the interface was recorded, with a framerate of 1000 fps, at a resolution of 1024×1024 px, with a total of 200 images.

Quantification of the interface deflection

As a first step, an average image is created from the recorded video, which is used for further processing of the interface deflection. Therefore, the short-term fluctuations, i.e., droplets moving through the domain, are removed, such that only the stationary deflections are present in each image. This is achieved using *Python* by applying a moving minimum filter along the time-axis for each pixel, forming the minimum over 12 consecutive image. Next, the mean greyscale value of each pixel over the whole image stack is formed, resulting in a single averaged image. Figure 7.5(b) shows a representative image obtained by the described procedure. Here, the interface is visible as a bright line in front of a dark background due to the reflections from the LED-panel, where the direct light is blocked by the matte screen, thus creating a strong signal-to-noise ratio. The edge of the screen at the bottom of the image is marked by a dotted line. Furthermore, the meniscus at the wall of the glass cylinder appears as a bright region in the image. The interface is extracted from the average image semi-automatically, using *Python*. First, a start point at the interface is fixed by user input, and all interconnected lines are identified using an edge-detection algorithm (function *feature.canny* of the toolbox *skimage*). Subsequently, the resulting interface is checked by user input for edges which are not part of the interface. In Fig. 7.5(b), the resulting interface is shown as the solid blue line. Then, the image coordinates are calibrated by imaging a grid of known distance, and the maximum deviation from the undeflected interface position is computed in physical coordinates.

7.5.1 Experimental results

Influence of the flow rate

Figure 7.6 shows the system response of the silicone oil with a kinematic viscosity of 5 cSt and a KCl concentration of the disperse phase of 1 mM, where both the volume flow of the spray Q , as well as the applied potential difference ϕ_n were varied. As is visible from Fig. 7.6(a), the resulting spray current depends only weakly on the volume flow, approximately proportional to $I \propto Q^{0.2}$. These observations are in line with other reports of submerged electrosprays in literature, such as by Gundabala et al. (2010). Similarly, the interface deflection depends also only weakly on the volume flow, as follows from Fig. 7.6(b). Comparing the results in between the different potentials shows a strong dependence on ϕ_n of both the spray current as well as the interface deflection. Here, the spray current shows an approximately linear dependence with the voltage, similarly to the results by Gundabala et al. (2010), and the deflection shows an even stronger dependence on the applied voltage. As the volume flow has only a weak influence on the system response, the flow rate was fixed for the remainder of the parameter studies to a constant value of $Q = 40 \mu\text{L min}^{-1}$.

Influence of the dielectric's viscosity

Figure 7.7 shows the response of both the spray current and the interface deflection to changes of the dielectric's viscosity, while the spray parameters were fixed to $Q = 40 \mu\text{L min}^{-1}$ and $c_{\text{KCl}} = 1 \text{ mM}$. The spray current shows a decrease with increasing viscosity and approaches a limiting value for higher

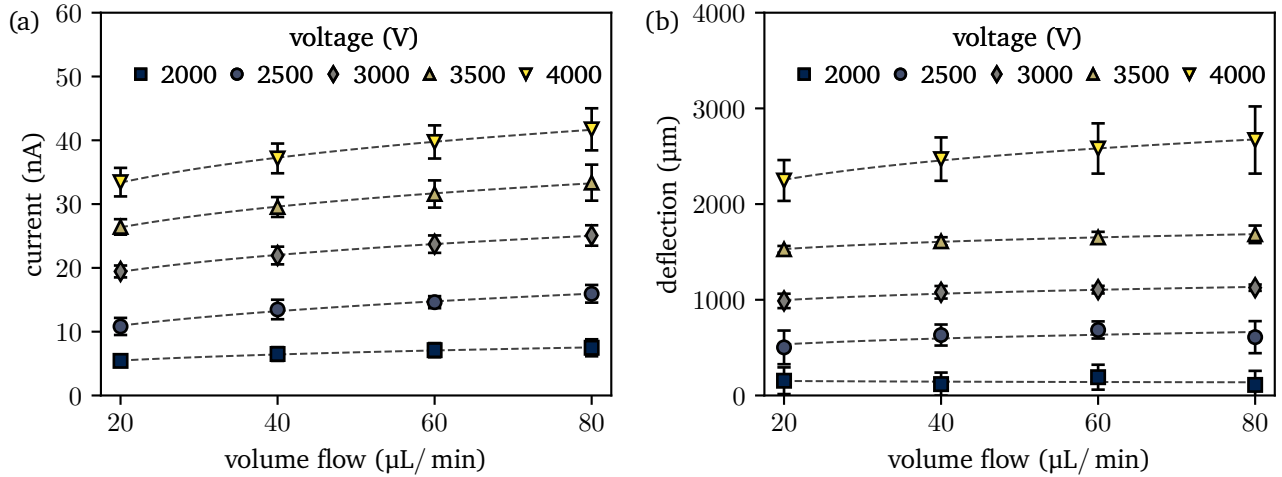


Figure 7.6: Measured current (a) and deflection (b) as a function of the volume flow Q and the applied potential difference ϕ_n . The silicone oil of viscosity 5 cSt was used as the dielectric liquid, and the KCl concentration of the electro spray was set to $c_{\text{KCl}} = 1 \text{ mM}$. Error bars represent the standard deviation of 5 measurements, and the dashed lines represent fit functions of the form $y = ax^b$ to guide the eye. Adapted figure with permission from Sebastian Dehe, and Steffen Hardt, Phys. Rev. Fluids, 6(12), 123702, 2021. Copyright (2021) by the American Physical Society.

viscosity. While the change from 1 cSt to 5 cSt induces a current change of approximately 30 %, a further increase to 10 cSt leads to no significant changes. This observation indicates a limiting mechanism which becomes important at high viscosities. Contrary to the current, the interface deflection increases with increasing viscosity, reaching its limit at a viscosity of 5 cSt. A further increase of the viscosity has no

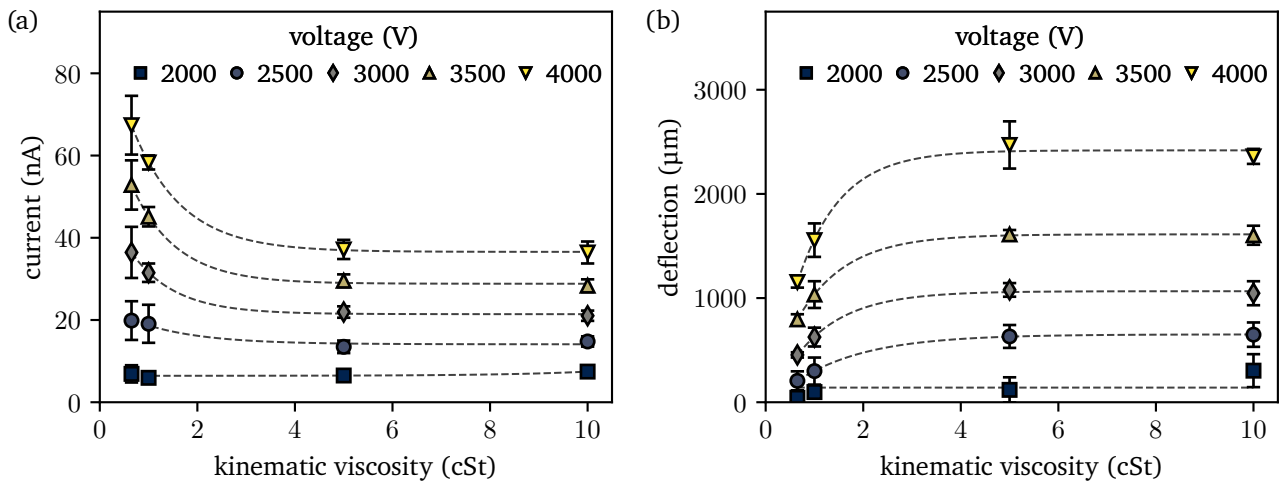


Figure 7.7: Measured current (a) and deflection (b) as a function of the silicone oil viscosity and the applied voltage ϕ_n . The volume flow rate was set to $40 \mu\text{L min}^{-1}$ and the KCl concentration of the spray to 1 mM. Error bars represent the standard deviation of 5 measurements, and the dashed lines represent exponential fit functions to guide the eye. Adapted figure with permission from Sebastian Dehe, and Steffen Hardt, Phys. Rev. Fluids, 6(12), 123702, 2021. Copyright (2021) by the American Physical Society.

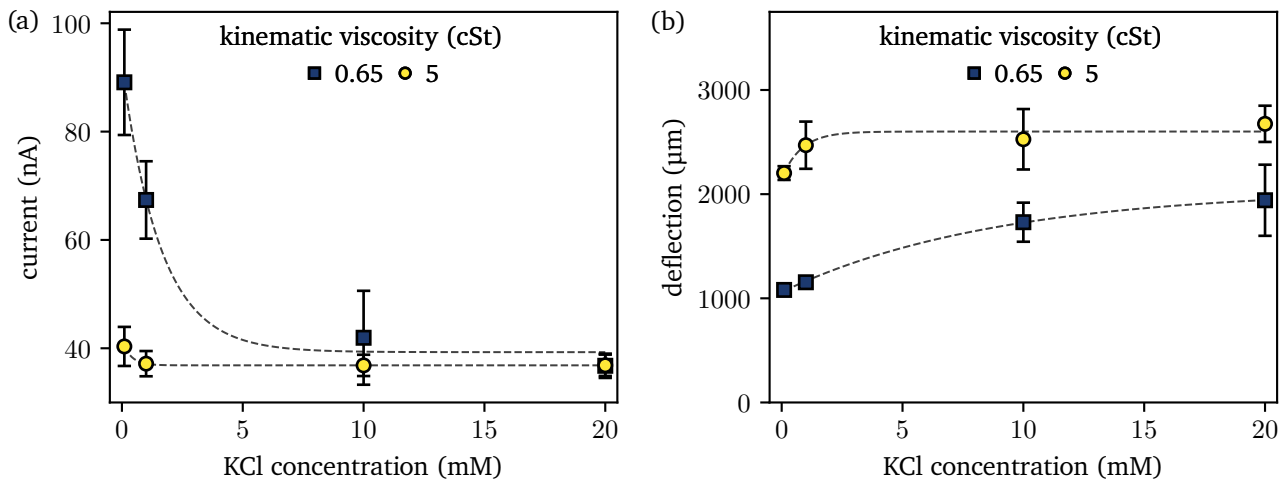


Figure 7.8: Measured current (a) and deflection (b) as a function of the KCl concentration of the submerged electro spray and the oil viscosity for a fixed volume flow of $40 \mu\text{L min}^{-1}$ and a potential difference of 4000 V. Error bars represent the standard deviation of 5 measurements, and the dashed lines represent exponential fit functions to guide the eye. Adapted figure with permission from Sebastian Dehe, and Steffen Hardt, Phys. Rev. Fluids, 6(12), 123702, 2021. Copyright (2021) by the American Physical Society.

significant effect as well.

Influence of the conductivity of the disperse liquid

Figure 7.8 shows both the spray current as well as the interface deflection as a response to the KCl concentration of the submerged electro spray. As is shown in section 7.3.2, the conductivity K of the electrolyte is fixed by the salt concentration, with an approximately linear dependence of the conductivity on the salt concentration. Thus, high concentrations correspond to high conductivities. The experiments were performed at a fixed volume flow rate of $40 \mu\text{L min}^{-1}$, a constant applied voltage of 4000 V and for two different oil viscosities (0.65 cSt and 5 cSt). As is visible from Fig. 7.8(a), the current remains nearly constant for all conductivities for a viscosity of 5 cSt. For 0.65 cSt, the spray current depends strongly on the conductivity of the dispersed phase, showing a strong decrease with increasing concentration. At high conductivities, the current measured for 0.65 cSt approaches the current observed for 5 cSt. Especially the result for 0.65 cSt is surprising, as the current decreases with increasing conductivity. As was summarized in section 7.2, for example for the steady cone-jet mode, the electro spray current scales with conductivity as $I \propto K^{0.5}$. The same scaling was experimentally observed by Marín et al. (2012) for submerged electro sprays. Also, in the work of Higuera (2010), either an increase of the current with conductivity, or an absence of influence was predicted. Thus, this behavior of the spray current is unexpected and needs further rationalization. However, it is important to keep in mind that the electro sprays in the works referenced above were operated in the steady cone-jet mode, which limits the comparability of the results.

Figure 7.8(b) shows the interface deflection, which increases with the KCl concentration for 0.65 cSt, and is nearly unaffected at 5 cSt. This behavior is inverse to the observed current, but similarly, a plateauing of the deflection at high KCl concentrations is observed.

Discussion of the experimental results

The experimental observations allow an evaluation of the potential driving mechanisms summarized in section 7.4. While in principle the sign of the Maxwell stress could be inverted at the interface, the experimental results render this hypothesis unlikely: Since the ion concentration of the lower phase is held constant, the conductivity of the lower phase is constant as well (K_2 in eq. 7.7). An increase of the spray current indicates an increase of the effective conductivity K_1 in the dielectric, and thus following eq. 7.7, the interface deformation should increase with increasing current. However, for both the variation of the viscosity as well as the spray conductivity, an inverse behavior is observed: A decreasing current is accompanied by an increasing surface deflection. Thus, it is unlikely that the Maxwell stress at the interface changes its sign.

In order to differentiate between the two remaining hypothesis, the momentum exchange with the liquid-liquid interface upon *droplet impact*, and the *viscous momentum exchange* when the droplets travel through the dielectric liquid, it is necessary to discuss the velocity of the droplets in the dielectric. If the momentum is exchanged at the droplet impact, a higher velocity of the droplets upon impact on the interface should lead to stronger deflections, in order to overcome the restoring capillary and hydrostatic forces. As was discussed in section 7.2.4, the spray is expected to consist of droplets with varying droplet sizes. Electrospays in air showed a large variation of resulting diameters for higher flow rates (Rosell-Llompart and Fernández de la Mora, 1994), so it is expected that a similar trend applies for submerged electrospays. Such a behavior was described by Marín et al. (2012), where the submerged electrospays exhibited satellite droplets in regimes of higher flow rates, in which the electro spray is operated in the experiments conducted here. Therefore, it is not possible to attribute a single diameter to the spray droplets, instead the qualitative dependency on the parameters is discussed.

As described in section 7.2.4, the conductivity has a strong influence on the resulting droplets from EHD tip streaming. For both the steady cone-jet and the Coulombic fission of droplets, a higher conductivity leads to smaller resulting droplets. Since no direct measurements of the droplet size can be performed due to the optical limitations of this setup, in the following, the reported behavior in literature is used to estimate the droplet diameters. For example, Hunter and Ray (2009) showed that the radius of the emitted progeny droplets in air scaled as $R_d \propto K^{-2/3}$, and the charge of the droplets were proportional to the Rayleigh charge (eq. 7.5) as $q/q_R \approx \text{const}$. Then, the proportionality of the droplet charge follows as $q \propto R_d^{3/2}$. Pillai et al. (2016) obtained a different scaling as $q/q_R \propto (R_d/R)^{5/2}$, where R denotes the radius of the mother droplet. However, their scaling was obtained for submicron droplets, which might show a different behavior than macroscopic droplets. All scalings have in common that the droplet size decreased with conductivity.

In order to approximate the resulting droplet velocity of the electro spray, they can be treated as spheres with an immobilized interface. In principle, other models could be used to relax the assumption of an immobilized interface such as the Hadamard–Rybczynski equation, however, the overall argument persists. Next, the terminal velocity of a droplet moving through the dielectric can be calculated by balancing the Stokes' drag force (Stokes, 1851) and the electric force on the droplet, resulting in

$$u_d = \frac{q_d E}{6\pi\mu R_d} \quad (7.8)$$

Here, E denotes the electric field magnitude acting on the droplet. For the following argument, the droplet charge is assumed to be proportional to the Rayleigh charge, and furthermore, the droplet radius is assumed to depend on the conductivity as $R_d \propto K^{-2/3}$. Then, the terminal velocity of the droplet is proportional to

$$u_d \propto \frac{q_R E}{\mu_o R_d} \propto \frac{E R_d^{1/2}}{\mu_o} \propto \frac{E}{K^{1/3} \mu_o}, \quad (7.9)$$

where the properties approximately constant for all experiments (ϵ_o, γ) were included into the proportionality factor. Equation 7.9 shows that the terminal droplet velocity will both decrease with increasing conductivity as well as viscosity, and increase with applied electric field. This approximate scaling allows a discussion of the remaining probable driving mechanisms.

The droplet velocity is expected to decrease for both an increase of the viscosity and conductivity. If the momentum exchange between droplets and interface would occur at the droplet impact, a smaller deviation would be expected at higher conductivity and viscosity. However, the inverse behavior is observed, and the interface deflection increases. Thus, it is unlikely that the momentum exchange occurs at the droplet impact. Instead, it is expected that the momentum is exchanged by viscous interactions between the moving droplets and the dielectric liquid, inducing a background flow which impinges on the interface, leading to the deformation. The magnitude of the drag force exerted by the dielectric liquid on the droplets is the same as the drag force exerted by the droplets on the dielectric liquid. Thus, the droplet effects can be interpreted as an electric volume force density \mathbf{f}_{el} on the dielectric liquid, given as

$$\mathbf{f}_{el} = \rho_{el}\mathbf{E}, \quad (7.10)$$

where ρ_{el} is the electric space charge due to the droplets. For a constant current, droplets moving more slowly through the dielectric form a larger space charge region than faster moving droplets, in turn leading to a higher volume force density. Therefore, the hypothesis is consistent with the observations for the increasing deflection with increasing KCl concentration and higher viscosity. Also, the strong dependency of the surface deflection with the applied electric field, and the small dependency on the flow rate can be rationalized by these observations. Larger electric fields lead to higher droplet velocities and thus drag on the viscous phase. Also, since the submerged electrospray is expected to experience large variations of droplet sizes, it is likely that an increase of the volume flow rate has no appreciable impact on the background flow. The space charge is determined by the slowest, and thus smallest droplets, which are expected to occur for all flow rates above the minimum flow rate. In addition, a potential self-regulating mechanism is identified that could account for the plateauing at high viscosities and concentrations, as well as the decreasing currents in both cases. As slower droplets form a larger space charge region between the needle and the liquid-liquid interface, it is possible that the space charge screens of the needle from the electric field, reducing the emitted current. Since both the conductivity as well as the viscosity lead to a reduction of the droplet velocity, the regulatory effect is caused by the same effect. In section 7.6, this limiting effect is addressed using numerical modeling.

In addition to the remarks made above, it is important to stress two more points: First, the resulting droplet velocity is determined by both the relative motion of the droplets to the background flow due to electric forces, as well as the background flow itself. In case the droplets become small, it is expected that the droplet motion is dominated by the background flow, and that they are mainly advected with the flow. Second, based on this observation, it is possible that the measured current, which is measured at the lower electrode, is not representative for the spray current. If the droplets become small, it is possible that not all droplets reach the liquid-liquid interface, but instead are advected by the background flow away from the dimple. This would lead to two effects: First, only a fraction of the real current would be measured by the ammeter, and second, over time, a significant space charge would accumulate in the dielectric liquid. However, the spray current carried by an electrospray is mostly associated with the large droplets, as was for example measured by Tang and Gomez (1994) for an electrospray in air. Thus, it is reasonable to expect that the majority of the spray reaches the lower phase and is measured using the ammeter. Overall, the experiments indicate that the relevant driving mechanism for the interface deflection is the *viscous momentum transfer*. In order to test this hypothesis in more detail, the experimental observations made in this section are accompanied by a numerical modeling approach in the next section.

7.6 Numerical modeling

In order to show that the impinging background flow is the governing mechanism for the interface deflection, a numerical model is implemented in *Comsol Multiphysics 5.5*. The goal is to verify that viscous flow induced by electric forces can indeed result in a deformation of the experimentally observed magnitude. It is important to emphasize that no full model was set up accounting for every physical mechanism present in the system, but rather a reduced order model which further corroborates our experimental findings. The goal is to determine the force field acting on the liquid self-consistently by modeling the charge transport in the liquid and calculating the resulting volume force density. Therefore, a series of simplifications is introduced, allowing to evaluate our hypothesis and making the problem numerically accessible. In principle, instead of calculating the volume force density from the current transport, one could also apply a force density directly to generate a background flow. However, the question would arise which spatial distribution the volume force should take. Thus, the approach followed here to determine it self-consistently is more physically motivated. In order to determine the free model parameter, an additional PTV measurement of the background velocity of the fluid is performed for calibration.

The underlying idea of the model is to solely model the fluid flow induced by the electric force on the background dielectric, without accounting for other external forces, such as the Maxwell stress at the liquid-liquid interface. If the obtained depression is of similar order as in the experiments, the hypothesis of *viscous momentum transfer* is further supported. In the following, the charge transport through the dielectric liquid is modeled by an advection-diffusion equation, without resorting to multiphase flow models, treating the space charge as an interpenetrating medium. The idea is that the current transported in the system passes the dielectric phase by droplets only, and the droplet velocity determines the advective velocity. In order to simplify the further treatment, the droplets are assumed to be monodisperse with radius R_d , which is a strong simplification as was discussed above. The transport equation for the charge determines the space charge distribution in the dielectric liquid, and can thus be used for fixing the volume force on the dielectric. As discussed, the literature on droplet charge and size distribution is sparse, and further assumptions have to be introduced. In the following, the droplet charge is fixed at a fraction of the Rayleigh charge $q_d/q_R = 0.44$ (eq. 7.5), following Collins et al. (2013). While this relation was obtained for electrospray in air, the model is calibrated based on an experimental particle tracking experiment, where the droplet radius R_d is used as a fitting parameter to tune the numerical to the experimental observations. As a result, the obtained droplet parameter does not have to correspond to experimental observations, and should not be compared to actual experimental measurements of droplet sizes. Furthermore, the droplets are assumed to exhibit an immobilized interface, such that the drag force on the droplets can be computed by Stokes' drag. Another assumption with respect to the droplet motion is that the droplets move with the terminal velocity relative to the background flow. Then, the relative droplet velocity compared to the background flow results in

$$\mathbf{u}_d = \frac{0.44 q_R \mathbf{E}}{6\pi\mu_o R_d} = 0.587 \frac{\sqrt{\epsilon_o \gamma} R_d}{\mu_o} \mathbf{E}, \quad (7.11)$$

which is now a function of the local electric field, liquid properties, and the droplet radius R_d .

The charge transport is modeled using an advection-diffusion equation, where the diffusion represents an ad-hoc approach to stabilize the numerics. The transport equation of charge reads

$$\frac{\partial \rho_{el}}{\partial t} + \nabla \cdot ((\mathbf{u}_d + \mathbf{u}_o) \rho_{el} - D_d \nabla \rho_{el}) = 0, \quad (7.12)$$

where ρ_{el} represents the charge density in the dielectric, the droplets move with the velocity \mathbf{u}_d relative to the background flow \mathbf{u}_o , and the diffusion coefficient D_d represents a numerical stabilization approach.

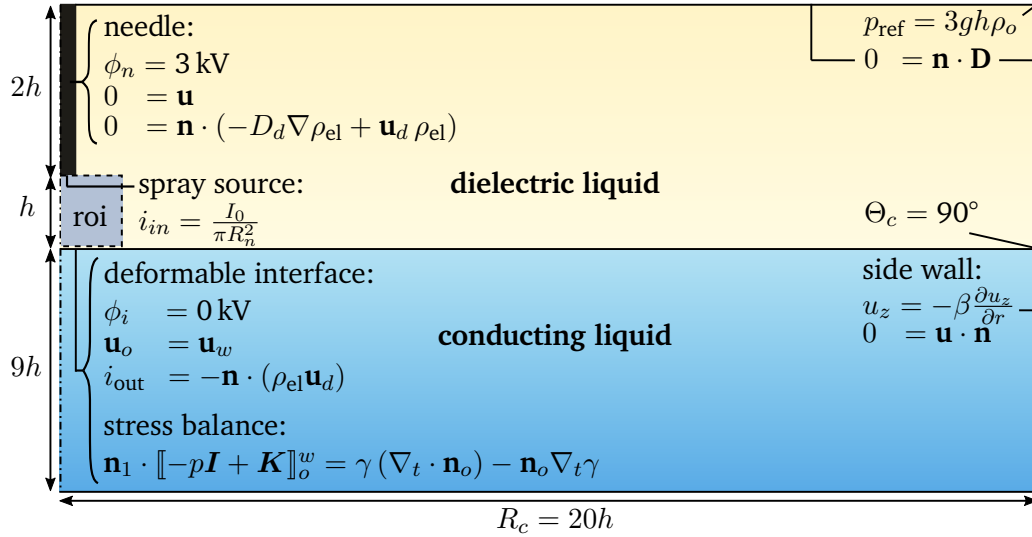


Figure 7.9: Schematic of the computational domain with relevant boundary conditions. The radial symmetry of the problem is utilized, with the symmetry axis coinciding with the needle axis. The liquid-liquid interface can be deformed due to the dynamic pressure of the flow, with capillary and hydrostatic forces acting to restore the interface. The numerical modeling accounts for charge transport and electrostatics in the dielectric liquid, and fluid flow in both liquids. Adapted figure with permission from Sebastian Dehe, and Steffen Hardt, Phys. Rev. Fluids, 6(12), 123702, 2021. Copyright (2021) by the American Physical Society.

Its numerical value is set such that the problem is advection-dominated, resulting in the condition that the diffusive time scale T_{dif} is much larger than the advective time scale. For a droplet with radius of $5 \mu\text{m}$ and an electric field strength of $(3000/0.05) \text{ V/m}$, corresponding to the electric field strength in the region between the needle and the liquid-liquid interface, a droplet velocity of 19.9 mm s^{-1} is obtained. As a result, the travel time between the needle and the interface results in $T_{\text{adv}} \approx 0.25 \text{ s}$. By setting $T_{\text{dif}} = 100 T_{\text{adv}}$, a diffusion constant of $D_d = 1 \times 10^{-6} \text{ m}^2/\text{s}$ is obtained. In order to ensure that the numerical value of D_d does not influence the results and the flow is indeed advection-dominated, a convergence study is performed later on.

Figure 7.9 shows an overview over the computational domain, including the relevant boundary conditions. The axial symmetry of the problem is used, where the needle axis is set as the symmetry axis. The electrospay charge is introduced at the upper electrode, using a boundary flux as

$$i_{\text{in}} = \frac{I_0}{\pi R_n^2}, \quad (7.13)$$

where R_n represents the radius of the needle, and I_0 the total spray current introduced into the system. The electric charge leaves the system at the lower interface, where the outflow is prescribed as

$$i_{\text{out}} = -(\mathbf{u}_d \cdot \mathbf{n}) \rho_{\text{el}}, \quad (7.14)$$

with \mathbf{n} denoting the local interface normal. At the other walls of the problem, a zero flux condition is prescribed.

The electric potential in the dielectric phase is governed by Poisson's equation (eq. 2.3) as

$$\nabla^2 \phi = -\frac{\rho_{\text{el}}}{\epsilon_0 \epsilon_o}, \quad (7.15)$$

where ϵ_o denotes the relative permittivity of the dielectric liquid. At the needle and at the liquid-liquid interface, the electric potential is fixed as

$$\phi_n = 3 \text{ kV} \quad \text{and} \quad \phi_i = 0 \text{ kV}, \quad (7.16)$$

where the large conductivity of the lower medium motivates the latter condition. Also, the charge transport in the lower phase is not modeled, as it is assumed to occur instantaneously compared to the transport through the dielectric liquid. At the other boundaries, the electric flux normal to the walls is assumed to vanish as $\mathbf{n} \cdot (\epsilon_0 \epsilon_r \mathbf{E}) = 0$.

While both the electric potential as well as the charge transport are solely modeled in the upper liquid phase, the fluid flow is solved for in both fluidic domains. The governing equations are the continuity equation for incompressible flow (eq. 2.16) and the Navier-Stokes equation (eq. 2.35), including a gravitational force term, and an electrostatic force term in the upper dielectric phase. The interface deformation is computed using an interface tracking scheme as implemented in *Comsol*, enforcing at the liquid-liquid interface

$$\mathbf{u}_o = \mathbf{u}_w \quad (7.17a)$$

$$\mathbf{n}_o \cdot \left[-p\mathbf{I} + \mu (\nabla \mathbf{u} + (\nabla \mathbf{u})^T) \right] = \gamma (\nabla_t \cdot \mathbf{n}_o) - \mathbf{n}_o \nabla_t \gamma, \quad (7.17b)$$

where the subscripts o and w denote the oil and water phase, \mathbf{I} denotes the identity matrix, γ the interfacial tension, and \mathbf{n}_o a unit normal vector on the interface. The boundary condition 7.17b balances the pressure difference over the interface with capillary forces. As was noted in the motivation for the model, the Maxwell stress at the interface is neglected, since the goal of this section is to verify that the dimple formation is solely due to the background flow in the dielectric liquid. For the surface deformation, it is important that the interface can move at the side-wall of the container, which is enabled by prescription of a Navier-slip condition and a no-penetration boundary condition as

$$u_z = -\beta \frac{\partial u_z}{\partial r}, \quad (7.18a)$$

$$u_r = 0. \quad (7.18b)$$

Here, the slip length β is fixed at a large value of $\beta = 20 \text{ mm}$, as only the steady-state solution is of interest. The contact angle of the interface at the container wall is fixed to 90° , and at the remaining walls and needle surfaces, no-slip conditions are enforced. In order to fix the pressure in the system, a reference pressure is defined in the upper right corner of the domain as $p_{\text{ref}} = 3\rho_o g h$, where g denotes the gravitational constant and h the distance between the unperturbed interface and the needle.

The numerical solution is obtained using a time-dependent solver, until a steady state is reached. A combination of an implicit solver based on a backward differentiation scheme (BDF) with variable time-stepping and a direct solver (MUMPS) is used, with the maximum step size set to 0.5 s. The computational domain is meshed using triangular cells with quadratic basis functions for the pressure and velocities, cubic basis functions for the electric potential and linear basis functions for the charge density, with a final number of cells of 22217. The grid independency study is performed on the tetrahedral mesh, in order to ensure mesh independency. The numerical parameter are chosen as described in section 7.6, except for $R_d = 3 \text{ }\mu\text{m}$ and $\rho_o = 760 \text{ kg/m}^3$. The number of mesh cells is increased by changing the number of boundary cells at the symmetry axis, and set the maximum growth ratio between adjacent cells to 1.015. Thus, the number of mesh cells changes in the computational domain, with the largest number of cells introduced near the symmetry axis. Therefore, the cells are added in the region of highest interest, without excessively straining computational resources by adding cells in less important regions, e.g., the conducting liquid far away from the symmetry axis. Overall, seven different resolutions are computed with the number of cells varying between 4661 for the coarsest mesh to 22217 for the finest

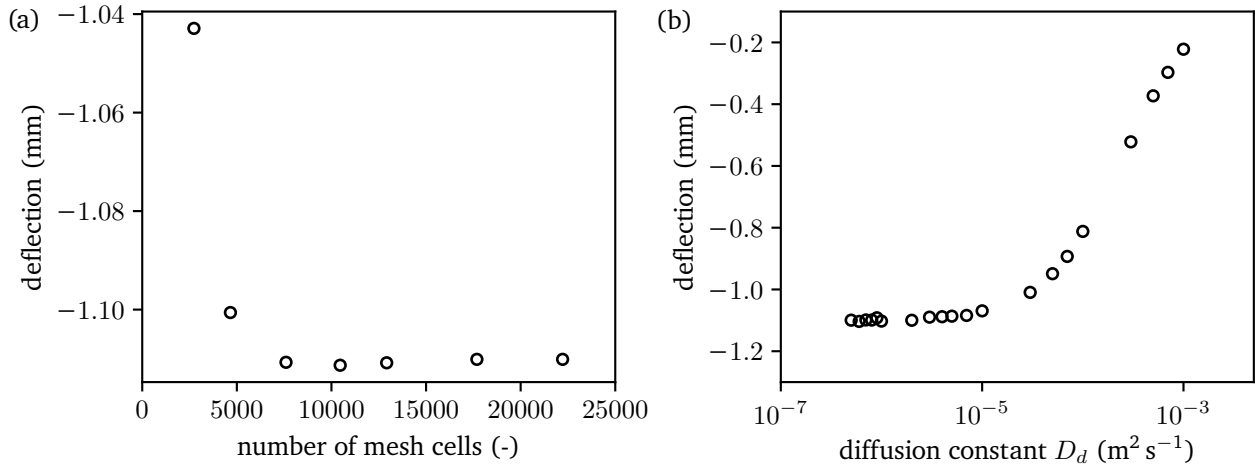


Figure 7.10: Numerical convergence study. (a) Grid convergence study. The number of mesh cells is increased as described in the text, and the influence on the interface deflection is shown. (b) Convergence study for the diffusion constant D_d for a droplet radius of $R_d = 17.5 \mu\text{m}$. As D_d is used as an ad-hoc approach to stabilize the numerics, its numerical value should not influence the solution and it has to be advection dominated. For the computations, a diffusion constant of $D_d = 1 \times 10^{-6} \text{m}^2 \text{s}^{-1}$ is used, well within the advection dominated regime. Adapted figure with permission from Sebastian Dehe, and Steffen Hardt, Phys. Rev. Fluids, 6(12), 123702, 2021. Copyright (2021) by the American Physical Society.

mesh. The resulting interface deflection is plotted in Fig. 7.10(a), and a convergence of the solution is visible with increasing spatial resolution. In the following, the highest mesh resolution is utilized to ensure grid-independence. Also, the independence of the solution on the diffusion constant D_d is shown in Fig. 7.10(b) for the droplet diameter of $R_d = 17.5 \mu\text{m}$ and the parameters described in section 7.6. For high diffusion constants D_d , the resulting deflection changes strongly and is dominated by diffusion. Below a specific value of D_d , the solution becomes independent of D_d and is thus advection-dominated. As is visible, the value of $D_d = 1 \times 10^{-6} \text{m}^2 \text{s}^{-1}$ utilized in the simulations is well within the advection dominated regime, and the solution is independent of the value of D_d .

To summarize, the numerical model governs the electric potential, charge transport, fluid flow, as well as the resulting interface deformation self-consistently. The electrostatic force on the dielectric liquid drives the background flow, which in turn induces the surface deformation. Continuing, the resulting surface depression can be computed for a fixed experimental condition. Only the droplet radius R_d remains to be determined, all other parameters are fixed according to the experimental measurements. By fitting R_d such that the numerically obtained velocity distribution corresponds to an experimentally obtained velocity distribution, all model parameters are fixed, and one can compare the numerically and experimentally obtained interface dimple. If the numerical surface depression corresponds to the experimental result, it follows that the model represents the governing mechanism sufficiently well, further corroborating the hypothesis of *viscous momentum transfer*.

Calibration measurements

In order to fix the free parameter R_d of the numerical model, the velocity field inside the dielectric liquid was characterized using particle tracking velocimetry. In order to avoid optical distortions due to the container size and to allow observation with a small distance between flow and optical components,

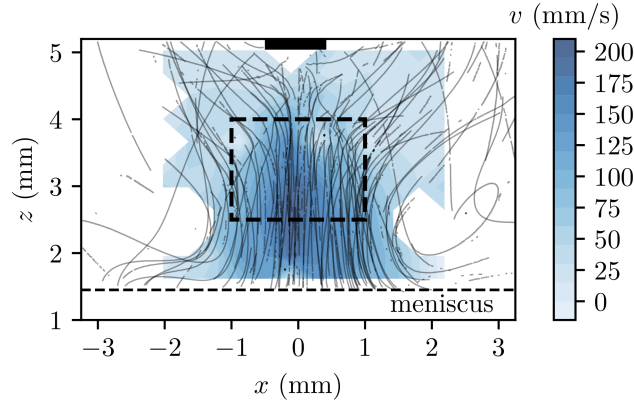


Figure 7.11: Particle streak lines and liquid velocity obtained from the calibration measurement. A submerged electro spray was induced by a potential difference of 3000 V, a volume flow rate of $20 \mu\text{L min}^{-1}$, as well as a KCl concentration of 0.1 mmol L^{-1} , and a silicone oil with a viscosity of 5 cSt was chosen as the dielectric. The magnitude of the vertical velocity component is shown as the color map. Only regions with more than 30 measured particle velocities are shown, and the meniscus at the container wall restricts the field of view. The needle position is indicated at the top of the image. The numerical data is compared to the average of the region indicated by the dashed rectangle. Adapted figure with permission from Sebastian Dehe, and Steffen Hardt, *Phys. Rev. Fluids*, 6(12), 123702, 2021. Copyright (2021) by the American Physical Society.

the pin electrode inside the rectangular glass container described in Fig. 7.3(a) was replaced by a hollow needle, and the particle motion in the region between the needle and the liquid-liquid interface was observed using the high-speed camera with a long-distance microscope ($6\times$ magnification) at a frame rate of 10 000 fps. The dielectric liquid was sparsely doped by hollow glass spheres (diameter $5 - 90 \mu\text{m}$, *Cospheric LLC*), such that the liquid and spray properties were not significantly changed. The movement of the tracer particles is due to the background flow, as is confirmed by the fact that no significant particle movement is visible when the volume flow of the electro spray is turned off. Thus, neither dielectrophoretic nor electrophoretic forces lead to the tracer particle motion. The submerged electro spray was induced by a potential difference of 3000 V, a volume flow rate of $20 \mu\text{L min}^{-1}$, and a KCl concentration of 0.1 mmol L^{-1} , and a silicone oil with a viscosity of 5 cSt was chosen as the dielectric. The particle motion was recorded for 0.15 s.

In Fig. 7.11, the particle streaklines and the magnitude of the vertical velocity field are shown. The particle velocities are extracted using the *Python* toolbox *trackpy* (Allan et al., 2018), based on the particle displacement between subsequent images. In order to map the particle velocities on a grid, the N vertical velocities v_i contained in each cell of a grid with 20×15 cells (cell size 54×48 px) are ensemble-averaged as

$$v = \sum_i^N \frac{1}{N} v_i. \quad (7.19)$$

Grid cells with less than 30 measured particle velocities v_i were omitted for the final representation. In Fig. 7.11, the streaklines demonstrate the flow field structure: The dielectric liquid reaches velocities of approximately 200 mm s^{-1} , with the most significant velocity in a plume below the needle (indicated by a black rectangle at the top). The plume is replenished by a radial inward flow close to the needle, where the liquid is strongly accelerated. The flow field impinges on the liquid-liquid interface, where the streaklines are curved outwards. Close to the interface, no particle motion can be observed, as the

Table 7.3: Numerical parameters used to calculate the interface deflection.

variable	description	value	variable	description	value
h	interface-needle distance	5 mm	ρ_o	density oil	910 kg/m ³
h_w	height water layer	$9h$	ρ_w	density water	1000 kg/m ³
h_o	height oil layer	$3h$	ν_o	kinematic viscosity oil	5 cSt
R_c	radius container	$20h$	ν_w	kinematic viscosity water	1 cSt
R_n	radius needle	0.45 mm	ϵ_o	relative permittivity oil	2.5
β	side wall slip length	20 mm	ϕ_n	needle potential	3 kV
Θ_c	side wall contact angle	90°	ϕ_i	interface potential	0 kV

meniscus at the container sidewall obstructs the optical access. Nevertheless, for the purpose of matching experimental and numerical velocities, sufficient data can be collected. The average vertical velocity field in the rectangular region $-1 \text{ mm} \leq r \leq 1 \text{ mm}$ and $2.5 \text{ mm} \leq z \leq 4 \text{ mm}$ results in a value of 130 mm/s, which can be compared to numerical results, in order to match R_d .

Numerical results

In the following, the interface deflection was computed as a function of the droplet radius R_d ranging from 0.5 μm to 50 μm , with a spray current of $I_0 = 20 \text{ nA}$. The numerical parameters are summarized in Table 7.3, which correspond to the calibration measurement. Figure 7.12(a) depicts the surface deflection, which increases exponentially with decreasing droplet radius R_d (as the x -axis is scaled logarithmically). The average vertical velocity in the rectangular region depicted in Fig. 7.11 show the closest match between the calibration experiments (130 mm/s) and the numeric results (127 mm/s) for a droplet radius of $R_d = 17.5 \mu\text{m}$. In Fig. 7.12(b), both the space charge density ρ_{el} (red) and the vertical velocity magnitude v (blue) are shown for this case. Similarly to the calibration experiments, the velocity field shows a maximum in a plume below the needle, and is replenished by radial inward flow. The space charge density accumulates in the central region as well, and its radial extend increases closer to the interface. Here, the fluid is accelerated along the electric field lines (depicted by arrows above the space charge density). The numerically obtained surface deflection results in a value of 1.1 mm, which is close to the experimental deflection of $1 \text{ mm} \pm 0.154 \text{ mm}$ (mean value $\pm 2 \times$ standard deviation). It is important to emphasize that the free parameter R_d was fixed by the velocity field. Then, without further fitting of parameters, the experimentally measured surface deflection is reproduced by the numerical approach, emphasizing that the impinging background flow is responsible for the observed deformations.

The electric field strength E_z at the needle center $r = 0 \mu\text{m}$ shows an interesting behavior, if compared to the droplet radius R_d , as shown in the inset of Fig. 7.12(a). For a constant spray current I_0 , the electric field strength changes its sign with decreasing droplet radius. This clearly unphysical result is an artifact of the fixed electric current at the needle, where a space charge region builds up in front of the needle, and leads to an inversion of the electric field. In reality, a change of sign of the electric field strength would lead to a change of the sign of the spray current as well. Incorporating a linear dependency of the spray current on the local electric field strength, resembling the results by Gundabala et al. (2010), leads to a different result. Here, the electric field strength $E_{z,0}$ obtained for the case of $R_d = 17.5 \mu\text{m}$ is used as the reference value, and the current is incorporated as $I = I_0 E_z(r = 0, z = h) / E_{z,0}$. As a result, the emitted current is regulated by the local electric field strength at the needle, and the electric field strength no longer changes its sign for small droplet radii R_d . In addition, the interface deflection reaches a plateau for small R_d , resembling the experimental observations for high conductivities and viscosities. In section 7.5.1, it was hypothesized that small droplet radii lead to long residence times, which in turn lead

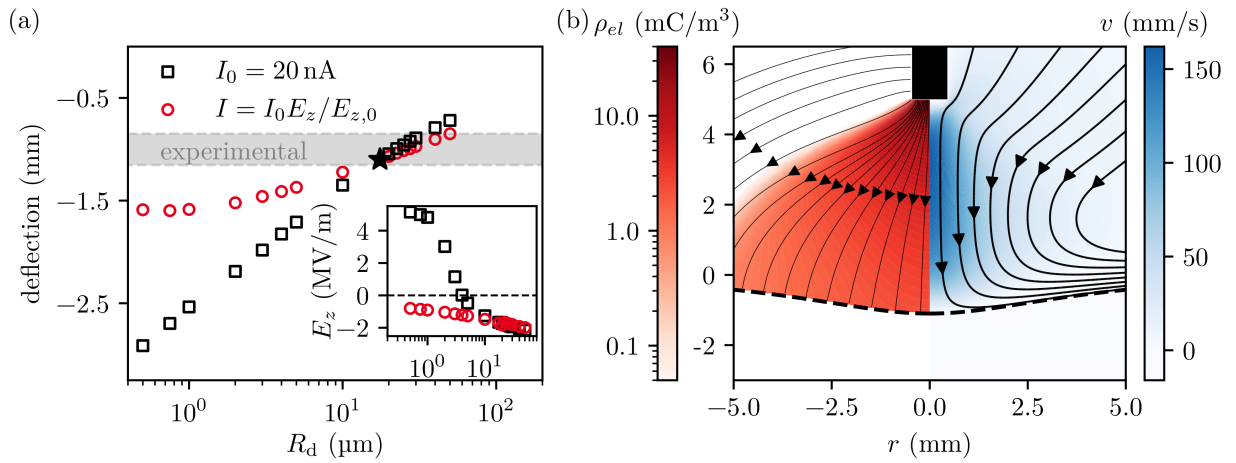


Figure 7.12: Numerically obtained interface deflections. (a) The deflection of the liquid-liquid interface is shown as a function of the droplet radius R_d for the parameters summarized in Table 7.3 and a fixed current I_0 (black symbols). The grey region depicts the experimental results (mean value $\pm 2 \times$ standard deviation). The velocity field of the calibration measurements is matched best by the velocity field of $R_d = 17.5 \mu\text{m}$ (indicated by a star symbol). Allowing the spray current to vary, depending on the electric field strength at the needle, the deflection reaches a plateau for small droplet sizes (red symbols). This is a result of space charges screening the electric field off. Inset: Electric field strength at the needle center in case of a constant and a variable spray current. For a constant spray current, the electric field changes its sign, showing a clearly unphysical result, which is rectified by introducing the current dependence. (b) Numerical results for a droplet radius $R_d = 17.5 \mu\text{m}$. The space charge density (red) and the vertical velocity magnitude (blue) are shown, in addition to the electric field lines (left) and the velocity streamlines (right). Adapted figure with permission from Sebastian Dehe, and Steffen Hardt, Phys. Rev. Fluids, 6(12), 123702, 2021. Copyright (2021) by the American Physical Society.

to a space charge that regulates the electro spray. Remarkably, the regulation mechanism is reproduced using this simple modeling approach, which allows to account for the regulation of the current. Overall, while the model introduces a series of simplifications, it shows quantitative agreement after calibration, and corroborates the regulatory mechanism observed in the experiments.

7.7 Summary and conclusion

In this chapter, the EHD instability of a liquid-liquid interface actuated by a spatially inhomogeneous DC electric field was studied, with a focus on the droplets of a conducting liquid inside the dielectric phase. First, the instability was triggered by a pin electrode placed within a dielectric liquid above the conducting phase, and it was shown that both a Taylor cone, as well as a surface depression can be formed. The latter phenomena was observed with a variety of dielectric liquids, conductivities, and independently of additional surfactants in the system. Instead, it was attributed to the existence of droplets in the dielectric. In order to analyze how the droplets lead to the surface depression, the pin electrode was replaced by a hollow needle, and a submerged electro spray was used to introduce charged droplets. Thereby, the existence of droplets and the interface breakdown were separated, rendering the system experimentally more accessible. The surface dimple increased with applied voltage difference, spray conductivity and

dielectric viscosity, and was nearly unaffected by the volume flow rate of the spray. Similarly, the spray current decreased with conductivity and dielectric viscosity. Scaling arguments demonstrated that the experimental observations are consistent with the background flow of the dielectric liquid impinging on the interface, and also provided an explanation for the current decrease and observed limits. The space charge due to the electrospray is expected to screen the needle from the electric field, leading to a self-regulatory behavior. In order to verify that the viscous momentum transport of the droplets on the background dielectric was responsible for the observed surface depression, it was reproduced by a numerical model of reduced order. Introducing a range of simplifying assumptions, the charge transport was modeled by an advection-diffusion process, and the only free parameter R_d was fitted using a PTV calibration measurement. Following, the numerically computed surface depression reproduced the experimentally measured deformation, and also showed the same regulatory effect of the space charge on the spray current. Overall, both the experimental and numerical results were consistent with the droplets influencing the background dielectric, leading to a strong background flow.

The exploration of the droplet influence on the EHD instability conducted in this chapter is of importance for a variety of reasons. First, it highlights how past experiments can influence the present behavior in EHD instabilities, and that the influence of the droplets can be hidden below the optical resolution. Even small amounts of residue of a conducting liquid either at the pin or engulfed in the dielectric can suffice to induce a strong background flow. The effect becomes more pronounced with increasing conductivity and viscosity of the dielectric. Even at the comparatively small viscosities used in this chapter, the effect can be severe, and at higher viscosities, the entrapment of droplets in the background phase is expected to be even stronger. Then, due to small differences of the density, the sedimentation of droplets is slow and they can remain in the dielectric phase for long times. This might necessitate refilling of a test cell after each experiment. Second, the experiments conducted with the submerged electrospray highlight the effects potentially induced by the background flow. Often, either the spray mode at the needle, or the droplet size and charge distribution are in focus, while the presence of the background flow is mentioned, but not studied in detail. Here, on the other hand, the emphasis was placed on the latter effect. Also, the influence of space charge effects was highlighted, being potentially crucial in viscous environments, and leading to a self-regulation of the electrospray.

In future work, several additional questions can be addressed. First, in this chapter, the focus was placed on the governing mechanism of droplets influencing the EHD instability by inducing a background flow, in conditions prior to interface breakdown. However, the regimes of different instabilities have not been systematically studied over the parameter range, which might lead to interesting effects. For example, it is not clear when single or multiple cones emerge from the dimple, and it might be interesting to study the later stages of the EHD breakdown in more detail. Second, the charge injection by a submerged electrospray bears some resemblance to the charge injection by Corona discharge (e.g., Kawamoto and Umezumi (2005)). It has been shown that the charge injection from sharp needles can induce a gas flow in an electric field. Similarly, the charged droplets injected by an electrospray can be used to induce a flow in a dielectric liquid. For example, with an applied voltage on the order of 3000 V, over a distance of 5 mm, a current on the order of tens of nA was induced, leading to an electric power loss on the order of tens to hundreds of μW . This power was converted to a liquid column with a diameter of a few mm moving at a velocity on the order of 0.2 m s^{-1} . While inducing charge into a dielectric liquid might not be favorable in some processes, it allows to pump dielectric liquids by means of electric fields, leading to compact pump designs without moving parts.

8 Concluding remarks

Over the course of this thesis, different electrohydrodynamic phenomena in the presence of fluidic interfaces were investigated. Specifically, the potential of electro-osmotic flow over superhydrophobic surfaces to create complex flow patterns in a Hele-Shaw geometry has been studied, with focus on the wetting state stability, the achievable flow velocities, as well as the transport and dispersion of a passive tracer in such a flow field. Furthermore, instabilities at the interface between a dielectric and a conducting liquid were analyzed, either actuated by a spatially homogeneous, harmonically oscillating or by a spatially inhomogeneous, time-constant electric field. The underlying phenomena have been examined using experimental, numerical, and analytical methods in varying constellations.

As the flow over superhydrophobic surfaces requires the existence of a stable gas-liquid interface, the wetting state stability of microstructured surfaces was characterized in chapter 3. As a base structure, micropillars with varying pitch were produced on a PDMS surface using soft-lithography. A secondary PVC nanostructure was applied using a solvent-nonsolvent evaporation process, leading to a hierarchy of length scales. Compared to the single-scale structure, the wetting state stability was enhanced versus electric field induced transitions. In addition, light-reflection microscopy demonstrated that the wetting states at hierarchical surfaces cannot be described using distinct wetting states (Cassie-Baxter, nano Cassie-Baxter and Wenzel), as they exhibit a continuous range of intermediate wetting states. Overall, the results of this chapter are fundamental for the utilization of superhydrophobic surfaces for driving electro-osmosis, as the maximum electric fields perpendicular to the interface with stable wetting states are identified, and they also emphasize the role of secondary structures.

The electro-osmotic flow over superhydrophobic surfaces was studied in chapter 4. Since it is experimentally advantageous to drive the EOF using synchronized AC-fields at both the gate and driving electrodes, the governing equations of the height-averaged flow field in a Hele-Shaw configuration were derived following previous work (Boyko et al., 2015; Rubin et al., 2017). From the derivation, it follows that purely oscillatory fields can lead to time-averaged flow, and the resulting height-averaged flow field due to a disc-shaped gate electrode was obtained. The experimental realization of the disc-shaped gate electrode was used to study the characteristics of EOF over superhydrophobic surfaces induced by gate electrodes. Especially two results are important: First, the resulting flow velocity scales linearly with both the effective slip length of the superhydrophobic surface as well as the applied gate potential. Thus, the observed flow velocity was an order of magnitude faster than on flat surfaces in corresponding conditions. Second, the resulting flow field is largely independent of pH, allowing to introduce significant flow rates in a wide range of pH between 3 and 11. This is a significant advantage over flat surfaces, where the pH value has a strong influence on the resulting velocity, which limits usability in biological applications. Combined, these results highlight the promising opportunities of EOF over superhydrophobic surfaces, supported by proof-of-principle experiments using multiple gate electrodes. Also, the influence of surfactants and the electrowetting stability were discussed, as they inhibit the achievable flow velocities, and potential strategies to overcome limitations were outlined.

In order to use electro-osmotic flow over superhydrophobic surfaces for biochemical applications, a transport model for a passive species was derived in chapter 5 using a perturbation approach. It supplements the flow field equations with an appropriate height-averaged species transport model,

specifically accounting for dispersion due to spatial and temporal flow inhomogeneities. The effects of non-isotropic dispersion is represented by a dispersion tensor in the resulting transport equation. The reduced-order model shows good agreement to three-dimensional Lagrangian particle simulations for three particular test cases. With the formulation of the transport model, a complete description is available to design biochemical applications in a Hele-Shaw geometry. Furthermore, the idea of dispersion shaping was discussed, where a desired dispersion field is achieved by adjusting the spatial distribution of the wall mobility. This is specifically interesting for mimicking biological systems, where regions of high directional transport are embedded in regions of low diffusivity, which can be adjusted temporally. Thereby, applications are enabled for example in the context of migration of biological organisms due to external stimuli (chemotaxis).

In chapter 6, the instability of a liquid-liquid interface due to a spatially homogeneous electric field was studied. The spatial structure of the instability was resolved using an algorithm to reconstruct the interface, based on the light-refraction. The experimentally determined wavelengths and critical voltages of the electrostatic Faraday instability were compared to the analytical model provided by Bandopadhyay and Hardt (2017), showing good agreement of the resulting wavelengths. From evaluation of the spatial structure of the instability, the experiments revealed a dominant influence of the domain boundary, visible in the excitation of discrete modes of the surface harmonics. These results contrast the experiments reported by Ward et al. (2019), where no discrete modes were observed, and no wavelengths could be determined. The discrepancies between observations can be rationalized by the mode of observation used by Ward et al., which possibly obscured the boundary influence due to refraction and edge-waves. Overall, the knowledge of the electrostatically excited Faraday instability is extended, and the theory of Bandopadhyay and Hardt (2017) with respect to the wavelengths confirmed.

The experimental investigations of the instability of a liquid-liquid interface due to a spatially inhomogeneous electric field in chapter 7 was triggered by the observation of an alternative mode of instability. When a pin electrode was deposited above the interface, either the classical Taylor cone formed, or the interface moved away from the electrode, with cones emerging from the rim of the formed depression. Using qualitative experiments, conducting droplets immersed in the dielectric phase due to past or the present experiment were identified as the cause for the surface depression. By replacing the pin electrode with a submerged electro-spray, the occurrence of droplets was decoupled from the EHD instability, and the influence of the spray parameters was characterized experimentally. Charged droplets moving through the dielectric liquid induce a strong background flow that impinges on the interface, which leads to the observed depression. The resulting spray current decreased and reached a lower limit for high liquid conductivities and dielectric viscosities, indicating a self-regulatory behavior due to the space charge of the electro-spray. By using numerical modeling with a reduced set of equations, it was shown that the surface depression can be formed by the background flow, and the regulating mechanism was reproduced as well. These results emphasize the role of the dielectric viscosity in such a prototypic experiment, which was used in numerical studies to observe scaling laws of the droplet charge (Collins et al., 2013). It highlights a potential mechanism that leads to deviations between predictions and observations, which becomes important when the numerical scaling is attempted to be reproduced experimentally.

All phenomena presented in this work involve the interaction of electric fields and fluidic interfaces, inspired by different research questions. In the first part of the thesis, the advancement of the technological applications was focused on, investigating the ability to utilize EOF over superhydrophobic surfaces as a tool in flow-shaping applications. The second part of the thesis was concerned with observations made in EHD instability experiments, which required further detailing and explanation. In each chapter, additional research questions were identified, which are worth pursuing in future investigations. Overall, utilizing a combination of analysis, experiments and numerical modeling, the knowledge in the area of the respective EHD phenomena was extended.

Bibliography

- A. Adrover. Effect of secondary flows on dispersion in finite-length channels at high Peclet numbers. *Physics of Fluids*, 25(9):093601, 2013. doi: 10.1063/1.4820214.
- A. Ajdari, N. Bontoux, and H. A. Stone. Hydrodynamic dispersion in shallow microchannels: The effect of cross-sectional shape. *Analytical Chemistry*, 78(2):387–392, 2006. doi: 10.1021/ac0508651.
- D. B. Allan, T. Caswell, N. C. Keim, and C. M. van der Wel. TrackPy. v0.4.2, 2018. doi: 10.5281/zenodo.3492186.
- V. Ananthakrishnan, W. N. Gill, and A. J. Barduhn. Laminar dispersion in capillaries: Part I. Mathematical analysis. *AIChE Journal*, 11(6):1063–1072, 1965. doi: 10.1002/aic.690110620.
- H. Aref. Stirring by chaotic advection. *Journal of Fluid Mechanics*, 143:1–21, 1984. doi: 10.1017/S0022112084001233.
- R. Aris. On the dispersion of a solute in a fluid flowing through a tube. *Proceedings of the Royal Society of London. Series A. Mathematical and Physical Sciences*, 235(1200):67–77, 1956. doi: 10.1098/rspa.1956.0065.
- R. Aris. On the dispersion of a solute in pulsating flow through a tube. *Proceedings of the Royal Society of London. Series A. Mathematical and Physical Sciences*, 259(1298):370–376, 1960. doi: 10.1098/rspa.1960.0231.
- M.-C. Audry, A. Piednoir, P. Joseph, and E. Charlaix. Amplification of electro-osmotic flows by wall slippage: Direct measurements on OTS-surfaces. *Faraday Discussions*, 146:113–124, 2010. doi: 10.1039/b927158a.
- V. Bacheva, F. Paratore, S. Rubin, G. V. Kaigala, and M. Bercovici. Tunable bidirectional electroosmotic flow for diffusion-based separations. *Angewandte Chemie*, 132(31):12994–12999, 2020. doi: 10.1002/ange.201916699.
- S. S. Bahga, O. I. Vinogradova, and M. Z. Bazant. Anisotropic electro-osmotic flow over super-hydrophobic surfaces. *Journal of Fluid Mechanics*, 644:245–255, 2010. doi: 10.1017/S0022112009992771.
- S. S. Bahga, M. Bercovici, and J. G. Santiago. Robust and high-resolution simulations of nonlinear electrokinetic processes in variable cross-section channels. *Electrophoresis*, 33(19-20):3036–3051, 2012. doi: 10.1002/elps.201200264.
- A. Bandopadhyay and S. Hardt. Stability of horizontal viscous fluid layers in a vertical arbitrary time periodic electric field. *Physics of Fluids*, 29(12):124101, 2017. doi: 10.1063/1.4999429.
- S. Bandyopadhyay and B. Mazumder. On contaminant dispersion in unsteady generalised Couette flow. *International Journal of Engineering Science*, 37(11):1407–1423, 1999. doi: 10.1016/S0020-7225(98)00132-3.

-
- S. Banerjee and S. Mazumdar. Electrospray ionization mass spectrometry: A technique to access the information beyond the molecular weight of the analyte. *International Journal of Analytical Chemistry*, 2012:282574, 2012. doi: 10.1155/2012/282574.
- J.-L. Barrat and L. Bocquet. Large slip effect at a nonwetting fluid-solid interface. *Physical Review Letters*, 82(23):4671–4674, 1999. doi: 10.1103/PhysRevLett.82.4671.
- A. Barrero, J. M. López-Herrera, A. Boucard, I. G. Loscertales, and M. Márquez. Steady cone-jet electrosprays in liquid insulator baths. *Journal of Colloid and Interface Science*, 272(1):104–108, 2004. doi: 10.1016/j.jcis.2003.10.035.
- W. Barthlott and C. Neinhuis. Purity of the sacred lotus, or escape from contamination in biological surfaces. *Planta*, 202(1):1–8, 1997. doi: 10.1007/s004250050096.
- N. G. Barton. On the method of moments for solute dispersion. *Journal of Fluid Mechanics*, 126:205–218, 1983. doi: 10.1017/S0022112083000117.
- G. K. Batchelor. *An Introduction to Fluid Dynamics*. Cambridge Mathematical Library. Cambridge University Press, 2000. ISBN 9780521663960. doi: 10.1017/CBO9780511800955.
- W. Batson, F. Zoueshtiagh, and R. Narayanan. Dual role of gravity on the Faraday threshold for immiscible viscous layers. *Physical Review E*, 88(6):063002, 2013a. doi: 10.1103/PhysRevE.88.063002.
- W. Batson, F. Zoueshtiagh, and R. Narayanan. The Faraday threshold in small cylinders and the sidewall non-ideality. *Journal of Fluid Mechanics*, 729:496–523, 2013b. doi: 10.1017/jfm.2013.324.
- A. V. Belyaev and O. I. Vinogradova. Electro-osmosis on anisotropic superhydrophobic surfaces. *Physical Review Letters*, 107(9):098301, 2011. doi: 10.1103/PhysRevLett.107.098301.
- T. B. Benjamin and F. Ursell. The stability of the plane free surface of a liquid in vertical periodic motion. *Proceedings of the Royal Society of London. Series A. Mathematical and Physical Sciences*, 225(1163): 505–515, 1954. doi: 10.1098/rspa.1954.0218.
- S. Berry, T. Fedynyshyn, L. Parameswaran, and A. Cabral. Switchable electrowetting of droplets on dual-scale structured surfaces. *Journal of Vacuum Science & Technology B*, 30(6):06F801, 2012. doi: 10.1116/1.4764092.
- J. Bico, C. Marzolin, and D. Quéré. Pearl drops. *Europhysics Letters (EPL)*, 47(2):220–226, 1999. doi: 10.1209/epl/i1999-00548-y.
- R. B. Bird, W. E. Stewart, and E. N. Lightfoot. *Transport Phenomena*. Wiley, New York, revised 2nd edition, 2007.
- C. J. C. Biscombe. The discovery of electrokinetic phenomena: Setting the record straight. *Angewandte Chemie International Edition*, 56(29):8338–8340, 2017. doi: 10.1002/anie.201608536.
- D. B. Bober and C. H. Chen. Pulsating electrohydrodynamic cone-jets: From choked jet to oscillating cone. *Journal of Fluid Mechanics*, 689:552–563, 2011. doi: 10.1017/jfm.2011.453.
- R. Bocanegra, D. Galán, M. Márquez, I. G. Loscertales, and A. Barrero. Multiple electrosprays emitted from an array of holes. *Journal of Aerosol Science*, 36(12):1387–1399, 2005. doi: 10.1016/j.jaerosci.2005.04.003.
- J. B. Boreyko and C.-H. Chen. Self-propelled dropwise condensate on superhydrophobic surfaces. *Physical Review Letters*, 103(18):184501, 2009. doi: 10.1103/PhysRevLett.103.184501.
- C. I. Bouzigues, P. Tabeling, and L. Bocquet. Nanofluidics in the Debye layer at hydrophilic and hydrophobic surfaces. *Physical Review Letters*, 101(11):114503, 2008. doi: 10.1103/PhysRevLett.101.114503.

-
- M. R. Bown and C. D. Meinhart. AC electroosmotic flow in a DNA concentrator. *Microfluidics and Nanofluidics*, 2(6):513–523, 2006. doi: 10.1007/s10404-006-0097-4.
- E. Boyko, S. Rubin, A. D. Gat, and M. Bercovici. Flow patterning in Hele-Shaw configurations using non-uniform electro-osmotic slip. *Physics of Fluids*, 27(10):102001, 2015. doi: 10.1063/1.4931637.
- E. Boyko, V. Bacheva, M. Eigenbrod, F. Paratore, A. D. Gat, S. Hardt, and M. Bercovici. Microscale hydrodynamic cloaking and shielding via electro-osmosis. *Physical Review Letters*, 126(18):184502, 2021. doi: 10.1103/PhysRevLett.126.184502.
- H. Brenner and D. A. Edwards. *Macrotransport Processes*. Butterworth-Heinemann series in chemical engineering. Elsevier Science, 1st edition, 1993. ISBN 9780080510590. doi: 10.1016/C2009-0-25915-0.
- W. Brevis, Y. Niño, and G. H. Jirka. Integrating cross-correlation and relaxation algorithms for particle tracking velocimetry. *Experiments in Fluids*, 50(1):135–147, 2011. doi: 10.1007/s00348-010-0907-z.
- V. A. Briskman and G. F. Shaidurov. Parametric instability of a fluid surface in an alternating electric field. *Soviet Physics Doklady*, 13:540–542, 1968.
- H. Bruus. *Theoretical microfluidics*. Oxford Master Series in Condensed Matter Physics. Oxford University Press, Oxford, 2008.
- J. M. Butler. Short tandem repeat typing technologies used in human identity testing. *BioTechniques*, 43(4):Sii–Sv, 2007. doi: 10.2144/000112582.
- H. Butt, K. Graf, and M. Kappl. *Physics and Chemistry of Interfaces*. Wiley, 2003. ISBN 9783527404131. doi: 10.1002/3527602313.
- T. Casalini, M. Salvalaglio, G. Perale, M. Masi, and C. Cavallotti. Diffusion and aggregation of sodium fluorescein in aqueous solutions. *The Journal of Physical Chemistry B*, 115(44):12896–12904, 2011. doi: 10.1021/jp207459k.
- A. B. D. Cassie and S. Baxter. Wettability of porous surfaces. *Transactions of the Faraday Society*, 40(5):546–551, 1944. doi: 10.1039/tf9444000546.
- E. Celia, T. Darmanin, E. Taffin de Givenchy, S. Amigoni, and F. Guittard. Recent advances in designing superhydrophobic surfaces. *Journal of Colloid and Interface Science*, 402:1–18, 2013. doi: 10.1016/j.jcis.2013.03.041.
- P. C. Chatwin. On the longitudinal dispersion of passive contaminant in oscillatory flows in tubes. *Journal of Fluid Mechanics*, 71(3):513–527, 1975. doi: 10.1017/S0022112075002716.
- H. Chen, Z. Yuan, J. Zhang, Y. Liu, K. Li, D. Zhao, S. Li, P. Shi, and J. Tang. Preparation, characterization and wettability of porous superhydrophobic poly (vinyl chloride) surface. *Journal of Porous Materials*, 16(4):447–451, 2009. doi: 10.1007/s10934-008-9217-8.
- Y.-C. Chen, Y. Suzuki, and K. Morimoto. Electrowetting-dominated instability of Cassie droplets on superhydrophobic pillared surfaces. *Langmuir*, 35(6):2013–2022, 2019. doi: 10.1021/acs.langmuir.8b02825.
- C.-H. Choi and C.-J. Kim. Large slip of aqueous liquid flow over a nanoengineered superhydrophobic surface. *Physical Review Letters*, 96(6):066001, 2006. doi: 10.1103/PhysRevLett.96.066001.
- C.-H. Choi, K. J. A. Westin, and K. S. Breuer. Apparent slip flows in hydrophilic and hydrophobic microchannels. *Physics of Fluids*, 15(10):2897, 2003. doi: 10.1063/1.1605425.

-
- H. C. W. Chu, S. Garoff, T. M. Przybycien, R. D. Tilton, and A. S. Khair. Dispersion in steady and time-oscillatory two-dimensional flows through a parallel-plate channel. *Physics of Fluids*, 31(2):022007, 2019. doi: 10.1063/1.5085006.
- N. Churaev, J. Ralston, I. Sergeeva, and V. Sobolev. Electrokinetic properties of methylated quartz capillaries. *Advances in Colloid and Interface Science*, 96(1-3):265–278, 2002. doi: 10.1016/S0001-8686(01)00084-7.
- S. Ciliberto and J. P. Gollub. Pattern competition leads to chaos. *Physical Review Letters*, 52(11):922–925, 1984. doi: 10.1103/PhysRevLett.52.922.
- R. T. Collins, J. J. Jones, M. T. Harris, and O. A. Basaran. Electrohydrodynamic tip streaming and emission of charged drops from liquidcones. *Nature Physics*, 4(2):149–154, 2008. doi: 10.1038/nphys807.
- R. T. Collins, K. Sambath, M. T. Harris, and O. A. Basaran. Universal scaling laws for the disintegration of electrified drops. *Proceedings of the National Academy of Sciences of the United States of America*, 110(13):4905–4910, 2013. doi: 10.1073/pnas.1213708110.
- COMSOL. COMSOL multiphysics reference manual, version 5.5. *COMSOL AB*, 2019.
- E. F. Cooper and A. F. A. Asfour. Densities and kinematic viscosities of some C6-C16 n-alkane binary liquid systems at 293.15 K. *Journal of Chemical & Engineering Data*, 36(3):285–288, 1991. doi: 10.1021/je00003a008.
- Y. Couder, S. Protière, E. Fort, and A. Boudaoud. Walking and orbiting droplets. *Nature*, 437(7056):208–208, 2005. doi: 10.1038/437208a.
- R. Datta and V. R. Kotamarthi. Electrokinetic dispersion in capillary electrophoresis. *AIChE Journal*, 36(6):916–926, 1990. doi: 10.1002/aic.690360613.
- S. Datta and S. Ghosal. Dispersion due to wall interactions in microfluidic separation systems. *Physics of Fluids*, 20(1):012103, 2008. doi: 10.1063/1.2828098.
- A. M. J. Davis and E. Lauga. Hydrodynamic friction of fakir-like superhydrophobic surfaces. *Journal of Fluid Mechanics*, 661:402–411, 2010. doi: 10.1017/S0022112010003460.
- P. G. de Gennes. Wetting: Statics and dynamics. *Reviews of Modern Physics*, 57(3):827–863, 1985. doi: 10.1103/RevModPhys.57.827.
- S. Dehe and S. Hardt. Deformation modes of an oil-water interface under a local electric field: From Taylor cones to surface dimples. *Physical Review Fluids*, 6(12):123702, 2021. doi: 10.1103/PhysRevFluids.6.123702.
- S. Dehe, B. Rofman, M. Bercovici, and S. Hardt. Electro-osmotic flow enhancement over superhydrophobic surfaces. *Physical Review Fluids*, 5(5):053701, 2020. doi: 10.1103/PhysRevFluids.5.053701.
- S. Dehe, M. Hartmann, A. Bandopadhyay, and S. Hardt. From Taylor cones to surface dimples: How droplets modify electrohydrodynamic instabilities. *arXiv*, (arXiv:2111.00049), 2021a.
- S. Dehe, I.-S. Rehm, and S. Hardt. Hydrodynamic dispersion in Hele-Shaw flows with inhomogeneous wall boundary conditions. *Journal of Fluid Mechanics*, 925:A11, 2021b. doi: 10.1017/jfm.2021.648.
- J. Diao, L. Young, S. Kim, E. A. Fogarty, S. M. Heilman, P. Zhou, M. L. Shuler, M. Wu, and M. P. DeLisa. A three-channel microfluidic device for generating static linear gradients and its application to the quantitative analysis of bacterial chemotaxis. *Lab on a Chip*, 6(3):381–388, 2006. doi: 10.1039/b511958h.
- F. T. Dodge, D. D. Kana, and H. N. Abramson. Liquid surface oscillations in longitudinally excited rigid cylindrical containers. *AIAA Journal*, 3(4):685–695, 1965. doi: 10.2514/3.2948.

- S. Douady. Experimental study of the Faraday instability. *Journal of Fluid Mechanics*, 221:383–409, 1990. doi: 10.1017/S0022112090003603.
- S. Douady and S. Fauve. Pattern selection in Faraday instability. *Epl*, 6(3):221–226, 1988. doi: 10.1209/0295-5075/6/3/006.
- W. S. Edwards and S. Fauve. Patterns and quasi-patterns in the Faraday experiment. *Journal of Fluid Mechanics*, 278:123–148, 1994. doi: 10.1017/S0022112094003642.
- A. Eifert. *Untersuchungen zur Koronaentladung, Oberflächenmodifikation mittels Koronaentladung und zu Benetzungsphänomenen auf imprägnierten Oberflächen*. PhD thesis, TU Darmstadt, 2015.
- A. Einstein. Über die von der molekularkinetischen Theorie der Wärme geforderte Bewegung von in ruhenden Flüssigkeiten suspendierten Teilchen. *Annalen der Physik*, 322(8):549–560, 1905. doi: 10.1002/andp.19053220806.
- H. B. Eral, D. J. C. M. ’t Mannetje, and J. M. Oh. Contact angle hysteresis: A review of fundamentals and applications. *Colloid and Polymer Science*, 291:247–260, 2013. doi: 10.1007/s00396-012-2796-6.
- H. Falahati, L. Wong, L. Davarpanah, A. Garg, P. Schmitz, and D. P. J. Barz. The zeta potential of PMMA in contact with electrolytes of various conditions: Theoretical and experimental investigation. *Electrophoresis*, 35(6):870–882, 2014. doi: 10.1002/elps.201300436.
- M. Faraday. XVII. On a peculiar class of acoustical figures; and on certain forms assumed by groups of particles upon vibrating elastic surfaces. *Philosophical Transactions of the Royal Society of London*, 121 (August 1827):299–340, 1831. doi: 10.1098/rstl.1831.0018.
- J. Fenn, M. Mann, C. Meng, S. Wong, and C. Whitehouse. Electrospray ionization for mass spectrometry of large biomolecules. *Science*, 246(4926):64–71, 1989. doi: 10.1126/science.2675315.
- J. Fernández de la Mora. The fluid dynamics of Taylor cones. *Annual Review of Fluid Mechanics*, 39(1): 217–243, 2007. doi: 10.1146/annurev.fluid.39.050905.110159.
- J. Fernández de la Mora and I. G. Loscertales. The current emitted by highly conducting Taylor cones. *Journal of Fluid Mechanics*, 260:155–184, 1994. doi: 10.1017/S0022112094003472.
- R. Fernández-Mateo and A. T. Pérez. Faraday waves under perpendicular electric field and their application to the walking droplet phenomenon. *Physics of Fluids*, 33(1):017109, 2021. doi: 10.1063/5.0028118.
- P. Fife and K. R. K. Nicholes. Dispersion in flow through small tubes. *Proceedings of the Royal Society of London. A. Mathematical and Physical Sciences*, 344(1636):131–145, 1975. doi: 10.1098/rspa.1975.0094.
- P. Forsberg, F. Nikolajeff, and M. Karlsson. Cassie–Wenzel and Wenzel–Cassie transitions on immersed superhydrophobic surfaces under hydrostatic pressure. *Soft Matter*, 7(1):104–109, 2011. doi: 10.1039/C0SM00595A.
- W. Förstner and E. Gülch. A fast operator for detection and precise location of distinct points, corners and centres of circular features. In *Proc. ISPRS intercommission conference on fast processing of photogrammetric data*, pages 281–305. Interlaken, 1987.
- I. Gabay, F. Paratore, E. Boyko, A. Ramos, A. D. Gat, and M. Bercovici. Shaping liquid films by dielectrophoresis. *Flow*, 1:E13, 2021. doi: 10.1017/flo.2021.13.
- P. Gambhire and R. Thaokar. Electrokinetic model for electric-field-induced interfacial instabilities. *Physical Review E*, 89(3):032409, 2014. doi: 10.1103/PhysRevE.89.032409.
- P. Gambhire and R. M. Thaokar. Electrohydrodynamic instabilities at interfaces subjected to alternating electric field. *Physics of Fluids*, 22(6):064103, 2010. doi: 10.1063/1.3431043.

-
- P. Gambhire and R. M. Thaokar. Role of conductivity in the electrohydrodynamic patterning of air-liquid interfaces. *Physical Review E*, 86(3):036301, 2012. doi: 10.1103/PhysRevE.86.036301.
- A. M. Gañán-Calvo, J. C. Lasheras, J. Dávila, and A. Barrero. The electrostatic spray emitted from an electrified conical meniscus. *Journal of Aerosol Science*, 25(6):1121–1142, 1994. doi: 10.1016/0021-8502(94)90205-4.
- A. M. Gañán-Calvo, J. M. López-Herrera, and P. Riesco-Chueca. The combination of electrospray and flow focusing. *Journal of Fluid Mechanics*, 566:421–445, 2006. doi: 10.1017/S0022112006002102.
- A. M. Gañán-Calvo, J. M. López-Herrera, M. A. Herrada, A. Ramos, and J. M. Montanero. Review on the physics of electrospray: From electrokinetics to the operating conditions of single and coaxial Taylor cone-jets, and AC electrospray. *Journal of Aerosol Science*, 125:32–56, 2018. doi: 10.1016/j.jaerosci.2018.05.002.
- L. Gao and T. J. McCarthy. How Wenzel and Cassie were wrong. *Langmuir*, 23(7):3762–3765, 2007. doi: 10.1021/la062634a.
- B. Gaš, M. Jaroš, V. Hruška, I. Zuskova, and M. Štědrý. PeakMaster - A freeware simulator of capillary zone electrophoresis. *LC-GC Europe*, 18(5):282–288, 2005.
- W. N. Gill, V. Ananthakrishnan, and R. J. Nunge. Dispersion in developing velocity fields. *AIChE Journal*, 14(6):939–946, 1968. doi: 10.1002/aic.690140621.
- W. N. Gill, R. Sankarasubramanian, and G. I. Taylor. Dispersion of a non-uniform slug in time-dependent flow. *Proceedings of the Royal Society of London. A. Mathematical and Physical Sciences*, 322(1548): 101–117, 1971. doi: 10.1098/rspa.1971.0057.
- M. Giona, A. Adrover, S. Cerbelli, and F. Garofalo. Laminar dispersion at high Péclet numbers in finite-length channels: Effects of the near-wall velocity profile and connection with the generalized Leveque problem. *Physics of Fluids*, 21(12):123601, 2009. doi: 10.1063/1.3263704.
- I. Glasgow, J. Batton, and N. Aubry. Electroosmotic mixing in microchannels. *Lab on a Chip*, 4(6):558–562, 2004. doi: 10.1039/b408875a.
- J. P. Gleeson and H. A. Stone. Taylor dispersion in electroosmotic flows with random zeta potentials. *TechConnect Briefs - Technical Proceedings of the 2004 NSTI Nanotechnology Conference and Trade Show*, 2(5):375–378, 2004.
- B. J. Gluckman, P. Marcq, J. Bridger, and J. P. Gollub. Time averaging of chaotic spatiotemporal wave patterns. *Physical Review Letters*, 71(13):2034–2037, 1993. doi: 10.1103/PhysRevLett.71.2034.
- J. P. Gollub and C. W. Meyer. Symmetry-breaking instabilities on a fluid surface. *Physica D: Nonlinear Phenomena*, 6(3):337–346, 1983. doi: 10.1016/0167-2789(83)90016-7.
- A. González, A. Ramos, N. G. Green, A. Castellanos, and H. Morgan. Fluid flow induced by nonuniform ac electric fields in electrolytes on microelectrodes. II. A linear double-layer analysis. *Physical Review E*, 61(4):4019–4028, 2000. doi: 10.1103/PhysRevE.61.4019.
- J. Grace and J. Marijnissen. A review of liquid atomization by electrical means. *Journal of Aerosol Science*, 25(6):1005–1019, 1994. doi: 10.1016/0021-8502(94)90198-8.
- S. Gray. IV. A letter from Mr. Stephen Gray to Dr. Mortimer, Secr. R. S. Containing a farther account of his experiments concerning electricity. *Philosophical Transactions of the Royal Society of London*, 37 (423):285–291, 1731. doi: 10.1098/rstl.1731.0050.

-
- N. G. Green, A. Ramos, A. González, H. Morgan, and A. Castellanos. Fluid flow induced by nonuniform ac electric fields in electrolytes on microelectrodes. I. Experimental measurements. *Physical Review E*, 61(4):4011–4018, 2000. doi: 10.1103/PhysRevE.61.4011.
- N. G. Green, A. Ramos, A. González, H. Morgan, and A. Castellanos. Fluid flow induced by nonuniform ac electric fields in electrolytes on microelectrodes. III. Observation of streamlines and numerical simulation. *Physical Review E*, 66(2):026305, 2002. doi: 10.1103/PhysRevE.66.026305.
- S. K. Griffiths and R. H. Nilson. Electroosmotic fluid motion and late-time solute transport for large zeta potentials. *Analytical Chemistry*, 72(20):4767–4777, 2000. doi: 10.1021/ac000539f.
- J. Guerrero, A. J. Hijano, M. A. Lobato, F. J. Higuera, I. G. Loscertales, and A. Fernandez-Nieves. Emission modes in electro co-flow. *Physics of Fluids*, 31(8), 2019. doi: 10.1063/1.5121714.
- V. R. Gundabala, N. Vilanova, and A. Fernández-Nieves. Current-voltage characteristic of electro-spray processes in microfluidics. *Physical Review Letters*, 105(15):1–4, 2010. doi: 10.1103/PhysRevLett.105.154503.
- Z. Guo and W. Liu. Biomimic from the superhydrophobic plant leaves in nature: Binary structure and unitary structure. *Plant Science*, 172(6):1103–1112, 2007. doi: 10.1016/j.plantsci.2007.03.005.
- H. C. Hardy, D. Telfair, and W. H. Pielemeier. The velocity of sound in air. *The Journal of the Acoustical Society of America*, 13(3):226–233, 1942. doi: 10.1121/1.1916169.
- R. P. Hartman, D. J. Brunner, D. M. Camelot, J. C. Marijnissen, and B. Scarlett. Electrohydrodynamic atomization in the cone-jet mode physical modeling of the liquid cone and jet. *Journal of Aerosol Science*, 30(7):823–849, 1999. doi: 10.1016/S0021-8502(99)00033-6.
- M. Hartmann and S. Hardt. Stability of evaporating droplets on chemically patterned surfaces. *Langmuir*, 35(14):4868–4875, 2019. doi: 10.1021/acs.langmuir.9b00172.
- H. Helmholtz. Studien über elektrische Grenzschichten. *Annalen der Physik und Chemie*, 243(7):337–382, 1879. doi: 10.1002/andp.18792430702.
- D. L. Herbertson, C. R. Evans, N. J. Shirtcliffe, G. McHale, and M. I. Newton. Electrowetting on superhydrophobic SU-8 patterned surfaces. *Sensors and Actuators A: Physical*, 130-131(SPEC. ISS.):189–193, 2006. doi: 10.1016/j.sna.2005.12.018.
- A. E. Herr, J. I. Molho, J. G. Santiago, M. G. Mungal, T. W. Kenny, and M. G. Garguilo. Electroosmotic capillary flow with nonuniform zeta potential. *Analytical Chemistry*, 72(5):1053–1057, 2000. doi: 10.1021/ac990489i.
- F. J. Higuera. Electrodispersion of a liquid of finite electrical conductivity in an immiscible dielectric liquid. *Physics of Fluids*, 22(11), 2010. doi: 10.1063/1.3493636.
- K. Horiuchi and P. Dutta. Electrokinetic flow control in microfluidic chips using a field-effect transistor. *Lab on a Chip*, 6(6):714–723, 2006. doi: 10.1039/b600067c.
- D. M. Huang, C. Cottin-Bizonne, C. Ybert, and L. Bocquet. Massive amplification of surface-induced transport at superhydrophobic surfaces. *Physical Review Letters*, 101(6):064503, 2008. doi: 10.1103/PhysRevLett.101.064503.
- H. C. Hunter and A. K. Ray. On progeny droplets emitted during Coulombic fission of charged microdrops. *Physical Chemistry Chemical Physics*, 11(29):6156–6165, 2009. doi: 10.1039/b820457h.

-
- M. Iino, M. Suzuki, and A. J. Ikushima. Surface-wave resonance method for measuring surface tension with a very high precision. *Le Journal de Physique Colloques*, 46(C10):C10-813-C10-816, 1985. doi: 10.1051/jphyscol:198510178.
- R. F. Ismagilov, A. D. Stroock, P. J. Kenis, G. Whitesides, and H. A. Stone. Experimental and theoretical scaling laws for transverse diffusive broadening in two-phase laminar flows in microchannels. *Applied Physics Letters*, 76(17):2376-2378, 2000. doi: 10.1063/1.126351.
- A. Jaworek and A. Krupa. Main modes of electrohydrodynamic spraying of liquids. *Third International Conference on Multiphase Flow, ICMF'98*, pages 1-5, 1998.
- F. Jiang, K. S. Drese, S. Hardt, M. Küpper, and F. Schönfeld. Helical flows and chaotic mixing in curved micro channels. *AIChE Journal*, 50(9):2297-2305, 2004. doi: 10.1002/aic.10188.
- S. Jin, P. Huang, J. Park, J. Y. Yoo, and K. S. Breuer. Near-surface velocimetry using evanescent wave illumination. *Experiments in Fluids*, 37:825-833, 2004. doi: 10.1007/s00348-004-0870-7.
- G. Job and R. Rüffler. *Physikalische Chemie*. Vieweg+Teubner, Wiesbaden, 2011. ISBN 978-3-8351-0040-4. doi: 10.1007/978-3-8348-9834-0.
- V. Jokinen, E. Kankuri, S. Hoshian, S. Franssila, and R. H. Ras. Superhydrophobic blood-repellent surfaces. *Advanced Materials*, 30(24):1705104, 2018. doi: 10.1002/adma.201705104.
- L. Joly, C. Ybert, E. Trizac, and L. Bocquet. Hydrodynamics within the electric double layer on slipping surfaces. *Physical Review Letters*, 93(25):257805, 2004. doi: 10.1103/PhysRevLett.93.257805.
- L. Joly, F. Detcheverry, and A. L. Biance. Anomalous ζ potential in foam films. *Physical Review Letters*, 113(8):088301, 2014. doi: 10.1103/PhysRevLett.113.088301.
- T. B. Jones and J. R. Melcher. Dynamics of electromechanical flow structures. *Physics of Fluids*, 16(3): 393-400, 1973. doi: 10.1063/1.1694354.
- J. W. Jorgenson and K. DeArman Lukacs. Zone electrophoresis in open-tubular glass capillaries: Preliminary data on performance. *Journal of High Resolution Chromatography*, 4(5):230-231, 1981. doi: 10.1002/jhrc.1240040507.
- P. Joseph and P. Tabeling. Direct measurement of the apparent slip length. *Physical Review E - Statistical, Nonlinear, and Soft Matter Physics*, 71(3):035303(R), 2005. doi: 10.1103/PhysRevE.71.035303.
- P. Joseph, C. Cottin-Bizonne, J. M. Benoît, C. Ybert, C. Journet, P. Tabeling, and L. Bocquet. Slippage of water past superhydrophobic carbon nanotube forests in microchannels. *Physical Review Letters*, 97(15):156104, 2006. doi: 10.1103/PhysRevLett.97.156104.
- C. H. Joshi, R. D. Kamm, J. M. Drazen, and A. S. Slutsky. An experimental study of gas exchange in laminar oscillatory flow. *Journal of Fluid Mechanics*, 133:245-254, 1983. doi: 10.1017/S0022112083001895.
- Y. C. Jung and B. Bhushan. Wetting behaviour during evaporation and condensation of water microdroplets on superhydrophobic patterned surfaces. *Journal of Microscopy*, 229(1):127-140, 2008. doi: 10.1111/j.1365-2818.2007.01875.x.
- L. Kahouadji, N. Périnet, L. S. Tuckerman, S. Shin, J. Chergui, and D. Juric. Numerical simulation of supersquare patterns in Faraday waves. *Journal of Fluid Mechanics*, 772:R2, 2015. doi: 10.1017/jfm.2015.213.
- A. E. Kamholz, B. H. Weigl, B. A. Finlayson, and P. Yager. Quantitative analysis of molecular interaction in a microfluidic channel: The T-sensor. *Analytical Chemistry*, 71(23):5340-5347, 1999. doi: 10.1021/ac990504j.

-
- H. Kawamoto and S. Umezu. Electrohydrodynamic deformation of water surface in a metal pin to water plate corona discharge system. *Journal of Physics D: Applied Physics*, 38(6):887–894, 2005. doi: 10.1088/0022-3727/38/6/017.
- J. Keller. *Experimentelle Untersuchung der Instabilitäten an fluiden Grenzflächen unter der Anregung durch homogene elektrische Wechselfelder*. Bachelor's thesis, Fachbereich Maschinenbau, TU Darmstadt, 2020.
- H. Kim, D. Luo, D. Link, D. A. Weitz, M. Marquez, and Z. Cheng. Controlled production of emulsion drops using an electric field in a flow-focusing microfluidic device. *Applied Physics Letters*, 91(13):133106, 2007. doi: 10.1063/1.2790785.
- M. Kim and A. L. Zydney. Effect of electrostatic, hydrodynamic, and Brownian forces on particle trajectories and sieving in normal flow filtration. *Journal of Colloid and Interface Science*, 269(2):425–431, 2004. doi: 10.1016/j.jcis.2003.08.004.
- Y. J. Kim, Y. T. Kang, and Y. H. Cho. Poly(ethylene glycol)-modified tapered-slit membrane filter for efficient release of captured viable circulating tumor cells. *Analytical Chemistry*, 88(16):7938–7945, 2016. doi: 10.1021/acs.analchem.5b04927.
- B. J. Kirby and E. F. Hasselbrink. Zeta potential of microfluidic substrates: 1. Theory, experimental techniques, and effects on separations. *Electrophoresis*, 25(2):187–202, 2004a. doi: 10.1002/elps.200305754.
- B. J. Kirby and E. F. Hasselbrink. Zeta potential of microfluidic substrates: 2. Data for polymers. *Electrophoresis*, 25(2):203–213, 2004b. doi: 10.1002/elps.200305755.
- A. V. Kityk, J. Embs, V. V. Mekhonoshin, and C. Wagner. Spatiotemporal characterization of interfacial Faraday waves by means of a light absorption technique. *Physical Review E*, 72(3):036209, 2005. doi: 10.1103/PhysRevE.72.036209.
- K. Koch, B. Bhushan, Y. C. Jung, and W. Barthlott. Fabrication of artificial Lotus leaves and significance of hierarchical structure for superhydrophobicity and low adhesion. *Soft Matter*, 5(7):1386–1393, 2009. doi: 10.1039/b818940d.
- J. Koo and C. Kleinstreuer. Liquid flow in microchannels: Experimental observations and computational analyses of microfluidics effects. *Journal of Micromechanics and Microengineering*, 13(5):568–579, 2003. doi: 10.1088/0960-1317/13/5/307.
- K. Kumar and L. S. Tuckerman. Parametric instability of the interface between two fluids. *Journal of Fluid Mechanics*, 279:49–68, 1994. doi: 10.1017/S0022112094003812.
- A. Lafuma and D. Quéré. Superhydrophobic states. *Nature Materials*, 2:457–460, 2003. doi: 10.1038/nmat924.
- C. Larriba-Andaluz and J. Fernández de la Mora. Electro spraying insulating liquids via charged nanodrop injection from the Taylor cone of an ionic liquid. *Physics of Fluids*, 22(7):072002, 2010. doi: 10.1063/1.3455992.
- D. J. Laser and J. G. Santiago. A review of micropumps. *Journal of Micromechanics and Microengineering*, 14(6):R35–R64, 2004. doi: 10.1088/0960-1317/14/6/R01.
- E. Lauga, M. P. Brenner, and H. A. Stone. Microfluidics: The no-slip boundary condition. In C. Tropea, A. L. Yarin, and J. F. Foss, editors, *Springer Handbook of Experimental Fluid Mechanics*, chapter 19, pages 1219 – 1240. Springer Berlin Heidelberg, Berlin, Heidelberg, 2007. ISBN 978-3-540-25141-5. doi: 10.1007/978-3-540-30299-5.

-
- C. Lee and C. J. Kim. Maximizing the giant liquid slip on superhydrophobic microstructures by nanostructuring their sidewalls. *Langmuir*, 25(21):12812–12818, 2009. doi: 10.1021/la901824d.
- C. Lee, C. H. Choi, and C. J. Kim. Structured surfaces for a giant liquid slip. *Physical Review Letters*, 101(6):064501, 2008. doi: 10.1103/PhysRevLett.101.064501.
- C. S. Lee, W. C. Blanchard, and C. T. Wu. Direct control of the electroosmosis in capillary zone electrophoresis by using an external electric field. *Analytical Chemistry*, 62(14):1550–1552, 1990. doi: 10.1021/ac00213a043.
- Y. Lee, S. H. Park, K. B. Kim, and J. K. Lee. Fabrication of hierarchical structures on a polymer surface to mimic natural superhydrophobic surfaces. *Advanced Materials*, 19(17):2330–2335, 2007. doi: 10.1002/adma.200700820.
- L. Lei, H. Li, J. Shi, and Y. Chen. Diffraction patterns of a water-submerged superhydrophobic grating under pressure. *Langmuir*, 26(5):3666–3669, 2010. doi: 10.1021/la903150h.
- D. Li and A. W. Neumann. Surface heterogeneity and contact angle hysteresis. *Colloid & Polymer Science*, 270:498–504, 1992. doi: 10.1007/BF00665995.
- J. Li and F. Lin. Microfluidic devices for studying chemotaxis and electrotaxis. *Trends in Cell Biology*, 21(8):489–497, 2011. doi: 10.1016/j.tcb.2011.05.002.
- X. M. Li, D. Reinhoudt, and M. Crego-Calama. What do we need for a superhydrophobic surface? A review on the recent progress in the preparation of superhydrophobic surfaces. *Chemical Society Reviews*, 36(8):1350–1368, 2007. doi: 10.1039/b602486f.
- H. Lin, B. D. Storey, and J. G. Santiago. A depth-averaged electrokinetic flow model for shallow microchannels. *Journal of Fluid Mechanics*, 608:43–70, 2008. doi: 10.1017/S0022112008001869.
- K. Liu and L. Jiang. Bio-inspired self-cleaning surfaces. *Annual Review of Materials Research*, 42:231–263, 2012. doi: 10.1146/annurev-matsci-070511-155046.
- K. Liu, X. Yao, and L. Jiang. Recent developments in bio-inspired special wettability. *Chemical Society Reviews*, 39(8):3240–3255, 2010. doi: 10.1039/b917112f.
- T. Liu and C. J. Kim. Turning a surface superrepellent even to completely wetting liquids. *Science*, 346(6213):1096–1100, 2014. doi: 10.1126/science.1254787.
- J. M. López-Herrera, A. Barrero, A. López, I. G. Loscertales, and M. Márquez. Coaxial jets generated from electrified Taylor cones. Scaling laws. *Journal of Aerosol Science*, 34(5):535–552, 2003. doi: 10.1016/S0021-8502(03)00021-1.
- J. W. S. Lord Rayleigh. XX. On the equilibrium of liquid conducting masses charged with electricity. *The London, Edinburgh, and Dublin Philosophical Magazine and Journal of Science*, 14(87):184–186, 1882. doi: 10.1080/14786448208628425.
- J. W. S. Lord Rayleigh. XXXIII. On maintained vibrations. *The London, Edinburgh, and Dublin Philosophical Magazine and Journal of Science*, 15(94):229–235, 1883. doi: 10.1080/14786448308627342.
- I.-S. Lorenz. *Optimized Micromixing by Influencing Electrokinetic Flow along Superhydrophobic Surfaces through Secondary Electric Fields*. Master's thesis, Fachbereich Maschinenbau, TU Darmstadt, 2018.
- I. G. Loscertales, A. Barrero, I. Guerrero, R. Cortijo, and A. M. Ganán-Calvo. Micro/nano encapsulation via electrified coaxial liquid jets. *Science*, 295(5560):1695–1698, 2002. doi: 10.1126/science.1067595.
- J. Lv, Y. Song, L. Jiang, and J. Wang. Bio-inspired strategies for anti-icing. *ACS Nano*, 8(4):3152–3169, 2014a. doi: 10.1021/nn406522n.

-
- P. Lv, Y. Xue, Y. Shi, H. Lin, and H. Duan. Metastable states and wetting transition of submerged superhydrophobic structures. *Physical Review Letters*, 112(19):196101, 2014b. doi: 10.1103/PhysRevLett.112.196101.
- J. Lyklema. Electrokinetics after Smoluchowski. *Colloids and Surfaces A: Physicochemical and Engineering Aspects*, 222(1–3):5–14, 2003. doi: 10.1016/S0927-7757(03)00217-6.
- G. Manukyan, J. M. Oh, D. Van Den Ende, R. G. Lammertink, and F. Mugele. Electrical switching of wetting states on superhydrophobic surfaces: A route towards reversible Cassie-to-Wenzel transitions. *Physical Review Letters*, 106(1):014501, 2011. doi: 10.1103/PhysRevLett.106.014501.
- I. Marginean, P. Nemes, L. Parvin, and A. Vertes. How much charge is there on a pulsating Taylor cone? *Applied Physics Letters*, 89(6):064104, 2006a. doi: 10.1063/1.2266889.
- I. Marginean, P. Nemes, and A. Vertes. Order-chaos-order transitions in electrosprays: The electrified dripping faucet. *Physical Review Letters*, 97(6):064502, 2006b. doi: 10.1103/PhysRevLett.97.064502.
- Á. G. Marín, I. G. Loscertales, M. Márquez, and A. Barrero. Simple and double emulsions via coaxial jet electrosprays. *Physical Review Letters*, 98(1):014502, 2007. doi: 10.1103/PhysRevLett.98.014502.
- Á. G. Marín, I. G. Loscertales, and A. Barrero. Surface tension effects on submerged electrosprays. *Biomicrofluidics*, 6(4):044104, 2012. doi: 10.1063/1.4762854.
- A. Marmur and E. Bittoun. When Wenzel and Cassie are right: Reconciling local and global considerations. *Langmuir*, 25(3):1277–1281, 2009. doi: 10.1021/la802667b.
- L. Matthiessen. Akustische Versuche, die kleinsten Transversalwellen der Flüssigkeiten betreffend. *Annalen der Physik und Chemie*, 210(5):107–117, 1868. doi: 10.1002/andp.18682100506.
- L. Matthiessen. Ueber die Transversalschwingungen tönender tropfbarer und elastischer Flüssigkeiten. *Annalen der Physik und Chemie*, 217(11):375–393, 1870. doi: 10.1002/andp.18702171104.
- C. C. Mei and B. Vernescu. *Homogenization Methods for Multiscale Mechanics*. World Scientific, 2010. ISBN 978-981-4282-44-4. doi: 10.1142/7427.
- C. C. Mei, J.-L. Auriault, and C.-O. Ng. Some applications of the homogenization theory. *Advances in Applied Mechanics*, 32:277–348, 1996. doi: 10.1016/S0065-2156(08)70078-4.
- J. R. Melcher. Traveling-wave induced electroconvection. *Physics of Fluids*, 9(8):1548–1555, 1966. doi: 10.1063/1.1761890.
- J. R. Melcher. *Continuum Electromechanics*. MIT press, Cambridge, MA, 1981. ISBN 9780262131650.
- J. R. Melcher and W. J. Schwarz. Interfacial relaxation overstability in a tangential electric field. *Physics of Fluids*, 11(12):2604–2616, 1968. doi: 10.1063/1.1691866.
- J. R. Melcher and G. I. Taylor. Electrohydrodynamics: A review of the role of interfacial shear stresses. *Annual Review of Fluid Mechanics*, 1(1):111–146, 1969. doi: 10.1146/annurev.fl.01.010169.000551.
- J. Miles. Parametrically forced surface waves. *Annual Review of Fluid Mechanics*, 22(1):143–165, 1990. doi: 10.1146/annurev.fluid.22.1.143.
- F. Moisy, M. Rabaud, and K. Salsac. A synthetic Schlieren method for the measurement of the topography of a liquid interface. *Experiments in Fluids*, 46:1021–1036, 2009. doi: 10.1007/s00348-008-0608-z.
- K. D. Möller. *Optics*. Springer New York, New York, NY, 2003. ISBN 978-1-4684-9276-7. doi: 10.1007/b97508.

-
- C. A. Monnig and R. T. Kennedy. Capillary electrophoresis. *Analytical Chemistry*, 66(12):280–314, 1994. doi: 10.1021/ac00084a013.
- S. Moulinet and D. Bartolo. Life and death of a fakir droplet: Impalement transitions on superhydrophobic surfaces. *European Physical Journal E*, 24(3):251–260, 2007. doi: 10.1140/epje/i2007-10235-y.
- A. Mukherjee and B. S. Mazumder. Dispersion of contaminant in oscillatory flows. *Acta Mechanica*, 74: 107–122, 1988. doi: 10.1007/BF01194345.
- H. W. Müller, R. Friedrich, and D. Papathanassiou. Theoretical and experimental investigations of the Faraday instability. In *Evolution of Spontaneous Structures in Dissipative Continuous Systems*, pages 230–265. Springer Berlin Heidelberg, Berlin, Heidelberg, 2011.
- J. Muñoz, J. Arcos, O. Bautista, and F. Méndez. Slippage effect on the dispersion coefficient of a passive solute in a pulsatile electro-osmotic flow in a microcapillary. *Physical Review Fluids*, 3(8):084503, 2018. doi: 10.1103/PhysRevFluids.3.084503.
- K. R. Murphy, W. T. McClintic, K. C. Lester, C. P. Collier, and J. B. Boreyko. Dynamic defrosting on scalable superhydrophobic surfaces. *ACS Applied Materials and Interfaces*, 9(28):24308–24317, 2017. doi: 10.1021/acsami.7b05651.
- S. Mutlu, F. Svec, C. H. Mastrangelo, J. M. J. Fréchet, and Y. B. Gianchandani. Enhanced electro-osmotic pumping with liquid bridge and field effect flow rectification. In *Proceedings of the IEEE International Conference on Micro Electro Mechanical Systems (MEMS)*, pages 850–853. IEEE, 2004. ISBN 0-7803-8265-X. doi: 10.1109/mems.2004.1290720.
- R. D. Narhe and D. A. Beysens. Nucleation and growth on a superhydrophobic grooved surface. *Physical Review Letters*, 93(7):076103, 2004. doi: 10.1103/PhysRevLett.93.076103.
- V. G. Nevolin. Parametric excitation of surface waves. *Journal of Engineering Physics*, 47(6):1482–1494, 1984. doi: 10.1007/BF00870072.
- C. O. Ng. Dispersion in steady and oscillatory flows through a tube with reversible and irreversible wall reactions. *Proceedings of the Royal Society A: Mathematical, Physical and Engineering Sciences*, 462 (2066):481–515, 2006. doi: 10.1098/rspa.2005.1582.
- C. O. Ng and Q. Zhou. Electro-osmotic flow through a thin channel with gradually varying wall potential and hydrodynamic slippage. *Fluid Dynamics Research*, 44(5):055507, 2012. doi: 10.1088/0169-5983/44/5/055507.
- M. Nosonovsky and B. Bhushan. Biomimetic superhydrophobic surfaces: Multiscale approach. *Nano Letters*, 7(9):2633–2637, 2007. doi: 10.1021/nl071023f.
- J. Ou, B. Perot, and J. P. Rothstein. Laminar drag reduction in microchannels using ultrahydrophobic surfaces. *Physics of Fluids*, 16(12):4635–4643, 2004. doi: 10.1063/1.1812011.
- P. Papadopoulos, L. Mammen, X. Deng, D. Vollmer, and H. J. Butt. How superhydrophobicity breaks down. *Proceedings of the National Academy of Sciences of the United States of America*, 110(9):3254–3258, 2013. doi: 10.1073/pnas.1218673110.
- F. Paratore, V. Bacheva, G. V. Kaigala, and M. Bercovici. Dynamic microscale flow patterning using electrical modulation of zeta potential. *Proceedings of the National Academy of Sciences of the United States of America*, 116(21):10258–10263, 2019a. doi: 10.1073/pnas.1821269116.
- F. Paratore, E. Boyko, G. V. Kaigala, and M. Bercovici. Electroosmotic flow dipole: Experimental observation and flow field patterning. *Physical Review Letters*, 122(22):224502, 2019b. doi: 10.1103/PhysRevLett.122.224502.

- J.-U. Park, M. Hardy, S. J. Kang, K. Barton, K. Adair, D. K. Mukhopadhyay, C. Y. Lee, M. S. Strano, A. G. Alleyne, J. G. Georgiadis, P. M. Ferreira, and J. A. Rogers. High-resolution electrohydrodynamic jet printing. *Nature Materials*, 6(10):782–789, 2007. doi: 10.1038/nmat1974.
- F. J. Peaudecerf, J. R. Landel, R. E. Goldstein, and P. Luzzatto-Fegiz. Traces of surfactants can severely limit the drag reduction of superhydrophobic surfaces. *Proceedings of the National Academy of Sciences*, 114(28):7254–7259, 2017. doi: 10.1073/pnas.1702469114.
- M. Perlin and W. W. Schultz. Capillary effects on surface waves. *Annual Review of Fluid Mechanics*, 32(1): 241–274, 2000. doi: 10.1146/annurev.fluid.32.1.241.
- A. M. Peters, C. Pirat, M. Sbragaglia, B. M. Borkent, M. Wessling, D. Lohse, and R. G. Lammertink. Cassie-Baxter to Wenzel state wetting transition: Scaling of the front velocity. *European Physical Journal E*, 29(4):391–397, 2009. doi: 10.1140/epje/i2009-10489-3.
- D. S. Pillai and R. Narayanan. Nonlinear dynamics of electrostatic Faraday instability in thin films. *Journal of Fluid Mechanics*, 855:R4, 2018. doi: 10.1017/jfm.2018.682.
- R. Pillai, J. D. Berry, D. J. Harvie, and M. R. Davidson. Electrokinetics of isolated electrified drops. *Soft Matter*, 12(14):3310–3325, 2016. doi: 10.1039/c6sm00047a.
- R. Pit, H. Hervet, and L. Léger. Friction and slip of a simple liquid at a solid surface. *Tribology Letters*, 7: 147–152, 1999. doi: 10.1023/a:1019161101812.
- R. Poetes, K. Holtzmann, K. Franze, and U. Steiner. Metastable underwater superhydrophobicity. *Physical Review Letters*, 105(16):166104, 2010. doi: 10.1103/PhysRevLett.105.166104.
- A. Ramachandran, D. A. Huyke, E. Sharma, M. K. Sahoo, C. Huang, N. Banaei, B. A. Pinsky, and J. G. Santiago. Electric field-driven microfluidics for rapid CRISPR-based diagnostics and its application to detection of SARS-CoV-2. *Proceedings of the National Academy of Sciences*, 117(47):29518–29525, 2020. doi: 10.1073/pnas.2010254117.
- K. Raman, T. R. Srinivasa Murthy, and G. M. Hegde. Fabrication of refractive index tunable Polydimethylsiloxane photonic crystal for biosensor application. *Physics Procedia*, 19:146–151, 2011. doi: 10.1016/j.phpro.2011.06.139.
- F. Reuss. Sur un Nouvel Effet de l'Electricite Galvanique. *Memoires de la Societe Imperiale des Naturalistes de Moscou*, 2:327–337, 1809.
- G. Riboux, A. G. Marín., I. G. Loscertales, and A. Barrero. Whipping instability characterization of an electrified visco-capillary jet. *Journal of Fluid Mechanics*, 671:226–253, 2011. doi: 10.1017/S0022112010005586.
- S. A. Roberts and S. Kumar. AC electrohydrodynamic instabilities in thin liquid films. *Journal of Fluid Mechanics*, 631:255–279, 2009. doi: 10.1017/S0022112009006843.
- J. A. Robinson, M. A. Bergougnou, W. L. Cairns, G. S. P. Castle, and I. I. Inculet. Breakdown of air over a water surface stressed by a perpendicular alternating electric field, in the presence of a dielectric barrier. *IEEE Transactions on Industry Applications*, 36(1):68–75, 2000. doi: 10.1109/28.821798.
- J. A. Robinson, M. A. Bergougnou, G. S. P. Castle, and I. I. Inculet. The electric field at a water surface stressed by an AC voltage. *IEEE Transactions on Industry Applications*, 37(3):735–742, 2001. doi: 10.1109/28.924753.
- J. A. Robinson, M. A. Bergougnou, G. S. P. Castle, and I. I. Inculet. A nonlinear model of AC-field-induced parametric waves on a water surface. *IEEE Transactions on Industry Applications*, 38(2):379–388, 2002. doi: 10.1109/28.993159.

-
- B. Rofman, S. Dehe, V. Frumkin, S. Hardt, and M. Bercovici. Intermediate states of wetting on hierarchical superhydrophobic surfaces. *Langmuir*, 36(20):5517–5523, 2020. doi: 10.1021/acs.langmuir.0c00499.
- Y. L. Roht, H. Auradou, J.-P. Hulin, D. Salin, R. Chertcoff, and I. Ippolito. Time dependence and local structure of tracer dispersion in oscillating liquid Hele-Shaw flows. *Physics of Fluids*, 27(10):103602, 2015. doi: 10.1063/1.4932302.
- J. Rosell-Llompart and J. Fernández de la Mora. Generation of monodisperse droplets 0.3 to 4 μm in diameter from electrified cone-jets of highly conducting and viscous liquids. *Journal of Aerosol Science*, 25(6):1093–1119, 1994. doi: 10.1016/0021-8502(94)90204-6.
- J. P. Rothstein. Slip on superhydrophobic surfaces. *Annual Review of Fluid Mechanics*, 42(1):89–109, 2010. doi: 10.1146/annurev-fluid-121108-145558.
- S. Rubin, A. Tulchinsky, A. D. Gat, and M. Bercovici. Elastic deformations driven by non-uniform lubrication flows. *Journal of Fluid Mechanics*, 812:841–865, 2017. doi: 10.1017/jfm.2016.830.
- D. A. Saville. Electrohydrodynamics: The Taylor-Melcher leaky dielectric model. *Annual Review of Fluid Mechanics*, 29(1):27–64, 1997. doi: 10.1146/annurev.fluid.29.1.27.
- M. Sbragaglia, A. M. Peters, C. Pirat, B. M. Borkent, R. G. Lammertink, M. Wessling, and D. Lohse. Spontaneous breakdown of superhydrophobicity. *Physical Review Letters*, 99(15):156001, 2007. doi: 10.1103/PhysRevLett.99.156001.
- D. Schäffel, K. Koynov, D. Vollmer, H. J. Butt, and C. Schönecker. Local flow field and slip length of superhydrophobic surfaces. *Physical Review Letters*, 116(13):134501, 2016. doi: 10.1103/PhysRevLett.116.134501.
- R. B. M. Schasfoort, S. Schlautmann, J. Hendrikse, and A. van den Berg. Field-effect row control for micro-fabricated fluidic networks. *Science*, 286(5441):942–945, 1999. doi: 10.1126/science.286.5441.942.
- C. A. Schneider, W. S. Rasband, and K. W. Eliceiri. NIH Image to ImageJ: 25 years of image analysis. *Nature Methods*, 9(7):671–675, 2012. doi: 10.1038/nmeth.2089.
- C. Schönecker and S. Hardt. Electro-osmotic flow along superhydrophobic surfaces with embedded electrodes. *Physical Review E - Statistical, Nonlinear, and Soft Matter Physics*, 89(6):063005, 2014. doi: 10.1103/PhysRevE.89.063005.
- V. Serpooshan, P. Chen, H. Wu, S. Lee, A. Sharma, D. A. Hu, S. Venkatraman, A. V. Ganesan, O. B. Usta, M. Yarmush, F. Yang, J. C. Wu, U. Demirci, and S. M. Wu. Bioacoustic-enabled patterning of human iPSC-derived cardiomyocytes into 3D cardiac tissue. *Biomaterials*, 131:47–57, 2017. doi: 10.1016/j.biomaterials.2017.03.037.
- X. Shao, P. Wilson, J. R. Saylor, and J. B. Bostwick. Surface wave pattern formation in a cylindrical container. *Journal of Fluid Mechanics*, 915:A19, 2021. doi: 10.1017/jfm.2021.97.
- N. J. Shirtcliffe, G. McHale, M. I. Newton, and Y. Zhang. Superhydrophobic copper tubes with possible flow enhancement and drag reduction. *ACS Applied Materials and Interfaces*, 1(6):1316–1323, 2009. doi: 10.1021/am9001937.
- R. H. Shreiner and K. W. Pratt. Standard reference materials: Primary standards and standard reference materials for electrolytic conductivity. *NIST Special Publication*, 260:142, 2004.
- A. H. Smith and A. W. Lawson. The velocity of sound in water as a function of temperature and pressure. *The Journal of Chemical Physics*, 22(3):351–359, 1954. doi: 10.1063/1.1740074.

-
- R. Smith. Contaminant dispersion in oscillatory flows. *Journal of Fluid Mechanics*, 114:379–398, 1982. doi: 10.1017/S0022112082000214.
- H. Sobral and M. Peña-Gomar. Determination of the refractive index of glucose-ethanol-water mixtures using spectroscopic refractometry near the critical angle. *Applied Optics*, 54(28):8453–8458, 2015. doi: 10.1364/ao.54.008453.
- H. Song, Y. Wang, and K. Pant. Cross-stream diffusion under pressure-driven flow in microchannels with arbitrary aspect ratios: A phase diagram study using a three-dimensional analytical model. *Microfluidics and Nanofluidics*, 12:265–277, 2012. doi: 10.1007/s10404-011-0870-x.
- T. M. Squires. Electrokinetic flows over inhomogeneously slipping surfaces. *Physics of Fluids*, 20(9):092105, 2008. doi: 10.1063/1.2978954.
- A. F. Stalder, G. Kulik, D. Sage, L. Barbieri, and P. Hoffmann. A snake-based approach to accurate determination of both contact points and contact angles. *Colloids and Surfaces A: Physicochemical and Engineering Aspects*, 286(1-3):92–103, 2006. doi: 10.1016/j.colsurfa.2006.03.008.
- C. Steffes, T. Baier, and S. Hardt. Enabling the enhancement of electroosmotic flow over superhydrophobic surfaces by induced charges. *Colloids and Surfaces A: Physicochemical and Engineering Aspects*, 376(1-3):85–88, 2011. doi: 10.1016/j.colsurfa.2010.09.002.
- G. G. Stokes. On the effect of the internal friction of fluids on the motion of pendulums. *Transactions of the Cambridge Philosophical Society*, 9:8, 1851.
- H. A. Stone and H. Brenner. Dispersion in flows with streamwise variations of mean velocity: Radial flow. *Industrial and Engineering Chemistry Research*, 38(3):851–854, 1999. doi: 10.1021/ie980355f.
- H. A. Stone, A. D. Stroock, and A. Ajdari. Engineering flows in small devices: Microfluidics toward a lab-on-a-chip. *Annual Review of Fluid Mechanics*, 36(1):381–411, 2004. doi: 10.1146/annurev.fluid.36.050802.122124.
- A. Sze, D. Erickson, L. Ren, and D. Li. Zeta-potential measurement using the Smoluchowski equation and the slope of the current-time relationship in electroosmotic flow. *Journal of Colloid and Interface Science*, 261(2):402–410, 2003. doi: 10.1016/S0021-9797(03)00142-5.
- K. Tajima. Radiotracer studies on adsorption of surface active substance at aqueous surface. III. The effects of salt on the adsorption of sodium dodecylsulfate. *Bulletin of the Chemical Society of Japan*, 44(7):1767–1771, 1971. doi: 10.1246/bcsj.44.1767.
- K. Tang and A. Gomez. On the structure of an electrostatic spray of monodisperse droplets. *Physics of Fluids*, 6(7):2317–2332, 1994. doi: 10.1063/1.868182.
- G. I. Taylor. Dispersion of soluble matter in solvent flowing slowly through a tube. *Proceedings of the Royal Society of London. Series A. Mathematical and Physical Sciences*, 219(1137):186–203, 1953. doi: 10.1098/rspa.1953.0139.
- G. I. Taylor. Conditions under which dispersion of a solute in a stream of solvent can be used to measure molecular diffusion. *Proceedings of the Royal Society of London. Series A. Mathematical and Physical Sciences*, 225(1163):473–477, 1954. doi: 10.1098/rspa.1954.0216.
- G. I. Taylor. Disintegration of water drops in an electric field. *Proceedings of the Royal Society of London. Series A. Mathematical and Physical Sciences*, 280(1382):383–397, 1964. doi: 10.1098/rspa.1964.0151.
- G. I. Taylor and A. D. McEwan. The stability of a horizontal fluid interface in a vertical electric field. *Journal of Fluid Mechanics*, 22(1):1–15, 1965. doi: 10.1017/S0022112065000538.

-
- W. E. Teo and S. Ramakrishna. A review on electrospinning design and nanofibre assemblies. *Nanotechnology*, 17(14):R89–R106, 2006. doi: 10.1088/0957-4484/17/14/R01.
- N. B. Tuffillaro, R. Ramshankar, and J. P. Gollub. Order-disorder transition in capillary ripples. *Physical Review Letters*, 62(4):422–425, 1989. doi: 10.1103/PhysRevLett.62.422.
- E. J. van der Wouden, T. Heuser, D. C. Hermes, R. E. Oosterbroek, J. G. Gardeniers, and A. van den Berg. Field-effect control of electro-osmotic flow in microfluidic networks. *Colloids and Surfaces A: Physicochemical and Engineering Aspects*, 267(1-3):110–116, 2005. doi: 10.1016/j.colsurfa.2005.06.048.
- E. J. van der Wouden, D. C. Hermes, J. G. Gardeniers, and A. van den Berg. Directional flow induced by synchronized longitudinal and zeta-potential controlling AC-electrical fields. *Lab on a Chip*, 6(10):1300–1305, 2006. doi: 10.1039/b607403k.
- C. Vargas, J. Arcos, O. Bautista, and F. Méndez. Hydrodynamic dispersion in a combined magnetohydrodynamic electroosmotic-driven flow through a microchannel with slowly varying wall zeta potentials. *Physics of Fluids*, 29(9):092002, 2017. doi: 10.1063/1.4991680.
- S. Vedel and H. Bruus. Transient Taylor-Aris dispersion for time-dependent flows in straight channels. *Journal of Fluid Mechanics*, 691:95–122, 2012. doi: 10.1017/jfm.2011.444.
- S. Vedel, E. Hovad, and H. Bruus. Time-dependent Taylor–Aris dispersion of an initial point concentration. *Journal of Fluid Mechanics*, 752:107–122, 2014. doi: 10.1017/jfm.2014.324.
- T. Verho, C. Bower, P. Andrew, S. Franssila, O. Ikkala, and R. H. Ras. Mechanically durable superhydrophobic surfaces. *Advanced Materials*, 23(5):673–678, 2011. doi: 10.1002/adma.201003129.
- T. Verho, J. T. Korhonen, L. Sainiemi, V. Jokinen, C. Bower, K. Franze, S. Franssila, P. Andrew, O. Ikkala, and R. H. Ras. Reversible switching between superhydrophobic states on a hierarchically structured surface. *Proceedings of the National Academy of Sciences of the United States of America*, 109(26):10210–10213, 2012. doi: 10.1073/pnas.1204328109.
- O. I. Vinogradova. Slippage of water over hydrophobic surfaces. *International Journal of Mineral Processing*, 56(1-4):31–60, 1999. doi: 10.1016/S0301-7516(98)00041-6.
- A. Volta. XVII. On the electricity excited by the mere contact of conducting substances of different kinds. In a letter from Mr. Alexander Volta, F. R. S. Professor of Natural Philosophy in the University of Pavia, to the Rt. Hon. Sir Joseph Banks, Bart. K.B. P. R. *Philosophical Transactions of the Royal Society of London*, 90:403–431, 1800. doi: 10.1098/rstl.1800.0018.
- M. von Brück. *Bhagavad Gita*. Kösel-Verlag GmbH & Co., München, 1993. ISBN 3466203732.
- M. von Smoluchowski. Zur kinetischen Theorie der Brownschen Molekularbewegung und der Suspensionen. *Annalen der Physik*, 326(14):756–780, 1906. doi: 10.1002/andp.19063261405.
- M. von Smoluchowski. Elektrische Endosmose und Strömungsströme. In L. Graetz, editor, *Handbuch der Elektrizität und des Magnetismus, Band II, Stationäre Ströme*. J.A. Barth, Leipzig, 1921.
- Wacker-Chemie GmbH. *Wacker silicone fluids AK*. Munich, 2002.
- K. Ward, S. Matsumoto, and R. Narayanan. The electrostatically forced Faraday instability: Theory and experiments. *Journal of Fluid Mechanics*, 862:696–731, 2019. doi: 10.1017/jfm.2018.940.
- E. J. Watson. Diffusion in oscillatory pipe flow. *Journal of Fluid Mechanics*, 133:233–244, 1983. doi: 10.1017/S0022112083001883.
- R. N. Wenzel. Resistance of solid surfaces to wetting by water. *Industrial and Engineering Chemistry*, 28(8):988–994, 1936. doi: 10.1021/ie50320a024.

-
- K. M. Wisdom, J. A. Watson, X. Qu, F. Liu, G. S. Watson, and C. H. Chen. Self-cleaning of superhydrophobic surfaces by self-propelled jumping condensate. *Proceedings of the National Academy of Sciences of the United States of America*, 110(20):7992–7997, 2013. doi: 10.1073/pnas.1210770110.
- M. Wu, B. Ma, T. Pan, S. Chen, and J. Sun. Silver-nanoparticle-colored cotton fabrics with tunable colors and durable antibacterial and self-healing superhydrophobic properties. *Advanced Functional Materials*, 26(4):569–576, 2016. doi: 10.1002/adfm.201504197.
- C. H. Xue, Z. D. Zhang, J. Zhang, and S. T. Jia. Lasting and self-healing superhydrophobic surfaces by coating of polystyrene/SiO₂ nanoparticles and polydimethylsiloxane. *Journal of Materials Chemistry A*, 2(36):15001–15007, 2014. doi: 10.1039/c4ta02396j.
- Y. Y. Yan, N. Gao, and W. Barthlott. Mimicking natural superhydrophobic surfaces and grasping the wetting process: A review on recent progress in preparing superhydrophobic surfaces. *Advances in Colloid and Interface Science*, 169(2):80–105, 2011. doi: 10.1016/j.cis.2011.08.005.
- X. Yao, Y. Song, and L. Jiang. Applications of bio-inspired special wettable surfaces. *Advanced Materials*, 23(6):719–734, 2011. doi: 10.1002/adma.201002689.
- C. Ybert, C. Barentin, C. Cottin-Bizonne, P. Joseph, and L. Bocquet. Achieving large slip with superhydrophobic surfaces: Scaling laws for generic geometries. *Physics of Fluids*, 19(12):123601, 2007. doi: 10.1063/1.2815730.
- C.-S. Yih. Stability of a horizontal fluid interface in a periodic vertical electric field. *Physics of Fluids*, 11(7):1447–1449, 1968. doi: 10.1063/1.1692127.
- J. Yong, Q. Yang, F. Chen, D. Zhang, G. Du, H. Bian, J. Si, F. Yun, and X. Hou. Superhydrophobic PDMS surfaces with three-dimensional (3D) pattern-dependent controllable adhesion. *Applied Surface Science*, 288:579–583, 2014. doi: 10.1016/j.apsusc.2013.10.076.
- Z. Yoshimitsu, A. Nakajima, T. Watanabe, and K. Hashimoto. Effects of surface structure on the hydrophobicity and sliding behavior of water droplets. *Langmuir*, 18(15):5818–5822, 2002. doi: 10.1021/la020088p.
- J. Zeleny. Instability of electrified liquid surfaces. *Physical Review*, 10(1):1–6, 1917. doi: 10.1103/PhysRev.10.1.
- X. Zhang, L. Wang, and E. Levänen. Superhydrophobic surfaces for the reduction of bacterial adhesion. *RSC Advances*, 3(30):12003–12020, 2013. doi: 10.1039/c3ra40497h.
- H. Zhao and H. H. Bau. Effect of secondary flows on Taylor-Aris dispersion. *Analytical Chemistry*, 79(20):7792–7798, 2007. doi: 10.1021/ac701681b.
- S. Zhao, M. Dietzel, and S. Hardt. Faraday instability of a liquid layer on a lubrication film. *Journal of Fluid Mechanics*, 879:422–447, 2019. doi: 10.1017/jfm.2019.684.
- E. K. Zholkovskij and J. H. Masliyah. Hydrodynamic dispersion due to combined pressure-driven and electroosmotic flow through microchannels with a thin double layer. *Analytical Chemistry*, 76(10):2708–2718, 2004. doi: 10.1021/ac0303160.
- E. K. Zholkovskij, J. H. Masliyah, and J. Czarnecki. Electroosmotic dispersion in microchannels with a thin double layer. *Analytical Chemistry*, 75(4):901–909, 2003. doi: 10.1021/ac0203591.
- E. K. Zholkovskij, A. E. Yaroshchuk, J. H. Masliyah, and J. d. P. Ribas. Broadening of neutral solute band in electroosmotic flow through submicron channel with longitudinal non-uniformity of zeta potential. *Colloids and Surfaces A: Physicochemical and Engineering Aspects*, 354(1-3):338–346, 2010. doi: 10.1016/j.colsurfa.2009.09.043.

W. B. Zimmerman and G. M. Homsy. Nonlinear viscous fingering in miscible displacement with anisotropic dispersion. *Physics of Fluids A: Fluid Dynamics*, 3(8):1859–1872, 1991. doi: 10.1063/1.857916.

Symbols and Abbreviations

Abbreviations

Abbreviation	Meaning	Page ¹
AC	Alternating current	p. 55
BDF	Backward differentiation scheme	p. 161
CCD	Charge-coupled device	p. 36
CE	Capillary electrophoresis	p. 1
CMC	Critical micelle concentration	p. 70
CMOS	Complementary metal–oxide–semiconductor	p. 36
DC	Direct current	p. 55
DFT	Discrete Fourier transform	p. 124
DI	De-ionized (water)	p. 64
DRIE	Deep reactive ion etching	p. 33
EDL	Electric double layer	p. 20
EHD	Electrohydrodynamics	p. 1
EOF	Electro-osmotic flow	p. 49
ESI	Electrospray ionization	p. 2
HEPES	4-(2-hydroxyethyl)-1-piperazineethanesulfonic acid	p. 64
ITO	Indium tin oxide	p. 36
NCT	Nano Cassie-Baxter transition point	p. 40
PDMS	Polydimethylsiloxane	p. 33
PFDTs	1H,1H,2H,2H-perfluorodecyl-trichlorosilane	p. 31
PIV	Particle image velocimetry	p. 52
PTFE	Polytetrafluoroethylene	p. 33
PTV	Particle tracking velocimetry	p. 65
PVC	Polyvinyl chloride	p. 34
RST	Reference state of transition	p. 38
sCMOS	Scientific complementary metal–oxide–semiconductor	p. 64
SDS	Sodium dodecyl sulfate	p. 70

Abbreviation	Meaning	Page ¹
SEM	Scanning electron microscopy	p. 33
THF	Tetrahydrofuran	p. 34
TIR-FRAP	Total internal reflection fluorescence recovery after photobleaching	p. 52
TIRV	Total internal reflection velocimetry	p. 52
TRIS	Tris(hydroxymethyl)aminomethane	p. 102

Latin Symbols

Symbol	Meaning	Unit
A, A_1	area	m^2
A_1, A_2, A_3	parameters of the stationary velocity field (chapter 5)	-
$A(k_x, k_y)$	amplitude of Fourier-transform (chapter 6)	m^2
A_{cap}	area of spherical cap	m^2
C_i	area of capacitor (chapter 4)	m^2
A_{sl}	contact area below droplet	m^2
B_1, B_2, B_3	parameters of the stationary velocity field (chapter 5)	-
$C_{\text{dif,a}}$	differential capacitance of EDL above air (chapter 4)	F
$C_{\text{dif,i}}$	differential capacitance of EDL (chapter 4)	F
$C_{\text{dif,p}}$	differential capacitance of EDL above pillar (chapter 4)	F
C_i	mass fraction (chapter 2)	-
C_i	capacitance of dielectric (chapter 4)	F
D, D_i	diffusion constant (of species i)	m s^{-1}
\mathbf{D}, \mathbf{D}_1	displacement field	C m^{-2}
D_c	diameter cell (chapter 7)	m
D_d	droplet diffusion constant (chapter 7)	$\text{m}^2 \text{s}^{-1}$
D_e	diameter pin electrode (chapter 7)	m
D_{eff}	effective diffusion coefficient (chapter 5)	$\text{m}^2 \text{s}^{-1}$
D_i	inner diameter needle (chapter 7)	m
D_n	diameter needle (chapter 7)	m
\mathbf{D}_{osc}	oscillatory dispersion tensor (chapter 5)	-
\mathbf{D}_{stat}	stationary dispersion tensor (chapter 5)	-
E	energy	J
E_0	electric field magnitude	V m^{-1}

¹First occurrence

Symbol	Meaning	Unit
\mathbf{E}	electric field vector	V m^{-1}
\mathbf{E}_{\parallel}	electric field vector parallel to bounding plates (chapters 4-5)	V m^{-1}
\mathbf{E}_t	tangential electric field vector	V m^{-1}
\mathbf{F}	force vector	N
G	Gibbs free energy	J
G_f	work performed on an external phase by displacement	J
G_s	Gibbs free energy of an interface	J
$\mathbf{G}_x, \mathbf{G}_y$	matrices following from difference approximation scheme (chapter 6)	m^{-1}
H	greyscale values of image (chapter 3)	-
H	Heavyside step function (chapter 4)	-
$H(k_x, k_y)$	two-dimensional discrete Fourier transform (chapter 6)	m
H_{cam}	distance objective - interface (chapter 6)	m
I	integrated intensity (chapter 3)	-
\mathbf{I}	identity tensor	-
I_0	spray current introduced into the system (chapter 7)	A
I_c	mixing intensity (chapter 5)	-
I_g	grid intensity (chapter 3)	-
$I_{g,\text{max}}$	maximum grid intensity (chapter 3)	-
I_j	jet current (chapter 7)	A
I_{max}	maximum integrated intensity (chapter 3)	-
I_p	integrated pressure deviation (chapter 5)	-
\mathbf{J}	mass current density	$\text{kg m}^{-2} \text{s}^{-1}$
\mathbf{J}_{dif}	diffusive flux	m s^{-1}
\mathbf{J}_{el}	free current density	$\text{C m}^{-2} \text{s}^{-1}$
J_l	Bessel function of the first kind (chapter 6)	-
\mathbf{J}_s	free surface current density	$\text{C m}^{-1} \text{s}^{-1}$
\mathbf{J}_u	convective flux	$\text{C m}^{-2} \text{s}^{-1}$
$J(x_1)$	mass flux over a plane located at x_1 (chapter 5)	$\text{mol m L}^{-1} \text{s}^{-1}$
K	electric conductivity	S m^{-1}
L_0	characteristic length scale	m
L	side length of Hele-Shaw cell (chapters 4-5)	m
W	side length y -direction (chapter 5)	m
$L_{\text{c,ini}}$	size of transition region of initial distribution (chapter 5)	m
L_{patch}	size of ζ potential patch (chapter 5)	m
L_{smooth}	size of diffusion zone (chapter 5)	m

Symbol	Meaning	Unit
L_x	cell side length in x -direction (chapter 5)	m
L_y	cell side length in y -direction (chapter 5)	m
$M(\Omega, t), M_i(\Omega, t)$	total mass (of species i) in Ω	kg
$\frac{\partial}{\partial t} \mathbf{M}^{\text{conv}}(\Omega, t)$	rate of change of mass of species i in Ω	kg s^{-1}
Ma	Mason-number (chapter 6)	-
$\frac{\partial}{\partial t} \mathbf{M}_i^{\text{conv}}(\Omega, t)$	rate of change of mass of species i in Ω due to convection	kg s^{-1}
$\frac{\partial}{\partial t} \mathbf{M}_i^{\text{conv}}(\Omega, t)$	rate of change of mass of species i in Ω due to molecular diffusion	kg s^{-1}
$\frac{\partial}{\partial t} \mathbf{M}_i^{\text{conv}}(\Omega, t)$	rate of change of mass of species i in Ω due to electrophoresis	kg s^{-1}
N	number of molecules	mol
N_p	number of particles (chapter 5)	-
\mathbf{P}	polarization field vector	C m^{-2}
$\mathbf{P}(\Omega, t)$	total momentum in Ω	kg m s^{-1}
P_0	characteristic pressure scale	N m^{-2}
$P_{1/2}$	Legendre function of order 1/2 (chapter 7)	-
$\frac{\partial}{\partial t} \mathbf{P}^{\text{conv}}(\Omega, t)$	rate of change of momentum in Ω due to convection	N
Pe	Péclet number (chapter 5)	-
$\frac{\partial}{\partial t} \mathbf{P}^{\text{elec}}(\Omega, t)$	rate of change of momentum in Ω due to electrical forces	N
$\frac{\partial}{\partial t} \mathbf{P}^{\text{body}}(\Omega, t)$	rate of change of momentum in Ω due to body forces	N
$\frac{\partial}{\partial t} \mathbf{P}^{\text{P}}(\Omega, t)$	rate of change of momentum in Ω due to pressure forces	N
$\frac{\partial}{\partial t} \mathbf{P}^{\text{visc}}(\Omega, t)$	rate of change of momentum in Ω due to viscous forces	N
Q	flow rate (chapter 7)	$\mu\text{L min}^{-1}$
R	spherical cap radius (chapter 3)	m
R	capillary radius (chapter 4)	m
R	domain radius (chapter 6)	m
R	droplet radius (chapter 7)	m
R_1, R_2	principle radii of curvature	m
R_d	progeny droplet radius (chapter 7)	m
Re	Reynolds number	-
R_l	reflectance (chapter 3)	-
R_n	radius of capillary (chapter 7)	m
S	smoothed step function (chapter 5)	-
$S_{l,n}, S_m$	surface harmonics (chapter 6)	-
St	Strouhal number (chapter 4)	-
T	temperature	K, °C
T_0	characteristic time scale	s

Symbol	Meaning	Unit
T_{adv}	time scale of advection (chapter 5)	s
$T_{dif,L}$	time scale of in-plane diffusion (chapter 5)	s
$T_{dif,h}$	time scale of cross-stream diffusion (chapter 5)	s
T_{osc}	oscillation period	s
U_0	characteristic velocity scale	m s^{-1}
U_{crit}	lowest critical voltage (chapter 6)	V
U_{wall}	wall velocity (chapter 5)	m s^{-1}
V	volume	m^3
V_{G1}, V_{G2}, V_{G3}	gate voltages of electrode 1, 2, 3 (chapter 5)	V
V_{gate}	gate voltage	V
W_0	characteristic velocity in z -direction (chapters 4-5)	m s^{-1}
a	radius of contact line (chapter 3)	m
a	stationary solution of $c^{(1)}$ (chapter 5)	-
a_{cal}	calibration factor (chapter 6)	mm/px
a_{disc}	geometric factor of flow field (chapter 4)	-
a_i	molecular radius (of species i)	m
a_{in}	parameter of the pressure field above a circular gate electrode (chapter 4)	-
a_m	time-dependent amplitude of surface harmonics (chapter 6)	m
a_{out}	parameter of the pressure field around a circular gate electrode (chapter 4)	-
b	oscillatory solution of $c^{(1)}$ (chapter 5)	-
b_{in}	parameter of the pressure field above a circular gate electrode (chapter 4)	-
b_{out}	parameter of the pressure field around a circular gate electrode (chapter 4)	-
c, c_i	molar concentration (of species i)	mol L^{-1}
c	cross-correlation (chapter 3)	-
$c^{(0)}, c^{(1)}, c^{(2)}$	expansions of non-dimensional concentration in ϵ (chapter 5)	-
c_{buf}	ionic concentration buffer (chapter 4)	mol L^{-1}
c_{tit}	ionic concentration titrant (chapter 4)	mol L^{-1}
d	interpillar distance (chapter 3)	m
d	domain diameter (chapter 6)	m
d_{bead}	diameter tracer particle (chapter 4)	m
d_c	critical gap size (chapter 3)	m
d_j	diameter jet (chapter 7)	m
d_p	particle diameter (chapter 5)	m

Symbol	Meaning	Unit
d_{path}	path width (chapter 5)	m
$d_{\text{transition}}$	path transition zone size (chapter 5)	m
$\mathbf{e}_x, \mathbf{e}_y, \mathbf{e}_z, \mathbf{e}_\theta, \mathbf{e}_r$	unit vectors	-
f_1, f_2	area fraction of material 1, 2 (chapter 3)	-
f	oscillation frequency (chapter 5)	s^{-1}
\mathbf{f}_{el}	electric force density	N m^{-3}
f_0	oscillatory frequency (chapters 4-5)	Hz
\mathbf{f}_s	surface force density	N m^{-2}
\mathbf{f}	position- and time-dependent vector function for dimensionless flow field parametrization (chapters 4-5)	-
\mathbf{g}	gravitational acceleration	m s^{-2}
\mathbf{g}	position- and time-dependent vector function for dimensionless flow field parametrization (chapters 4-5)	-
h_1, h_2	height of layer 1 or 2 (chapter 6)	m
h	height of spherical cap (chapter 3)	m
h	bounding plate distance (chapters 4-5)	m
$h(x, y)$	interface coordinate (chapter 6)	m
$\nabla h(x, y)$	interface gradient (chapter 6)	-
h_i	plate distance of capacitor (chapter 4)	m
h_o	filling height oil layer (chapter 7)	m
h_p	pillar height (chapter 3)	m
h^*	effective layer height (chapter 6)	mm
h_{sub}	sublayer height (chapter 3)	m
h_w	filling height water layer (chapter 7)	m
i_{in}	spray current density introduced into the system (chapter 7)	A m^{-2}
i_{out}	spray current density leaving the system (chapter 7)	A m^{-2}
k_{eff}	one-dimensional effective wavenumber (chapter 6)	m^{-1}
$k_{l,n}$	n -th zero of $J'_l(k_{l,n}R)$ (chapter 6)	m^{-1}
k_m	eigenvalue of surface harmonics (chapter 6)	m^{-1}
k_{max}	maximum effective wavenumber (chapter 6)	m^{-1}
\mathbf{k}_{osc}	oscillatory advection correction term (chapter 5)	-
\mathbf{k}_{stat}	stationary advection correction term (chapter 5)	-
k_{th}	most unstable wavenumber (chapter 6)	m^{-1}
m_i	mass of a single molecule of species i	kg
m_p	particle mass (chapter 5)	kg
n_i	refractive index (chapters 3 and 6)	-



Symbol	Meaning	Unit
\mathbf{n}, \mathbf{n}_i	normal vector (on interface i)	-
p	pressure	N m^{-2}
p	pillar pitch (chapters 3-4)	m
p	restoring parameter of Mathieu's equation (chapter 6)	-
p_{avg}	average pressure (chapter 5)	N m^{-2}
p_{ref}	reference pressure (chapter 7)	N m^{-2}
$\mathbf{P}_x, \mathbf{P}_y$	vectors of surface gradients (chapter 6)	m^{-1}
q	forcing parameter of Mathieu's equation (chapter 6)	-
q_d	droplet charge (chapter 7)	C
q_R	Rayleigh charge (chapter 7)	C
r	ratio of real surface to projected surface (chapter 3)	-
r_0	dimensionless radius of circular gate electrode (chapter 4)	-
t	time	s
t_0	arbitrary time	s
t_i	time-variables used in the perturbation approach (chapter 5)	s
t_{final}	simulation time span (chapter 5)	s
$\mathbf{t}_1, \mathbf{t}_2$	tangential vectors	-
u	velocity component in x -direction (chapters 4-5)	m s^{-1}
\mathbf{u}	velocity field	m s^{-1}
\mathbf{u}'	fluctuating velocity field (chapters 4-5)	m s^{-1}
$\bar{\mathbf{u}}$	time averaged velocity field (chapters 4-5)	m s^{-1}
\mathbf{u}_{\parallel}	velocity vector parallel to bounding plates (chapters 4-5)	m s^{-1}
\mathbf{u}_{\perp}	velocity vector perpendicular to bounding plates (chapters 4-5)	m s^{-1}
u_1	transformed velocity u (chapter 5)	m s^{-1}
u_{avg}	measured average velocity (chapter 4)	m s^{-1}
u_{comp}	equivalent height-averaged velocity (chapter 4)	m s^{-1}
u_d	droplet velocity (chapter 7)	m s^{-1}
\mathbf{u}_{HS}	Helmholtz-Smoluchowski velocity	m s^{-1}
\mathbf{u}_c	particle velocity when hitting the wall (chapter 5)	m s^{-1}
\mathbf{u}_p	particle velocity (chapter 5)	m s^{-1}
$\langle \mathbf{u}_{\parallel} \rangle$	height-averaged velocity vector parallel to bounding plates (chapters 4-5)	m s^{-1}
$\mathbf{u}_{\text{ROI},i}$	velocity vector of particle i in ROI (chapter 4)	m s^{-1}
\mathbf{u}_{slip}	slip-velocity at boundary	m s^{-1}
\mathbf{u}_w	wall velocity	m s^{-1}



Symbol	Meaning	Unit
u_{wall}	reference wall velocity (chapter 5)	m s^{-1}
v	velocity component in y -direction (chapters 4-5)	m s^{-1}
w	velocity component in z -direction (chapters 4-5)	m s^{-1}
\mathbf{x}	position vector	m
x_1	transformed coordinate x (chapter 5)	m
$x_{0,2D}$	size of the concentration region of 2D simulations (chapter 5)	m
$x_{0,3D}$	size of the concentration region of 3D simulations (chapter 5)	m
$\Delta \mathbf{x}$	displacement field (chapter 6)	px
y_{off}	side length parameter of initial distribution (chapter 5)	m
z_i	charge number (of species i)	-

Greek Symbols

Symbol	Meaning	Unit
Δ	layer thickness	m
Θ_c	contact angle side wall (chapter 7)	-
Θ_0	equilibrium contact angle	-
Θ, Θ_i	contact angle of material i	-
Θ_{adv}	advancing contact angle	-
Θ_{cb}	Cassie-Baxter contact angle	-
Θ_{rec}	receding contact angle	-
Θ_w	Wenzel contact angle	-
Λ	relative conductivity (chapter 7)	$\text{S m}^2 \text{mol}^{-1}$
Λ_0	relative conductivity at infinite dilution (chapter 7)	$\text{S m}^2 \text{mol}^{-1}$
$\mathbf{\Pi}'$	momentum flux density tensor	$\text{kg m}^{-1} \text{s}^{-2}$
$\partial \Omega$	boundary enclosing the volume Ω	m^2
Ω	volume element	m^3
α	ratio refractive indices (chapter 6)	-
$\boldsymbol{\alpha}$	random number vector (chapter 5)	-
β	slip length	m
β	unscaled driving parameter of Mathieu's equation (chapter 6)	s^{-2}
β^{L}	wall slip length field at the lower wall	m
β^{U}	wall slip length field at the upper wall	m
$\boldsymbol{\beta}$	slip length tensor	m
γ	interfacial tension	N m^{-1}

Symbol	Meaning	Unit
γ_{rel}	relative amplitude of random noise (chapter 6)	-
δ_{ij}	Kronecker delta (chapter 5)	-
ϵ	small parameter for expansion (chapters 4-5)	-
ϵ_{rel}	relative permittivity	-
ζ	surface potential	V
ζ	interface perturbation (chapter 6)	m
$\hat{\zeta}$	transient interface amplitude (chapter 6)	m
ζ_{NS}	surface potential at no-slip interface	V
ζ_{S}	surface potential at slip interface	V
θ_T	cone angle (chapter 7)	-
$\lambda_{l,n}$	wavelength corresponding to surface harmonics of $k_{l,n}$ (chapter 6)	m
λ_D	Debye length	m
λ	dominant instability wavelength (chapter 6)	m
λ_{th}	most unstable wavelength (chapter 6)	m
μ	dynamic viscosity	Pa s
$\mu_{\text{EOF},0}$	characteristic wall mobility scale	$\text{m}^2 \text{V}^{-1} \text{s}^{-1}$
$\langle \mu^{\text{EOF}} \rangle$	height-averaged EOF wall-mobility (chapters 4-5)	-
μ^{L}	wall mobility field at the lower wall	$\text{m}^2 \text{V}^{-1} \text{s}^{-1}$
$\langle \mu^{\text{P}} \rangle$	height-averaged pressure wall-mobility (chapters 4-5)	-
μ^{U}	wall mobility field at the upper wall	$\text{m}^2 \text{V}^{-1} \text{s}^{-1}$
ξ	generalized coordinate in the parameter space	case-dependent
ξ	arbitrary, non-zero vector (chapter 5)	-
ρ, ρ_i	mass density (of species i)	kg m^{-3}
ρ_{pol}	polarization density	C m^{-3}
ρ_{el}	free charge density	C m^{-3}
ρ_p	particle density (chapter 5)	kg m^{-3}
ρ_{sol}	solvent density	kg m^{-3}
σ_{DL}	surface double layer density	C m^{-1}
σ_{el}	free surface charge	C m^{-2}
σ_l	liquid-gas surface tension	N m^{-1}
σ	stress tensor	N m^{-2}
σ^{el}	Maxwell stress tensor	N m^{-2}
σ^{visc}	viscous stress tensor	N m^{-2}
σ_s	solid-gas surface tension	N m^{-1}
σ_{sl}	solid-liquid surface tension	N m^{-1}

Symbol	Meaning	Unit
τ	normalized time of Mathieu's equation (chapter 6)	-
τ_p	response time particle (chapter 5)	s
ϕ	electric potential	V
ϕ_g	gravitational potential	N m^{-2}
ϕ_i	interface potential (chapter 7)	V
ϕ_n	needle potential (chapter 7)	V
ϕ_S	ratio of the slip interface (chapters 3-4)	-
χ	susceptibility	-
ψ	stream function (chapters 4-5)	$\text{m}^2 \text{s}^{-1}$
ω	circular frequency	s^{-1}
ω_0	natural frequency of Mathieu's equation (chapter 6)	s^{-1}
∇	nabla-operator	m^{-1}

Physical Constants

Symbol	Meaning	Value
ϵ_0	vacuum permittivity	$8.854\,187 \times 10^{-12} \text{ F m}^{-1}$
k_B	Boltzmann constant	$1.38 \times 10^{-23} \text{ m}^2 \text{ kg s}^{-2} \text{ K}^{-1}$
c_0	speed of light in vacuum	$2.9979 \times 10^8 \text{ m s}^{-1}$
e	elementary charge	$1.602\,17 \times 10^{-19} \text{ C}$

List of Figures

2.1	Shell balance used to derive the jump conditions at a sharp interface (blue). The interface normal \mathbf{n} is directed into domain 1. The interface of area A is enclosed by an volume element Ω of thickness Δ	7
2.2	Depiction of the region Ω with corresponding mass flux density and area dA	9
2.3	Geometric relations of a curved interface with the two principle radii R_1, R_2 displaced by $\delta\xi$. Based on Bruus (2008, p. 125).	14
2.4	Shell balance used to derive the jump conditions at a free interface (blue). The interface normal \mathbf{n} is directed into domain 1. The interface of area dA is enclosed by an volume element dV of thickness Δ . The outward normal on the pillbox is denoted by \mathbf{n}_i	15
2.5	Wall boundary conditions at a solid wall for a velocity driven by a shear force far away from the interface. (a) No-slip boundary condition. (b) Navier-slip boundary condition with slip length β	16
2.6	Depiction of the region Ω with corresponding species flux density and area dA . For better visibility, the contributions due to convection (blue), diffusion (orange) and electrophoresis (green) are shown in separate surface sections dA	17
2.7	Schematic of a diffusive double layer forming due to a fixed charge at an solid-liquid interface, including a Schematic of the ion distribution (a), the Electric potential distribution (b) and the charge density distribution (c).	20
3.1	Macroscopic contact angles for different substrates and wetting states. (a) The contact angle on a flat surface is defined by Young's equation (eq. 3.10). (b) On a microstructured surface, a droplet in the Cassie-Baxter wetting state rests on a surface microstructure, with air entrapped under the droplet. The contact angle is defined by Cassie-Baxter equation (eq. 3.12). (c) A droplet in Wenzel state conforms to the surface microstructure, without air entrapment. The contact angle is governed by Wenzel's equation (eq. 3.18).	25
3.2	Possible collapse mechanisms on superhydrophobic surfaces with large aspect ratio structures. (a) Depinning instability. Once the advancing contact angle at the side-wall is reached, the contact line depins from the top of the microstructure, and starts moving downwards. (b) Advancing of a locally transitioned state from the side. If the surface collapsed locally, the Wenzel state can spread in between the microstructures. The condition for energetically favorable wetting front propagation is shown in eq. 3.19. (c) Condensation of microdroplets. Droplets can condensate from humid air into the microstructure, which ultimately fills up the whole gap. (d) Surface instability. Upon application of a sufficiently strong electric field, the Laplace-pressure at the interface cannot support the Maxwell stress anymore, and the interface breaks down in analogy to classical Taylor cones, leading to a local transition. (e) Electric breakdown of the gas. If the electric field strength in the air gap exceeds the breakdown strength, ionization of the gas and sparking between the liquid and a conducting bottom can occur.	29

3.3	Strategies to delay wetting state transitions. (a) Chemical surface modification. By increasing the contact angle at the side-wall using chemical modification, the wetting state transition can be delayed. (b) Secondary structures increase the effective contact angle at the side-wall, delaying the wetting state transition. (c) Re-entrant structures. Instead of modifying the complete side-wall structure, only the top is modified, such that the effective contact angle increases.	31
3.4	Schematic of the soft lithography process. A silicon wafer is used as the master structure, and an anti-sticking layer is applied by silanization in a vacuum chamber. Degassed PDMS is deposited on the wafer, and by spin-coating a structure of fixed thickness is created. Then, the PDMS is cured at 85 °C, and subsequently demolded.	32
3.5	Scanning electron microscopy (SEM) images of the resulting PDMS microstructure. (a) Top-view of the rectangular grid with pillar pitch p and side-length a . (b) Side-view under 45°, illustrating the homogeneity of the microstructure. (c) Detailed pillar image under 45° with visible scalloped side-walls due to the homogeneous etching during the DRIE-process. Also, the pillar side-wall is slightly tilted inwards. (d) Detailed pillar top view with rounded off pillar edges.	33
3.6	Schematic of the surface modification process. On a PDMS cast, a mixture of THF, PVC and ethanol is deposited. The solution is allowed to evaporate in a chemical fume hood, leading to the formation of a PVC nanostructure. Excess PVC is removed mechanically from the top of the pillars with a synthetic fiber brush.	34
3.7	SEM images of the resulting dual-scale microstructure. (a) Modified microstructure, demonstrating the general distribution of the PVC. Both the surface bottom as well as the pillars are coated, with local variations in structure. (b) Detailed image of a single pillar. The scallops at the side-walls provide contact points of the PVC nanostructure. (c) Detailed image of the PVC nanostructure. Due to the solvent-nonsolvent process, submicron structures form. As is visible, they form interconnected agglomerates, leading to multiple length scales. Subfigure (c): Adapted with permission from Rofman et al. (2020). Copyright 2020 American Chemical Society.	35
3.8	Schematic of the experimental setups used to characterize the wetting state stability (not drawn to scale). (a) Setup utilized for the single-scale microstructures. The interface is illuminated and observed from the bottom. Due to the change in reflectivity, the wetting states can be pictured directly. (b) Adapted setup utilized for the dual-scale microstructures. Due to the nano-structure, the surface is rendered opaque, requiring illumination and observation through the upper liquid phase. During the electrowetting, the interface changes the observed reflection pattern.(c) Exemplary dataset for the single-scale microstructure. Initially, only the pillar contact area appears as dark spots, whereas the rest of the surface appears as a bright region. Upon wetting state transition, a strong contrast is visible, with the dark regions corresponding to Wenzel state. (d) Exemplary dataset for the dual scale surface. Initially, the contact points of the pillar tops are visible. Due to PVC crystals at the top, the liquid meniscus is supported by regions of varying size. With increasing electric potential, the contact points at the pillars increase, and the distinct reflection pattern appears in form of a grid. With further increase of the electrowetting potential, the grid disappears locally. Additionally, local variations in the reflection intensity are observed in form of a blinking, most likely due to small shifts of the interface position. Adapted with permission from Rofman et al. (2020). Copyright 2020 American Chemical Society.	37

3.9	Electrowetting evaluation for the hierarchical surfaces. (a) The integrated intensity I shows a continuous decay over time. The grid intensity I_g shows a distinct maximum corresponding to the strongest reflection pattern, which is defined as the reference state of transition (RST, red circle). The cross-correlation c of the images with the image at the RST is used to extract the nano Cassie-Baxter transition point (NCT, blue diamond). The roman numerals indicate the electrowetting potentials corresponding to the images shown in (b-d). (b) Original images showing the decay in illumination. (c) Extracted grid reflection pattern obtained by subtracting the local background. (d) Illustration of the wetting states. Subfigure (d): Adapted with permission from Rofman et al. (2020). Copyright 2020 American Chemical Society.	39
3.10	Resulting electrowetting transition points for varying pillar pitch. Only datapoints are shown where the filling of the basin was successful. For $p = 25 \mu\text{m}$, no single-scale surface could be filled without transition to Wenzel state. Therefore, 0 V is shown instead. The error bars represent the 95%-confidence interval based on at least 6 independent measurements. Datapoints are connected by quadratic interpolation to guide the eye. Adapted with permission from Rofman et al. (2020). Copyright 2020 American Chemical Society.	40
3.11	Evaluation of the reversibility of the wetting state transition. (a) The voltage difference is varied using a saw-tooth function with increasing maximum value. The grid intensity I_g follows the same initial increase, with the consecutive decrease once the RST is transitioned. The cross-correlation with the first image (note that this is different than for Fig. 3.9) shows a distinct decrease over time, which becomes stronger with emerging reflection grid. With each voltage release, the correlation increases, indicating that the wetting state returns closer to the initial state, but never fully recovers the plateau from the relaxation before. This indicates a partial reversible relaxation of the interface. (b,c) Images before and after the voltage is released at the denoted roman numerals. Note that the regions, in which the grid vanished, appear darker than their surrounding after releasing the voltage. Here, the interface still touches the PVC structure in between the pillars.	42
3.12	Setup utilized to measure the contact angle. (a) Kruess DSA-100 measurement setup. The sample is observed from the side using back-illumination, after a droplet is deposited on the surface, and its volume is increased. (b) Exemplary dataset of a dual-scale surface during the advancing contact angle measurement. (c) Exemplary dataset of a single-scale microstructure, with a local transition to Wenzel state providing a strong pinning of the contact line during the measurement of the receding contact angle.	44
3.13	Experimentally obtained advancing and receding contact angles. (a) On single-scale microstructures, the measured advancing and receding angles enclose the theoretically predicted Cassie-Baxter contact angle. (b) The contact angles on a hierarchical microstructure show little change after prewetting the surface using electrowetting. The error bars represent the 95%-confidence interval on the mean. Subfigure (b): Adapted with permission from Rofman et al. (2020). Copyright 2020 American Chemical Society.	45
4.1	Schematic of electro-osmotic flow over a homogeneously charged surface, induced by an electric field directed in the $x - y$ -plane. Close to the wall, the EDL with a charge density ρ_{el} due to a surface potential ζ is present (depicted in green). Outside the EDL, the electrolyte is electroneutral. (a) In case of a no-slip boundary condition at the wall, the classical Helmholtz-Smoluchowski velocity u_{HS} (eq. 4.4) is obtained outside of the Debye-layer. (b) In case of a homogeneously charged surface with an isotropic slip length β , an equivalent to the Helmholtz-Smoluchowski equation is obtained, with an enhancement factor of β/λ_D compared to a no-slip surface of similar surface potential.	52

4.2	Schematic of the effective boundary condition for electro-osmotic flow over microstructured surfaces, exhibiting alternating no-slip patches and stress-free regions, following Squires (2008). The vertical dimension inside the liquid is not drawn to scale for better visibility. (a) In case of vanishing ζ_S potential at the gas-liquid interfaces, the only contribution to the flow stems from the no-slip regions exhibiting ζ_{NS} . The resulting velocity is equivalent to the Helmholtz-Smoluchowski velocity for a homogeneous no-slip surface without no-stress regions. (b) If the gas-liquid interface exhibits a surface potential ζ_S , the resulting velocity has an additional contribution due to the stress-free regions. Due to the ratio of the slip length compared to the Debye-length, already small potentials ζ_S suffice to dominate the resulting flow velocity for sufficiently large slip lengths.	54
4.3	Principle of electro-osmotic flow induced by gate electrodes. By applying a potential difference between a gate electrode below the microstructured surface and the electrolyte, additional charges are brought into the proximity of the gas-liquid and the solid-liquid interface. For simplicity, only the induced charges are shown in this schematic, as if the interface was initially uncharged. The gas-liquid and the solid-liquid interface exhibit different ζ potentials due to the different permittivities of the gas and the solid. The EOF can be induced either by using a constant driving field (DC mode, subfigure (a)) or by using a synchronized, time-variant signal for both the driving field and gate potential, where T_{osc} denotes the period (AC mode, subfigure (b)). If a time-variant signal is used, the induced EOF is solely due to the induced potential, as the velocity contribution due to the native ζ potential averages to zero.	56
4.4	Illustration of a Hele-Shaw cell under electric field actuation. The fluidic domain of constant thickness h is bound by two plates with varying electro-osmotic wall mobilities μ^U, μ^L that can exhibit a spatial and temporal variation, and slip length distributions β^U, β^L that exhibit a spatial variation. The characteristic length scale L_0 of the variation of the wall mobilities is assumed to be much larger than the gap thickness ($h \ll L_0$). The variations of the wall mobilities can lead to internal pressure gradients, which in turn induce a height-averaged flow field.	58
4.5	Schematic of the experimental setup. (a) Illustration of the resulting flow field induced by a circular gate electrode embedded below a microstructured, superhydrophobic surface. The fluidic cell is bound by a glass slide at the top (not shown). Inside the cell, a dipole flow field is induced. (b) Particle tracking velocimetry setup utilized to characterize the flow velocity using fluorescent tracer particles. The fluid motion is induced by two wire electrodes embedded into the reservoirs of the channel, actuated by a rectangular wave signal with a voltage difference V_{EOF} . At the synchronized gate electrode, a voltage amplitude of V_{gate} is applied. Adapted figure with permission from Sebastian Dehe, Baruch Rofman, Moran Bercovici, and Steffen Hardt, Phys. Rev. Fluids, 5(5), 053701, 2020. Copyright (2020) by the American Physical Society.	64
4.6	Measurement of EOF over superhydrophobic surfaces. (a) Particle streakline image showing the resulting flow field induced by a circular gate electrode (shown as dark overlay). The resulting flow field is obtained by ensemble-averaging the measured particle velocities according to eq. 4.36 within the region of interest (ROI). (b) Experimentally obtained flow velocity above the gate electrode for varying pillar pitches p with a driving field of 50 V cm^{-1} and a driving frequency of 5 Hz using a buffer solution with an ionic strength $I = 10 \text{ mM}$ at pH 7. The error bars represent the 95 %-confidence interval based on at least 6 independent measurements. The dashed lines represent linear fits for the range $V_{gate} = -750 \text{ V}$ to 750 V . Adapted figure with permission from Sebastian Dehe, Baruch Rofman, Moran Bercovici, and Steffen Hardt, Phys. Rev. Fluids, 5(5), 053701, 2020. Copyright (2020) by the American Physical Society.	66

- 4.7 Scaling of flow velocity with theoretical predictions. (a) Electric circuit model used to calculate the resulting gas-liquid ζ_S potential. The EDL size is exaggerated for clarity. (b) The experimental results presented in Fig. 4.6 are rescaled according to eq. 4.39. Here, ζ_S is predicted using the equivalent circuit model, and β using eq. 4.7. The data collapses to one dataset, corroborating the theoretical modeling. Interestingly, induced ζ_S below mV (compare to Table 4.2) lead to an effective ζ potential $\zeta_S^{\text{ind}}\beta/\lambda_D$ of several V. (c, inset to b) The ratio of the experimentally observed velocity to the theoretically predicted velocity for different pillar pitches at a gate voltage of $V_{\text{gate}} = 750$ V. The experimentally measured velocities are about 50 % smaller than predicted. The error bars represent the 95 %-confidence interval based on at least 6 independent measurements. Subfigure (a): Adapted figure with permission from Sebastian Dehe, Baruch Rofman, Moran Bercovici, and Steffen Hardt, Phys. Rev. Fluids, 5(5), 053701, 2020. Copyright (2020) by the American Physical Society. 68
- 4.8 Dependency of the experimentally obtained velocity on the electrolyte properties. (a) Velocity as a function of pH for varying pillar pitch at an ionic strength of 10 mM and $V_{\text{gate}} = 500$ V. The averages over all pH are represented by the dashed lines. Error bars represent the 90%-confidence interval based on 5 independent measurements. (b) Velocity as a function of ionic strength for a pillar pitch $p = 15$ μm , pH = 7, and $V_{\text{gate}} = 250$ V. N denotes the number of independent measurements taken. Adapted figure with permission from Sebastian Dehe, Baruch Rofman, Moran Bercovici, and Steffen Hardt, Phys. Rev. Fluids, 5(5), 053701, 2020. Copyright (2020) by the American Physical Society. 69
- 4.9 Surfactant effects on the EOF over superhydrophobic surfaces. (a) Experimentally obtained velocities for a channel with $p = 15$ μm , pH = 7, and $V_{\text{gate}} = 250$ V. In order to analyze the influence of surfactants, the anionic surfactant SDS was added with a concentration of 0.2 mM, corresponding to 2.5 % of the critical micelle concentration. (b) Top-view schematic of a pumping mechanism allowing for backflow, leading to a net transport from the left to the right. By allowing for controlled backflow, the build-up of a strong surfactant gradient immobilizing the interface could potentially be prevented, at the cost of diminished pumping rate. 71
- 4.10 Demonstration of flow shaping using multiple gate electrodes. (a) Streakline image of a vortex flow created by two electrodes of size 1000 $\mu\text{m} \times 500$ μm each, with an intermittent spacing of 100 μm . The streaklines were recorded above a microstructure with $p = 20$ μm and a driving field of 50 V cm^{-1} using an exposure time of 1 s. The scale bar represents 500 μm . (b) Demonstration of the blinking vortex principle. A superposition of two streakline images above three gate electrodes (marked in red, blue and orange) is shown. The upper and lower gate electrode (red and orange) exhibit a gate potential amplitudes of 150 V and -150 V, respectively. The gate voltage amplitude of the centered electrode changed its sign, so that the position of the resulting vortex shifted positions. The blinking frequency between the flow fields was set to 0.1 Hz. The scale bar represents 500 μm 72

4.11	Influence of the electrowetting stability of the Cassie-Baxter state on the flow field. (a) Experimentally observed streaklines of the flow field presented in Fig. 4.10(a) after locally inducing wetting state transitions with an increased gate voltage. Due to local transitions, the streaklines are curved, leading to low-velocity regions embedded within high velocity regions. (b) Experimentally observed flow velocities for 4 specific measurements with varying pillar pitch at pH = 7. With increasing gate voltage magnitude, the resulting velocity deviates from the initial linear scaling with gate voltage, with diminishing velocities for increasing gate potentials. The colored boxes denote the wetting state stabilities determined experimentally in section 3.4. The edge with the lower magnitude of V_{gate} corresponds to the RST and the edge with the higher magnitude to the NCTP. The maximum velocity is observed in between these lower and upper limits, respectively.	73
5.1	Taylor-Aris dispersion in a circular capillary. (a) An initially confined soluble species with concentration c_0 is released in a pressure-driven flow with velocity variations in the radial direction. (b) Without diffusion, only advection would lead to a variation of the concentration field, leading to a broad distribution in x -direction. (c) Molecular diffusion leads to a re-distribution in the radial direction, resulting in a height-averaged concentration distribution.	77
5.2	Shear-enhanced dispersion in an oscillatory flow field in a slit channel infinitely extending in y -direction. (a) An initially confined distribution of a soluble species is released in a shear-flow with a circular frequency ω . (b) If the oscillation frequency is much faster than the radial diffusion process, the soluble species is spread after one quarter of the oscillation period. In a height-averaged framework (top-view), the concentration field widens strongly. (c) After one half of the oscillation period, the concentration field returns to its initial concentration, with a slightly wider distribution width. In a height-averaged framework, the solution concentration contracts during the second quarter of the oscillation, corresponding to a negative dispersion coefficient.	79
5.3	Schematic of internal pressure gradients in capillaries created by electro-osmosis with non-homogeneous wall mobilities. The region with wall mobility drives a flow field through the whole capillary. Due to the region without wall mobility, an internal pressure gradient builds up, which deforms the EOF profile. Due to the velocity changes in radial direction, sample dispersion increases.	81
5.4	Illustration of species transport in a Hele-Shaw cell geometry under electric field actuation. (a) The upper and lower fluidic walls can both exhibit a non-uniform slip length as well as electro-osmotic mobility, and are separated by a gap width h . As a result, a non-uniform flow field develops. (b) The dissolved species is transported by different mechanisms, including advection and diffusion. (c) Reduced-order representation of the system. The concentration field (red) is redistributed due to advection, dispersion and molecular diffusion. The species transport processes occurring over the cross-stream direction are incorporated into the transport coefficients of the two-dimensional model. Reprinted with permission from Cambridge University Press, J. Fluid Mech. 925, 2021, Dehe et al. (2021b).	83
5.5	Convergence study of the time-stepping in the particle-tracking simulations. The mixing intensity (eq. 5.60) is evaluated after $t = 872.9 T_{\text{dif,h}}$. Reprinted with permission from Cambridge University Press, J. Fluid Mech. 925, 2021, Dehe et al. (2021b).	93
5.6	Convergence study of the maximum element size of the 2D model. (a) The global measure I_p (eq. 5.62) for the flow field convergence shows an asymptotic behavior for decreasing cell size. (b) The mixing intensity I_c (eq. 5.60) converges for small cell sizes at the final time step $t = 918 T_{\text{dif,h}}$. The second-finest mesh size was utilized in the final computations. Reprinted with permission from Cambridge University Press, J. Fluid Mech. 925, 2021, Dehe et al. (2021b).	94

5.7	<p>Test case A: Hydrodynamic dispersion inside a Hele-Shaw cell for a stationary flow field, as obtained using the 2D model (c-e) as well as the 3D particle tracking simulations (f-h). (a) A shear flow with zero height-averaged flow is created due to wall mobilities of similar magnitude, but varying sign in a Hele-Shaw configuration. (b) Initial distribution of the soluble species. (c-h) Resulting flow field for a simulation time of $t = 70.59 T_{\text{dif,h}}$, with the direction of the electric field indicated in the top-right corner of each panel. Reprinted with permission from Cambridge University Press, <i>J. Fluid Mech.</i> 925, 2021, Dehe et al. (2021b).</p>	95
5.8	<p>Test case B: Hydrodynamic dispersion inside a Hele-Shaw cell for an oscillatory flow field, as obtained using the 2D model (c-e) as well as the 3D particle tracking simulations (f-h). (a) A shear flow with vanishing height- and time-averaged flow is created due to wall mobilities of similar magnitude, but varying sign in a Hele-Shaw configuration, and an oscillatory driving field in the x-direction. (b) Initial distribution of the soluble species. (c-h) Resulting flow field for a simulation time of $t = 70.59 T_{\text{dif,h}}$, with the non-dimensional oscillation frequency of the electric field $\hat{f} = f T_{\text{dif,h}}$ indicated in the top-right corner of each panel. Reprinted with permission from Cambridge University Press, <i>J. Fluid Mech.</i> 925, 2021, Dehe et al. (2021b).</p>	97
5.9	<p>Test case B: Resulting non-zero entry of the dispersion matrix, shown for varying oscillation frequencies. In the limit of fast oscillations, the dispersion asymptotically approaches zero, and in the limit of slow oscillations, it approaches one half of the value obtained for a stationary flow field of same magnitude. Reprinted with permission from Cambridge University Press, <i>J. Fluid Mech.</i> 925, 2021, Dehe et al. (2021b).</p>	98
5.10	<p>Test case C: Dispersion in a circulatory flow field. (a) The flow field is induced by a wall mobility distribution on the upper and the lower bounding plate, where the mobilities exhibit opposing signs. Additionally, the mobility at the upper plate has a magnitude of 75 % of the lower wall mobility. The electric field is directed into the x-direction. (b) Streamlines of the average flow velocity, resulting in a circulating flow field. The normalized wall mobility distribution is shown as the colormap. (c-e) Resulting dispersion tensor components. In x-direction, the dispersion is enhanced in the regions of the mobility patches, and in the y-direction, it is comparable to molecular diffusion. Reprinted with permission from Cambridge University Press, <i>J. Fluid Mech.</i> 925, 2021, Dehe et al. (2021b).</p>	100
5.11	<p>Test case C: Resulting concentration distributions as computed with 3D particle simulations (a,d,g,j), the 2D dispersion model (b,e,h,k) and purely 2D molecular diffusion (c,f,i,l). The concentration field is shown for the three time steps $t = 0 T_{\text{dif}}$ (a-c), $t = 306 T_{\text{dif}}$ (d-f), $t = 612 T_{\text{dif}}$ (g-i) and $t = 918 T_{\text{dif}}$ (j-l). Since advection dominates the species transport, the structure of the concentration field is the same in all three cases. Once the lamella passes the regions with enhanced dispersion, the size of the mixing zones, as obtained for molecular diffusion only, is smaller compared to the 3D simulations and the reduced order model. Reprinted with permission from Cambridge University Press, <i>J. Fluid Mech.</i> 925, 2021, Dehe et al. (2021b).</p>	101
5.12	<p>Variation of test case C with an upper wall mobility of $\mu^U = -0.95\mu^L$. The resulting concentration distribution as obtained from the dispersion model (b) and the molecular diffusion model (c) at $t = 4693 T_{\text{dif,h}}$. As is visible, dispersion can have a strong influence on the flow field. Reprinted with permission from Cambridge University Press, <i>J. Fluid Mech.</i> 925, 2021, Dehe et al. (2021b).</p>	101

5.13	Experimental setup for the blinking vortex demonstration. (a) Layout of the microfluidic chip. A superhydrophobic surface (SHS) with side lengths $2\text{ cm} \times 1\text{ cm}$ is positioned above three gate electrodes that can be controlled individually. A fluidic lamella of different fluorescein concentrations is created by pressure-driven flow at the inlet. The driving electric field is applied by wire electrodes inside the reservoirs. Once the lamella is created, the pressure-driven flow is stopped, and the experiments are performed. (b) Control schematic of the gate electrodes. By changing the sign of the central gate electrode after each $T = 60\text{ s}$, the center of the circulatory flow field shifts, while maintaining the rotation direction. Both the driving field as well as the gate potentials are driven using a rectangular waveform with a frequency of 5 Hz.	102
5.14	Experimentally obtained fluorescence images. The initially created lamella with a confined mixing region is deformed using a circulatory flow field. The depicted time steps are denoted in the upper left corner of each panel. The center of the past $T = 60\text{ s}$ is denoted by the arrow. Over time, a homogeneous mixing region is achieved, occurring on timescales much shorter than molecular diffusion ($(3\text{ mm})^2/D \approx 6.25\text{ h}$).	103
5.15	Dispersion shaping by flow fields used to enhance dispersion along defined pathlines. (a) Within a Hele-Shaw cell, the dispersion is enhanced along arbitrary pathlines, here forming the letters <i>NMF</i> . The effective diffusivity is much higher than in the surrounding liquid. (b-d) Components of the symmetric dispersion tensor ($D_{xy} = D_{yx}$).	104
5.16	Wall mobilities required to create the dispersion tensor fields shown in Fig. 5.15, during each of the time-intervals $i = 1, \dots, 4$. The directions of the electric field during the time-interval i is indicated in the lower right corner of each panel. The upper and lower wall mobility have the same spatial distribution, but opposing signs.	106
5.17	Resulting concentration fields created by the dispersion shaping outlined in Fig. 5.15 for the time steps $t/T_{\text{diff,h}} = 1 \times 10^3, 5 \times 10^3, 1 \times 10^4, 4 \times 10^4$. The bounding walls in y -direction are connected to reservoirs of concentration $c = 1$. Along the pathlines, transport is enhanced, and outside, molecular diffusion leads to a much smaller concentration change.	107
6.1	Faraday instability due to different actuations. (a) Electrostatically induced Faraday instability. An interface between a dielectric liquid and a conducting liquid is excited by a harmonically oscillating electric field. (b) Mechanically induced Faraday instability between two liquids. A container is mechanically vibrated in the direction normal to the interface. Due to the mechanical actuation, an instability is induced at the interface. (c) Mechanically induced Faraday instability of a fluidic layer in contact with air. The upper layer can be viewed as a fluid with negligible viscosity.	112
6.2	Stability of Mathieu's equation in the p - q -space. A point located in the white region is stable, a point located in the blue region is unstable. The black line denotes the marginal stability curves. Even at small forcing q , unstable values of p exist. Depending on the specific point (p, q) , the solution is either harmonic or subharmonic with the characteristic frequency of the normalized time scale τ	113
6.3	Theoretically obtained stability curve for the fluid pair of silicone oil of 0.65 cSt and 0 wt% glycerol (described in section 6.3.4). (a) Marginal stability curve for a driving frequency of $f = 2\text{ Hz}$. The wavenumbers become unstable at different voltages, and the lowest critical voltage U_{crit} represents the onset voltage of instability. (b) Stability map. For otherwise constant parameters, the lowest critical voltage can be plotted versus the driving frequency, and represents the experimentally measurable stability curve. (c) Corresponding critical wavelength for the given onset voltage. The wavelengths are expected to be observed for instabilities close to the onset voltage.	115

6.4	Surface harmonics of the form $S_{l,n} = J_l(k_{l,n}r) \cos(l\theta)$ for a circular domain, where J_l denotes the Bessel function of the first kind and $k_{l,n}$ the n -th zero of $J'_l(k_{l,n}R)$ (Benjamin and Ursell, 1954). The data is normalized, with red denoting the maximum and blue denoting the minimum value.	117
6.5	Refraction at an interface of two media with different refractive indices ($n_1 < n_2$). (a) Refraction of a single optical path at a flat interface. (b) Refraction of a regular grid (black rectangles) immersed in medium 1 at a non-flat interface. The regularly spaced grid appears to be non-regularly spaced if projected on a screen far away from the interface, as can be seen from the varying distances of the light paths.	118
6.6	Schematic of the experimental measurement setup. (a) Experimental setup cell. A glass cylinder is clamped in between two metal electrodes by using a plastic holder. At the upper electrode, a grid with a line-spacing of 0.5 mm is engraved. The grid is imaged through a glass at the bottom electrode. A high-voltage power source provides a time-dependent potential difference between the electrodes and induces the instability at the interface. (b) Schematic of the interface reconstruction algorithm. The grid at the upper electrode is imaged through the interface and appears distorted. For known refractive indices, the 3D interface can be reconstructed from the 2D images, yielding information about the third dimension.	119
6.7	Displacement field detection. (a) Schematic of the measurement method with the respective relevant properties. (b,c) Exemplary displacement field in x - and y -direction, as obtained from the measurements. The displacement field is linearly proportional to the surface gradient ∇h	121
6.8	Pattern wavelength extraction. (a) Reconstructed interface for the displacement field shown in Fig. 6.7(b,c). (b) Resulting FFT power spectrum. The power spectrum exhibits peaks due to the Fourier-transform (I), the physical interface pattern (II) and due to the interface reconstruction (III). The detected value of k_{eff} is used for further processing and can be transformed into a respective wavelength (eq. 6.18). (c) Measured dominant wavelengths for one period of oscillation (7 Hz, 143 ms period length). As is visible, the dominant pattern wavelength persists over the majority of the measurement, resulting in an average value of 14.23 mm (shown as a dashed line). During parts of the oscillation, the Faraday instability has small amplitudes. Then, a different wavelength is obtained, which can be attributed to the edge-waves of the system.	123
6.9	Influence of the salt concentration on the instability. (a) Comparison between the experimental stability map and theoretical predicted onset voltage amplitude $U_{\text{crit}} = 2393 \text{ V}$ obtained from the perfect-dielectric / perfect-conductor model. (b) Comparison between dominant pattern wavelength and theoretical predicted dominant wavelength $\lambda_{\text{th}} = 11.35 \text{ mm}$ obtained from the perfect-dielectric / perfect-conductor model. Error bars denote the standard deviation for the determined patterns within one experiment. .	127
6.10	Influence of the dielectric's viscosity. The dielectric liquid is varied, while using DI-water with a KCl concentration of $c = 1 \text{ mmol L}^{-1}$. The theoretical results are shown as a dashed line. (a-c) Experimentally obtained stability maps. (d-f) Dominant pattern wavelengths. Error bars represent the standard deviation in each experiment. In the upper right corner, the number of critical experiments shown in the respective panel is shown.	128

- 6.11 Influence of the electrolyte’s viscosity. The viscosity of the conducting liquid is varied by changing the wt% glycerol, while using silicone oil with 0.65 cSt as the dielectric, and retaining the KCl concentration of $c = 1 \text{ mmol L}^{-1}$. The theoretical results are shown as a dashed line. (a-c) Experimentally obtained stability maps. (d-f) Dominant pattern wavelengths. Error bars represent the standard deviation in each experiment. In the upper right corner, the number of critical experiments shown in the respective panel is shown. 130
- 6.12 Reconstructed spatial structure of the instability using silicone oil with a viscosity of 0.65 cSt and 0 wt% glycerol. The interface deviation Δh is normalized, with blue denoting negative interface deflections and red positive deflections. The theoretical prediction of the wavelength for the given driving frequency is shown at the top of each row. Below each panel, the respective driving amplitude as well as the measured pattern wavelengths are shown. 132
- 6.13 Reconstructed spatial structure of the instability using silicone oil with a viscosity of 1 cSt and 0 wt% glycerol. The interface deviation Δh is normalized, with blue denoting negative interface deflections and red positive deflections. The theoretical prediction of the wavelength for the given driving frequency is shown at the top of each row. Below each panel, the respective driving amplitude as well as the measured pattern wavelengths are shown. 133
- 6.14 Reconstructed spatial structure of the instability using silicone oil with a viscosity of 0.65 cSt and 60 wt% glycerol. The interface deviation Δh is normalized, with blue denoting negative interface deflections and red positive deflections. The theoretical prediction of the wavelength for the given driving frequency is shown at the top of each row. Below each panel, the respective driving amplitude as well as the measured pattern wavelengths are shown. 134
- 6.15 Robustness of wavelength extraction algorithm versus noise. (a) Artificial interface in a $1024 \text{ px} \times 1024 \text{ px}$ domain. (b) Reconstructed interface on a reduced grid of 51×51 grid points, for the relative error amplitude of $\gamma_{\text{rel}} = 2$. As is visible, the reconstructed interface becomes noisy, with locally strong deviations from the original data. (c,d) Corresponding gradients from which the interface in (b) is reconstructed. The noise corresponds to $\gamma_{\text{rel}} = 2$. (e) Variation of the extracted wavenumber with relative error amplitude γ_{rel} 136
- 7.1 Exemplary instability modes of a liquid-liquid interface due to a pin electrode positioned above the interface. The upper dielectric liquid is a silicone oil of 0.65 cSt viscosity, the lower liquid is a grounded aqueous KCl solution with an ionic concentration of 10 mmol L^{-1} . Additionally, the non-ionic surfactant Triton-X100 was added to the conducting liquid ($6 \mu\text{mol L}^{-1}$). (a) The system forms a Taylor cone, and a fine jet of droplets is issued from its tip. (b) The system forms a surface depression below the electrode, and from its rim, a Taylor cone emerges towards the electrode. This image corresponds to Fig. 7.4(b). Adapted figure with permission from Sebastian Dehe, and Steffen Hardt, Phys. Rev. Fluids, 6(12), 123702, 2021. Copyright (2021) by the American Physical Society. 140

- 7.2 Schematic of different operating modes of a Taylor cone. A conducting liquid (blue) is emitted into a second liquid or gas by means of an electric field. The principle direction of the electric field is indicated at the top of the sketch, denoting the initial electric field direction, without considering the changes introduced by the presence of the cone. (a) Stationary Taylor cone of a liquid with infinite conductivity following Taylor (1964). The cone takes the characteristic cone-angle of 98.6° , and no emission of liquid occurs. (b) EHD tip streaming in the steady cone-jet mode. A small jet is emitted from the tip of the Taylor cone, since the tangential electrostatic stress cannot be balanced by conduction. Further downstream, the jet can undergo Rayleigh-Plateau instabilities and break-up into droplets. (c) Pulsating Taylor cone. The Taylor cone emits droplets in a pulsating mode, with an advancing and receding cone-tip. 142
- 7.3 Schematic of the experimental setups utilized to study the EHD instability at a liquid-liquid interface and the influence of droplets on the instability. (a) Experimental setup in a pin-interface configuration. The pin electrode is positioned above an interface between a dielectric liquid (e.g., silicone oil) and an aqueous KCl solution, which is contacted by a second electrode. The interface in the square container of side length $a = 36$ mm is observed using a high-speed camera and either a DSLR-camera objective or a long working distance microscope. (b) Replacement cell used to introduce electrified droplets into the system. A hollow needle is positioned into the cell made from a glass cylinder with inner diameter $D_c = 12.4$ cm, which is sealed by a clamping plastic holder. By providing a potential difference between the needle and the lower electrode, and a volume flow rate through the needle, droplets are introduced. (c) Overview over peripheral equipment. In both setups, the voltage is provided by a high voltage power source, and the electric current is monitored using a pico-ammeter protected from overvoltage by a safety mechanism. A syringe pump controls the flow rate. Adapted figure with permission from Sebastian Dehe, and Steffen Hardt, Phys. Rev. Fluids, 6(12), 123702, 2021. Copyright (2021) by the American Physical Society. 147
- 7.4 EHD tip streaming at a liquid-liquid interface induced by a pin electrode, close to the time of surface disintegration. Images with the same letter denote experiments performed for the same liquid-liquid combination at comparable experimental conditions. (a) Interface between silicone oil (0.65 cSt) and a 10 mM KCl solution, resulting in the formation of a classical Taylor cone (a1) or a surface dimple with a cone emerging from the rim (a2). (b) Interface between silicone oil (0.65 cSt) and a 10 mM KCl solution with additional non-ionic surfactant (Triton-X100), resulting in the formation of a classical Taylor cone (b1) or a surface dimple with a cone emerging from the rim (b2). (c) Interface between n-dodecane and a KCl solution with a concentration of 0.1 M and additional surfactant Triton-X100, resulting in a dimple with multiple cones forming from the rim. (d) Image sequence of the interface between dodecane and a KCl solution with a concentration of 0.1 M and additional surfactant Triton-X100. First, a Taylor-cone is formed and droplets are ejected (d1), then the interface forms a dimple (d2), and subsequently a cone is formed again (d3). Adapted figure with permission from Sebastian Dehe, and Steffen Hardt, Phys. Rev. Fluids, 6(12), 123702, 2021. Copyright (2021) by the American Physical Society. 149

- 7.5 Interface deflection characterization. (a) Schematic of the system with a submerged electro spray. As the dielectric liquid, silicone oils with varying dynamic viscosity η_o , dielectric permittivity ϵ_o , and mass density ρ_o were used. As the conducting liquid, an aqueous KCl solution with a concentration of $c_{\text{KCl}} = 0.1 \text{ mM}$ was used. A second conducting liquid was emitted from the hollow needle, with a supplied volume flow rate Q and a KCl concentration c_{KCl} , which were both varied in the experiments. The electro spray was formed by supplying an electric potential ϕ_n to the metallic needle, and the lower electrode was held constant at 0 V. The submerged electro spray (blue region) was dispersed in the dielectric and finally merged with the lower phase. (b) Representative interface deflection as observed in sideview. The averaged image was created from the recorded video (see main text for details), with the interface appearing as a bright line in front of a dark screen. The surface depression was extracted via postprocessing (solid blue line) and compared to the undeflected interface (dashed line). The meniscus at the side-wall of the glass cylinder is visible as a bright region above the undistorted interface position. The dark background results from a matte screen, which is placed outside the cell and prevented the illumination to enter directly the region of interest, whereas the interface reflects the light entering from outside the field of view, thus creating a strong contrast for the postprocessing. The screen boundary is visible at the bottom (dotted line). Adapted figure with permission from Sebastian Dehe, and Steffen Hardt, Phys. Rev. Fluids, 6(12), 123702, 2021. Copyright (2021) by the American Physical Society. 153
- 7.6 Measured current (a) and deflection (b) as a function of the volume flow Q and the applied potential difference ϕ_n . The silicone oil of viscosity 5 cSt was used as the dielectric liquid, and the KCl concentration of the electro spray was set to $c_{\text{KCl}} = 1 \text{ mM}$. Error bars represent the standard deviation of 5 measurements, and the dashed lines represent fit functions of the form $y = ax^b$ to guide the eye. Adapted figure with permission from Sebastian Dehe, and Steffen Hardt, Phys. Rev. Fluids, 6(12), 123702, 2021. Copyright (2021) by the American Physical Society. 155
- 7.7 Measured current (a) and deflection (b) as a function of the silicone oil viscosity and the applied voltage ϕ_n . The volume flow rate was set to $40 \mu\text{L min}^{-1}$ and the KCl concentration of the spray to 1 mM. Error bars represent the standard deviation of 5 measurements, and the dashed lines represent exponential fit functions to guide the eye. Adapted figure with permission from Sebastian Dehe, and Steffen Hardt, Phys. Rev. Fluids, 6(12), 123702, 2021. Copyright (2021) by the American Physical Society. 155
- 7.8 Measured current (a) and deflection (b) as a function of the KCl concentration of the submerged electro spray and the oil viscosity for a fixed volume flow of $40 \mu\text{L min}^{-1}$ and a potential difference of 4000 V. Error bars represent the standard deviation of 5 measurements, and the dashed lines represent exponential fit functions to guide the eye. Adapted figure with permission from Sebastian Dehe, and Steffen Hardt, Phys. Rev. Fluids, 6(12), 123702, 2021. Copyright (2021) by the American Physical Society. 156
- 7.9 Schematic of the computational domain with relevant boundary conditions. The radial symmetry of the problem is utilized, with the symmetry axis coinciding with the needle axis. The liquid-liquid interface can be deformed due to the dynamic pressure of the flow, with capillary and hydrostatic forces acting to restore the interface. The numerical modeling accounts for charge transport and electrostatics in the dielectric liquid, and fluid flow in both liquids. Adapted figure with permission from Sebastian Dehe, and Steffen Hardt, Phys. Rev. Fluids, 6(12), 123702, 2021. Copyright (2021) by the American Physical Society. 160

- 7.10 Numerical convergence study. (a) Grid convergence study. The number of mesh cells is increased as described in the text, and the influence on the interface deflection is shown. (b) Convergence study for the diffusion constant D_d for a droplet radius of $R_d = 17.5 \mu\text{m}$. As D_d is used as an ad-hoc approach to stabilize the numerics, its numerical value should not influence the solution and it has to be advection dominated. For the computations, a diffusion constant of $D_d = 1 \times 10^{-6} \text{m}^2 \text{s}^{-1}$ is used, well within the advection dominated regime. Adapted figure with permission from Sebastian Dehe, and Steffen Hardt, Phys. Rev. Fluids, 6(12), 123702, 2021. Copyright (2021) by the American Physical Society. . 162
- 7.11 Particle streak lines and liquid velocity obtained from the calibration measurement. A submerged electrospray was induced by a potential difference of 3000 V, a volume flow rate of $20 \mu\text{L min}^{-1}$, as well as a KCl concentration of 0.1mmol L^{-1} , and a silicone oil with a viscosity of 5 cSt was chosen as the dielectric. The magnitude of the vertical velocity component is shown as the color map. Only regions with more than 30 measured particle velocities are shown, and the meniscus at the container wall restricts the field of view. The needle position is indicated at the top of the image. The numerical data is compared to the average of the region indicated by the dashed rectangle. Adapted figure with permission from Sebastian Dehe, and Steffen Hardt, Phys. Rev. Fluids, 6(12), 123702, 2021. Copyright (2021) by the American Physical Society. 163
- 7.12 Numerically obtained interface deflections. (a) The deflection of the liquid-liquid interface is shown as a function of the droplet radius R_d for the parameters summarized in Table 7.3 and a fixed current I_0 (black symbols). The grey region depicts the experimental results (mean value $\pm 2 \times$ standard deviation). The velocity field of the calibration measurements is matched best by the velocity field of $R_d = 17.5 \mu\text{m}$ (indicated by a star symbol). Allowing the spray current to vary, depending on the electric field strength at the needle, the deflection reaches a plateau for small droplet sizes (red symbols). This is a result of space charges screening the electric field off. Inset: Electric field strength at the needle center in case of a constant and a variable spray current. For a constant spray current, the electric field changes its sign, showing a clearly unphysical result, which is rectified by introducing the current dependence. (b) Numerical results for a droplet radius $R_d = 17.5 \mu\text{m}$. The space charge density (red) and the vertical velocity magnitude (blue) are shown, in addition to the electric field lines (left) and the velocity streamlines (right). Adapted figure with permission from Sebastian Dehe, and Steffen Hardt, Phys. Rev. Fluids, 6(12), 123702, 2021. Copyright (2021) by the American Physical Society. . 165

List of Tables

2.1	Overview over additional introductory sections with respective descriptions.	22
3.1	Parameters of the PDMS microstructured surfaces. Also, the observed failure probability upon filling a gasket with a 2 cm × 1 cm microstructured region at the bottom is shown, as described in the text.	36
3.2	Theoretical contact angles predicted according to eq. 3.13 and eq. 3.18 for $\Theta_0 = 108^\circ$	44
4.1	Buffer composition of the experiments. Aqueous solutions are used, based on a 50 % H ₂ O / D ₂ O mixture, with the ionic strength fixed to $I = 10$ mM. The pH value is changed by adding a weak base or acid and shifting the chemical equilibrium with a strong acid or base as titrant, respectively. The ionic strengths as well as buffer capacitance is calculated using <i>peakmaster</i> 5.3 (Gaš et al., 2005).	65
4.2	Geometric parameters of the superhydrophobic surface. The production of the surfaces is described in section 3.3. The solid interface fraction ϕ_{PVC} is computed for the PVC-coated hierarchical pillars. Based on SEM images, the resulting structures are approximated as circular pillars with a diameter $d = 6.5$ μm. The effective slip length follows from Davis and Lauga (2010) based on ϕ_{PVC} . The induced potential ζ_s is based on the equivalent electric circuit for a gate potential $V_{\text{gate}} = 500$ V.	67
5.1	Parameter values used in the particle-tracking simulations. The values were chosen specifically to yield a molecular diffusion coefficient of 1×10^{-10} m ² s ⁻¹	92
5.2	Parameter values as used in test cases A and B (see Fig. 5.7 and Fig. 5.8).	96
5.3	Numerical parameters utilized in test case C (see Fig. 5.10).	99
5.4	Parameters utilized in the calculations of the dispersion shaping, as indicated in Fig. 5.15.	105
6.1	Parameters of eq. 6.1 for electrostatic and mechanical forcing.	112
6.2	Substance properties of the used liquids. Values are composed of mean and standard deviation. In case of the dynamic viscosity, the measured density and kinematic viscosity from the data sheet are used (c), and for the dielectric permittivity, the values taken from the respective data sheet (l) (Wacker-Chemie GmbH, 2002). The values are composed of mean and standard deviation of five individual measurements.	125
6.3	Interfacial tensions for the used liquid-liquid combinations. The values are composed of mean and standard deviation of five individual measurements.	126
6.4	Mode numbers, corresponding wavelengths and critical voltage in the range between 40 mm and 48 mm for a container diameter of 125 mm, sorted by wavelength.	137
7.1	Conductivity data for KCl solutions computed from reference data (Shreiner and Pratt, 2004).	148
7.2	Fluid properties of the silicone oils as obtained from the data sheets and interfacial tension measurements. The data is obtained according to section 6.3.4.	148
7.3	Numerical parameters used to calculate the interface deflection.	164